Yijian Zeng

Coupled Dynamics in Soil

Experimental and Numerical Studies of Energy, Momentum and Mass Transfer

Springer

Springer Theses

Recognizing Outstanding Ph.D. Research

Aims and Scope

The series "Springer Theses" brings together a selection of the very best Ph.D. theses from around the world and across the physical sciences. Nominated and endorsed by two recognized specialists, each published volume has been selected for its scientific excellence and the high impact of its contents for the pertinent field of research. For greater accessibility to non-specialists, the published versions include an extended introduction, as well as a foreword by the student's supervisor explaining the special relevance of the work for the field. As a whole, the series will provide a valuable resource both for newcomers to the research fields described, and for other scientists seeking detailed background information on special questions. Finally, it provides an accredited documentation of the valuable contributions made by today's younger generation of scientists.

Theses are accepted into the series by invited nomination only and must fulfill all of the following criteria

- They must be written in good English.
- The topic should fall within the confines of Chemistry, Physics, Earth Sciences, Engineering and related interdisciplinary fields such as Materials, Nanoscience, Chemical Engineering, Complex Systems and Biophysics.
- The work reported in the thesis must represent a significant scientific advance.
- If the thesis includes previously published material, permission to reproduce this must be gained from the respective copyright holder.
- They must have been examined and passed during the 12 months prior to nomination.
- Each thesis should include a foreword by the supervisor outlining the significance of its content.
- The theses should have a clearly defined structure including an introduction accessible to scientists not expert in that particular field.

Yijian Zeng

Coupled Dynamics in Soil

Experimental and Numerical Studies
of Energy, Momentum
and Mass Transfer

Doctoral Thesis accepted by
University of Twente, The Netherlands

Springer

Author
Dr. Yijian Zeng
Faculty of Geo-Information Science
   and Earth Observation
Water Resource Department
University of Twente
Enschede
The Netherlands

Supervisor
Prof. Z. Su
Faculty of Geo-Information Science
   and Earth Observation
Water Resource Department
University of Twente
Enschede
The Netherlands

Printed on acid-free paper

Dedicated to my parents (曾积专 & 李秀珠)

Supervisor's Foreword

In arid and semiarid areas, surface evaporation is among the main components of land surface process. In the top soil layer, the coupled heat and mass flux is the dominant flux controlling the evaporation process, influencing local climate patterns, and playing a critical role in maintaining the local ecosystem.

In order to understand the importance of surface evaporation, Yijian Zeng systematically investigated the theory on coupled moisture and heat transport in the soil developed by Philip and de Vries in 1957 (thereafter PdV theory). The PdV theory postulated that vapor transfer in the soil would be enhanced due to the local air temperature gradient, which accelerates the pore-scale condensation and evaporation processes. However, because of the difficulties to observe this pore-scale process, many researchers have questioned the existence and physics basis of the vapor enhancement. The author decided to tackle the enhanced vapor transfer in the PdV theory as the key issue.

Although the enhanced vapor diffusion was proven to be present in the soil and the omission of vapor convection in PdV theory had been pointed out by many researchers, there was no satisfactory explanation of the mechanism involved after more than a decade of debates. The author is the first to tackle this issue by using a two-phase heat and mass transport model. He analysed the airflow effects on surface evaporation and pointed out the necessity of including airflow mechanism in land surface process studies.

With a control sand bunker experiment, Yijian discovered how the thermal or isothermal soil moisture fluxes can alternatively dominate in soil on a daily scale. In order to generalize this finding to a natural environment, he designed a field experiment in the Badain Jaren Desert. With detailed observation of micrometeorological and soil physics parameters, he assessed how much precipitation could be evaporated and how much could be conserved in the sand. This helps to understand how the evaporation process can be explained by the PdV model, and can be subsequently used to evaluate the water sources for desert plants.

On the basis of the experimental analysis, he realized that the single-phase transport mechanism of the PdV theory cannot explain the discrepancy between model estimates and field observations of vapor fluxes in the soil. In order to

overcome this, he built a two-phase heat and mass transport model to consider vapor transport with diffusion, advection, and dispersion mechanism, based on previous works. The results show that the newly developed model outperforms the PdV model in calculating surface evaporation by comparison with field observations in desert. This supports that the vapor convection should be taken into account in the PdV model, especially in desert areas.

To further explain why the newly developed model is better than the PdV model in the desert, Yijian conducted an insightful investigation on the driving forces of the two models. He found that the difference between the two models can be attributed to the movement of vapor from the atmosphere to the soil. Furthermore, in order to understand how a changing climate can affect patterns of evaporation at a regional scale, he investigated the use of the newly developed model in a data assimilation framework to retrieve soil moisture and temperature profiles. This opens a new avenue for retrieving profile information that is not directly observable by Earth Observation of land surface properties.

Enschede, August 2012   Prof. Z. Su

Acknowledgments

This story may track back to a discussion between Prof. Bob Su and Prof. Li Wan about a phenomenon they found from a satellite map, from which they found the upward latent heat flux at night. To understand that seeming conflict with the normal knowledge of evaporation, Prof. Li Wan and Wenbing Cao from Chinese University of Geosciences (Beijing) conducted a field experiment on a sand dune located in Gansu Province, North Western China. The experiment was designed to check if there was a loss of soil water content at night. The result of that experiment convinced Prof. Wan to continue this topic. I was one of the main investigators involved in this interesting topic. Prof. Wan was a visionary promoter to self-finance me to carry out several experiments for understanding the phenomenon.

The preliminary experimental results suggested that the coupled moisture and heat transport in the soil should be the key to explain the phenomenon. In 2007, I was fortunate to have Bob Su as my promoter and supervisor, who offered me a PhD scholarship to dig deeper into this topic. Since then, my research has been on a platform I could not have reached before, with strong and robust supports and guidance. After the qualification, I went to conduct the fieldwork in the Badain Jaran Desert, where one can find a unique landscape of coexisting sand dunes and lakes. Such a unique landscape had been attracting the continuous attention of hydrologists to investigate the water cycle in the desert, where the soil water dynamics in the unsaturated soil is characterized by the dominant vapor transport. This represents the extremely strong coupled moisture and heat transport process in the soil. The understanding of the soil–water dynamics in such areas may explain the phenomenon mentioned in the first paragraph.

Although many difficulties stood before conducting an in situ measurement in the Badain Jaren desert, Prof. Su, Prof. Wen and Prof. Wan gave their full support for this experiment. Fortunately, their support finally led me to present this book. As can be understood from its involved origin, this book required the help from many people, whom I gratefully remember.

I owe my deepest gratitude to Prof. Li Wan for his patient and constructive suggestions and guidance at the beginning of the research. He is the professor

who introduced me how to do research and how to present scientific results. My most deeply felt appreciation goes to his recommendation of me to Prof. Bob Su.

I feel most deeply indebted to Prof. Dr. Ir. Bob Su for his deep and useful discussions and suggestions, and countless remarks pinpointed on each chapter. The book could not be in the current state without his patient reviews and rechecks. He even pointed out a very unnoticeable mistake (e.g. a differentiable term outside a differentiation operator), which had escaped my eyes. I am most grateful to him for his efforts to support me in spending time with occupations other than writing this book. His consistent supports, enlightenments, and encouragements, during the research and the writing are the driving forces behind pursuing this degree.

I am deeply indebted to Prof. Jun Wen for his efforts to organize the field campaign to the Badain Jaran Desert, for his help in conducting the laboratory experiment, and for his efforts to edit the experimental results to reach the publication standard. I am also indebted to him for his efforts to make me the co-supervised Ph.D. candidate in ITC.

Many people participated in the data collection activity in the Badain Jaran Desert and the sand bunker experiment and I remain indebted to them. To Dr. Tangtang Zhang of CAREERI, I am indebted for his friendship during these years, his efforts to ensure the installation of sensors and instruments, and for his supportive company during the field campaign. I am indebted to Dr. Hui Tian, Dr. Xiaokang Shi, Dr. Rong Liu, Dr.Leihua Chen for participating in the data collection program for the Badain Jaran Desert experiment. To Dr. Xiaowei Jiang, Dr. Deqiang Mao, Dr. Bing Gong, Dr. Liangping Li, Msc. Zhenlei Yang, Msc. Xingxing Kuang, and Msc. Yujie Liu for their nocturnal work to record the measurements during the sand bunker experiment.

Many thanks are due to Prof. Xiaomei Jin for her mental and practical support during my research. To Prof. Xusheng Wang, I am indebted for his enlightenments and insightful discussions during the research. I am indebted to Prof. Chuanping Feng and Prof. Dameng Liu for their support and offers in practicing my ability to organize international conferences. Many thanks are due to Prof. Wenbing Cao for his interests, supports, and discussions on my research. I feel personally indebted to Dr. Liang Zhao for his friendship and his efforts to assist me when I needed.

I am indebted to my WRS colleagues for their support and company during these years. Special thanks to Alain, Enrico, Fouad, Joris, Mariela, Laura, Mireia, Leo, Guido, Mustafa, Chandra, Tanvir, Haris, Syarif, Kitsiri, Lau, Alex and Jennifer, Marcel van Helvoirt, Christiaan, Rogier, Suhyb. I am grateful to Ms. Anke de Koning, Ms. Tina Butt-Castro, Ms. Loes Colebrander for their warmest support and suggestions during the research. Many thanks are due to Drs. Marga Koelen, Carla and the library colleagues for their help in collecting literature. I am appreciative to Ms. T.B. van den Boogaard and her colleagues for their assistance. Many thanks are due to Eva Skidmore for her useful corrections of English. Many thanks are due to David Rossiter for his patience and efforts in reading this book and correcting typographical errors and wrong spellings.

Contents

Chapter 1
General Introduction

1.1 Scientific Background

1.1.1 Soil Moisture

In unsaturated soils, soil water transport has both a liquid and a vapor phase. This implies the frequent exchange of mass and energy between liquid and vapor. Such a coupled soil moisture and heat transport mechanism in the top shallow soil layer reflects the land surface process, which plays a critical role in partitioning the precipitation into surface runoff, evaporation, and groundwater recharge. Simultaneously, it controls the conversion of incoming solar and atmospheric radiation into sensible, latent, and radiant heat loss. One of the key parameters in the land surface process is soil moisture.

Soil moisture could potentially affect the global climate and is considered a critical factor by global change studies [29, 50]. There are many existing land surface schemes, which provide boundary conditions for global climate models and atmospheric weather prediction models, estimating the exchange of energy, heat and water vapor between the land surface and the atmosphere [24]. All these schemes are based on parameterization of plot scale sensible heat and moisture transfers in the soil–vegetation–atmosphere system and scaled up to a model grid using a statistical approach. To a large extent the treatment of soil moisture processes determines the amount of exchange taking place in these schemes, consequently influencing other variables in the atmosphere (e.g. cloud and precipitation).

However, due to high nonlinearities, moisture retention hysteresis, soil heterogeneity and multiple length and time scales, soil moisture transport is difficult to model. The usual approach to solving the numerical model of water flow in the soil involves the assumption that soil water flow is a single-phase flow (e.g. liquid phase). This assumption causes the discrepancy between model-calculated and field-measured soil moisture fluxes. This discrepancy led to the pioneering work by Philip and de Vries [73], who developed a coupled moisture and heat transport

model (hereafter PdV model) considering the enhanced water vapor transport in an effort to eliminate this discrepancy. Their work advanced hydrological research in the arid and semi-arid regions [8, 62], where the soil moisture variation in bare soil is characterized by vapor transport in the upper soil layer, while water movement in the liquid phase is negligible, as the surface layer is extremely dry [35, 36, 85]. Dominant vapor transport in the surface soil layer can result in cumulative reservation of water in the unsaturated zone [86–88] and play a critical role in maintaining the vegetation as well as the whole ecosystem in arid areas [94]. However, although the PdV model improves the estimation of soil moisture flux, the discrepancy still partly exists.

1.1.2 Land Surface Models and Data Assimilation System

Even though modelling soil moisture is difficult, as mentioned above, the importance of soil moisture has resulted in a large number of land surface models to investigate the exchange of energy, mass and momentum between the atmosphere and the land surface. However, the complex interactions between numerous intricate land-surface processes make it impossible, and probably unnecessary, to integrate all the details of these processes into a numerical scheme. Hence, most land surface models (LSMs) are based on various simplifications and parameterizations of evapotranspiration [61, 100], soil moisture [52, 59, 102], surface energy [21, 101, 118], snow [119], runoff [56, 58], vegetation [19, 22, 69], or interception [23, 113], to name a selection. According to Sellers (91), these parameterizations in land-surface processes can be defined with a wide range of LSMs from the first generation with roots in Manabe's philosophy [59] to the third generation that originate from Deardorff's research [19].

Most aforementioned LSMs have been extensively incorporated into atmospheric general circulation models (AGCMs) to investigate land-atmosphere coupling strength [51]. A problem in the land-surface/atmosphere coupling simulation is that the space–time scales of evolutions between AGCMs and land-surface processes differ greatly. This problem cannot be explicitly resolved within numerical model discretization [27]. Numerical weather prediction (NWP) usually requires initialization of global or regional AGCMs at 6-hourly intervals for all land prognostic variables in the entire three-dimensional domain. Compared to such requirements, in situ measurements of the earth system and satellite remote sensing observations are not sufficient [77], in spite of improved availability of varied data sources. Hence an alternative approach was developed, assimilating observed hydrological and climatological conditions into LSMs to produce continuous spatial and temporal land-surface state variables, which can subsequently be assimilated into AGCMs to forecast the state of the atmosphere [70]. A land data assimilation system (LDAS) [40] has been developed to implement this alternative approach, using advanced land surface modeling and data assimilation techniques. LDAS aims to constrain spatial and temporal errors in

land-surface prognostic variables (e.g. soil moisture and temperature), providing optimal initialization for AGCMs by interpolating/extrapolating the remote sensing and ground-based observation data. LDAS thus aims to determine the best possible representation of the coupled land-surface/atmosphere system.

1.1.3 A Brief History of Hydrological Data Assimilation

In essence, the application of data assimilation methods to hydrological problems can be put into the category of land surface data assimilation, as it aims to utilize hydrological process knowledge incorporated in a land surface model, as well as information gained from observations. There have been several reviews on hydrological data assimilation. Most recently, Houser et al. [45] gave a brief history of hydrological data assimilation and described the data assimilation techniques used. The direct insertion assimilation method was used first in hydrological problems [6, 46, 76]. Then, the statistically optimal techniques [i.e. the Kalman filter (KF) and the extended Kalman filter (EKF)] were implemented by Milly [64] and Milly and Kabala [65]. Years later Entekhabi et al. [28] and Galantowicz et al. [32] extended the application of optimal estimation techniques, assimilating synthetically-derived data and field observations into a one-dimensional soil moisture and temperature diffusion model, using the EKF. Since then, there have been many one-dimensional KF/EKF assimilation studies, such as Walker et al.'s [110, 111] work on assimilating soil moisture and temperature profile using synthetic data, which has been widely recognized.

Above-mentioned research mainly focused on classical one-dimensional soil water diffusion models for point profile estimation, where statistical rigour could be applied due to the low computational requirements. When the problem size increased from one dimension to three dimensions and even to the catchment/ continental scale, applying statistical rigour became more difficult. The KF and the EKF proved impractical for large, highly nonlinear, three-dimensional models [30]. Nevertheless, Georgakakos and Baumer [33] and Walker et al. [110] used the KF to update a hydrologic basin model with near-surface soil moisture measurements and to use the three-dimensional KF based assimilation in a small catchment distributed hydrologic model.

To solve the large-scale problems, the Ensemble Kalman Filter (EnKF) was widely applied to satisfy the requirements for field estimations. For lumped spatial field estimations (e.g. single soil column or point-scale), Crow [14] used EnKF to correct for the impact of poorly sampled rainfall data on land surface predictions of root-zone soil moisture and surface energy fluxes, through daily assimilation of brightness temperature observations. Crow and Wood [15] also applied EnKF to compensate for errors due to the use of climatological rainfall data in predictions of surface latent heat flux and root-zone water storage, by assimilating remotely sensed soil brightness temperatures using point-scale TOPLATS results at two sites. Apart from EnKF, EKF was also applied at a single site by Wilker et al. [116]

to show the representativeness error induced by not properly representing soil moisture from the NWP of the ECMWF. However, Reichle et al. [79, 80] were among the first to assess the performance of the EnKF in hydrological data assimilation and compare this to the performance of the EKF. Since then, the application of the EnKF in hydrological problems has received wide attention. Hydrological models that have used the EnKF include the one-dimensional Richards' equation [16], the three-dimensional saturated groundwater flow [78, 112] and transport model [57], a snow model [96], a distributed hydrological model [11], an integral-balance saturated-unsaturated subsurface model [95] as well as land surface models [55].

Land surface data assimilation represents the conjunction between data assimilation and land surface models, and is frequently studied to improve the accuracy of retrieving soil moisture content and soil temperature in the topsoil and root zone layer [105]. Apart from estimating the soil state variables, the land surface data assimilation is also applied to issues such as the impact of observation frequency [109] and of model bias [17, 18, 81], parameter estimation [10, 49], a combined state and parameter estimation [104], and dual estimation using two interactive filters or optimization procedures [34, 68, 108].

Since the conceptual framework of the LDAS was established [66], LDAS systems have been developed at a varying range of scales with near real-time and high spatial resolutions, such as the NLDAS [13], the ELDAS [106], and the GLDAS [83]. The specific assimilation approach of the NLDAS is a 4-dimensional data assimilation system [67]; the ELDAS [102] employs a simplified EKF developed by Seuffert et al. [93]; while the GLDAS [83] includes several data assimilation approaches such as the EnKF, the EKF, optimal interpolation (OI), and hybrid insertion techniques. The GLDAS is actually based on a land information system (LIS) developed by the hydrological sciences branch at NASA's Goddard Space Flight Center [53].

1.2 Problem Statement

With the scientific background mentioned above, this thesis tries to identify the basic study topics related to soil moisture and LSMs and LDAS, from a physical process point of view. For soil moisture, the focus of this study is to understand the enhanced vapor transport concept of the PdV model, which is the core of soil water dynamics in arid and semi-arid areas. For LSMs and LDAS, this study tries to investigate the performance of LSMs in hydrological data assimilation system, which is essential to retrieving soil moisture and soil temperature successfully. The rest of Sect. 1.2 will state the problems related to the above-mentioned topics, and the problem definition is presented at the end of the section.

1.2.1 Enhanced Vapor Transport

The major contribution of the PdV model is the enhanced vapor transport theory [73], which includes two parts: (i) pore-level phase change effects within liquid islands between solid particles. The temperature-gradient-induced liquid flow through the island equals the rate of evaporation and condensation, and the total flux adjusts itself to equal the vapor flux in the air-filled pore; and (ii) the local temperature gradient in the air-filled pores, which may be significantly higher than the average temperature gradient as a result of different thermal conductivities. The concurrent vapor and liquid flux through a series of liquid islands forms the basis of the PdV model, considering the microscopic thermal gradient in air-filled pores. However, due to the lack of evidence gained from direct measurements, the enhanced vapor transport has been questioned for more than a decade, ever since Webb and Ho's [115] comprehensive review.

The PdV enhancement factor is analogous to the expression derived from the thermodynamic theory of irreversible processes [48], and its existence has been examined experimentally, studying pore-scale condensation and evaporation [37]. According to Webb and Ho's statement [115], the PdV enhancement factor is limited to temperature gradient. There is no enhancement if there is no temperature gradient. The above-described facts actually demonstrated that the PdV enhancement factor should be taken into account when there is a pore-scale condensation and evaporation process (i.e. the existence of liquid islands and a local temperature gradient in the air-filled pores). However, the limitation of the PdV enhancement factor is that it cannot account for the enhanced vapor diffusion induced by a concentration gradient under isothermal conditions [115], the mechanism of which has been suggested to be included in the PdV enhancement factor. Webb and Ho [114] even suggested that gas and vapor diffusion should be treated differently. Gas diffusion decreases slightly in the presence of liquid islands, while vapor diffusion may be considerably enhanced.

The above-mentioned literature illustrates that the PdV enhancement factor exists when there are liquid islands between particles under temperature gradient. At the same time, other mechanisms, such as concentration-gradient-induced vapor diffusion, should be taken into account. The dry air concentration-gradient-forced vapor diffusion can be one of these mechanisms. Although the PdV model improves the theoretical predication of water vapor flux in the soil, compared to the "simple theory" [39, 84, 97, 98, 100, 103], it doesn't consider a two-phase flow mechanism to include soil airflow induced by a dry air concentration gradient. The water vapor transport is actually the gaseous phase transport of soil water, and is a two-phase flow problem [89]. The application of Richards' approximation (i.e. the dry air in the soil is regarded as an inert gas) has caused discrepancy between theory prediction and field data. Examples are the significant underestimation of the magnitude and direction of vapor flux predicted by the PdV theory [9], or the noticeable difference in the redistribution pattern of soil moisture and temperature between prediction and measurement [41]. Both studies suggested that

further development of the PdV theory to improve the description of field conditions will need to consider additional mechanisms. Although the additional mechanisms are not mentioned specifically, the gas phase flow, involving dry air and vapor flow, is recognized to be an important mechanism that needs to be taken into account.

Actually, there are three transport mechanisms for vapor transfer in the soil: diffusion, advection and dispersion. The PdV model only considers diffusion of water vapor in the soil. The enhancement factor of the PdV model enhances the driving force for vapor diffusion (e.g. the microscopic thermal gradient in air-filled pores). It is necessary to consider all vapor transport mechanisms in the soil to estimate the soil moisture flux realistically. With the two-phase mass and heat flow mechanism, not only diffusion can be considered, but advection of vapor transfer (e.g. as part of bulk flow of air driven by dry air pressure gradient) as well. When advection and diffusion are both considered, the dispersion of vapor transfer should also be taken into account.

1.2.2 LSMs Performance

While LDAS systems aim to provide optimal fields of land surface state variables and fluxes, LSMs-generated soil moisture data are often prone to error due to insufficient model physics, inaccurate parameterization, initialization states, and forcing data [45, 72]. Soil moisture in LSMs is usually regarded more as an index used for land-surface water balance calculations rather than as a representation of the physically-based moisture data [82] Seneviratne et al. [92]. The model-specific indexation makes it inappropriate to directly transfer one LSM's soil moisture into another LSM for land-atmosphere coupling strength studies [52].

In order to systematically analyse the reason for the imperfect indexation of soil moisture and improve its transferability in the coupled land-surface/atmosphere system, extensive studies on evaluating model performance have been ongoing for the past several decades [31]. The early-stage evaluations usually involve comparing simulations with ground-based measurements, focusing on certain parts of the hydrological processes [82], or using the earlier version of the same LSM as benchmark [19, 90]. Since Bastidas (5) and Gupta [38] introduced the multi-criteria method to analyse the sensitivity of land-surface parameterizations, model performance has typically been evaluated by searching for sets of parameters that minimize the error across multiple model responses [43, 117]. The multi-criteria method provides a more rigorous framework for analysis of multi-input/multi-output models of dynamic earth system responses than the traditional single-criterion approach [38], and helps to reduce the dimensionality of the parameter estimation problem for LSMs by identifying insensitive parameters that can safely be given default values regardless of the application site [5].

Along with the development of more complex LSMs in the past decade [74], more sophisticated statistical approaches have been adopted to evaluate the model

errors (and thus model performance). Abramowitz [1] benchmarked the performance of LSMs against that of a statistically-based Artificial Neural Network (ANN). The ANN captures the relationship between meteorological forcing and surface fluxes, solely based on observational data without knowing the biophysics or soil physics of LSMs. The philosophy behind applying an ANN is the question "If a LSM can outperform a simple statistical model without time dependency?" considering that an ANN has an instantaneous response to the atmospheric forcing data operating on a per time step basis [1]. The use of a statistical model as a benchmark for a physical LSM may assist modelers in understanding how much model-output residual (distance between model results and observations) is acceptable, what the weakness is of a LSM and if that can be overcome by developing a more physically-based representation of land-surface state variables (e.g. soil moisture and temperature) [75].

Most aforementioned statistical models are mainly used to identify the weaknesses of LSMs in order to improve the model physics [2, 70], to scale land-surface state variables for monitoring the real world's hydrological state [52], or to correlate soil moisture anomalies in the surface layer with anomalies in root zone soil moisture for surface-root zone coupling strength studies [54]. The statistical models can, for instance, provide statistical descriptions of the physical interactions between the land surface and the atmosphere, the surface moisture and the root-zone moisture, and between the instantaneous land-surface fluxes and the real-time meteorological variables. However, these statistical models have no mechanism to allow the internal state variables (e.g. soil moisture and temperature profile) to evolve with time [3].

The model performance evaluations focus on model development by identifying dominant parameters that dictate the physical realism of LSMs, responsible for the right physical interactions between land-surface and atmosphere. On the other hand, some of the key complexities have to be simplified in the operational off-line mode of LDAS, due to the far from comprehensive model-physics representation of the complicated feedbacks between the surface and the atmosphere. In order to understand the local conditions and processes in environmental or agricultural management studies, LSMs should be developed with a higher degree of complexity [26, 45]. Nonetheless, Beven [7] and Duan et al. [25] have stated that more complex LSMs result in more parameters to be estimated, probably leading to over-parameterization given the data typically available for calibration. Although it is precarious to over-parameterize land-surface processes [20], from the subsurface physical point of view, soil moisture and soil temperature are still under-parameterized, even though they are the most studied estimation variables in LSMs [12].

In land-atmosphere interaction studies, implementing operational schemes to assimilate remotely sensed observations or focusing on a certain specific purpose (e.g. retrieval of a soil moisture profile), the data assimilation system typically simplifies or avoids a number of key complexities in LSMs [99]. In terms of the assimilation of soil moisture and soil temperature, the most common simplification is the decoupling of concurrent flow of water and heat in soil [28]. However, the traditional coupled process model (e.g. the PdV model) has been proven to

perform better than the simplified model considering water vapor flux [47], which is crucially important in calculating evaporation, subsequently affecting the atmospheric modelling. Nevertheless, the vapor flow is only considered to be the result of vapor diffusion, while the gas-phase flow mechanism (e.g. vapor flow as part of the bulk flow of air in the soil) is ignored.

1.2.3 Problem Definition

This study, therefore, aims to tackle the following problems:

1. While the application of the PdV model has improved the estimation of soil moisture fluxes, the discrepancy between theory prediction and field data still exists. Although the need to consider additional mechanisms (e.g. gas-phase flow) has been recognized [9, 41], the inclusion of airflow mechanisms in the PdV model has not been explored and the uncertainty caused by this neglect has not been quantified.
2. The practical implementation of assimilating satellite data requires simplification of subsurface physics, leading to the popularity of decoupling the concurrent flow of soil water and heat (thus, no inclusion of airflow mechanism) in data assimilation systems [28]. However, ignoring the airflow mechanism in such a simplification may have a considerably negative impact on understanding the transport of CO_2, and other trace gases [60], as well as surface evaporation [120].

1.3 Statement of Objectives

In the coupled land-atmosphere system (vertical, one-dimensional), the land surface provides water and heat to the atmosphere through surface evaporation (latent heat flux) and sensible heat flux. To understand this coupled system, there is a need to have a physics-based land model (e.g. inclusion of airflow in the PdV model), combining water and heat dynamics in the soil and their transfer at the land–atmosphere interface. This study aims to understand soil water and heat dynamics taking the airflow mechanism into consideration, by developing a two-phase mass and heat flow model. In accordance with the problem statement, the specific objectives are:

1. **Development of a two-phase mass and heat transport model (Problem A)**
   This model is designed to include an airflow mechanism in the PdV model. In addition, in order to quantify the uncertainty caused by neglecting airflow, the two-phase flow model development will be based on the PdV model. Thus, the differences between the proposed model and the PdV model can be made explicit.

2. **To detect the impact of soil airflow on the evaporation (Problem A)**
   Evaporation occurs on the surface in initially wet conditions, and takes place
   below the surface when the soil dries. The impact of coupled moisture and heat
   transport on evaporation has been studied in detail by Milly [63] and Novak
   [71]. However, the effect of airflow on evaporation was not described, due to
   the lack of knowledge of soil airflow in these studies.
3. **To retrieve the soil moisture and temperature profile considering airflow
   with a data assimilation system (Problem B)**
   The importance of profile retrieval of soil state variables (moisture and tem-
   perature) by data assimilation has been discussed extensively [44, 32, 42, 110].
   However, the inclusion of airflow in a land model for retrieving soil state
   variable profiles has not been discussed in the context of data assimilation.
   There is a need to check the necessity of considering an airflow mechanism and
   how it performs in the data assimilation system for profile retrieval.

1.4 The Proposed Procedure

With these specific objectives in mind, the proposed procedure may be described as:

1. **Investigating the diurnal pattern of the coupled process using the PdV
   model**
   Before developing a two-phase mass and heat transport model, a full under-
   standing of the traditional theory (PdV model) is needed. The diurnal pattern of
   the coupled process can be constructed using the PdV model to analyse a field
   experiment.
2. **Exploring the hydrological application of the PdV model**
   It is worth exploring how the diurnal pattern may be used in a hydrological
   application (e.g. effective infiltration). Thus, the redistribution of soil moisture
   and temperature after rainfall will be examined.
3. **Understanding the impact of including/excluding airflow on the evaporation**
   To implement the second objective, a two-phase mass and heat flow model needs
   to be developed (the first objective). Then, the impact of airflow on surface
   evaporation will be examined to evaluate the performance of this model
   regarding hydrological applications, and to compare this with the PdV model.
4. **Investigating the mechanisms of the airflow impact**
   It is worthwhile to understand how the airflow affects the soil moisture fluxes,
   through investigating the driving forces and conductivities.
5. **Retrieving soil moisture and temperature profile with a data assimilation
   system**
   As final step, the developed model will be combined with a data assimilation
   system to retrieve soil state variable profiles considering the airflow mecha-
   nism. Its performance in the DAS will be compared to those of the PdV model
   and the simplest soil moisture and heat diffusion model.

1.5 Structure of the Thesis

To understand the soil water dynamics, two outdoor experiments (i.e. a sand bunker experiment and the Badain Jaran Desert experiment) have been designed to observe soil physical elements (e.g. soil moisture content, soil temperature and soil matric potential) and micro-meteorological elements (e.g. air temperature, relative humidity, solar radiations, wind speed, precipitation, and evaporation). In Chap. 2 the sand bunker experiment is used to investigate the diurnal pattern of the coupled moisture and heat transport process using the PdV model. To examine whether the diurnal pattern can be applied under real arid/semi-arid conditions, the Badain Jaran Desert experiment has been conducted. In Chap. 3, the hydrological application of the diurnal pattern of soil water dynamics is introduced.

Based on the understanding of the diurnal pattern derived with the PdV model, the two-phase mass and heat flow model is developed in Chap. 4. The difference between the newly developed model and the PdV model is discussed. The developed model is verified using two benchmark tests, one on soil water–air transport (i.e. isothermal two-phase mass flow), and the other on highly coupled soil moisture and heat transport (i.e. the extreme test case of the PdV model).

In Chap. 5, the Badan Jaran Desert experiment is used to validate the newly developed model. The comparison between the PdV model and the proposed model in calculating evaporation indicates the existence of an advective effect. The effect soil airflow has on soil moisture fluxes is discussed. The feasibility of retrieving soil state variable profiles in a data assimilation system is examined in Chap. 6, taking soil airflow into consideration. In the same chapter, the impact of the soil physics complexity on the performance of retrieving soil state variables is evaluated. Conclusions and discussion are presented in Chap. 7.

References

1. Abramowitz G (2005) Towards a benchmark for land surface models. Geophys Res Lett 32(22):L22702
2. Abramowitz G, Pitman A (2007) Systematic bias in land surface models. J Hydrometeorol 8(5):989–1001
3. Abramowitz G, Leuning R, Clark M, Pitman A (2008) Evaluating the performance of land surface models. J Clim 21(21):5468–5481
4. Bastidas LA, Gupta HV, Sorooshian S, Shuttleworth, WJ, Yang ZL (1999) Sensitivity analysis of a land surface scheme using multicriteria methods. J Geophys Res Atm 104(D16):19481–19490
5. Bastidas LA, Hogue TS, Sorooshian S, Gupta HV, Shuttleworth WJ (2006) Parameter sensitivity analysis for different complexity land surface models using multicriteria methods. J Geophys Res Atmos 111:D20101
6. Bernard R, Vauclin M, Vidal-Madjar D (1981) Possible use of active microwave remote sensing data for prediction of regional evaporation by numerical simulation of soil water movement in the unsaturated zone. Water Resour Res 17:1603–1610

7. Beven K (1989) Changing ideas in hydrology—the case of physically-based models. J Hydrol 105(1–2):157–172

8. Bittelli M, Ventura F, Campbell GS, Snyder RL, Gallegati F, Pisa PR (2008) Coupling of heat, water vapor, and liquid water fluxes to compute evaporation in bare soils. J Hydrol 362(3–4):191–205

9. Cahill AT, Parlange MB (1998) On water vapor transport in field soils. Water Resour Res 34(4):731–739

10. Chen Y, Zhang D (2006) Data assimilation for transient flow in geologic formations via ensemble Kalman filter. Adv Water Resour 29:1107–1122

11. Clark MP, Rupp DE, Woods RA, Zheng X, Ibbitt RP, Slater AG, Schmidt J, Uddstrom MJ (2008) Hydrological data assimilation with the ensemble Kalman filter: use of streamflow observations to update states in a distributed hydrological model. Adv Water Resour 31(10):1309–1324

12. Cornwell AR, Harvey LDD (2007) Soil moisture: a residual problem underlying AGCMs. Clim Chang 84(3–4):313–336

13. Cosgrove BA, Lohmann D, Mitchell KE, Houser PR, Wood EF, Schaake JC, Robock A, Sheffield J, Duan QY, Luo LF, Higgins RW, Pinker RT, Tarpley JD (2003) Land surface model spin-up behavior in the North American land data assimilation system (NLDAS). J Geophys Res Atmos 108(D22):8845

14. Crow WT (2003) Correcting land surface model predictions for the impact of temporally sparse rainfall rate measurements using an ensemble Kalman filter and surface brightness temperature observations. J Hydrometeorol 4:960–973

15. Crow W, Wood EF (2003) The assimilation of remotely sensed soil brightness temperature imagery into a land surface model using ensemble Kalman filtering: a case study based on ESTAR measurements during SGP97. Adv Water Resour 26:137–149

16. Das NN, Mohanty BP (2006) Root zone soil moisture assessment using remote sensing and vadose zone modeling. Vadose Zone J 5:296–307

17. De Lannoy GJM, Reichle RH, Houser PR, Pauwels VRN, Verhoest NEC (2007) Correcting for forecast bias in soil moisture assimilation with the ensemble Kalman filter. Water Resour Res 43(9):W09410

18. De Lannoy GJM, Houser PR, Verhoest NEC, Pauwels VN (2009) Adaptive soil moisture profile filtering for horizontal information propagation in the independent column-based CLM2.0. J Hydrometeorol 10:766–779

19. Deardorff JW (1978) Efficient prediction of ground surface-temperature and moisture, with inclusion of a layer of vegetation J Geophys Res Ocean Atmos 83(NC4):1889–1903

20. Demaria EM, Nijssen B, Wagener T (2007) Monte Carlo sensitivity analysis of land surface parameters using the Variable Infiltration Capacity model. J Geophys Res Atmos 112(D11):D11113

21. Desborough CE (1999) Surface energy balance complexity in GCM land surface models. Clim Dyn 15(5):389–403

22. Dickinson RE, Henderson-Sellers A, Kennedy PJ, Wilson MF (1986) Biosphere atmosphere transfer scheme (BATS) for the NCAR community climate model. NCAR technical note, pp 72

23. Dickinson RE, Henderson-Sellers A, Rosenzweig C, Sellers PJ (1991) Evapotranspiration models with canopy resistance for use in climate models- a review. Agric For Meteorol 54(2–4):373–388

24. Dickinson RE, Oleson KW, Bonan G, Hoffman F, Thornton P, Vertenstein M, Yang Z, Zeng X (2006) The community land model and its climate statistics as a component of the community climate system model. J Clim 19(11):2302–2324

25. Duan QY, Sorooshian S, Gupta V (1992) Effective and efficient global optimization for conceptual rainfall-runoff models. Water Resour Res 28(4):1015–1031

26. Ek MB, Mitchell KE, Lin Y, Rogers E, Grunmann P, Koren V, Gayno G, Tarpley JD (2003) Implementation of Noah land surface model advances in the National Centers for

Environmental Prediction operational mesoscale Eta model. J Geophys Res Atmos 108(D22):8851

27. Entekhabi D, Eagleson PS (1991) Climate and the equilibrium state of land surface hydrology parameterizations. Surv Geophys 12(1–3):205–220
28. Entekhabi D, Nakamura H, Njoku EG (1994) Solving the inverse problems for soil-moisture and temperature profiles by sequential assimilation of multifrequency remotely-sensed observations. IEEE Trans Geosci Remote Sens 32(2):438–448
29. Entekhabi D, Njoku E, Houser P, Spencer M, Doiron T, Smith J, Girard R, Belair S, Crow W, Jackson T (2004) The hydrosphere state (HYDROS) mission concept: an earth system pathfinder for global mapping of soil moisture and land freeze/thaw. IEEE Trans Geosci Remote Sens 42(10):2184–2195
30. Evensen G (2006) Data assimilation: the ensemble Kalman filter. Springer, New York
31. Fox S, Pitman AJ, Boone A, Habets F (2006) The relationship between intermodel differences and surface energy balance complexity in the Rhone-Aggregation Intercomparison Project. J Hydrometeorol 7(1):81–100
32. Galantowicz JF, Entekhabi D, Njoku EG (1999) Tests of sequential data assimilation for retrieving profile soil moisture and temperature from observed L-band radiobrightness. IEEE Trans Geosci Remote Sens 37(4):1860–1870
33. Georgakakos KP, Baumer OW (1996) Measurement and utilization of on-site soil moisture data. J Hydrol 184:131–152
34. Gove JH, Hollinger DY (2006) Application of a dual unscented Kalman filter for simultaneous state and parameter estimation in problems of surface atmosphere exchange. J Geophys Res Atmos 111:D08S07
35. Gowing JW, Konukcu F, Rose DA (2006) Evaporative flux from a shallow watertable: the influence of a vapor–liquid phase transition. J Hydrol 321:77–89
36. Grifoll J, Cohen Y (1999) A front-tracking numerical algorithm for liquid infiltration into nearly dry soils. Water Resour Res 35(8):2579–2585
37. Gu LM, Ho CK, Plumb OA, Webb SW (1998) Diffusion with condensation and evaporation in porous media. Sandia National Laboratories, SAND98-0618C Albuquerque, NM, USA
38. Gupta HV, Bastidas LA, Sorooshian S, Shuttleworth WJ, Yang ZL (1999) Parameter estimation of a land surface scheme using multicriteria methods. Jeophys Res Atmos 104(D16):19491–19503
39. Gurr CG, Marshall TJ, Hutton JT (1952) Movement of water in soil due to a temperature gradient. Soil Sci 74(5):335–345
40. Hazeleger W, Severijns C, Semmler T, Stefanescu S, Yang ST, Wang XL, Wyser K, Dutra E, Baldasano JM, Bintanja R, Bougeault P, Caballero R, Ekman AML, Christensen JH, van den Hurk B, Jimenez P, Jones C, Kallberg P, Koenigk T, McGrath R, Miranda P, Van Noije T, Palmer T, Parodi JA, Schmith T, Selten F, Storelvmo T, Sterl A, Tapamo H, Vancoppenolle M, Viterbo P, Willen U (2010) EC-earth a seamless earth-system prediction approach in action. Bull Am Meteorol Soc 91(10):1357–1363
41. Heitman JL, Horton R, Ren T, Nassar IN, Davis DD (2008) A test of coupled soil heat and water transfer prediction under transient boundary temperatures. Soil Sci Soc Am J 72(5):1197–1207
42. Hoeben R, Troch PA (2000) Assimilation of active microwave observation data for soil moisture profile estimation. Water Resour Res 36(10):2805–2819
43. Hogue TS, Bastidas L, Gupta H, Sorooshian S, Mitchell K, Emmerich W (2005) Evaluation and transferability of the Noah land surface model in semiarid environments. J Hydrometeorol 6(1):68–84
44. Houser PR, De Lannoy GJM, Walker JP (2010). Land surface data assimilation. In: Lahoz W, Khattatov B, Menard R (eds) Data assimilation: making sense of observation. Springer, Heidelberg, pp 549–597
45. Houser PR, Shuttleworth WJ, Famiglietti JS, Gupta HV, Syed KH, Goodrich DC (1998) Integration of soil moisture remote sensing and hydrologic modeling using data assimilation. Water Resour Res 34(12):3405–3420

46. Jackson TJ, Schmugge TJ, Nicks AD, Coleman GA, Engman ET (1981) Soil moisture updating and microwave remote sensing for hydrological simulation. Hydrol Sci Bull 26:305–319

47. Jassal RS, Novak MD, Black TA (2003) Effect of surface layer thickness on simultaneous transport of heat and water in a bare soil and its implications for land surface schemes. Atmos Ocean 41(4):259–272

48. Jury WA, Letey JJ (1979) Water vapor movement in soil: reconciliation of theory and experiment. Soil Sci Soc Am J 43(5):823–827

49. Katul G, Wendroth O, Parlange MB, Puente CE, Folegatti MV, Nielsen DR (1993) Estimation of in situ hydraulic conductivity function from nonlinear filtering theory. Water Resour Res 29:1063–1070

50. Kerr YH, Waldteufel P, Wigneron JP, Martinuzzi J, Font J, Berger M (2001) Soil moisture retrieval from space: the soil moisture and ocean salinity (SMOS) mission. Geoscience and Remote Sensing, IEEE Transactions on Geoscience and Remote Sensing 39(8):1729–1735

51. Koster RD, Guo ZC, Dirmeyer PA, Bonan G, Chan E, Cox P, Davies H, Gordon CT, Kanae S, Kowalczyk E, Lawrence D, Liu P, Lu CH, Malyshev S, McAvaney B, Mitchell K, Mocko D, Oki T, Oleson KW, Pitman A, Sud YC, Taylor CM, Verseghy D, Vasic R, Xue YK, Yamada T (2006) GLACE: the global land-atmosphere coupling experiment. Part I: Overview. J Hydrometeorol 7(4):590–610

52. Koster RD, Guo ZC, Yang RQ, Dirmeyer PA, Mitchell K, Puma MJ (2009) On the nature of soil moisture in land surface models. J Clim 22(16):4322–4335

53. Kumar SV, Reichle RH, Peters-Lidard CD, Koster RD, Zhan XW, Crow WT, Eylander JW, Houser PR (2008) A land surface data assimilation framework using the land information system: description and applications. Adv Water Res 31(11):1419–1432

54. Kumar SV, Reichle RH, Koster RD, Crow WT, Peters-Lidard CD (2009) Role of subsurface physics in the assimilation of surface soil moisture observations. J Hydrometeorol 10(6):1534–1547

55. Li J, Islam S (1999) On the estimation of soil moisture profile and surface fluxes partitioning from sequential assimilation of surface layer soil moisture. J Hydrol 220(1–2):86–103

56. Liang X, Xie ZH (2001) A new surface runoff parameterization with subgrid-scale soil heterogeneity for land surface models. Adv Water Resour 24(9–10):1173–1193

57. Liu G, Chen Y, Zhang D (2008) Investigation of flow and transport processes at the MADE site using ensemble Kalman filter. Adv Water Resour 31:975–986

58. Liu JM, Ding YG, Zhou XJ, Li Y (2010) A parameterization scheme for regional average runoff over heterogeneous land surface under climatic rainfall forcing. Acta Meteorologica Sinica 24(1):116–122

59. Manabe S (1969) Climate and ocean circulation. 1. Atmospheric circulation and hydrology of earth's surface. Mon Weather Rev 97(11):739–774

60. Massman WJ (2006) Advective transport of CO_2 in permeable media induced by atmospheric pressure fluctuations: 1. An analytical model. J Geophys Res Biogeosci 111:G03004

61. Mihailovic DT, Rajkovic B, Lalic B, Dekic L (1995) Schemes for parameterizing evaporation from a non-plant-covered surface and their impact on partitioning the surface-energy in land air exchange parameterization. J Appl Meteorol 34(11):2462–2475

62. Milly PCD (1982) Moisture and heat transport in hysteretic, inhomogeneous porous media: a matric head-based formulation and a numerical model. Water Resour Res 18(3):489–498

63. Milly PCD (1984) A simulation analysis of thermal effects on evaporation from soil. Water Resour Res 20(8):1087–1098

64. Milly PCD (1986) Integrated remote sensing modelling of soil moisture: sampling frequency, response time, and accuracy of estimates. Integrated design of hydrological networks. In: Proceedings of the Budapest Symposium, Budapest, IAHS Publication No 158, pp 201–211

65. Milly PCD, Kabala Z (1986) Integrated modelling and remote sensing of soil moisture. Hydrologic applications of space technology. In: Proceedings of the Cocoa beach workshop, Florida, IAHS Publication No 160, pp 331–339
66. Mitchell KE, Houser PR, Wood EF, Schaake JC, Tarpley JD, Lettenmaier DP, Higgins RW, Marshall C, Lohmann D, Ek M (1999) GCIP land data assimilation system (LDAS) project now underway. GEWEX News 9:3–6
67. Mitchell KE, Lohmann D, Houser PR, Wood EF, Schaake JC, Robock A, Cosgrove BA, Sheffield J, Duan QY, Luo LF, Higgins RW, Pinker RT, Tarpley JD, Lettenmaier DP, Marshall CH, Entin JK, Pan M, Shi W, Koren V, Meng J, Ramsay BH, Bailey AA (2004) The multi-institution North American land data assimilation system (NLDAS): utilizing multiple GCIP products and partners in a continental distributed hydrological modeling system. J Geophys Res Atmos 109:D07S90
68. Moradkhani H, Sorooshian S, Gupta HV, Houser PR (2005) Dual state-parameter estimation of hydrological models using ensemble Kalman filter. Adv Water Resour 28:135–147
69. Muchoney D, Strahler A (2002) Regional vegetation mapping and direct land surface parameterization from remotely sensed and site data. Int J Remote Sens 23(6):1125–1142
70. Nijssen B, Bastidas LA (2005) Land-atmosphere models for water and energy cycle studies. In: Anderson MG (ed) Encyclopedia of hydrological sciences. Wiley, Chichester, pp 3089–3101
71. Novak MD (2010) Dynamics of the near-surface evaporation zone and corresponding effects on the surface energy balance of a drying bare soil. Agr Forest Meteorol 150(10): 1358–1365
72. Ni-Meister W (2008) Recent advances on soil moisture data assimilation. Phys Geogr 29(1):19–37
73. Philip JR, de Vries DA (1957) Moisture movement in porous materials under temperature gradient. Trans Am Geophys Union 38(2):222–232
74. Pitman AJ (2003) The evolution of, and revolution in, land surface schemes designed for climate models. Int J Climatol 23(5):479–510
75. Pitman AJ, Abramowitz G (2005) What are the limits to statistical error correction in land surface schemes when projecting the future? Geophys Res Lett 32(L14403):4
76. Prevot L, Bernard R, Taconet O (1984) Evaporation from a bare soil evaluated using a soil water transfer model and remotely sensed surface soil moisture data. Water Resour Res 20:311–316
77. Reichle RH (2008) Data assimilation methods in the earth sciences. Adv Water Resour 31(11):1411–1418
78. Reichle RH, Koster RD (2003) Assessing the impact of horizontal error correlations in background fields on soil moisture estimation. J Hydrometeorol 4(6):1229–1242
79. Reichle RH, McLaughlin DB, Entekhabi D (2002) Hydrologic data assimilation with the ensemble Kalman filter. Mon Weather Rev 130(1):103–114
80. Reichle RH, Walker JP, Koster RD, Houser PR (2002) Extended versus ensemble Kalman filtering for land data assimilation. J Hydrometeorol 3(6):728–740
81. Reichle RH, Crow WT, Keppenne CL (2008) An adaptive ensemble Kalman filter for soil moisture data assimilation. Water Resour Res 44(3):W03423
82. Robock A, Schlosser CA, Vinnikov KY, Speranskaya NA, Entin JK, Qiu S (1998) Evaluation of the AMIP soil moisture simulations. Global Planet Change 19(1–4):181–208
83. Rodell M, Houser PR, Jambor U, Gottschalck J, Mitchell K, Meng CJ, Arsenault K, Cosgrove B, Radakovich J, Bosilovich M, Entin JK, Walker JP, Lohmann D, Toll D (2004) The global land data assimilation system. Bull Am Meteorol Soc 85(3):381–394
84. Rollins RL (1954) Movement of soil moisture under a thermal gradient. Highw Res Board Proc 33:492–508
85. Salzmann W, Bohne K, Schmidt M (2000) Numerical experiments to simulate vertical vapor and liquid water transport in unsaturated non-rigid porous media. Geoderma 98(3):127–155

86. Scanlon BR (1992) Evaluation of liquid and vapor water flow in desert soils based on chlorine 36 and tritium tracers and nonisothermal flow simulations. Water Resour Res 28(1):285–297

87. Scanlon BR, Milly PCD (1994) Water and heat fluxes in desert soils 1. Field studies. Water Resour Res 30(3):709–720

88. Scanlon BR, Milly PCD (1994) Water and heat fluxes in desert soils 2. Numerical simulations. Water Resour Res 30(3):721–734

89. Schrefler BA, Zhan XY (1993) A fully coupled model for water-flow and air-flow in deformable porous-media. Water Resour Res 29(1):155–167

90. Sellers PJ, Dorman JL (1987) Testing the simple biosphere model (SiB) using point micrometeorological and biophysical data. J Climate Appl Meteorol 26(5):622–651

91. Sellers PJ, Dickinson RE, Randall DA, Betts AK, Hall FG, Berry JA, Collatz GJ, Denning AS, Mooney HA, Nobre CA, Sato N, Field CB, Henderson-Sellers A (1997). Modeling the exchanges of energy, water, and carbon between continents and the atmosphere. Science 275(5299):502–509

92. Seneviratne SI, Corti T, Davin EL, Hirschi M, Jaeger EB, Lehner I, Orlowsky B, Teuling AJ (2010) Investigating soil moisture-climate interactions in a changing climate. Earth-Sci Rev 99(3-4):125–161

93. Seuffert G, Wilker H, Viterbo P, Drusch M, Mahfouf JF (2004) The usage of screen-level parameters and microwave brightness temperature for soil moisture analysis. J Hydrometeorol 5(3):516–531

94. Shiklomanov IA, Gu W-Z, Lu J-J (2004). Experimental research on the role of dew in arid ecosystem of Gobi desert, Inner Mongolia. In: Ru-Ze Xi, K-P Seiler, We-Zu Gu (ed) Research basins and hydrological. Kluwer Academic Publishers, Dordrecht, pp 329–332

95. Shu Q, Kemblowsky MW, McKee M (2005) An application of ensemble Kalman filter in integral-balance subsurface modeling. Stoch Env Res Risk Assess 19:361–374

96. Slater AG, Clark MP (2006) Snow data assimilation via an ensemble Kalman filter. J Hydrometeorol 7(3):478–493

97. Smith WO (1943) Thermal transfer of moisture in soils. Trans Am Geophys Un 24:511–560

98. Staple WJ, Lehane JJ (1954) Movement of moisture in unsaturated soils. Can J Agr Sci 34:329–342

99. Stieglitz M, Rind D, Famiglietti J, Rosenzweig C (1997) An efficient approach to modeling the topographic control of surface hydrology for regional and global climate modeling. J Clim 10(1):118–137

100. Su Z (2002) The surface energy balance system (SEBS) for estimation of turbulent heat fluxes. Hydrol Earth Syst Sci 6(1):85–99

101. Su Z, Schmugge T, Kustas WP, Massman WJ (2001) An evaluation of two models for estimation of the roughness height for heat transfer between the land surface and the atmosphere. J Appl Meteorol 40(11):1933–1951

102. Su Z, Yacob A, Wen J, Roerink G, He YB, Gao BH, Boogaard H, van Diepen C (2003) Assessing relative soil moisture with remote sensing data: theory, experimental validation, and application to drought monitoring over the North China Plain. Phys Chem Earth 28(1–3):89–101

103. Taylor SA, Cavazza L (1954) The movement of soil moisture in response to temperature gradients. Proc Soil Sci Soc Am 18:351–360

104. Thiemann M, Trosset M, Gupta H, Sorooshian S (2001) Bayesian recursive parameter estimation for hydrological models. Water Resour Res 37:2521–2535

105. Toll D, Arsenault K, Houser P, Entin J, Cosgrove B, Peters-Lidard C, Rodell M (2004). Terrestrial water and energy systems for water resource applications. Sensors, Systems and Next-Generation Satellites Vii. R. Meynart, S. P. Neeck, H. Shimoda, J. B. Lurie and M. Aten. 5234:744–753

106. van den Hurk BJJM (2002) European LDAS established. GEWEX News 12(2):9–9

107. van den Hurk BJJM, Ettema J, Viterbo P (2008) Analysis of soil moisture changes in Europe during a single growing season in a new ECMWF soil moisture assimilation system. J Hydrometeorol 9(1):116–131
108. Vrugt JA, Clark MP, Diks CGH, Duan Q, Robinson BA (2006) Multi-objective calibration of forecast ensembles using Bayesian model averaging. Geophys Res Lett 33(19):L19817, pp 6. doi:10.1029/2006GL027126
109. Walker JP, Houser PR (2001) A methodology for initialising soil moisture in a global climate model: assimilation of near-surface soil moisture observations. J Geophys Res Atmos 106:11761–11774
110. Walker JP, Willgoose GR, Kalma JD (2001) One-dimensional soil moisture profile retrieval by assimilation of near-surface measurements: a simplified soil moisture model and field application. JHydrometeorol 2(4):356–373
111. Walker JP, Willgoose GR, Kalma JD (2001) One-dimensional soil moisture profile retrieval by assimilation of near-surface observations: a comparison of retrieval algorithms. Adv Water Resour 24(6):631–650
112. Walker JP, Willgoose GR, Kalma JD (2002) Three-dimensional soil moisture profile retrieval by assimilation of near-surface measurements: simplified Kalman filter covariance forecasting and field application. Water Resour Res 38(12):1301
113. Wang DG, Wang GL, Anagnostou EN (2005) Use of satellite-based precipitation observation in improving the parameterization of canopy hydrological processes in land surface models. J Hydrometeorol 6(5):745–763
114. Webb SW, Ho CK (1997) Pore-scale modeling of enhanced vapor diffusion in porous media. Sandia National Laboratories SAND-97-2013C, Albuquerque, NM, USA
115. Webb SW, Ho CK (1998) Review of enhanced vapor diffusion in porous media. Sandia National Laboratories SAND-98-1819C, Albuquerque, NM, USA
116. Wilker H, Drusch M, Seuffert G, Simmer C (2006) Effects of the near-surface soil moisture profile on the assimilation of L-band microwave brightness temperature. J Hydrometeorol 7(3):433–442
117. Xia Y, Pittman AJ, Gupta HV, Leplastrier M, Henderson-Sellers A, Bastidas LA (2002) Calibrating a land surface model of varying complexity using multicriteria methods and the Cabauw dataset. J Hydrometeorol 3(2):181–194
118. Xin X, Liu Q (2010) The two-layer surface energy balance parameterization scheme (TSEBPS) for estimation of land surface heat fluxes. Hydrol Earth Syst Sci 14(3):491–504
119. Yang ZL, Dickinson RE, Shuttleworth WJ, Shaikh M (1998) Treatment of soil, vegetation and snow in land surface models: A test of the biosphere–atmosphere transfer Scheme with the HAPEX-MOBILHY, ABRACOS and Russian data. J Hydrol 213(1–4):109–127
120. Zeng Y, Su Z, Wan L, Wen J (2011) A simulation analysis of advective effect on evaporation using a two-phase heat and mass flow model. Water Resour Res 47(10): W10529. doi:10.1029/2011WR010701

Chapter 2
Diurnal Pattern of Coupled Moisture and Heat Transport Process

2.1 Introduction

The importance of soil moisture has resulted in a very large number of numerical models, which simulate water transport in both a liquid and a vapor phase within the uppermost soil layer. These are based on theories that describe the coupled flow of energy and mass, considering the microscopic structure of porous medium [1–5]. Another theory, which is based on the thermodynamics of irreversible process, was also adopted to analyse the transport of heat and mass and to derive general equations for the coupled flow in soil [6–9].

The soil moisture variation in arid and semi-arid regions is characterized by vapor transport in the surface soil layer, because the liquid water movement could be infinitesimal due to extremely dry soil conditions [10, 11]. This dominant vapor transport can result in accumulation of liquid water in the unsaturated zone [12–14]; in addition, the vapor transport plays a very important role in maintaining vegetation and ecosystems in arid or semi-arid areas [15]. Moreover, the way of accumulating liquid water from vapor transport has been applied to produce fresh drinkable water in the dry areas by burying perforated pipes in soil [16, 17].

Due to the importance of soil moisture, many field or laboratory experiments were conducted to observe the changes in water content in soil due to vapor transport and consequently to analyse the soil water dynamics that involve the movement of liquid water, water vapor and heat. To verify the theory for vapor and heat flow derived from the thermodynamic of irreversible process [18, 19],

---

from 1962 to 1979, Cary and co-workers conducted a number of indoor experiments that investigated thermally driven moisture transport in soil [20–23]. In the same period, Rose published many papers [24–28] that tested the theory for heat and moisture movement in porous medium, which was developed by Philip and de Vries [2]. Unlike the experiments, which were restricted to the laboratory, quantitative study of moisture transport in soil in the field environment has been conducted by some investigators [29, 30]. Through about two decades' discussion from the above experiments, Philip and de Vries' model (hereafter, referred to as the PdV model) stands out and is widely used, even today, after some slight revisions [31–37].

The reason for the wide use of the PdV model is mainly due to the enhancement factor for water vapor transport. There are two postulated mechanisms for enhanced vapor transfer [2]: the first assumption is that the water vapor can flow through the liquid island between solid particles by condensing on one side of the liquid island and subsequently evaporating on the other side; the second postulate considers local temperature gradients in the air-filled pores, which might be significantly higher than the average temperature gradient. According to these assumptions, the humidity of the air adjacent to the water in soil pores, which is determined by the local equilibrium hypothesis, is often substituted for the land surface humidity. However, such substitution is invalid, except for the humid conditions below the evaporation front. This takes place near the surface when the evaporative demand is greater than the ability of the soil to conduct water in the liquid phase and a liquid–vapor phase discontinuity occurs [38, 39]. This invalidation triggered studies on the changes in soil water content in the topsoil, which include the parameterization of evaporation from the soil surface [40–44] and explorations of the mechanisms by which water is added to the surface soil layer [45–48].

Although the theory of coupled water, vapor and heat transport in soil is widely recognized and thus extensively tested and reinforced, very few studies have demonstrated and evaluated the soil water dynamics in time and space, simultaneously and continuously. The common approach to address this issue is either to analyse the soil water and temperature information at specific times [49–53] or to assess the time-series information at specific depths [54–58]. In this study, observed soil water content and temperature were used to calibrate the performance of the modified HYDRUS1D-1D code in sand. Then, the HYDRUS1D-1D code was used to produce temporal and spatial information on coupled water, vapor and heat transport in soil. The space-time information represents a two-dimensional field and a dependent specific flux (e.g. thermal water vapor flux) or temperature as a third dimension. The space-time information and dependent specific fluxes or temperatures, all of which contain discrete values, were used directly in an interpolation and smoothing procedure. This was done in order to create a continuous three-dimensional field for the diurnal pattern interpretation of soil water dynamics.

2.2 Materials and Methods

2.2.1 In Situ Setup

The experiment was conducted in an outdoor sand bunker in a field of the China University of Geosciences (Beijing) from October 4th to October 7th in 2004. Although there were trees in the surroundings, this field was almost flat and directly exposed to sunshine without any hindrances. Before and during the observation period, there was no precipitation in the field but clear skies and light winds. Maximum and minimum air temperatures in this field ranged from 28.3 to 35 °C (12:00–14:00) and 10.8 to 12 °C (05:00–07:00); at the meantime, the maximum and minimum relative humidity ranged from 85.5 to 97.9 % (04:00–07:00) and 33.2 to 34 % (12:00–15:00); the atmosphere pressure and wind speed ranged from 1012.25 to 1017.54 hPa and 0 to 1.45 m/s, respectively. The sand-filled bunker (1 m × 1 m × 1 m) was located in the center part of this field. The surrounding soil was paved with a poly-chlorothene film in order to avoid its influence on the distribution of soil water. The measurement instruments, which included thermometers, tensiometers and soil moisture sensors, were carefully installed during the process of packing sand into the bunker.

The micro-meteorological and soil thermal elements, which included atmospheric pressure, solar radiation, wind speed, air temperature, air relative humidity, ground surface temperature, and soil temperature profile, were measured hourly. During the observation, atmospheric pressure and solar radiation were measured at a fixed position above the ground near the sand bunker, where the measurement instruments could not influence the interactions between the atmosphere and the sand bunker. The atmospheric pressure was measured by the YM4-1 aneroid barometer (Chan Chun Meteorological Instrument Factory, Inc., China), and the solar radiation was monitored by the Testo-545 pyranometer (Testo, Inc., Flanders, NJ). Wind speed, air temperature and air humidity were measured hourly at a fixed position, 20 cm above the ground surface. The Testo 405-v1 hot-wire anemometer (Testo, Inc., Flanders, NJ) was used to measure the wind speed. The air temperature and air humidity were measured hourly by the DT-615 hygrothermography (CEM, Ltd., HK). The ground surface temperature was measured hourly by the Fluck66 handheld infrared radiometer (Fluke UK Ltd, Norwich, Norfolk). At 5, 10, 15, 20 and 30 cm depth, the soil temperatures were measured hourly by bent stem mercury thermometers.

Besides for the micro-meteorological and soil temperatures, the water content (at 10 and 30 cm depth) and the soil matric potential (at 10, 15 and 30 cm depth) were measured hourly. The water content was measured by the Intelligent Apparatus of Measuring Soil Moisture (TSCII), manufactured by the Institute of Sensor and Detection Technology at China Agriculture University. The measurement of soil water content by TSCII is based on the determination of soil dielectric constant using the principle of standing-wave ratio [59]. The TSCII was installed horizontally in sand to minimize the disturbance of vertical coupled

liquid water, water vapor and heat transport. The soil water potential was measured by the WM-1 tensiometer, which was made by the Institute of Hydrogeology and Engineering Geology, Chinese Academy of Geological Sciences.

2.2.2 Field Data

Figure 2.1 shows measured soil temperatures and water contents. The soil temperature fluctuated strongly on the soil surface, and the range of variation was 35.2 °C. However, at 30 cm depth, there was only small fluctuation, and the variation was only 1.8 °C during the observation. Although the changes in soil temperature decrease with increasing depth, the temperature data show a typical sinusoidal diurnal behavior at all depths (Fig. 2.1 a).

The water content at 10 cm depth varied from 4.4 to 6.1 % (Fig. 2.1 b). Its maximum value (5.9–6.1 %) occurred at midday (12:00–13:00), while its minimum value (4.4–4.5 %) occurred before dawn (02:00–03:00). The water content at 30 cm depth varied from 10.4 to 13.1 % (Fig. 2.1 b). Its maximum value (11.9–13.1 %) was identified at afternoon (14:00–15:00), and its minimum value (10.4–10.8 %) was observed before dawn (04:00–05:00). The water content data also show a sinusoidal diurnal behavior.

Although there are laboratory experiments [60], which measured the vapor diffusion in porous medium directly, it is very difficult to observe the water vapor transport in situ directly. The feasible method to measure the water vapor transport in field is the indirect method, which infers the water vapor flux from soil matric potential and soil temperature using modified Fickian-diffusion equation [61–63]. Figure 2.2 shows the diurnal variation of water vapor flux between depths of 10 and 30 cm from October 4th to October 7th 2004. The positive value indicates the upward water vapor transport. During the observation, the water vapor transported upwards to the ground surface at night (21:00–22:00 to 11:00–12:00) and downwards to the deeper soil in day (11:00–12:00 to 21:00–22:00).

2.2.3 Model Description

The modified HYDRUS1D code, which refers to the coupled water, vapor and heat transport in soil (i.e. the PdV model), was applied to simulate soil water fluxes. The governing equation for one-dimensional vertical flow of liquid water and water vapor in variably saturated media is given [53] by the following mass conservation equation:

$$\frac{\partial \theta}{\partial t} = -\frac{\partial q_L}{\partial z} - \frac{\partial q_v}{\partial z} - S \qquad (2.1)$$

(a)

(b)
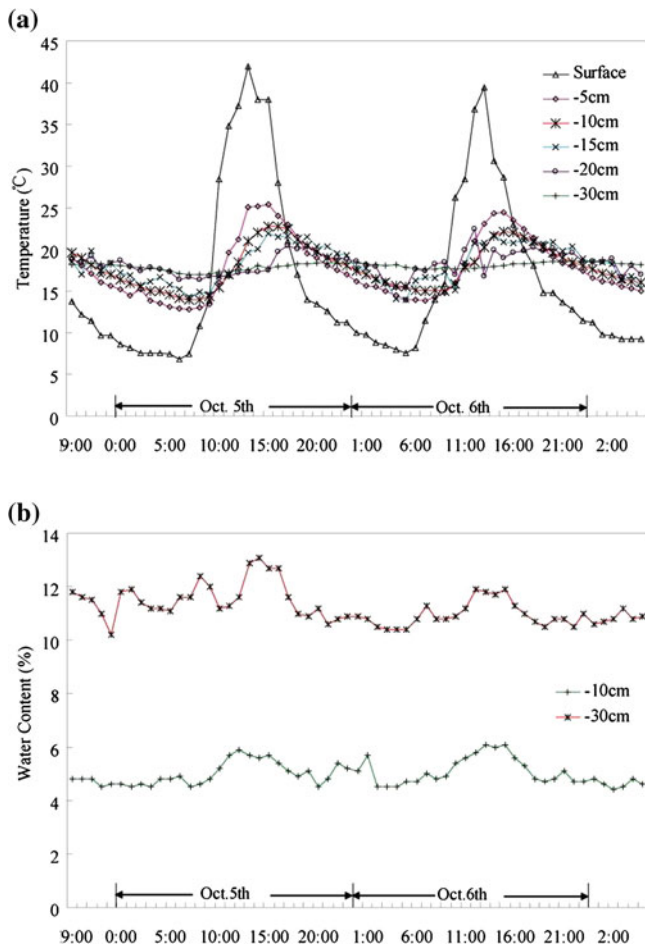
Fig. 2.1 Diurnal changes in (**a**) soil temperature and (**b**) soil moisture

where q_L and q_v are the flux densities of liquid water and water vapor (cm d^{-1}), respectively; t is time (d); z is the vertical axis positive upward (cm); and S is a sink term accounting for root water uptake (d^{-1}). In this experiment, there were not roots in the sand and so S was not be taken into account.

The flux density of liquid water, q_L, is defined [2] as

$$q_L = q_{Lh} + q_{LT} = -K_{Lh}\left(\frac{\partial h}{\partial z} + 1\right) - K_{LT}\frac{\partial T}{\partial z} \tag{2.2}$$

where q_{Lh} and q_{LT} are respectively the isothermal and thermal liquid water flux densities (cm d^{-1}); h is the matric potential head (cm); T is the temperature (K); and K_{Lh} (cm d^{-1}) and K_{LT} (cm^2 K^{-1} d^{-1}) are the isothermal and thermal hydraulic conductivities for liquid-phase fluxes due to gradients in h and T, respectively.
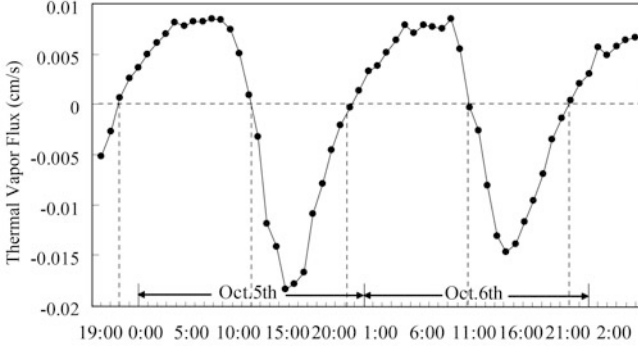
Fig. 2.2 Diurnal variation of the indirect measured thermal vapor flux

Using the product rule for differentiation and assuming the relative humidity in soil pores keeps constant with temperature [2], the flux density of water vapor, q_v, can be written as

$$q_v = q_{vh} + q_{vT} = -K_{vh} \frac{\partial h}{\partial z} - K_{vT} \frac{\partial T}{\partial z} \tag{2.3}$$

where q_{vh} and q_{vT} are the isothermal and thermal water vapor flux densities (cm d^{-1}), respectively; K_{vh} (cm d^{-1}) and K_{vT} (cm^2 K^{-1} d^{-1}) are the isothermal and thermal vapor hydraulic conductivities, respectively. Combining Eqs. (2.1), (2.2), and (2.3), we obtain the governing liquid water and water vapor flow equation:

$$\begin{aligned}
\frac{\partial \theta}{\partial t} &= \frac{\partial}{\partial z} \left[K_{Lh} \frac{\partial h}{\partial z} + K_{Lh} + K_{LT} \frac{\partial T}{\partial z} + K_{vh} \frac{\partial h}{\partial z} + K_{vT} \frac{\partial T}{\partial z} \right] - S \\
&= \frac{\partial}{\partial z} \left[K_{Th} \frac{\partial h}{\partial z} + K_{Lh} + K_{TT} \frac{\partial T}{\partial z} \right] - S
\end{aligned} \tag{2.4}$$

where K_{Th} (cm d^{-1}) and K_{TT} (cm^2 K^{-1} d^{-1}) are the isothermal and thermal total hydraulic conductivities, respectively, and where:

$$K_{Th} = K_{Lh} + K_{vh} \tag{2.5}$$

$$K_{TT} = K_{LT} + K_{vT} \tag{2.6}$$

For the sake of brevity, the detailed description of the modified HYDRUS1D code would not be shown here. Readers are referred to Saito et al. [53].

2.2.4 Soil Characteristics Data

The water retention curve (WRC) is one of the most fundamental hydraulic characteristics of a soil to solve the flow equation of water in soils. The soil water retention equation is given [64] by

Fig. 2.3 Fitted soil water retention curve using the field data
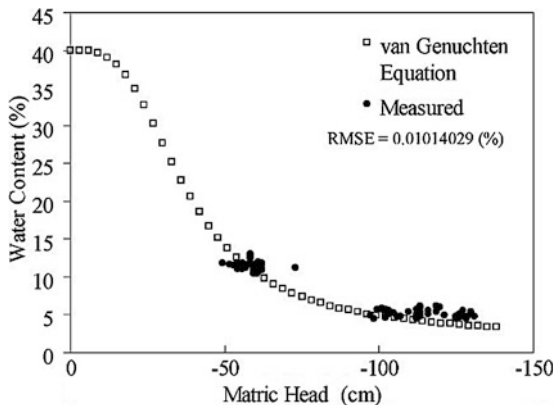
$$\theta(h) = \begin{cases} \theta_{res} + \dfrac{\theta_{sat} - \theta_{res}}{[1 + |\alpha h|^n]^m} & h \leq 0 \\ \theta_{sat} & h > 0 \end{cases} \tag{2.7}$$

where θ is the volumetric water content (cm^3 cm^{-3}) at pressure head h (cm); θ_{res} and θ_{sat} are the residual and saturated water contents, respectively (cm^3 cm^{-3}); $\alpha (> 0$, in cm^{-1}) is the parameter characteristic of the particular soil material; n (> 1) is a measure of the pore-size distribution affecting the slope of the retention function.

The above soil water retention equation (Eq. (2.7)) was fitted to the measured water content and soil matric potential data using inverse method, leading to $\theta_{res} = 0.01$ cm^3 cm^{-3}, $\theta_{sat} = 0.39$ cm^3 cm^{-3}, $\alpha = 0.0316$ cm^{-1}, and $n = 3.3$ (Fig. 2.3). The goodness of fit of Eq. (2.7) was quantified with the root mean square error [65] as

$$RMSE = \sqrt{\dfrac{\sum\limits_{i=1}^{N_W} (\theta_i - \theta_i')^2}{N_W - n_p}} \tag{2.8}$$

where N_w is the number of water retention measurements (θ—h pairs); θ' is the calculated water content and n_p is the number of parameters that were optimized.

Although the RMSE is 0.01 (%) for 106 in situ measured θ—h pairs, the measurements did not include the higher pressure heads (0 cm > h > –50 cm). This would cause uncertainties in representing the moist state of the experimental sand by water retention curve. However, the determinations of the model parameters ($\theta_{res,}$ $\theta_{sat,}$ α, n) of the experimental sand were referenced to that of the Wagram sand. The water retention data of Wagram sand (in Clayton, NC, USA) were acquired from UNSODA database. There are 42 θ—h pairs at three depth ranges (0–23 cm, 23–36 cm, 36–56 cm), and each depth range has 14 pairs. The ranges of the model parameters for the Wagram sand are: $0.078 < \theta_{res} < 0.098$, $0.239 < \theta_{sat} < 0.374$, $0.019 < \alpha < 0.026$ and $3.269 < n < 4.248$. The residual

water content and the saturated water content of the experimental sand are respectively lower and higher than that of the Wagram sand. It might be the uncertainties, which could be caused by the manually packing process of the experimental sand. This packing process cannot make the experimental sand has the same pore-size distribution as the Wagram sand in Clayton, NC, USA; and this also causes the uncertainty in α and n, which are the shape factors in the water retention curve model. To analyse this uncertainty may offer an opportunity to improve the prediction of water movement in the vadose zone [66], but this is beyond the scope of this chapter and will not be discussed here.

2.2.5 Initial and Boundary Conditions

The soil profile was considered to be 80 cm deep. The nodes located at depths of 0, 5, 10, 15, 20, 25 and 30 cm were selected for comparing calculated temperatures and volumetric water contents with measured values. The spatial discretization of 1 cm was used, leading to 81 nodes across the profile. The calculations were performed for a period of 2.5 days from October 4th to October 7th in 2004. Discretization in time is varying between a minimum and a maximum time-step, controlled by a timestep criterion. To solve the problem it is necessary to specify initial conditions for temperature and matric potential.

   The initial matric potentials and soil temperatures were determined from measured values on October 4th by interpolating the measured values between different depths. Boundary conditions at the soil surface for liquid water, water vapor, and heat transport were determined from the meteorological data. In order to provide the values of meteorological variables at a time interval of interest for the calculation at the same or similar time intervals, relatively simple approaches were used [53]. The free drainage was considered as the bottom boundary condition and the discharge rate assigned to the bottom node was determined by the program [67]. The lower boundary condition for heat transport was a Neumann type boundary condition with zero temperature gradient.

2.3 Simulation Results

In this section, the measured water contents, soil temperatures and thermal water vapor fluxes are compared with those that were numerical simulated by the modified HYDRUS1D-1D code. The predicted and observed soil temperatures at depths of 5, 10, 15, 20 and 30 cm are shown in Fig. 2.4. Predicted temperatures below 10 cm depth had bigger divergence from the measurements than those above that depth. The goodness of fit of simulation was quantified with the relative root mean square error:

Fig. 2.4 Simulated and measured soil temperatures at all observed depths
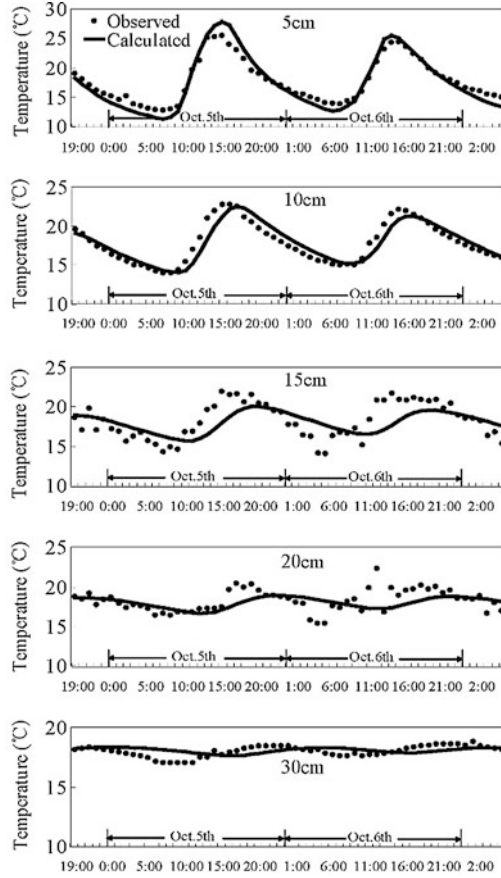
$$RRMSE = \frac{\sqrt{\sum\limits_{i=1}^{N_w} (M_i - C_i)^2 \Big/ N_w}}{Max(M_1, M_2, \ldots\ldots, M_{N_w}) - Min(M_1, M_2, \ldots\ldots, M_{N_w})} \qquad (2.9)$$

where N_w is the number of the measurements; M_i and C_i are measurements and calculations, respectively; $Max(M_1, M_2, \ldots, M_{N_w})$ and $Min(M_1, M_2, \ldots, M_{N_w})$ are the maximum and minimum value of the measurements, respectively. The *RRMSE* is dimensionless and $RRMSE = 0$ indicates the best fit. The smaller the *RRMSE*, the better the fit of simulation.

The *RRMSE*s of the temperature at depths of 5, 10, 15, 20 and 30 cm were respectively 0.094, 0.108, 0.236, 0.198 and 0.280. Although there were obvious delays in the simulation for the occurrence of maximum temperature below 15 cm depth, simulated and measured temperatures generally agreed at all five depths and
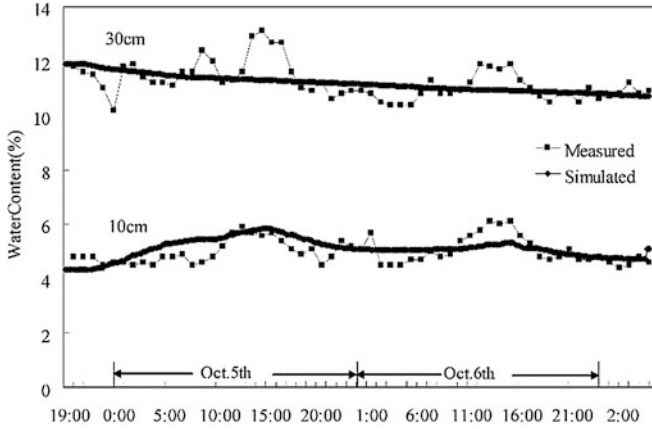
Fig. 2.5 Simulated and measured soil moistures

both showed typical sinusoidal diurnal variation, with the maximum absolute deviation of 5.126 °C at 20 cm depth.

Figure 2.5 depicts simulated and measured soil water content at two depths. There was imperfect agreement between the observed and simulated water contents. The *RRMSE*s of the water content at depths of 10 cm and 30 cm were 0.289 and 0.211, respectively. At 10 cm depth, the simulated water content could merely follow the general trend of observation; while at 30 cm depth, the simulation showed a decreasing trend instead of a variation like the measurement had. However, apart from the poor fit of the simulation to the trend of water content variation at 30 cm depth, the mean of the simulated water contents was close to that of the measurements. The means of simulated and observed water contents were 5.00 and 5.08 % at 10 cm depth, and 11.22 and 11.24 % at 30 cm depth, respectively. Furthermore, the average relative errors at depths of 10 cm and 30 cm were 1.02 and 1.00; both are close to 1. This indicates that the simulated water contents could fit most measured values fairly well. The average relative error is defined [68] as

$$AVRE = \sum (C_i/M_i)/N_w \tag{2.10}$$

where the symbols were the same in Eq. (2.9).

Calculated thermal water vapor fluxes were compared with measurements in Fig. 2.6. The predicted thermal vapor fluxes followed fairly well the measured values and the *RRMSE* is 0.111. To summarize, after calibration, the modified HYDRUS1D code can be applied in the analysis of coupled liquid water, water vapor and heat transport in this experiment.
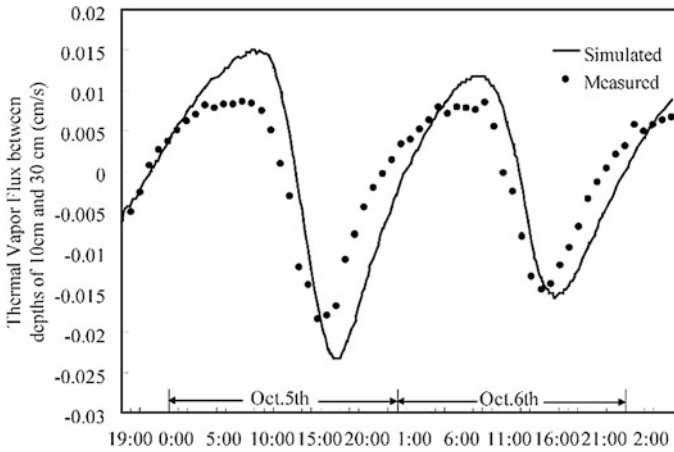
Fig. 2.6 Simulated and measured thermal vapor fluxes

2.4 Discussion

Numerical modeling of isothermal and non-isothermal liquid and vapor flow plays a critical role in evaluating the physical processes, that governing soil heating, spatial distribution of water, and gaseous exchange between the soil and atmosphere. In this section, the modified HYDRUS1D code was used to produce the hourly profiles of isothermal and non-isothermal water vapor fluxes, liquid water fluxes and soil temperatures from October 4th to October 7th in 2004. Then, an interpolation and smoothing program, SURFER, was used to create continuous three-dimensional fields for the diurnal pattern interpretation of soil water dynamics. The three dimensional fields consisted of a space-time field (two-dimensional field) and a dependent specific flux or temperature (third dimension). Finally, the basic soil water dynamics was conceptualized with a schematic map.
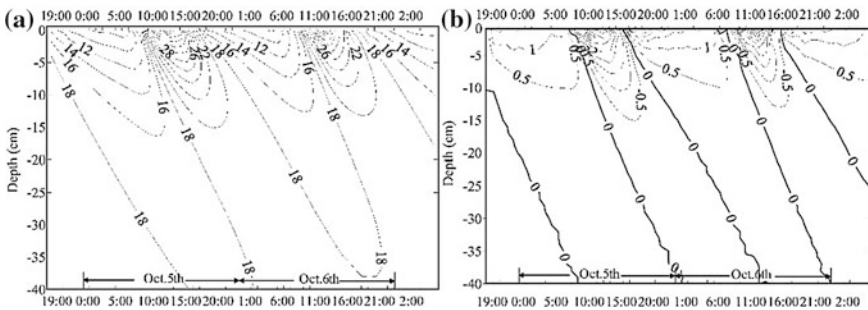
Fig. 2.7 Distributions of (**a**) soil temperatures and (**b**) temperature gradients in space and time

2.4.1 Temperature and Temperature Gradients Fields

In order to understand the diurnal variation and the mechanism of heating of the soil profile, there is a need to look at the temperature variation in the soil profile. The contour chart of temperature, in Fig. 2.7a, shows the hourly variation of soil temperature profiles. The interval of contours was 2 °C.

Before 07:00 5th October, the contours at the surface were sparse and the surface temperature varied slowly with the rate of 0.53 °C per hour. From 07:00 to 19:00 5th October, the contours became dense and the surface temperature fluctuated strongly with the rate of 5.2 °C per hour. During this period, the surface temperature increased from 7.4 °C at 07:00 to the highest value of 42 °C at 13:00, and dropped to 14 °C at 19:00, which was the transition point for the contours that varied from denseness to sparseness.

From 19:00 5th October to 06:00 6th October, the contours were sparse again and the variations of the surface temperature were reduced. In this period, the surface temperature changed from 14 °C (at 19:00 5th October) to 8.2 °C (at 06:00 6th October) with the rate of 0.52 °C per hour. After 06:00, the contours would experience the period of denseness again, in which the surface temperature varied strongly. It is important to note that the denseness and sparseness indicated the rapid variation and slow variation of soil temperature, respectively.

As shown in Fig. 2.7a, the density of contours decreased with depth. This indicates that the variation of soil temperature was reduced with depth. During the observation period, the surface temperature varied from 6.8 to 42 °C, while from 17 to 18.8 °C at 30 cm depth. At 40 cm depth, the variation of temperature was less than 0.3 °C. Because the variation of temperature was close to zero below 40 cm depth, the soil temperature profile information below 40 cm depth is not shown here.

Figure 2.7b shows the space-time temperature gradient field, which clearly shows how the heat transport in soil controls the dependence of the temperature gradient profiles in time and space. The temperature gradients were derived by $\Delta T = (T_{i+1} - T_i)$/cm, where T_i represented the soil temperature at i cm depth. The variation of contours in Fig. 2.7b was accordant with that in Fig. 2.7a. The denseness of contours change with elapsed time, and become sparser with depth.

From temperature gradient profiles, it was seen that there was an active layer for heat exchange, which was about 10 cm deep below the ground surface. Between depths of 0 and 1 cm, the temperature gradient could reach 6.9 °C cm^{-1}. At 10 cm depth, the gradients were between 0 and 0.6 °C cm^{-1}, and there was almost no temperature gradient below 10 cm depth. In additional, there were five contours for the temperature gradient of 0 °C cm^{-1}, which indicated no heat conduction in the space-time field. Accordingly, these five contours were defined as zero heat flux planes.

There were two types of zero heat flux planes: one was the divergent plane and the temperature gradient, above and below this plane, was respectively positive and negative (upwards and downwards); the other was the convergent plane, and

the directions of the temperature gradient were completely reverse (downwards and upwards) compared with those to the divergent plane. During the whole observation, there were three divergent zero heat flux planes and two convergent heat flux planes. The zero heat flux plane could be regarded as the changing point, at which the direction of the temperature gradient reversed. The divergent planes started in afternoon (16:00–17:00), while the convergent planes happened in morning (06:00–08:00).

2.4.2 Non-isothermal Flux Fields

The non-isothermal liquid water (q_{LT}) and water vapor (q_{vT}) fluxes are controlled not only by the temperature gradient, but also by the thermal liquid (K_{LT}) and vapor (K_{vT}) hydraulic conductivities. The functions for the thermal hydraulic conductivities are defined [69, 70] as:

$$K_{LT} = K_{Lh}(hG_{wT}\frac{M}{\gamma_0}\frac{d\gamma}{dT}) \qquad (2.11)$$

$$K_{vT} = \frac{D}{\rho_w}\eta H_r \frac{d\rho_{sv}}{dT} \qquad (2.12)$$

where K_{Lh} is the isothermal unsaturated hydraulic conductivity (cm d^{-1}), which is decided by the van Genuchten's [64] model; G_{wT} is the gain factor (dimensionless), which assesses the temperature dependence of the soil water retention curve and is set as 7 for sand [71]; γ is the surface tension of soil water (J cm^{-2}), and γ_0 is the surface tension at 25 °C (g d^{-2}); D is the vapor diffusivity in soil (cm^2 d^{-1}); ρ_w is the density of liquid water (g cm^{-3}); ρ_{sv} is the saturated vapor density (g cm^{-3}); M is the molecular weight of water (g mol^{-1}); g is the gravitational acceleration (= 981 cm s^{-2}); R is the universal gas constant (mol^{-1} K^{-1}); η is the enhancement factor (dimensionless); and H_r is the relative humidity (dimensionless).

Figure 2.8a shows the variations of the thermal liquid hydraulic conductivity profiles in space-time field. The K_{LT} increased with depth and kept this trend during the whole observation period. However, the temporal variation of K_{LT} was not uniform throughout the profile. Above 13 cm depth, K_{LT} varied in a certain small range with time: the extent of variation was from 0.009 to 0.024 (cm^2 K^{-1} d^{-1}) and the maximum changing rate was 0.0007 (cm^2 K^{-1} d^{-1}) per hour. However, below 13 cm depth, it started to drop rapidly with time. The maximum decreasing rate was 0.005 (cm^2 K^{-1} d^{-1}) per hour, and the extent of variation was from 0.041 to 0.296 (cm^2 K^{-1} d^{-1}).

The thermal vapor hydraulic conductivities (Fig. 2.8b) experienced a reverse trend throughout the profile, when it was compared to Fig. 2.8a. Below the depth of 15 cm, the K_{vT} decreased with depth, compared to the increase of K_{LT} with
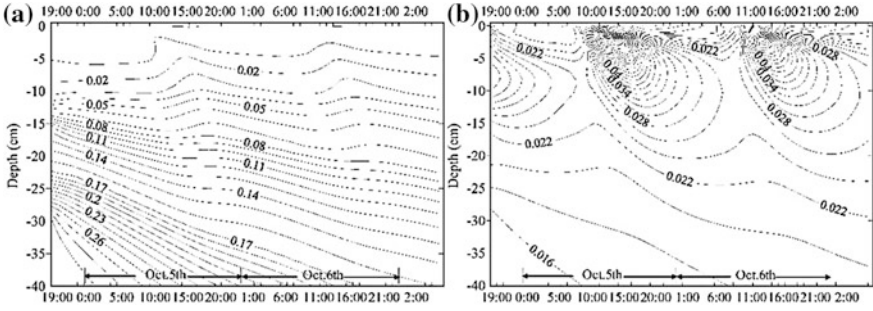
Fig. 2.8 Distributions of (**a**) the thermal liquid hydraulic conductivity and (**b**) the thermal vapor hydraulic conductivity in space and time

depth. The temporal variation was also opposite to that in Fig. 2.8a. The K_{vT} fluctuated strongly from 0.005 to 0.661 (cm^2 K^{-1} d^{-1}), between depths of 0 and 15 cm, compared to the small variation of K_{LT} in the shallow layer.

From the comparison, although the variation of the K_{vT} and K_{LT} in space-time field is almost opposite, they are of about the same order of magnitude. However, K_{vT} varied more strongly than K_{LT}, especially, in the shallow layer right below the ground surface (between depths of 0 and 15 cm). This indicates that the non-isothermal vapor flow was more important in the upper soil layer, in this case. In addition, the larger variation of K_{vT} also denoted its higher sensitivity to the temperature variation than that of K_{LT}.

The space-time fields of non-isothermal liquid and vapor fluxes are shown in Fig. 2.9. Corresponding to the zero heat flux planes in Fig. 2.7b, the q_{LT} and q_{vT} field have zero thermal liquid flux planes (Fig. 2.9a) and the zero thermal vapor flux planes (Fig. 2.9b), both of which were sub-classified into divergent and convergent planes according to the definitions of zero heat flux planes in the temperature gradient field. The downward propagation of the zero thermal liquid and vapor flux planes were accordant with that of the zero heat flux planes over simulation period.
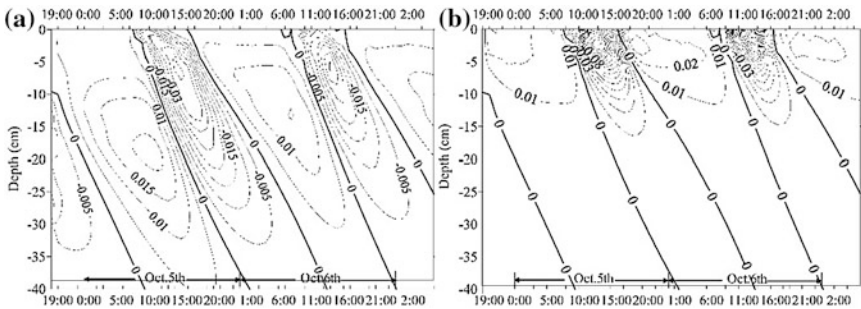
Fig. 2.9 Distributions of (**a**) the thermal liquid fluxes and (**b**) the thermal vapor fluxes in space and time
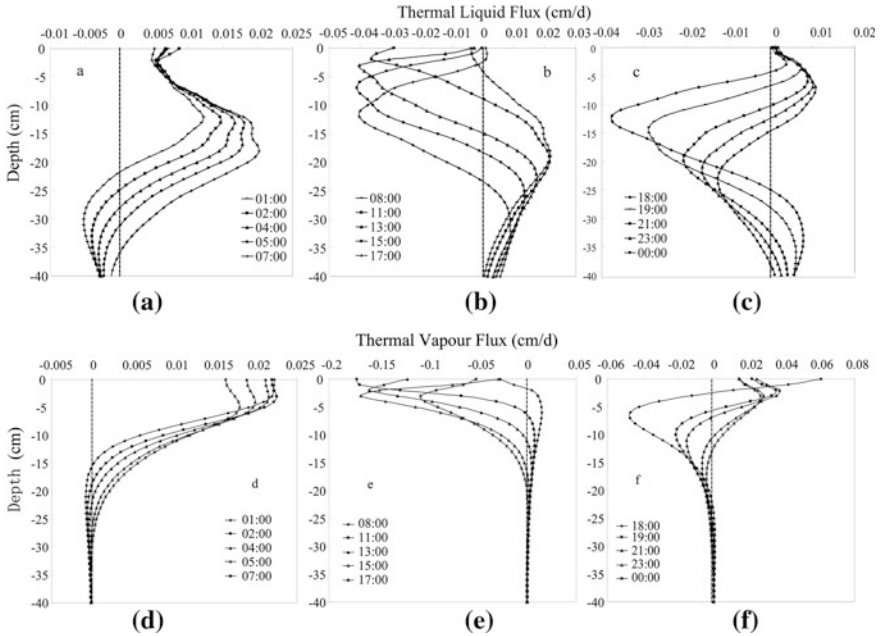
Fig. 2.10 Different types of (**a**, **b**, **c**) thermal liquid flux profiles and (**d**, **e**, **f**) thermal vapor flux profiles

There were closures between the planes of divergence and convergence in both q_{LT} and q_{vT} fields. The closures in q_{LT} field were much more obvious than those in q_{vT} field. The occurrence of closures was dependent on the thermal liquid and vapor fluxes profiles. In the q_{LT} field (Fig. 2.9a), there were three types of liquid flux profiles in soil:

(a) The first type occurred before dawn (01:00–07:00). During this period, there were only the divergent planes in the profile. After 07:00, the plane of divergence had almost reached the depth of 40 cm, and liquid flux is upward almost throughout the entire profile above 40 cm. In additional, the bulge of thermal liquid flux moved deeper with time and the peak flux increase with time, which varied from 0.012 cm d^{-1} of 01:00 to 0.020 cm d^{-1} of 07:00 (Fig. 2.10a). The increasing upward flux showed that the liquid water in deeper soil was drawn to the surface layer at night by temperature gradient. The propagation of the bulge of fluxes indicated the formation of the closures in Fig. 2.9a;

(b) There were only the convergent planes of zero thermal liquid flux existed in the second type profile. The directions of the thermal liquid fluxes were opposite to those in the first type. The propagation of the bulge of fluxes was accordant with that in type one, but the direction was reversed; the peak flux varied from −0.036 cm d^{-1} of 08:00 to −0.040 cm d^{-1} of 17:00 (Fig. 2.10b). The second type profiles happened in day (08:00–17:00). During this period, the convergent plane reached the depth of 24 cm. This indicated that the

downward flow of the thermal liquid water occurred in day and in the top ~ 24 cm; below the depth of 24 cm, the liquid water was upward and the peak flux decreased from 0.022 to 0.009 cm d^{-1};

(c) The third type profile was the transition between the first type and second type. Both the divergent planes and convergent planes were shown in this profile. The divergent plane was above the convergent plane, which indicated that the profile was changing from the second type to the first type. The third type profile occurred before midnight (18:00–24:00). During this period, the divergent plane moved from surface to -15 cm, and the convergent plane moved from -25 to -38 cm. This indicated that the liquid water flux in top layer (above -25 cm) started to be upward and increase after 18:00, from 0.004 to 0.011 cm d^{-1}; below -25 cm, the liquid water flux started to decrease from 0.008 to 0.001 cm d^{-1} (Fig. 2.10c). After the upward peak flux at greater depth reached zero, the flux profile became the first type again.

Referring to the space-time field of the thermal vapor flux (Fig. 2.9b), there were three corresponding types of vapor flux profiles, compared with those in q_{LT} field. From the thermal vapor flux profiles, it was seen that the bulges of vapor fluxes, above -20 cm, fluctuated from 0.061 to -0.177 cm d^{-1} throughout all profiles (from Fig. 2.10d–f); below -20 cm, the fluctuation of the bulge of flux was small and varied from 0.003 to -0.004 cm d^{-1}. The range of variation for the thermal vapor flux was 0.238 cm d^{-1} above -20 cm and 0.009 cm d^{-1} at greater depth, and the corresponding variation range of the thermal liquid flux was 0.063 and 0.042 cm d^{-1}. The variation of thermal vapor flux was one order of magnitude more than that of thermal liquid flux in subsurface layer, while one order of magnitude less than that in deeper layer. It indicated that the thermal vapor flux dominated in the top ~ 20 cm, while the thermal liquid flux dominated at greater depth.

As shown in Fig. 2.10d, the flow of thermal vapor was upward throughout the entire profile after 05:00 and indicated that the evaporation in soil occurred before dawn (01:00–07:00). The second type of vapor flux profile was shown in Fig. 2.10e, and the thermal vapor flux was moving downward in day (from 08:00 to17:00). The transition type profile of the thermal vapor flux was not obvious due to the small variation of the vapor flux at greater depth (Fig. 2.10f). The maximum thermal vapor flux was only 0.003 cm d^{-1} below the plane of convergence. However, it was still seen that the evaporation started to develop from the uppermost soil to the deeper soil, and the thermal vapor flux was changing from the second type to the first type.

2.4.3 Matric Potential and Its Gradient Field

The soil water potential reflects the energy state of water in porous media and subsequently influences the flow of liquid water and water vapor in the vadose zone. Direction of water movement can be determined using potential gradients in
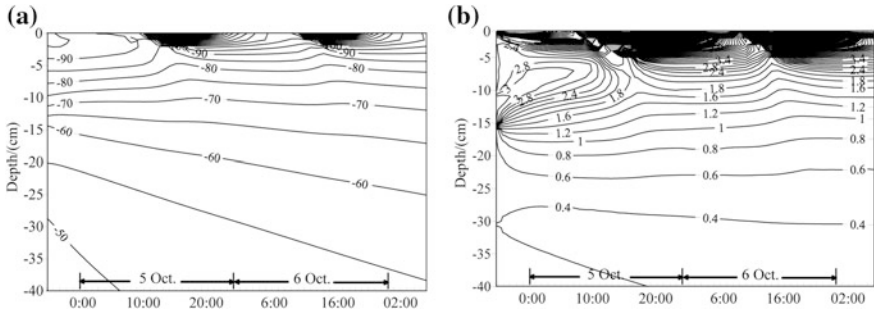
Fig. 2.11 Distributions of (**a**) the matric potentials and (**b**) the matric potential gradients in space and time

soil, because water moves from regions of high kinetic energy to regions of low kinetic energy [72]. Gravitational potential is equal to the elevation above (positive) or below (negative) a datum. In this case, the ground surface is regarded as the datum and the gravitational potential is negative; for example, the gravitational potential at the depth of 5 cm is −5 cm. Matric potential represents the driving force related to the matrix. Osmotic potential results from the difference in the concentration of the pore water. However, there is no solute considered. Then, the water potential includes matric and gravitational potential in this case. It is necessary to understand how the soil matric potential varied in space and time field.

The hourly variation of matric potential profile was shown in Fig. 2.11a. The interval of the contours was −10 cm (water column). From Fig. 2.11a, the matric potential was lowest near the surface and increased with depth, which indicated that there was an upward driving force for liquid water and water vapor during the whole simulation period. The matric potential fluctuated from −3084 to −94.11 cm at surface, while varied from −54.58 to −49.26 cm at −40 cm. The rapid variation of the matric potential happened from 10:00 to 23:00, and was restricted in the uppermost soil layer.

Figure 2.11b shows the distribution of the matric potential gradient in space and time. The interval of the contours was 0.2 cm cm^{-1}. The potential gradients were decided by $\Delta h = (h_{i+1} - h_i)/cm$, where h_i represented the soil matric potential at i cm depth. From Fig. 2.11b, it was seen that the contours in the soil layer, between 0 and −5 cm, was most intensive, which indicated the fluctuation of the matric potential gradient was strongest near the surface. The gradient varied from 2923.63 to 1.027 cm cm^{-1} at surface, and varied from 4.23 to 1.28 cm cm^{-1} at −5 cm. The top 5 cm layer could be regarded as the active layer for the isothermal flux driven by the matric potential. Below −5 cm, the variation of the gradient tended to be steady, except for the occurrence of the bulge of gradient in the initial period. The matric potential gradient was positive throughout the entire profile.
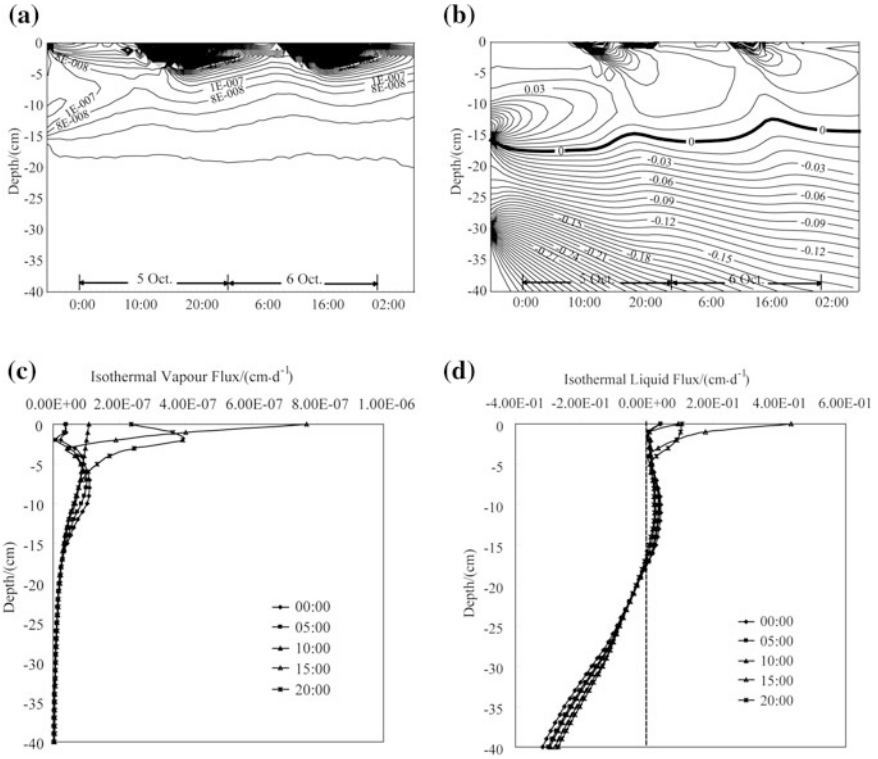
Fig. 2.12 Distribution of (**a**) the isothermal vapor fluxes and (**b**) the isothermal liquid fluxes in space and time; (**c**) Isothermal vapor flux profiles and (**d**) isothermal liquid flux profiles

2.4.4 Isothermal Flux Fields

The variation of the isothermal vapor flux was shown in Fig. 2.12a. From the flux profiles, it was seen clearly how the matric potential determines the dependence of isothermal vapor on space and time. In top 5 cm layer, the fluctuation was strong. The isothermal vapor flux varied from 4.02×10^{-4} to 6.75×10^{-9} cm d^{-1} at surface, and from 2.37×10^{-7} to 5.13×10^{-8} cm d^{-1} at -5 cm. At deeper soil layer, there was almost no fluctuation. For example, at -40 cm, the maximum flux was 5.31×10^{-9} cm d^{-1} and the minimum flux was 1.74×10^{-11} cm d^{-1}. During the whole simulation period, the direction of the isothermal vapor flux was upward throughout the entire profile (Fig. 2.12c).

Although the matric potential was upward throughout the entire profile during the simulation period, the isothermal liquid water flux was not upward in the space-time filed (Fig. 2.12b), and there was a reversal in the direction from upward to downward. From the isothermal liquid flux profiles, there was a plane of divergence developed from -16 cm and fluctuated between -13 and -17 cm. The reason for this was that the isothermal liquid water was driven not only by the

matric potential gradient, but also the gravitational gradient. The gravitational gradient was -1 cm cm^{-1} between two nodes. When the matric potential gradient was larger than 1 cm cm^{-1}, the flux of the isothermal liquid water would be upward. Otherwise, the matric potential would be smaller than the gravitational potential and the flux of the isothermal liquid water would be downward. In the matric potential gradient field, there was a plane with the gradient of 1 cm cm^{-1}, which fluctuated between -13 and -17 cm. It was accordant to the fluctuation of the plane of divergence in Fig. 2.12b. The isothermal liquid water flux was upward above the plane of divergence, while downward below the plane, during the simulation period (Fig. 2.12d).

2.4.5 Soil Water Dynamics

Generally, three stages could be recognized from the spatial-temporal distributions of liquid water flux and water vapor flux (Fig. 2.13). The determination of the stages was corresponding to the occurrences of the three types of thermal flux profiles, due to the isothermal flux profiles kept fixed during the whole simulation period. The isothermal vapor flux was upward through all three stages, and the magnitude of it was at least two orders of magnitude less than other fluxes. Considering its stability and small magnitude, the isothermal vapor flux is not discussed in specific stages.

The first stage started from midnight and ended before dawn (01:00–07:00) (Fig. 2.13). During this stage, the isothermal liquid flux, the non-isothermal liquid flux and the vapor flux were upward above the plane of divergence, and downward below this plane. The magnitude of the upward value of thermal vapor flux (0.238–0.0007 cm d^{-1}) was the same as that of thermal liquid flux (0.202–0.0002 cm d^{-1}). Compared to the thermal liquid and vapor flux, the isothermal liquid flux (0.064–0.0001 cm d^{-1}) was less significant in this stage. However, below the
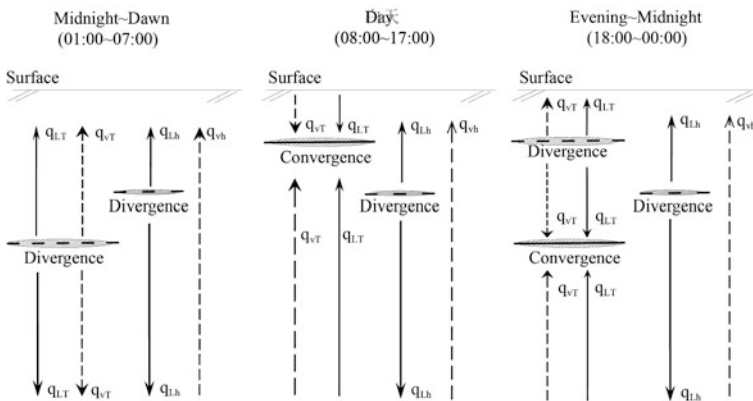
Fig. 2.13 Schematic illustrations of the diurnal soil water dynamics

divergent plane, the downward isothermal liquid flux (-0.329 to -0.378 cm d^{-1}) dominated, while the thermal vapor flux (-2.15×10^{-6} to 3.83×10^{-4} cm d^{-1}) was most insignificant. The plane of divergence developed from -23 cm at the beginning of this stage and propagated downward to -36 cm at the end. This stage indicated that the upward thermal flux dominated in the upper soil layer, while the downward isothermal flux dominated in the deeper soil layer.

The second stage was in day between 08:00 and 17:00. In this stage, the plane of convergence occurred at -3 cm and moved downward to the depth of 24 cm. Above the convergent plane, the magnitude of the downward thermal vapor flux (-0.244 cm d^{-1} to -2.409×10^{-3} cm d^{-1}) was larger than the thermal liquid flux (-0.040 cm d^{-1} to -5.509×10^{-5} cm d^{-1}). However, the thermal vapor flux was not the dominant flux. The magnitude of upward isothermal liquid flux (0.423–0.029 cm d^{-1}) exceeded the thermal flux above the convergent plane. In additional, the downward isothermal liquid flux was over the thermal flux below the convergent plane. It indicated that the isothermal liquid flux dominated in day throughout the entire profile.

The third stage was from evening to midnight (18:00–00:00). It was the transition stage between the second stage and the first stage. The plane of divergence started from -5 cm and ended at -15 cm. In the initial period of this stage (18:00 $-$ 19:00), the upward isothermal liquid flux were over the thermal flux above the divergent plane. In the top 5 cm soil layer, the average of the isothermal liquid flux was 0.033 cm d^{-1}, compared with 0.031 cm d^{-1} of thermal vapor flux and 0.004 cm d^{-1} of thermal liquid flux. In the rest of this stage, the average of the thermal vapor flux (0.022 cm d^{-1}) was over those of the isothermal liquid flux (0.021 cm d^{-1}) and the thermal liquid flux (0.005 cm d^{-1}). The plane of convergence occurred at -24 cm and developed downward to -38 cm. The direction of the thermal liquid flux, thermal vapor flux and isothermal liquid flux were the same between -15 and -24 cm; while the isothermal liquid flux dominated in this soil layer. Below -24 cm, the downward isothermal liquid flux was still the dominant flux. During this transition stage, the dominant flux in the top 5 cm soil layer changes from the isothermal liquid flux to the thermal vapor flux; at the meantime, the isothermal kept the dominance at greater depth. This indicates that the third stage was changing toward the situation in the first stage.

2.5 Brief Summary

The modified HYDRUS1D code, which refers to the coupled transport of liquid water, water vapor and heat, could be applied to further evaluate the mechanisms affecting unsaturated flow at the site. It was convenient to use the space-time fields to investigate the propagation of the heat and water flow in soil. According to the space-time fields of the nonisothermal and isothermal flux, three stages of the soil water dynamics were determined. Generally, the thermal vapor and liquid flux was dominant in uppermost soil layer at night, while the isothermal liquid water

dominated in day and at deeper soil layer. The numerical simulations suggested that the isothermal liquid flux, the nonisothermal liquid flux and the nonisothermal vapor flux should be considered in the conceptualization of the unsaturated flow in the relatively coarse sand. Although this study was for the relatively coarse sand in the sand bunker, further studies for sand in the natural conditions (particularly in desert) are necessary, where the simulation of soil moisture dynamics is poor [73].

References

1. Philip JR (1957) Evaporation, and moisture and heat fields in the soil. J Atmospheric Sci 14(4):354–366
2. Philip JR, de Vries DA (1957) Moisture movement in porous materials under temperature gradient. Trans Am Geophys Union 38(2):222–232
3. de Vries DA (1958) Simultaneous transfer of heat and moisture in porous media. Trans Am Geophys Union 39(5):909–916
4. Milly PCD, Eagleson PS (1980) The coupled transport of water and heat in a vertical soil column under atmospheric excitation, Massachusetts Institute of Technology, Department of Civil Engineering, Ralph M. Parsons Laboratory for Water Resources and Hydrodynamics
5. Milly PCD (1984) A simulation analysis of thermal effects on evaporation from soil. Water Resour Res 20(8):1087–1098
6. Taylor SA, Stewart GL (1960) Some thermodynamic properties of soil water. Soil Sci Soc Am Proc 24:243–247
7. Taylor SA, Cary JW (1964) Linear equations for the simultaneous flux of matter and energy in a continuous soil system. Soil Sci Soc Am J 28:167–172
8. Groenevelt PH, Kay BD (1974) On the interaction of water and heat transport in frozen and unfrozen soils: II. the liquid phase. Soil Sci Soc Am Proc 38:400–404
9. Kay BD, Groenevelt PH (1974) On the interaction of water and heat transport in frozen and unfrozen soils: I. basic theory: the vapor phase. Soil Sci Soc Am Proc 38:395–400
10. Grifoll J, Cohen Y (1999) A front-tracking numerical algorithm for liquid infiltration into nearly dry soils. Water Resour Res 35(8):2579–2585
11. Salzmann W, Bohne K, Schmidt M (2000) Numerical experiments to simulate vertical vapor and liquid water transport in unsaturated non-rigid porous media. Geoderma 98(3):127–155
12. Scanlon BR (1992) Evaluation of liquid and vapor water flow in desert soils based on chlorine 36 and tritium tracers and nonisothermal flow simulations. Water Resour Res 28(1):285–297
13. Scanlon BR, Milly PCD (1994) Water and heat fluxes in desert soils 1. Field studies. Water Resour Res 30(3):709–720
14. Scanlon BR, Milly PCD (1994) Water and heat fluxes in desert soils 2. Numerical simulations. Water Resour Res 30(3):721–734
15. Shiklomanov IA, Gu W-Z, Lu J-J (2004) Experimental research on the role of dew in arid ecosystem of Gobi desert, Inner Mongolia. In: Xi R-Z, Seiler K-P, Gu W-Z (eds) Research basins and hydrological. A A Balkema Publishers, Leiden,pp 329–332
16. Gustafsson AM, Lindblom J (2001) Underground condensation of humid air-a solar driven system for irrigation and drinking-water production. Master thesis, CIV, Luleå University of Technology, Sweden, 140 pp
17. Lindblom J, Nordell B (2006) Water production by underground condensation of humid air. Desalination 189:248–260
18. Cary JW, Taylor SA (1962) Thermally driven liquid and vapor phase transfer of water and energy in soil. Soil Sci Soc Am Proc 26:417–420

19. Cary JW, Taylor SA (1962) The interaction of the simultaneous diffusions of heat and water vapor. Soil Sci Soc Am Proc 26:413–416
20. Cary JW (1963) Onsager's relation and the non-siothermal diffusion of water vapor. J Phys Chem 67(1):126–129
21. Cary JW (1964) An evaporation experiment and its irreversible thermodynamics. Int J Heat Mass Transfer 7:531–538
22. Cary JW (1965) Water flux in moist soil: thermal versus suction gradients. Soil Sci 100(3):168–175
23. Cary JW (1979) Soil heat transducers and water vapor flow. Soil Sci Soc Am J 43(5):835–839
24. Rose DA (1963) Water movement in porous materials: Part 1- Isothermal vapor transfer. Br J Appl Phys 14(5):256–262
25. Rose DA (1963) Water movement in porous materials: Part 2- The separation of the components of water movement. Br J Appl Phys 14(8):491–496
26. Rose DA (1968) Water movement in dry soils:I. physical factors affecting sorption of water by dry soil. J Soil Sci 19(1):81–93
27. Rose DA (1968) Water movement in porous materials. Part 3- Evaporation of water from soil. Br J Appl Phys 2(1):1779–1791
28. Rose DA (1971) Water movement in dry soils.II. An analysis of hysteresis. J Soil Sci 22(4):490–507
29. Cary JW (1966) Soil moisture transport due to thermal gradients: practical aspects. Soil Sci Soc Am Proc 30:428–433
30. Jackson RD (1973) Diurnal changes in soil water content during drying. Field soil water regime, Madison 5, pp 37–55
31. Milly PCD (1982) Moisture and heat transport in hysteretic, inhomogeneous porous media: a matric head-based formulation and a numerical model. Water Resour Res 18(3):489–498
32. Milly PCD (1984) A linear analysis of thermal effects on evaporation from soil. Water Resour Res 20(8):1075–1085
33. Milly PCD (1984) A simulation analysis of thermal effects on evaporation from soil. Water Resour Res 20(8):1087–1098
34. Milly PCD (1996) Effects of thermal vapor diffusion on seasonal dynamics of water in the unsaturated zone. Water Resour Res 32(3):509–518
35. Braud I, Dantasantonino AC, Vauclin M, Thony JL, Ruelle P (1995) A simple soil-plant-atmosphere transfer model (Sispat) development and field verification. J Hydrol 166(3–4):213–250
36. Shurbaji ARM, Phillips FM (1995) A numerical-model for the movement of H2o, H-2 O-18, and (Hho)-H-2 in the unsaturated zone. J Hydrol 171(1–2):125–142
37. Nassar IN, Horton R (1997) Heat, water, and solution transfer in unsaturated Porous media: I-Theory development and transport coefficient evaluation. Transp Porous Media 27(1):17–38
38. Asghar MN (1996) Computer simulation of salinity control by means of an evaporative sink. PhD thesis, University of Newcastle upon Tyne
39. Rose DA, Konukcu F, Gowing JW (2005) Effect of watertable depth on evaporation and salt accumulation from saline groundwater. Aust J Soil Res 43(5):565–573
40. Kondo J, Okusa N (1990) A simple numerical prediction model of nocturnal cooling in a basin with various topographic parameters. J Appl Meteorol 29(7):604–619
41. Kondo J, Saigusa N, Sato T (1992) A model and experimental-study of evaporation from bare-soil surfaces. J Appl Meteorol 31(3):304–312
42. Yamanaka T, Yonetani T (1999) Dynamics of the evaporation zone in dry sandy soils. J Hydrol 217(1–2):135–148
43. Konukcu F, Istanbulluoglu A, Kocaman I (2004) Determination of water content in drying soils: incorporating transition from liquid phase to vapor phase. Aust J Soil Res 42(1):1–8
44. Gowing JW, Konukcu F, Rose DA (2006) Evaporative flux from a shallow watertable: the influence of a vapor-liquid phase transition. J Hydrol 321:77–89

45. Jacobs AFG, Heusinkveld BG, Berkowicz SM (2000) Force-restore technique for ground surface temperature and moisture content in a dry desert system. Water Resour Res 36(5):1261–1268
46. Jacobs AFG, Heusinkveld BG, Berkowicz SM (1999) Dew deposition and drying in a desert system: a simple simulation model. J Arid Environ 42:211–222
47. Agam N, Berliner PR (2006) Dew formation and water vapor adsorption in semi-arid environments–A review. J Arid Environ 65(4):572–590
48. Agam N, Berliner PR, Zangvil A, Ben-Dor E (2004) Soil water evaporation during the dry season in an arid zone. J Geophys Res 109:161–173
49. Zhang T, Berndtsson R (1991) Analysis of soil-water dynamics in time and space by use of pattern-recognition. Water Resour Res 27(7):1623–1636
50. Athavale RN, Rangarajan R, Muralidharan D (1998) Influx and efflux of moisture in a desert soil during a 1 year period. Water Resour Res 34(11):2871–2877
51. Mmolawa K, Or D (2003) Experimental and numerical evaluation of analytical volume balance model for soil water dynamics under drip irrigation. Soil Sci Soc Am J 67(6):1657–1671
52. Grifoll J, Gast JM, Cohen Y (2005) Non-isothermal soil water transport and evaporation. Adv Water Resour 28:1254–1266
53. Saito H, Simunek J, Mohanty BP (2006) Numerical analysis of coupled water, vapor, and heat transport in the vadose zone. Vadose Zone J 5(2):784–800
54. Kemp PR, Reynolds JF, Pachepsky Y, Chen JL (1997) A comparative modeling study of soil water dynamics in a desert ecosystem. Water Resour Res 33(1):73–90
55. Schelde K, Thomsen A, Heidmann T, Schjoenning P, Jansson PE (1998) Diurnal fluctuations of water and heat flows in a bare soil. Water Resour Res 34(11):2919–2929
56. Starr JL, Paltineanu IC (1998) Soil water dynamics using multisensor capacitance probes in nontraffic interrows of corn. Soil Sci Soc Am J 62(1):114–122
57. Wang D (2002) Dynamics of soil water and temperature in aboveground sand cultures used for screening plant salt tolerance. Soil Sci Soc Am J 66(5):1484–1491
58. Starr JL, Timlin DJ (2004) Using high-resolution soil moisture data to assess soil water dynamics in the vadose zone. Vadose Zone J 3(3):926–935
59. Zhao Y, Paul W, Yiming W (2002) Comparison of soil water content measurements with SWR-, FD- and TDR sensors. Z Bewässerungswirtsch 37(1):17–31
60. Ho CK, Webb SW (1999) Enhanced vapor-phase diffusion in porous media—LDRD Final report. USDOE, Sandia National Laboratories, Albuquerque, NM, and Livermore, CA
61. Bear J (1972) Dynamics of fluid in porous media. Dover, New York
62. Miyazaki T (1993) Water flow under the effects of temperature gradients. Water Flow in Soils: 169–196
63. Tindall JA, Kunkel JR (1999) Unsaturated zone hydrology for scientists and engineers. Prentice-Hall Inc, Upper Saddle River
64. van Genuchten MT (1980) A closed-form equation for predicting the hydraulic conductivity of unsaturated soils. Soil Sci Soc Am J 44(5):892–898
65. Schaap MG, Leij FJ (2000) Improved prediction of unsaturated hydraulic conductivity with the Mualem-van Genuchten Model. Soil Sci Soc Am J 64(3):843–851
66. Carsel RF, Parrish RS (1988) Developing joint probability distributions of soil water retention characteristics. Water Resour Res 24(5):755–769
67. Simunek J, Sejna M, van Genuchten MT (2005) The HYDRUS1D-1D software package for simulating the one-dimensional movement of water, heat, and multiple solutes in variably-saturated media. University of California-Riverside, Research reports, pp 1–240
68. Kleijnen JPC, Cheng RCH, Bettonvil B (2001) Validation of trace-driven simulation models: bootstrap tests. Manage Sci 47(11):1533–1538
69. Noborio K, McInnes KJ, Heilman JL (1996) Two-dimensional model for water, heat, and solute transport in furrow-irrigated soil: II. Field evaluation. Soil Sci Soc Am J 60(4):1010–1021

70. Fayer MJ (2000) UNSAT-H Version 3.0: Unsaturated soil water and heat flow model-theory, user manual, and examples, Washington, Pacific Northwest National Laboratory, p 331
71. Noborio K, McInnes KJ, Heilman JL (1996) Measurements of cumulative infiltration and wetting front location by time domain reflectometry. Soil Sci 161(8):480–483
72. Jury WA, Gardner WR, Gardner WH (1991) Soil physics. Wiley, New York, p 328
73. Walker JP, Willgoose GR, Kalma JD (2001) One-dimensional soil moisture profile retrieval by assimilation of near-surface measurements: a simplified soil moisture model and field application. J Hydrometeorol 2(4):356–373

Chapter 3
Application of Diurnal Soil Water Dynamics in Determining Effective Precipitation

3.1 Introduction

Infiltration has long been regarded as one of the most important problems for hydrological forecasting, due to its relevance to runoff, soil moisture storage, evapotranspiration, groundwater recharge and unsaturated flow [12, 24, 32]. Its significance on assessing the hydrological process, which is the main plant community shaping process, is even magnified in the arid ecosystems. In deserts, precipitation is often the sole source of water replenishment, while infiltration is the main process to understand how much rainfall could be retained in sand for some time before being either passed downward as percolation or returned to the atmosphere by evapotranspiration.

One of the main hydrological issues in water scarce regions is to demonstrate whether modern rainfall is recharging aquifers through infiltration and on what rate or scale. The Badain Jaran Desert with unexpected numerous groundwater-fed perennial lakes has attracted substantial research interest in investigating the desert hydrological process, and the infiltration in this special landscape, with lakes among inter-dune areas [14, 36], has been widely studied. Hofmann [15, 16] stated there was an aquifer in the northern areas of the eastern lakes region, recharged directly by precipitation through infiltration process, while he did not study the infiltration rate. Based on hydrochemical and isotopic analysis, Gu et al. [14] pointed out that groundwater flowed from adjacent areas in the south to the north western part with a historic and fossil recharge (1,000–30,000 BP); and with the actual analytical results on groundwater chlorides, he estimated that 1–1.5 mm/yr

of groundwater recharge would occur by direct infiltration from precipitation. With tracer methods, more and more recharge rate data were reported and added to a growing catalogue of tracer results for the Badain Jaran Desert region, which led estimates of the average recharge rate in this region vary from 0.95 to 3.6 mm yr^{-1} [3, 7–9, 11, 15, 18, 21, 22, 43, 44, 49].

Aforementioned studies were mainly focused on the rate at which the infiltrated rainfall recharged the groundwater, which could be called the effective infiltration or the effective rainfall [1, 41]. However, the effective infiltration or rainfall can also be defined as the amount of rainfall stored in the shrub root zone, excluding the fraction that runs off the soil surface or passes through the root zone that does not contribute to shrub growth and the fraction that evaporates [39]. From above two definitions, obviously, the effective infiltration or rainfall can be generally defined as the portion of rainfall that penetrates and remains in a domain of interest. With this general definition, in this study, the effective infiltration is defined as the amount of soil water remained in sand beneath the drying front (making the interface between the upward and downward soil water fluxes) by infiltrated water of a rainfall event, and thus not evaporated, and is evaluated based on the vadose zone soil water balance method.

As mentioned above, the estimates of infiltration rate in deserts have mostly been conducted with the tracer method, which is mainly used to evaluate variations of flow and transport in thick desert vadose zones in response to paleoclimatic forcing, and thus with the time scale of thousand-year [29]. While with the soil water balance model, the infiltration and soil water redistribution process in the unsaturated zone could be tracked at any meaningful time scale of interest. In order to do that, quantifying changes in infiltration properties by a reliable observation and measurement is needed. Previous studies has indicated the feasibility of using soil water content probes installed into the soil to track the propagation of the wetting front during infiltration [10, 23, 26, 32–34, 39, 40, 46, 47].

In this chapter, the measurements of soil water content, soil temperature and precipitation are used to calibrate the performance of HYDRUS1D, which is subsequently used to produce the temporal and spatial information of coupled water, water vapor and heat transport. This enables us to characterize the variation pattern of the drying front before, during and after rainfall, so that we can assess how much precipitation is evaporated and how much is conserved in sand. Our goal is to understand the capacity of the sand dune to capture certain amounts of rainfall during a single precipitation event. The first section of the chapter thus describes the experiments and methods used. Then follows simulation results based on experimental observations. We conclude the chapter with a discussion of practical results.

3.2 Materials and Methods

3.2.1 Study Site Description

The study site is a relatively flat area at the foot of dunes, with an area of about 100 m^2, located in the southeast Badain Jaran Desert, which lies in the northwest of the Alashan plateau in western Inner Mongolia of China, between 39°20$'$N–41°30$'$N and 100°E–104°E. The Badain Jaran Desert is regarded as the second largest desert in China, and covers an area of about 49000 km^2 [42]. The desert landscape primarily consists of unvegetated or sparsely vegetated aeolian sand dune fields as a core, surrounded by desert plains, with pediments on the margin [45]. The elevation ranges from 1500 m in the southeast to 900 m above sea level in the northwest, with the mega dunes up to 400 m high in the southeast aligned in a SW–NE pattern [4]. The mean grain size of the dune sand in this desert is between 0.21 and 0.22 mm [18, 44]. There are over 70 lakes among the interdune areas, of which the surface area vary from 0.2 km^2 on the southeastern edge of the desert to 1.6 km^2 slightly northwards, and the water depth from 2 to 16 m [44]. On the surface, there is neither recharging into these lakes nor discharging from them, and there is no river in the entire desert [38, 42]. With such kind of hydrological conditions, vegetation in the study area is sparse. The plant or shrub communities depend mainly on the geomorphology and on edaphic conditions. The dominant plant species are *Haloxylon ammodendron*, *Psammochoa villosa*, *Phragmites communis*, *Artemisia ordosica*, while in the area around lakes and springs the denser groundcover observable could be found (*Polypogon monspeliensis*, *Triglochin maritima*, *Achnatherum splendens*, Carex sp., *Glaux maritima*) [8, 9].

The distribution of sparse vegetation in this area is mainly caused by the dominated climate pattern in the Alashan Plateau, which is characterized by a markedly arid and continental climate. During the winter months, a well-developed high pressure system, cold and dry continental air masses with temperatures below zero, influences the area, which makes the mean monthly temperature −10 °C in January. In the summer months, the tropical air masses from the Pacific Ocean hits the Badain Jaran Desert with more than half of the average annual precipitation fell in July. The spatial and temporal distribution of the precipitation in the area is determined by the Asian summer monsoons at the present time, and the mean monthly temperatures in July is 25 °C with a diurnal temperature variation up to more than 45 °C. The mean annual precipitation varies from 84 to 120 mm in the southeast, from 37 to 40 mm in the northwest, and the potential evaporation is approximately 2600 mm/yr, being the highest in China [8, 9, 21, 22].

3.2.2 Experimental Design and Data Collection

In order to quantify the effective infiltration of soil water content, measurements of soil temperature and soil matric potential were conducted in the observation period, from 3 June to 20 June in 2008. The instruments used for measuring soil moisture and temperature are the profile sensors, using numerous of transducers combined in one probe with a certain distance interval between them. It is especially necessary to use the profile sensor in desert, considering the sand profile would collapse easily during digging. As for the soil matric potential, there was not a profile sensor available and four separate transducers, pF-meters (GeoPrecision GmbH, Ettlingen, Germany), were installed at the corresponding depth of soil water content monitoring.

The soil water content profile sensor is called as EasyAG50 (Sentek Pty. Ltd., Stepny, South Australia), the principles of operation and design of which are described in detail by *Fares* and *Polyakov* [5] and the manufacture's calibration manual [30]. An individual probe consisted of a printed circuit board, five capacitance sensors (Multi-sensor Capacitance Probes, MCP), and a polyvinyl chloride (PVC) access tube with external and internal diameters of 32 and 28 mm, respectively. Capacitance sensors are set at 10, 20, 30, 40, and 50 cm from the sand surface. The reading range of these capacitance sensors is from oven dry to saturation. The correlation coefficient between the readings and actual soil water content based on field calibration is 89.39 %, with a resolution of 0.008 %, and a precision of ± 0.06 % Vol. The temperature effects on readings of MCP were conducted in the lab with the standard procedures described in detail by Polyakov et al. [27] and Fares et al. [6]. The temperature effects for the capacitence sensors were 14.4 % of readings from 12 to 45 °C at 10 cm, 13.9 % from 11 to 50 °C at 20 cm, 14 % from 9 to 51 °C at 30 cm, 13 % from 9 to 55 °C at 40 cm, and 15 % of readings from 8 to 55 °C at 50 cm, respectively. After the calibration, the temperature effects at the depth of 10, 20, 30, 40, and 50 cm were reduced by 92, 93, 93.8, 88, and 82 %, respectively.

The soil temperature profiles were measured by STP01 (Hukseflux Thermal Sensors B.V., Delft, The Netherlands), which was designed to measure the soil temperature at specific depths by determining the thermal gradients between a certain specific depth and the reference point. It improves the accuracy in positioning, the uncertainty of which is usually large when using a series of separate sensors. This makes the temperature gradient measurement more correctly, which subsequently improves the accuracy of the absolute temperature measurement. The principles of measurement by STP01 had been described in detail by the manufacture's manual [17]. A single probe generally contains five thermocouples, a copper lead, a Pt100, a TC junctions and a sensor foil with the thickness of 0.6 mm. The thermocouples are set at 2, 5, 10, 20, and 50 cm from the sand surface. The measurement range of STP01 is from -30 to 70 °C, with an accuracy of ± 0.02 °C.

During installation, a single MCP probe (soil water content profile sensor) was inserted into a 60 cm long access, which was put into a pit with sufficient width and depth. The probe was inserted into the sand through the side of the pit that was unaltered and was placed vertically to the sand surface. At the same time, about 30 cm away from MCP probe on the same side of the pit, the STP01 (soil temperature profile sensor) was installed vertically with the aid of a steel ruler, considering the sensor foil was too soft to be inserted in sand directly. After the setup of MCP and STP01 probe, the pit was carefully refilled, avoiding perturbations as far as possible. During the refilling, the separate soil matric potential sensors, pF-meters, were also inserted vertically on the same side of the pit as the two probes were installed, at the depth of 50, 40, 30 and 20 cm from the sand surface. The pF-meter is based on the registration of the molar heat capacity of the ceramic cup, which is in contact with the soil for balance, to record the matric potential over a large measurement range from pF 0 to 7.0, with an accuracy of $\pm$pF 0.05, an precision of less than $\pm$pF 0.015, and a resolution power of pF 0.01.

The precipitation was measured using a tipping bucket rain gauge, model TR-5251 (RST Instruments Ltd., Coquitlam, Canada), with a precision of $\pm$0.01 mm and a resolution of 0.01 mm. At the same time, other micrometeorological parameters such as the air temperature, relative humidity, net radiation and wind velocity were also measured at a height of 2 m above the surface layer. Two data collection and processing systems CR1000 and CR5000 (Campbell Scientific Inc., Logan, Utah, USA) were used to record the field data at half-hourly intervals. The first one was used to record the soil physical parameters, while the second one for the micrometeorological parameters.

3.3 Soil Water Balance Model

3.3.1 Model Description

The HYDRUS1D code, which refers to the coupled water, vapor and heat transport in the soil, was applied in order to determine the temporal and spatial soil water fluxes. The governing equation for one-dimensional vertical flow of liquid water and water vapor in the soil is given by Eqs. (2.1)–(2.6).

3.3.2 Material Properties

For the hourly time scale, the most active layer for the coupled liquid water, water vapor and heat in sand was near the surface and usually was limited in the depth of less than 50 cm [48], which was also the frequent influence depth of a typical rainfall in the desert environment [39, 40]. In the field site, we sampled sand at the

depth of 10, 20, 30, 40, and 50 cm, respectively; and all samples were used for the basic soil tests and soil water characteristic curves determinations (see later for details). It was found that the test results for these five samples were closed to each other, and the deviation from the averaged value was less than ±1 %. Then, the final results of the material properties were derived by averaging the results of these samples.

The field site consists of fine type sand. The grain-size distribution was deter-mined and classified following the Specification of Soil Test (SST), using sieve analysis method [25]. The fine sand had a coefficient of uniformity of 2.072, and a coefficient of curvature of 0.998. The particle-size distribution curve of the fine sand was shown in Fig. 3.1.

The soil water retention curve is one of the most fundamental hydraulic charac-teristics to solve the flow equation of water in soils, describing the relationship between volumetric water content and matric potential (i.e., the suction head) in the soil. According to the field measurement, the volumetric water content and matric potential data pairs (θ- h pairs) at all measured depths were pooled in Fig. 3.2a. For every single depth, there was a different pattern, especially at the depth of 50 cm. The data points highlighted by the oval-shaped curve were recorded after the occurrence of rainfall. These points indicate that there is hysteresis. It means that the soil undergoing drying processes such as evaporation or gravity drainage generally tends to retain a greater amount of water than during wetting processes (e.g. infiltration or capillary rise) for the same magnitude of suction [20]. The data points in the oval-shaped curve represented the wetting process of the sand after the rainfall, which did not follow the drying process (data points outside the oval-shaped curve) before the rainfall. At the depth of 50 cm, the hysteresis phenomena were more conspicuous than other depths. It was because hysteresis was less pronounced near the residual
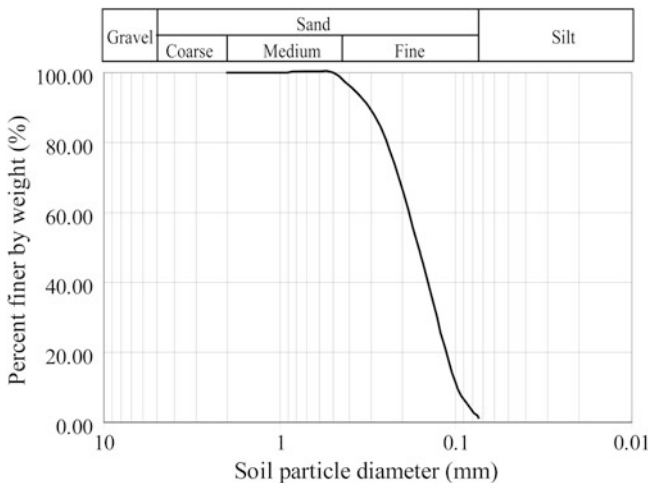
Fig. 3.1 Particle size distribution curve

water content where pore water retention felt within the pendular regime [20]. Due to the complicated hysteresis pattern, which was beyond the scope of this study, it was difficult to use the inverse method to get the van Genuchten's parameters using the in situ θ- h data pairs [48]. Instead, the pressure extraction chamber, model 1600 (Soil Moisture Equipment Corp., Santa Barbara, CA), was used to determine the water-holding characteristics with the soil water retention equation, which was given by van Genuchten [35] (see Eq. 2.7).

The fitted result between the in situ θ- h data pairs and the van Genuchten model was shown in Fig. 3.2b. The good fitness was found at low water content level, while the model fitted only part of the data at the depth of 50 cm, which was due to the pronounced hysteresis in moist sand [20]. The part of unfitted data represented the drying process of sand at the depth of 50 cm. Considering the scope of this study was on the determination of effective rainfall, the data of interest at −50 cm depth would be located at the wetting process, which were fitted well by the *van Genuchten* model, with $\theta_{res} = 0.017 \text{ cm}^3 \text{ cm}^{-3}$,
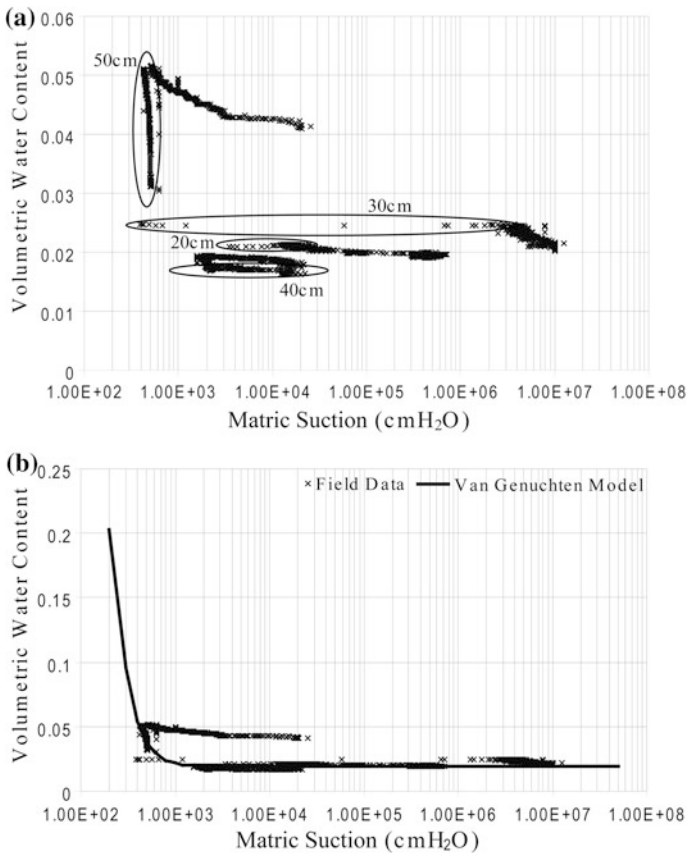
Fig. 3.2 The field measurement of **a** the soil matric potentials and **b** the fitted results

$\theta_{sat} = 0.382$ cm^3 cm^{-3}, $\alpha = 0.00236$ cm^{-1}, and $n = 3.6098$ (Fig. 3.2b). The hysteretic behaviour in the soil water retention curve should be understood, due to its consequent impact on the stress, strength, flow and deformation behaviour of unsaturated soil systems. However, this issue was beyond the scope of this study and will not be discussed here, and any interested readers are referred to Lu and Likos [20].

3.3.3 Initial and Boundary Conditions

Considering the groundwater table in the Badain Jaran Desert was at a depth of 2 m [8, 9], the soil profile was considered to be 100 cm deep and the bottom condition for this profile was regarded as the free drainage, and the nodes located at depths of 2, 5, 10, 20, 30, 40 and 50 cm were selected for comparing calculated temperatures and volumetric water contents with measured values. The spatial discretization of 1 cm was used, leading to 101 nodes across the profile. The calculations were performed for a period of 17.6 days from 3 June to 20 June in 2008. Discretization in time varied between a minimum and a maximum time-step (i.e. 1 s–1800 s), controlled by some time-step criterion [28]. Except for the aforementioned geometry and time information, it is necessary to specify initial conditions for temperature and soil water content in order to solve this problem by HYDRUS1D.

The initial soil water content and temperature distributions across the profile were determined from measured values on 3 June by interpolating the measured values between two adjacent depths. Boundary conditions at the soil surface for liquid water, water vapor and heat were determined from the surface energy balance equation (van Bavel and Hillel 1976):

$$R_n - H - LE - G = 0 \qquad (3.1)$$

where R_n is the net radiation, H is the sensible heat flux density, LE is the latent heat flux density, L is the latent heat, E is the evaporation rate, and G is the surface heat flux density. Net radiation (Brutsaert 1982) and sensible heat flux (van Bavel and Hillel 1976) were defined as:

$$R_n = \varepsilon_s \varepsilon_a \sigma T_a^4 - \varepsilon_s \sigma T_s^4 H = C_a \frac{T_s - T_a}{r_H} \qquad (3.2)$$

where ε_a is the emissivity of the atmosphere, ε_s is the emissivity of the bare soil, σ is the Stefan-Bolzmann constant, T_a is the air temperature, T_s is the soil surface temperature, C_a is the volumetric heat capacity of air, and r_H is the aerodynamic resistance to heat transfer. The surface evaporation is calculated as

$$E = \frac{\rho_{vs} - \rho_{va}}{r_v + r_s} \qquad (3.3)$$

where ρ_{vs}, ρ_{va} are the water vapor density at the soil surface and the atmospheric vapor density, respectively; r_v, r_s are the aerodynamic resistance to water vapor flow and the soil surface resistance to water vapor flow that acts as an additional resistance along with aerodynamic resistance, respectively [2]. As for the heat transport domain, the upper boundary condition was determined by the measured surface temperature, while the lower boundary condition was considered as zero temperature gradient [28].

3.4 Results and Discussion

The physics of infiltration has been developed and improved during the last almost seven decades. The numerical models play a critical role in evaluating this physical process, that governing soil heating, spatial distribution of water, and gaseous exchange between the soil and the atmosphere [10, 23, 24, 31]. The most widely used model is the Richards' equation, which has been modified into the HYDRUS1D considering the coupled liquid water, vapor and heat transport. With the soil hydraulic properties and the initial and boundary conditions introduced above, the HYDRUS1D was calibrated with the field data, which was subsequently used to calculate and analyze the detailed information of the soil water flow processes.

3.4.1 Model Verification

In this section, the measured water contents and soil temperatures were compared to those calculated by the HYDRUS1D code. The predicted and observed soil temperatures at depths of 2, 5, 10, 20, and 50 cm were shown in Fig. 3.3. The simulation's goodness of fit was quantified with the following relative root mean square error measure:

$$RRMSE = \frac{\sqrt{\sum_{i=1}^{N_w} (M_i - C_i)^2 \Big/ N_w}}{Max(M_1, M_2, \ldots \ldots, M_{N_w}) - Min(M_1, M_2, \ldots \ldots, M_{N_w})} \qquad (3.4)$$

where, N_w is the number of the measurements; M_i and C_i are measurements and calculations, respectively; $Max\,(M_1, M_2, \ldots \ldots, M_{N_w})$ and $Min\,(M_1, M_2, \ldots \ldots, M_{N_w})$ are the maximum and minimum value of the measurements. The $RRMSE$ is dimensionless and $RRMSE = 0$ indicates the best fit. The smaller is the $RRMSE$, the better the fit of simulation.

The $RRMSEs$ of the temperatures at depths of 2, 5, 10, 20, and 50 cm were 0.063, 0.061, 0.096, 0.183, and 0.17, respectively. Although the $RRMSEs$ of the
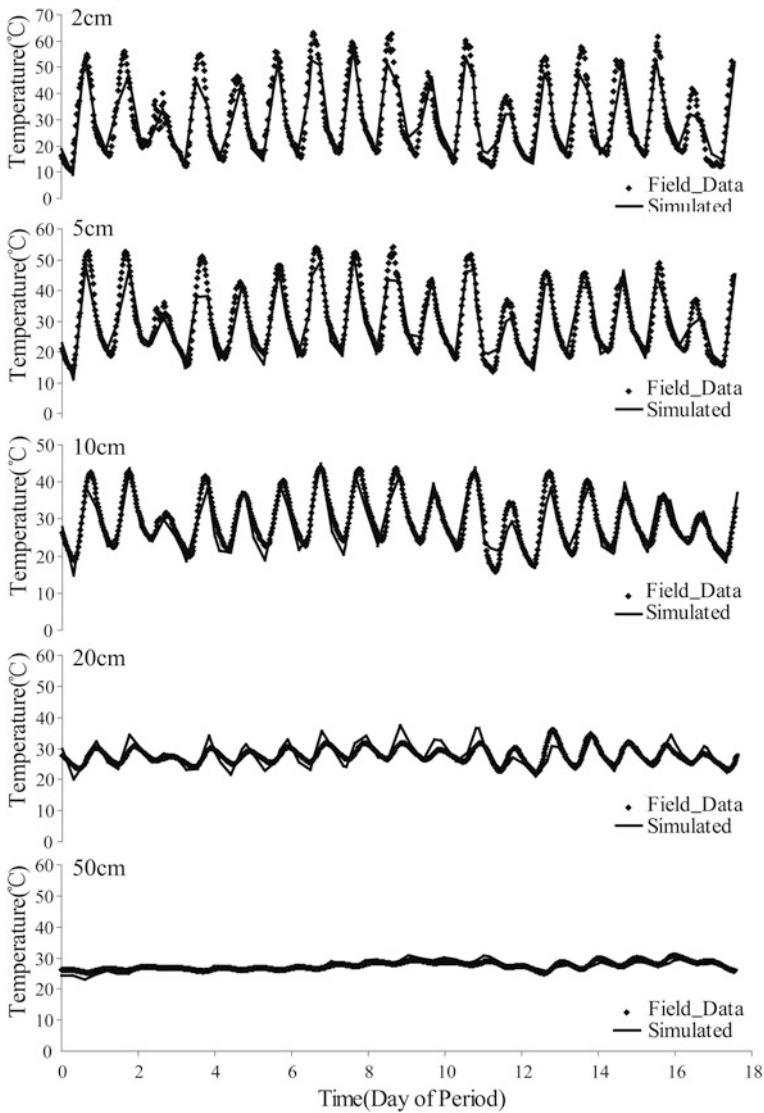
Fig. 3.3 The calculated and measured soil temperature at all depths

fitness at the depth of 20 and 50 cm were larger than 0.1 and close to 0.2, which means the largest deviation were −6 °C and 2.3 °C, the calculated and measured temperature generally agreed at all five depths and the typical sinusoidal diurnal variation of soil temperature were captured.

During the field monitoring, an incident precipitation was captured. The evaporation after rainfall was an exponential function of elapsed time [19], which was used in the calculation of soil moisture variation in HYDRUS1D. The

simulated and measured soil water content at the depths of 10 and 20 cm was depicted in the Fig. 3.4, while the simulated results for the soil moisture at the depths of 30, 40, and 50 cm were not shown here, which kept almost the same value during the period of field measurement. The *RRMSEs* of the soil water content at the depths of 10 and 20 cm were 0.048 and 0.19, respectively. Both temperature and soil water content were simulated well by using HYDRUS1D.

3.4.2 Determination of the Drying Front

The drying front is defined as the interface between the upward and downward soil water fluxes. In order to understand the variation of drying front, the detailed soil water content and temperature variability were shown as the projections of the relative altitude coordinates (Z-axis) to constant depth coordinates (Y-axis) and elapsed time coordinates (X-axis). The interpolating and smoothing procedure for projected soil water and temperature data were carried out by using the Surfer plotting software [13]. The interpolation was done using the Kriging option in Surfer. The fake virtual three dimensional fields, consisting of a space–time field (two-dimensional field) and a dependent altitude variable (e.g. specific flux, temperature or soil matric potential) [48], were plotted to understand the time series information of specific flux, soil temperature and soil matric potential for the whole soil profile, which presented a clear overview on the physical flow processes in soil.
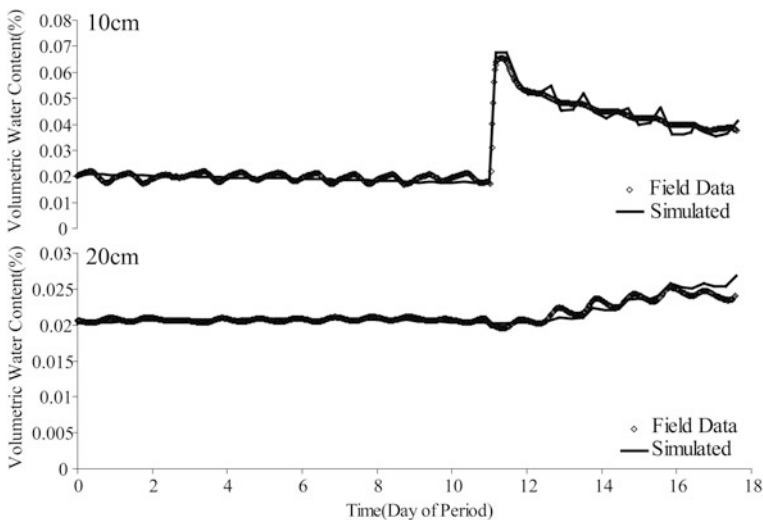
Fig. 3.4 The calculated and measured soil moisture content at the depth of 10 and 20 cm

3.4.2.1 The Driving Force

The driving forces causing flow in soil are inter-dependent, for example, as temperature gradients are accompanied by gradients of surface tension at the air–water interface, there is a possibility of thermal capillary flow and thermal capillary film flow of water in liquid phase [12]. There is a need to identify the soil matric potential and temperature pattern for the coupled flow processes.

Figure 3.5a shows daily time series of soil matric potential profile during the calculation period. On the day before the rainfall, the potential varied radically in the top 2cm layer, from −10556.4 to −1049.89 cm water column. While between 5 and 20 cm, a low potential zone developed with the lowest value of −31932 cm water column at the depth of 15 cm. It means that the soil water above and below this zone will be transported toward this low potential layer due to the convergent potential gradients, because the potential gradients above and below certain depth are directed to this depth and form a convergent zero soil matric potential gradient plane (Fig. 3.5b). The potential gradients were decided by $\triangle h = (h_{i+1} - h_i)$ (cm cm^{-1}), where h_i represented the soil matric potential at a depth of i cm.

After rainfall, the pattern of the soil matric potential was totally changed. The rainfall broke the original low potential zone and pushed it down to the layer between 20 and 30 cm, with lowest value of −3989 cm water column. The rainfall increased the soil matric potential almost nine times. At the meantime, the zero soil matric potential gradient planes moved downwards, and this was shown clearly in Fig. 3.5b. According to the pattern of the soil matric potential and its gradient, the soil moisture will transport upwards from the bottom of the soil profile during the whole period, which is accordant with *Walvoord*'s statements [37]. However, the soil moisture flux driven by soil matric potential gradient would be kept in soil due to the existence of zero potential gradient planes that varied from the surface to the depth of about 26 cm.
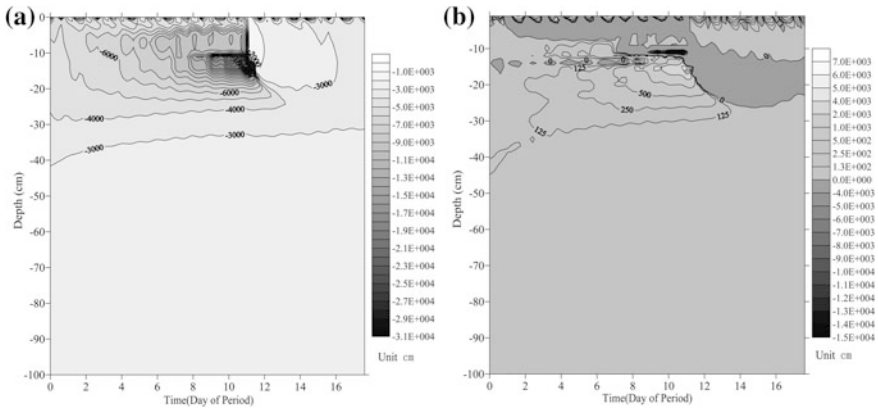
Fig. 3.5 The time series of **a** soil matric potential profile and **b** its gradient profile

Figure 3.6a shows the daily time series of soil temperature profiles, where the interval of isolines is 2 °C. The densities of isolines indicate how strongly the soil temperature at certain depth fluctuates. The dense and sparse isolines represent the rapid and slow variation of soil temperature with time, respectively. The isolines near the surface were the densest, while the isolines at the bottom of soil profile were the sparsest. During the observation period, the surface temperature varied from 9.16 to 63 °C, with a range of daily maximum surface temperature between 39 and 63 °C, and a range of daily minimum surface temperature between 9.16 and 19.6 °C. While at the depth of 50 cm, the soil temperature varied from 25.1 to 30.66 °C, with a variation span of 4.36 and 3.35 °C for the maximum and minimum soil temperature.

Figure 3.6b shows the space–time temperature gradient field, which clearly shows how heat transport in soil controls the dependence of the temperature gradient profiles on time and space. The temperature gradients were derived from $\triangle T = (T_{i+1}-T_i)$ (°C/cm^{-1}), where T_i represented the soil temperature at a depth of i cm. The variation of isolines in Fig. 3.6b is similar to that in Fig. 3.6a. The isolines experienced alternatively the sparseness and denseness with time elapsed on the surface, and developed downwards from denser to sparser with depth. According to the pattern of the soil temperature and its gradient, the thermal soil water transport is more complicated than the isothermal one. The positive temperature gradient distributed throughout the whole soil profile on the twelfth day of period. This meant that the thermal fluxes transported soil water to the surface from the bottom of the soil profile. On the other hand, the negative temperature gradient distributed throughout the whole soil profile at most of the period. However, during the whole period, most of downward thermal fluxes due to the negative temperature gradient would not transport the soil moisture from the surface to the bottom of the soil profile. They were retarded by the upward isothermal fluxes. The soil water fluxes were discussed with more details in the following section.
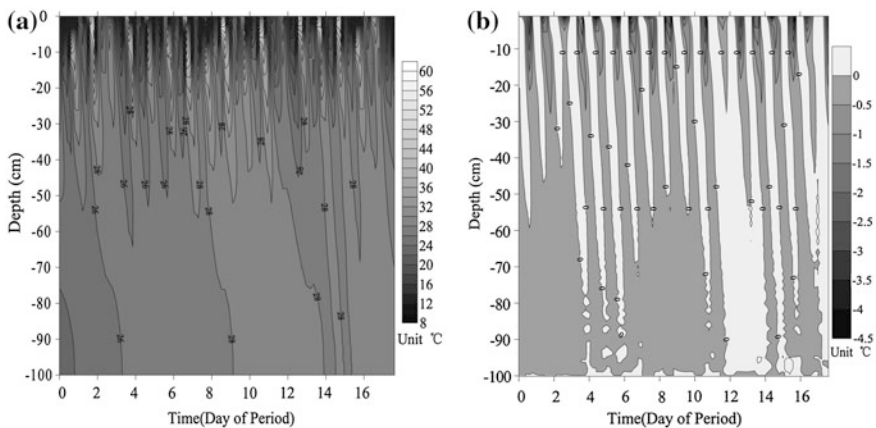
Fig. 3.6 The time series of **a** soil temperature profile and **b** its gradient

3.4.2.2 The Drying Fronts

With driving forces, the soil water flux pattern can be determined, which is subsequently used to identify the drying fronts. Figure 3.7a depicts the variation of the soil water flux profiles with time elapsed. The darker color indicated the negative fluxes, which meant that the soil moisture located in the darker area would be kept in soil and not be evaporated at that time. According to Fig. 3.7a, there were two types of darker areas: the first type of darker area occurred in the shallow layer limited above the depth of 45 cm with small time intervals and isolated shapes (A-type); the second type occurred below the depth of 45 cm with variation of the upper borderline, while the darker area kept continuity (B-type).

   Almost all of the A-type and B-type darker areas were located in the negative (/downwards) temperature gradient zones, except for the darker areas triggered by the rainfall event. The isolated shapes of A-type darker areas were activated when the upward isothermal fluxes (driven by soil matric potential gradient) were greater than the downward thermal fluxes (driven by soil temperature gradient). The space gaps between the A-type and B-type areas were likewise contributed by the dominance of the upward isothermal fluxes. Between the eighth and tenth day of the observation period, the negative temperature gradients were over the positive matric potential gradients, which led to the connection of the A-type and B-type areas. After the rainfall, the negative matric potential gradient above the low matric potential zone (Fig. 3.5b) kept dominant for almost 3 days with the propagation of the convergent matric potential planes, from the depth of 15 to 26 cm. The rainfall event also caused the positive temperature gradient through almost the whole profile, between the twelfth and fourteenth day of the observation period. However, it does not mean that the soil water can be transport from the bottom to the surface. The soil water fluxes, driven by the summation of the positive
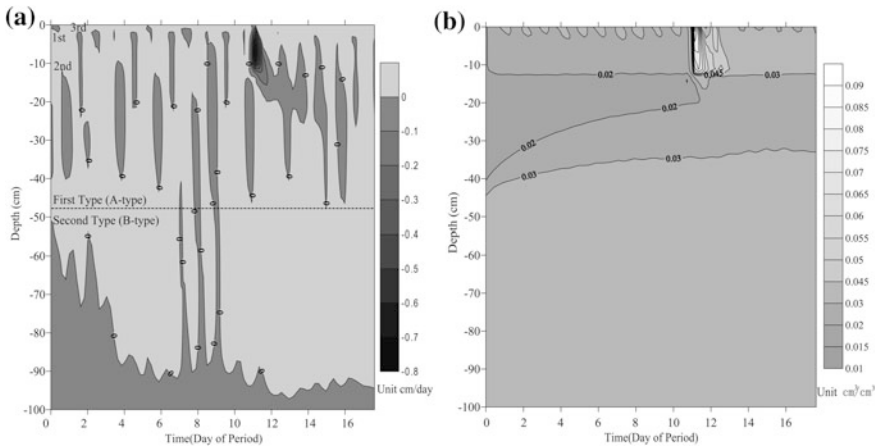
Fig. 3.7 The time series of **a** soil moisture flux pattern and **b** volumetric soil moisture content pattern

temperature gradient and matric potential gradient, were blocked by the convergent matric potential planes.

The drying front could be identified by the borderlines of darker areas. On the first day of the calculation period, the drying front started from the surface due to a small A-type darker area near the surface. As time elapsed, the drying front dropped to the second A-type darker area at the depth of about 12 cm. Since there was a gap between the second A-type darker area and the third one, which developed from 2 to 24 cm. The drying front fell to the B-type darker area at 60 cm and varied during the course of time, which was occupied by the gap between the second and third A-type darker area. After this, the drying front jumped to the third A-type darker area from the B-type darker area. Following the processes described above, the drying front fluctuated sharply from the surface to the upper borderlines of A-type and B-type darker areas. It should be noted that the upward fluxes underneath the lower borderlines of A-type darker areas and above the upper borderlines of B-type darker areas (the grey color area between A-type and B-type darker areas) would not be evaporated, due to the existence of convergent zero flux planes [48] at the lower borderlines of A-type areas.

The sharp fluctuation of the drying front was interrupted by the occurrence of precipitation, which was clearly shown in Fig. 3.7. After the rainfall of 6.604 mm, the drying front was limited at the depth of 20 cm for 3 days, from the eleventh to fourteenth day of the period. Then, the drying front experienced the wide fluctuation between the A-type and B-type darker areas again. It meant that the upward soil moisture flux above the upper borderlines of the B-type darker areas was kept at the lower borderlines of the A-type darker areas during these 3 days, and increased the moisture content near the borderlines.

The corresponding variation of soil moisture profile was shown in Fig. 3.7b. On the day before the rainfall, due to the sharp fluctuation of the drying front, the moisture content at the depth of 10 and 20 cm were kept between the value of 0.017 and 0.021 cm^3 cm^{-3}; 0.0201 and 0.0216 cm^3 cm^{-3}, respectively. After the rainfall, the interruption of the fluctuation of drying front increased the moisture at the depth of 10 and 20 cm to 0.065 and 0.0256 cm^3 cm^{-3}, respectively. However the moisture content at the depth of 30, 40, and 50 cm were not influenced by this rainfall event. After the stop of the rainfall, the moisture content at the depths of 10 and 20 cm decreased with time due to the propagation of the drying fronts. When the connected A-type areas were separated due to increasing evaporation, the moisture content at the depths of 10 and 20 cm would go back to the value before the rainfall gradually.

From above discussion, the 6.604 mm of rainfall would not be remained in sand, and would be evaporated to the atmosphere eventually. But, the rainfall interrupted the fluctuation of the drying front and made the isolated A-type darker areas connected for 3 days, which subsequently limited the upwards soil water flux from the deeper sand layer. All these kept the sand in the shallow layer moister than before the rainfall. Furthermore, 7 days after the rainfall, the moisture content at the depth of 10 cm was 0.036 cm^3 cm^{-3}, which was 0.015 cm^3 cm^{-3} higher than its daily averaged value before the rainfall. However, the 6.604 mm of

rainfall was not enough to penetrate into the B-type darker area, which would keep the soil moisture in soil and form the effective infiltration. It should be noted that the effective rainfall requires the rainfall penetrating below the deepest drying front, for example, in this case, under the depth of 94 cm (Fig. 3.7a).

3.4.3 Determination of Effective Infiltration

After the rainfall, the infiltrating process will form a downward wetting front in soil. When the rainfall stops, the evaporation on the surface will dry the wetted soil and form a drying front. During the redistribution of the infiltrated rainfall, the drying front chases the wetting front. If the infiltrated rainfall could not penetrate into the deepest drying front before the stop of redistributing process and be caught up by the drying front, there would be no effective infiltration in the sand. On the other hand, if the rainfall does penetrate into the deepest drying front, the determination of this part of rainfall requires the calculation of the cumulative infiltration under the deepest drying front, which can be determined by the HYDRUS1D with field data. With the HYDRUS1D, the volumetric soil moisture could be retrieved with a spatial resolution of 1 cm, which helps to know exactly when and where the redistribution of infiltrated rainfall stops. The effective rainfall below the deepest drying front can be determined by the difference of the volumetric soil moisture profiles before and after the redistribution, which can be described as

$$R_{eff} = \bar{\theta}_{wetted} - \bar{\theta}_{original}, \quad \bar{\theta} = \sum_{i=1}^{n} (\frac{\theta_i + \theta_{i+1}}{2})\Delta z, \quad i = 1, 2, 3, \ldots, n \qquad (3.5)$$

where R_{eff} is the effective infiltration, $\bar{\theta}_{wetted}$ is the average volume of soil moisture after the redistribution, $\bar{\theta}_{original}$ is the average volume of soil moisture before the redistribution, θ_i and θ_{i+1} are the volumetric soil moistures below the deepest drying front with an interval of Δz, and n is determined by the difference between the deepest drying front and the infiltrated depth [(the infiltrated depth − the depth of deepest drying front)/Δz]. For example, in the case of the deepest drying front of 94 cm, if the infiltrated depth was 98 cm and the interval (Δz) was set as 1 cm, the n would be equal to 4 [(98 cm − 94 cm)/1 cm]; while, $\theta_1, \theta_2, \theta_3, \theta_4$ and θ_5 would be the volumetric moisture content at the depth of 94, 95, 96, 97, and 98 cm (Fig. 3.8).

The precipitation of 6.604 mm was not enough to penetrate into the deepest drying front in this case. In order to have an idea on how much volume of rainfall could penetrate into sand and became the effective infiltration, the volume of precipitation was set as 33.02 mm with a rainfall rate of 6.6 mm hr^{-1} [19, 39]. According to the calculation result, the rainfall penetrated to the depth of 98 cm. The original volumetric soil moisture content at the depth of 94, 95, 96, 97, and

98 cm were 0.0429, 0.043, 0.0432, 0.0433, and 0.0434 cm^3 cm^{-3}, respectively, while they became 0.0465, 0.0459, 0.0455, 0.045 and 0.0445 cm^3 cm^{-3} after the stop of redistribution. According to the Eq. (3.5), the effective infiltration was 0.0925 mm.

3.5 Brief Summary

The effective infiltration is defined here as the amount of rainfall remained in sand beneath the deepest drying front from an incident rainfall event. In order to understand the effective infiltration, the coupled liquid water, vapor and heat transport in sand was analyzed to determine the drying front, using the HYDRUS1D code. According to the calculation results, the drying fronts were mainly determined by the shapes of the zero flux isolines. There were two kinds of shapes of zero flux isolines: A-type, which occurred in the shallow layer limited in the depth of 45 cm with small time intervals and isolated shapes; and B-type, which occurred below the depth of 45 cm (from the depth of 45–94 cm) and kept the continuity. Consequently, the drying front fluctuated sharply during the whole calculation period. The rainfall interrupted the fluctuation of the drying front and kept it at the depth of 20 cm for 3 days. Although, the 6.604 mm of rainfall was not able to penetrate into the lowest evaporation during the whole period, it did keep sand moister than before rainfall in the shallow layer (surface to the depth of 20 cm). Based on the HYDRUS1D code, a simple method was used to estimate the effective infiltration. With the artificial set rainfall of 33.02 mm and the rainfall rate of 6.6 mm hr^{-1}, the effective infiltration was estimated as 0.0925 mm.

Fig. 3.8 Schematic calculation of effective infiltration
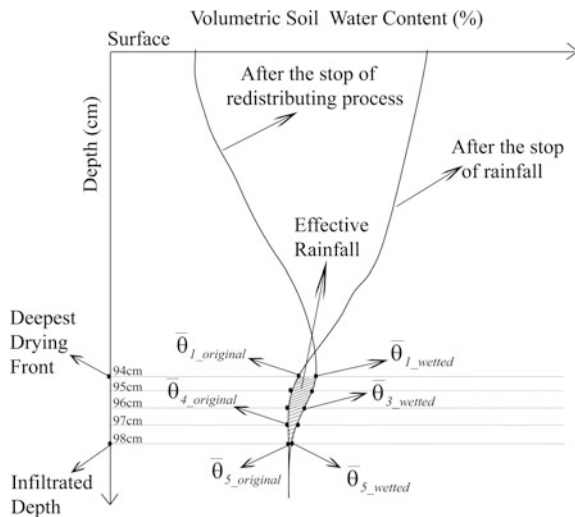
Considering the maximum annual precipitation of 120 mm, simply multiplying the estimated effective infiltration with a factor of 3.6 (120/33.02 mm), the value of 0.336 mm yr^{-1} was lower than the historic records based on hydrochemical and isotopic methods, which was from 0.95 to 3.6 mm yr^{-1}. In fact, the annual precipitation of 120 mm would not be simply characterized by about four single rainfalls, each of which was of 33.02 mm with the rainfall rate of 6.6 mm hr^{-1}. The actual annual effective infiltration was possibly lesser. The characteristics of individual rainfall events, such as the amount, the density, the duration, and the variation pattern of the drying front will affect the infiltrating and redistributing process in the soil and thus the effective infiltration. Furthermore, the annual spatial and temporal variation pattern of the precipitation plays a critical role in determining the effective infiltration. In order to understand the effective infiltration in the Badain Jaran Desert, a long-term observation should be established.

References

1. Bonacci O, Jukic D, Ljubenkov I (2006) Definition of catchment area in karst: case of the rivers Krcic and Krka, Croatia. Hydrol Sci J 51(4):682–699
2. Camillo PJ, Gurney RJ (1986) A resistance parameter for bare-soil evaporation models. Soil Sci 141(2):95–105
3. Chen JS, Li L, Wang JY, Barry DA, Sheng XF, Gu WZ, Zhao X, Chen L (2004) Water resources—groundwater maintains dune landscape. Nature 432(7016):459–460
4. Dong ZB, Wang T, Wang XM (2004) Geomorphology of the megadunes in the Badain Jaran desert. Geomorphology 60(1–2):191–203
5. Fares A, Polyakov V (2006). Advances in crop water management using capacitive water sensors. Adv Agron 90: 43–77
6. Fares A, Hamdhani H, Jenkins DM (2007) Temperature-dependent scaled frequency: Improved accuracy of multisensor capacitance probes. Soil Sci Soc Am J 71(3):894–900
7. Gates JB, Edmunds WM, Ma JZ (2006). Groundwater recharge rates to the Badain Jaran desert: preliminary results from environmental tracer studies. Groundwater-present status and future task. In: 34th IAH Congress proceeding. Beijing, China
8. Gates JB, Edmunds W, Ma J, Scanlon BR (2008) Estimating groundwater recharge in a cold desert environment in northern China using chloride. Hydrogeol J 16(5):893–910
9. Gates JB, Edmunds WM, Ma JZ (2008) Estimating groundwater recharge in a cold desert environment in northern China using chloride. Hydrogeol J 16:893–910
10. Geiger SL, Durnford DS (2000) Infiltration in homogeneous sands and a mechanistic model of unstable flow. Soil Sci Soc Am J 64(2):460–469
11. Geyh MA, Gu WZ, Jakel D (1996) Groundwater recharge study in the Gobi desert, China. Geowissenschaften 14(7–8):279–280
12. Ghildyal BP, Tripathi RP (1987) Soil physics. Rajkamal Electric Press, India
13. Golden Software (1990) Surfer reference manual, version 4 edn. Golden Software CO
14. Gu WZ, Seiler KP, Stichler W, Lu JJ (2006). Groundwater recharge in the badain jaran shamo, inner mongolia, P.R. China. Groundwater-present status and future task, In: 34th IAH Congress proceedings. Beijing, China
15. Hofmann J (1996) Lakes in the SE part of Badain Jaran Shamo, their limnology and geochemistry. Geowissenschaften 14(7–8):275–278

16. Hofmann J (1999). Geo-ecological investigations of the waters in the south-eastern Badain Jaran desert, in: Status und spatquartare Gewasserentwicklung, Berliner Geogr. Abh. 64, Habilitationsschrift, Berlin, 1–164

17. Hukseflux Thermal Sensors (2007) Soil temperature profile sensor user manual (version 0606). Hukseflux Thermal sensors, Delft

18. Jakel D (1996) The Badain Jaran desert: its origin and development. Geowissenschaften 14(7–8):272–274

19. Li S, Xiao H, Cheng G, Luo F, Liu L (2006) Mechanical disturbance of microbiotic crusts affects ecohydrological processes in a region of revegetation-fixed sand dunes. Arid Land Res Manag 20(1):61–77

20. Lu N, Likos WJ (2004) Unsaturated soil mechanics. Wiley, Hoboken

21. Ma JZ, Edmunds WM (2006) Groundwater and lake evolution in the Badain Jaran desert ecosystem, Inner Mongolia. Hydrogeol J 14(7):1231–1243

22. Ma JZ, Li D, Zhang JW, Edmunds WM, Prudhomme C (2003) Groundwater recharge and climatic change during the last 1000 years from unsaturated zone of SE Badain Jaran desert. Chin Sci Bull 48(14):1469–1474

23. Melone F, Corradini C, Morbidelli R, Saltalippi C (2006) Laboratory experimental check of a conceptual model for infiltration under complex rainfall patterns. Hydrol Process 20(3):439–452

24. Mitkov I, Tartakovsky DM, Winter CL (1998) Dynamics of wetting fronts in porous media. Phys Rev E 58(5):R5245–R5248

25. NJHRI (1999) Specification of soil test (SL 237-1999). China water power press, M. o. W. R. o. PRC

26. Noborio K, McInnes KJ, Heilman JL (1996) Measurements of cumulative infiltration and wetting front location by time domain reflectometry. Soil Sci 161(8):480–483

27. Polyakov V, Fares A, Ryder MH (2005) Calibration of a capacitance system for measuring water content of tropical soil. Vadose Zone J 4(4):1004–1010

28. Saito H, Simunek J, Mohanty BP (2006) Numerical analysis of coupled water, vapor, and heat transport in the vadose zone. Vadose Zone J 5(2):784–800

29. Scanlon BR, Keese K, Reedy RC, Simunek J, Andraski BJ (2003) Variations in flow and transport in thick desert vadose zones in response to paleoclimatic forcing (0–90 kyr): field measurements, modeling, and uncertainties. Water Resour Res 39(7):1179 (17 pp)

30. Sentek Pty Ltd (2001) Calibration of Sentek Pty Ltd soil moisture sensors. Sentek Sensor Technologies, Stepney

31. Shigeru O, Yosuke K, Ayumi Y (1992) Studies on the infiltration-discharge of rain water and translation penomena in soil. J Hydrol 132:1–23

32. Tami D, Rahardjo H, Leong EC (2004) Effects of hysteresis on steady-state infiltration in unsaturated slopes. J Geotechn Geoenviron Eng 130(9):956–967

33. Timlin D, Pachepsky Y (2002) Infiltration measurement using a vertical time-domain reflectometry probe and a reflection simulation model. Soil Sci 167(1):1–8

34. Topp GC, Davis JL, Annan AP (1982) Electromagnetic determination of soil water content using TDR: I. Applications to wetting fronts and steep gradients. Soil Sci Soc Am J 46:672–678

35. van Genuchten MT (1980) A closed-form equation for predicting the hydraulic conductivity of unsaturated soils. Soil Sci Soc Am J 44(5):892–898

36. Walker AS, Olsen and Bagen JW (1987) The Badain Jaran desert: remote sensing investigations. Geogr J 153(2):205–210

37. Walvoord MA, Plummer MA, Phillips FM, Wolfsberg AV (2002) Deep arid system hydrodynamics. 1. Equilibrium states and response times in thick desert vadose zones. Water Resour Res 38(12):1308

38. Wang GX, Cheng GD (1999) Water resource development and its influence on the environment in arid areas of China—the case of the Hei River basin. J Arid Environ 43(2):121–131

39. Wang XP, Li XR, Xiao HL, Berndtsson R, Pan YX (2007) Effects of surface characteristics on infiltration patterns in an arid shrub desert. Hydrol Process 21(1):72–79
40. Wang XP, Cui Y, Pan YX, Li XR, Yu Z, Young MH (2008) Effects of rainfall characteristics on infiltration and redistribution patterns in revegetation-stabilized desert ecosystems. J Hydrol 358(1–2):134–143
41. Wu JQ, Zhang RD, Yang JZ (1997) Estimating infiltration recharge using a response function model. J Hydrol 198(1–4):124–139
42. Yang XP (2001) Landscape evolution and palaeoclimate in the deserts of northwestern China, with a special reference to Badain Jaran and Taklamakan. Chin Sci Bull 46:6–11
43. Yang XP (2006) Chemistry and late quaternary evolution of ground and surface waters in the area of Yabulai mountains, western Inner Mongolia, China. Catena 66(1–2):135–144
44. Yang XP, Williams MAJ (2003) The ion chemistry of lakes and late Holocene desiccation in the Badain Jaran desert, Inner Mongolia, China. Catena 51(1):45–60
45. Yang XP, Liu TS, Xiao HL (2003) Evolution of megadunes and lakes in the Badain Jaran desert, Inner Mongolia, China during the last 31,000 years. Quatern Int 104:99–112
46. Yang H, Rahardjo H, Wibawa B, Leong EC (2004) A soil column apparatus for laboratory infiltration study. Geotech Test J 27(4):347–355
47. Yang H, Rahardjo H, Leong EC (2006) Behavior of unsaturated layered soil columns during infiltration. J Hydrol Eng 11(4):329–337
48. Zeng Y, Wan L, Su Z, Saito H, Huang K, Wang X (2009) Dirnal soil water dynamics in the shallow vadose zone. Environmental Geology 58:11–23
49. Zhang HC, Ming QZ (2006) Hydrology and lake Evolution in Hyperarid Northwestern China and the mystery of megadune formation in Badain Jaran Desert. Adv Earth Sci 21(5):532–538 (in Chinese)

Chapter 4
Two-Phase Mass and Heat Flow Model

4.1 Introduction

To improve the model representation of multiphase systems, there have been continuous efforts to build comprehensive multiphase models. At present, most modern two-phase flow and transport models have overcome most of the difficulties [40] mentioned in Sect. 1.1.1. Based on a series of works by Hassanizadeh and Gray [26–28], Niessner and Hassanizadeh [54, 56] recently presented a non-equilibrium two-phase heat and mass flow model including the interfacial area as a state variable. Furthermore, in order to build rigorous multiphase models, a thermodynamically constrained averaging theory approach was developed to model flow and transport phenomena in porous medium systems [22, 32, 41]. Although the weaknesses of classical, empirical approaches are discussed systematically in these papers, it is not easy to form an illustrative picture of the differences between a two-phase heat and mass flow model and the traditional unsaturated soil moisture and heat flow model. The latter model is still widely used in many unsaturated flow simulators [16, 17, 77], and subsequently adopted as sub-model in hydrological integration models [82, 83]. Furthermore, to estimate soil moisture dynamics using remote sensing data, most land surface models (LSMs) do not base soil moisture transport on two-phase flow approaches [58, 85]. There is a need to elucidate mechanically how the traditional coupled moisture and heat flow model can be improved by applying a two-phase flow approach.

Under the Richards approximation (e.g., no gas phase transport in the soil), using practical or phenomenological approaches, common empirical constitutive

relations (e.g., the laws of Darcy, Fick, Henry, Dalton and Kelvin) are directly incorporated in formulating the model for heat and mass transfer in a partially saturated porous medium, often called diffusion-based model with roots in Philip and de Vries [62]. The diffusion-based model has been adopted and extended by numerous authors [46, 47, 51, 70, 71]. Yet, unsatisfactory discrepancy is often found between theory prediction and field data. For example, Cahill and Parlange [5] demonstrated the significant underestimation of the magnitude as well as the incorrect direction predicted by the diffusion-based theory for vapor flux in their field experiments. Heitman et al. [30] revealed the noticeable differences between measured and calculated patterns of heat and moisture redistribution when the boundary temperature gradient was instantly reversed. As a result, both Cahill and Heitman suggested that to further develop the theory for better description of field conditions additional mechanisms need to be taken into consideration. Although no additional mechanism is pointed out specifically, the gas phase flow, which involves dry air and vapor flow, is an important mechanism that needs to be taken into account.

The gas phase flow in unsaturated soil has been studied for more than a century, since Buckingham [4] described the movement of air in soil in response to atmospheric pressure. However, not much attention was paid to this until the importance of gas flow in various engineering fields became apparent. Especially in environmental engineering, where gas flow is the major mechanism for assessing contaminant mass depletion due to volatilization and removing the volatile organic chemicals from the vadose zone by vapor extraction. From a theoretical point of view, the gas phase flow problem has been analyzed using numerical or analytical approaches. Although many numerical simulators were developed to simulate gas flow problems in complex conditions [39, 15, 64], the capacity of analytical solutions to verify numerical codes led to the development of analytical solutions for soil gas flow in the vadose zone in the past two decades. For example, Massmann [37] and McWhorter [38] presented analytical solutions to solve one-dimensional radial gas flow with simple initial and boundary conditions; Shan [75, 76] developed analytical solutions for transient gas flow caused by barometric pumping in both one and two dimensions. These studies provided a good knowledge base on the induced gas flow field in soil, needed to successfully design a cleanup system for contaminated vadose zones. At the same time, simultaneous flow of water and air through unsaturated porous media was intensively studied due to its vast applications in petroleum reservoir engineering, which also led to the development of either numerical or quasi-analytical solutions [48, 49, 60]. However, for the analysis of simultaneous flow of heat and mass through unsaturated porous media, a two phase flow model should also take the energy balance equation into account.

In nuclear or geothermal engineering, where an assessment of coupled liquid water, vapor, dry air and heat transport is required, the two-phase heat and mass flow model has been widely researched [1, 20, 73, 74, 78, 79]. Application of the two-phase heat and mass flow model is not limited to this. It is also important in the drying technology, where a precise thermo-hydro-mechanical model is highly

recommended [34] for obtaining dried products of good quality, as well as being important in the storage of liquefied natural gas [53], where a comprehensive understanding of the processes of freezing and thawing is necessary for safety assessment, and in the CO2 sequestration system in a fault environment [35], where assessment of fault instability due to the impact of CO2 injection is a typical two-phase heat and mass flow problem, and so on. Although all the above-mentioned studies analyzed the heat and mass transfer with a two-phase flow approach, which may fill the gap between theory and measurement pointed out by Cahill and Parlange [5] and Heitman et al. [30]. However, most of these studies did not put focus on this gap. Further consideration of the coupled liquid, vapor, dry air and heat transport mechanism is needed to investigate the gap.

From a mechanistic point of view, primary mechanisms of two phase heat and mass flow in unsaturated porous media include convection (movement with the bulk fluid) and hydrodynamic dispersion (mechanical dispersion and molecular diffusion) [2]. Mechanical dispersion, resulting from variations in fluid velocity at the micro pore scale, is the product of dispersion and convection. In most cases, the mechanical dispersion of gas phase is neglected due to its very small velocity compared to the dominant molecular diffusion [72]. This assumption is also applied in two-phase heat and mass flow models mentioned in the above paragraph. However, it has been argued that standard phenomenological approaches to modelling two-phase flow based on empirical constitutive relations (simplification of transport mechanisms) are not founded on an entirely sound physical basis [55]. Based on a series of work by Hassanizadeh and Gray [26–28], Niessner and Hassanizadeh [54, 56] presented a non-equilibrium two-phase heat and mass flow model including the interfacial area as state variable. The reliability of their physically-based model was made successful by capturing additional physical processes (hysteresis) compared to the standard model. However, the focus of their research is on microscopic scale problems, which is beyond the scope of this study. This chapter aims to build a two-phase mass and heat flow model based on the PdV model physics considering airflow mechanisms. The difference between the proposed model and the PdV model is discussed.

4.2 Model Description

In this section, two main groups of equations (balance equations and constitutive equations) have been used to describe the two-phase heat and mass flow model. Milly's equations, considering the predominantly vertical interactive process between atmosphere and soil, have been introduced first to describe the traditional coupled heat and mass flow model scheme. Then, the two-phase heat and flow model has been developed on this basis. Next, considering dry air as a single phase of the gaseous phase in soil, the balance equation of dry air was introduced. Henry's law has been used to express the equilibrium of dissolved air in liquid. In addition, the thermal equilibrium assumption between phases has been adopted

and the equation for energy balance established taking into account the internal energy in each phase (liquid, vapor, and dry air). After the constitutive equations have been presented, the numerical approach is briefly introduced.

4.2.1 Governing Equations

4.2.1.1 Liquid Transfer

Soil water is present in a liquid and a gaseous phase, and following Milly [43], the total moisture balance is expressed as

$$\frac{\partial}{\partial t}(\rho_L \theta_L + \rho_V \theta_V) = -\frac{\partial}{\partial z}(q_L + q_V) \tag{4.1}$$

where ρ_L (kg m^{-3}) represents the density of liquid water; ρ_V (kg m^{-3}) the density of water vapor; θ_L (m^3 m^{-3}) the volumetric water content; z (m) the vertical space coordinate, positive upwards; θ_V (m^3 m^{-3}) the volumetric vapor content; q_L (kg m^{-2} s^{-1}) the liquid flux; and q_V (kg m^{-2} s^{-1}) the vapor flux. The liquid flux is expressed by a generalized form of Darcy's law

$$q_L = -\rho_L K \frac{\partial \left(\frac{h_w}{\gamma_w} + z\right)}{\partial z} \tag{4.2}$$

where h_w (Pa) is the pore-water pressure; γ_w (kg m^{-2} s^{-2}) the specific weight of water; and K (m s^{-1}) the unsaturated hydraulic conductivity. According to Groenevelt and Kay [24], the effect of the heat of wetting on the pressure field and the resulting flow is taken into account by Milly [43], which leads to an additional liquid flow term in Eq. (4.2) resulting in

$$q_L = -\rho_L K \frac{\partial \left(\frac{h_w}{\gamma_w} + z\right)}{\partial z} - \rho_L D_{TD} \frac{\partial T}{\partial z} \tag{4.3}$$

where D_{TD} (m^2 s^{-1} °C^{-1}) is the transport coefficient for adsorbed liquid flow due to temperature gradient; and T (°C) the temperature. According to the definition of capillary potential, h could be expressed as the difference between the pore-air pressure and the pore-water pressure [19, 21, 80]

$$h = \frac{h_w - p_g}{\gamma_w} \tag{4.4}$$

where h (m) is the capillary pressure head; and P_g (Pa) the pore-air pressure. Substituting Eq. (4.4) into (4.3) yields

$$q_L = -\rho_L K \frac{\partial}{\partial z}\left(h + \frac{P_g}{\gamma_w} + z\right) - \rho_L D_{TD} \frac{\partial T}{\partial z} \tag{4.5}$$

Equation (4.5) can be rewritten [43] as

$$q_L = -\rho_L \underbrace{\left[K \frac{\partial}{\partial z} \left(h + \frac{P_g}{\gamma_w} \right) + \underbrace{D_{TD} \frac{\partial T}{\partial z}}_{q_{LT}} + K \right]}_{q_{Lh} + q_{La}}$$ (4.6)

in which q_{Lh} (kg m^{-2} s^{-1}) is the isothermal liquid flux; q_{LT} (kg m^{-2} s^{-1}) the thermal liquid flux; q_{La} (kg m^{-2} s^{-1}) $\left(= \rho_L \frac{K}{\gamma_w} \frac{\partial P_g}{\partial z} = K_{La} \frac{\partial P_g}{\partial z} \right)$ the advective liquid flux due to air pressure gradient; K_{La} (s) the advective liquid transport coefficient.

4.2.1.2 Vapor Transfer

The vapor flux is expressed by a generalized form of Fick's law

$$q_V = -D_e \frac{\partial \rho_V}{\partial z}$$ (4.7)

where D_e (m^2 s^{-1}) is the molecular diffusivity of water vapor in soil. When dry air is considered, the vapor flow is assumed to be induced in three ways: firstly diffusive transfer, driven by a vapor pressure gradient (Eq. 4.7); secondly advective transfer, as part of the bulk flows of air $\left(\rho_V \frac{q_{aa}}{\rho_{da}} \right)$; and thirdly dispersive transfer, due to longitudinal dispersivity $\left(-D_{Vg} \frac{\partial \rho_V}{\partial z} \right)$. Accordingly, Eq. (4.7) can be rewritten as

$$q_V = -\underbrace{\left[D_e \frac{\partial \rho_V}{\partial z} \right.}_{\text{Diffusion}} - \underbrace{\rho_V \frac{q_{aa}}{\rho_{da}}}_{\text{Advection}} + \underbrace{\left. \theta_V D_{Vg} \frac{\partial \rho_V}{\partial z} \right]}_{\text{Dispersion}}$$ (4.8)

where q_{aa} (kg m^{-2} s^{-1}) is the advective dry air flux $\left(q_{aa} = -\rho_{da} K_g \frac{\partial P_g}{\partial z} \right)$; ρ_{da} (kg m^{-3}) the dry air density; D_{Vg} (m^2 s^{-1}) the gas-phase longitudinal dispersion coefficient; and K_g the gas conductivity (m s^{-1}).

Considering vapor density to be a function of matric potential and temperature, the vapor flux can be divided into isothermal and thermal components. According to the chain rule for partial derivatives, the vapor flux in Eq. (4.8) could be rewritten using the three state variables as

$$q_V = q_{Vh} + q_{VT} + q_{Va}$$
$$= -\left[(D_e + \theta_V D_{Vg}) \frac{\partial \rho_V}{\partial h} \frac{\partial h}{\partial z} + (D_e + \theta_V D_{Vg}) \frac{\partial \rho_V}{\partial T} \frac{\partial T}{\partial z} + \rho_V K_g \frac{\partial P_g}{\partial z} \right]$$ (4.9)

where q_{Vh} (kg m^{-2} s^{-1}) is the isothermal vapor flux; q_{VT} (kg m^{-2} s^{-1}) the thermal vapor flux; and q_{Va} (kg m^{-2} s^{-1}) the advective vapor flux.

Combining the governing equations for liquid water (Eq. 4.6) and vapor flow (Eq. 4.9) leads to the governing differential equation for moisture transfer:

$$
\begin{aligned}
\frac{\partial}{\partial t}(\rho_L \theta_L + \rho_V \theta_V) &= -\frac{\partial}{\partial z}(q_L + q_V) \\
&= -\frac{\partial}{\partial z}(q_{Lh} + q_{LT} + q_{La}) - \frac{\partial}{\partial z}(q_{Vh} + q_{VT} + q_{Va}) \\
&= \rho_L \frac{\partial}{\partial z}\left[K\left(\frac{\partial h}{\partial z} + 1\right) + D_{TD}\frac{\partial T}{\partial z} + \frac{K}{\gamma_w}\frac{\partial P_g}{\partial z}\right] \\
&\quad + \frac{\partial}{-}\left[D_{vh}\frac{\partial h}{\partial z} + D_{vT}\frac{\partial T}{\partial z} + D_{va}\frac{\partial P_g}{\partial z}\right]
\end{aligned}
\tag{4.10}
$$

where

$$
D_{vh} = (D_e + \theta_V D_{Vg})\frac{\partial \rho_V}{\partial h}; \;\; D_{va} = \rho_V K_g; \;\; D_{vT} = (D_e + \theta_V D_{Vg})\frac{\partial \rho_V}{\partial T}
$$

D_{vh} (kg m^{-2} s^{-1}) is the isothermal vapor conductivity; D_{vT} (kg m^{-1} s^{-1} °C^{-1}) the thermal vapor diffusion coefficient; and D_{va} (s) the advective vapor transfer coefficient.

The terms within the square brackets in Eq. (4.6) represent the liquid flux. The term (P_g/γ_w) is the atmospheric pressure expressed as the height of a water column. The terms within the square brackets in Eq. (4.8) represent the water vapor flux, with the first term representing the diffusive flux (Fick's law), the second representing the advective flux (Darcy's law) and the third the dispersive flux (Fick's law).

Equation (4.3) shows clearly that only thermal (e.g. explicitly through the temperature dependence of K) and isothermal liquid advection and water vapor diffusion are considered in the traditional coupled heat and mass transport model (PdV model). However, Eq. (4.6) shows that dry air is considered to be a single phase. Thus not only diffusion, but also advection and dispersion become included in the water vapor transport mechanism. As for the liquid transport, the mechanism remains the same, but with atmospheric pressure acting as driving force gradient.

4.2.1.3 Dry Air Transfer

Dry air transport in unsaturated soil is driven by two main gradients, the dry air concentration or density gradient and the air pressure gradient. The first one diffuses dry air in soil pores, while the second one causes advective flux of dry air. At the same time, the dispersive transfer of dry air should also be considered. In addition, to maintain mechanical and chemical equilibrium, a certain amount of dry air will dissolve into liquid according to Henry's law. Considering the above four effects, the balance equation for dry air may be presented [80] as

$$\frac{\partial}{\partial t}[\epsilon \cdot \rho_{da}(S_a + H_c S_r)] = -\frac{\partial q_a}{\partial z} \tag{4.11}$$

and

$$q_a = \underbrace{-D_e \frac{\partial \rho_{da}}{\partial z}}_{Diffusion} \underbrace{-\rho_{da}K_g \frac{\partial P_g}{\partial z}}_{Convection} \underbrace{-\theta_a D_{Vg} \frac{\partial \rho_{da}}{\partial z}}_{Dispersion} + \underbrace{H_c \rho_{da} \frac{q_L}{\rho_L}}_{Dissolving} \tag{4.12}$$

where q_a (kg m^{-2} s^{-1}) is the dry air flux; and H_c (=0.02 for air at 1 atm and 25 °C) Henry's constant; S_a ($= 1 - S_r$) the degree of air saturation of soil; S_r ($= \theta_L/\epsilon$)) the degree of saturation of soil; ε the porosity. In the RHS of Eq. (4.12), the first term depicts diffusive flux (Fick's law), the second term advective flux (Darcy's law), the third dispersive flux (Fick's law), and the fourth advective flux due to dissolved air (Henry's law). Considering dry air density is a function of matric potential, temperature and air pressure, Eq. (4.12) could be rewritten with three state variables. Combining Eq. (4.12) with Eq. (4.11), the governing equation for dry air can be expressed as

$$\begin{aligned}
\frac{\partial}{\partial t}[\epsilon \cdot \rho_{da}(S_a + H_c S_r)] &= -\frac{\partial}{\partial}(q_{ah} + q_{aT} + q_{aa}) \\
&= \frac{\partial}{\partial}\left[K_{ah}\frac{\partial h}{\partial z} + K_{aT}\frac{\partial T}{\partial z} + K_{aa}\frac{\partial P_g}{\partial z}\right] \\
&\quad + V_{ah}\frac{\partial}{\partial z} + V_{aT}\frac{\partial T}{\partial z} + V_{aa}\frac{\partial P_g}{\partial z} + H_c \rho_{da}\frac{\partial K}{\partial z}
\end{aligned} \tag{4.13}$$

where q_{ah} (kg m^{-2} s^{-1}) is the isothermal air flux; q_{aT} (kg m^{-2} s^{-1}) the thermal air flux; q_{aa} (kg m^{-2} s^{-1}) the advective flux; and

$$K_{ah} = (D_e + \theta_a D_{Vg})\frac{\partial \rho_{da}}{\partial h} + H_c \rho_{da}K$$

$$K_{aT} = (D_e + \theta_a D_{Vg})\frac{\partial \rho_{da}}{\partial T} + H_c \rho_{da}D_{TD}$$

$$K_{aa} = (D_e + \theta_a D_{Vg})\frac{\partial \rho_{da}}{\partial P_g} + \rho_{da}\left(K_g + H_c \frac{K}{\gamma_w}\right)$$

$$V_{ah} = \left[K_g \frac{\partial P_g}{\partial z} - H_c \frac{q_L}{\rho_L}\right]X_{ah}$$

$$V_{aT} = \left[K_g \frac{\partial P_g}{\partial z} - H_c \frac{q_L}{\rho_L}\right]X_{aT}$$

$$V_{aa} = \left[K_g \frac{\partial P_g}{\partial z} - H_c \frac{q_L}{\rho_L}\right]X_{aa}$$

where X_{ah}, X_{aT} and X_{aa} are introduced in Sect. 4.2.2.3.

4.2.1.4 Energy Equation

In the vadose zone, the mechanisms for energy transport include conduction and convection. The conductive heat transfer contains contributions from liquids, solids and gas. Conduction is the main mechanism for heat transfer in soil and contributes to the energy conservation by solids, liquids and air. Advective heat in soil is conveyed by liquid flux, vapor flux, and dry air flux. On the other hand, heat storage in soil includes the bulk volumetric heat content, the latent heat of vaporization and a source term associated with the exothermic process of wetting of a porous medium (integral heat of wetting) [11]. Accordingly, following the general approach by de Vries [11], the energy balance equation in unsaturated soil may be written as four parts

Solid: $\frac{\partial \left[\rho_s \theta_s c_s \left(T - T_r\right)\right]}{\partial t} = \frac{\partial}{\partial z}\left(\lambda_s \theta_s \frac{\partial T}{\partial z}\right)$

Liquid: $\frac{\partial \left[\rho_L \theta_L c_L \left(T - T_r\right)\right]}{\partial t} = \frac{\partial}{\partial z}\left(\lambda_L \theta_L \frac{\partial T}{\partial z}\right) - \frac{\partial}{\partial z}\left[q_L c_L \cdot \left(T - T_r\right)\right]$

Air and vapor:

$$
\begin{aligned}
&\frac{\partial}{\partial t}\left[(\rho_{da} c_a + \rho_V c_V)\theta_g(T - T_r) + \rho_V L_0 \theta_g\right] \\
&= \frac{\partial}{\partial z}\left(\lambda_g \theta_g \frac{\partial T}{\partial z}\right) - \frac{\partial}{\partial z}\left\{q_V(c_V \cdot (T - T_r) + L_0) + q_a c_a \cdot (T - T_r)\right\}
\end{aligned}
\tag{4.14}
$$

Heat of wetting: $H_w = -\rho_L W \frac{\partial \theta_L}{\partial t}$

where λ_s, λ_L and λ_g (w m^{-1} °C^{-1}) represent the thermal conductivities of solids, liquids and pore gas ($= \lambda_a + \lambda_V$) respectively; θ_s the volumetric content of solids in the soil; θ_g the volumetric content of gas ($= \theta_V = \theta_a$) in the soil; c_s, c_L, c_a and c_v (J kg^{-1} °C^{-1}) specific heat of solids, liquids, air and vapor, respectively; T_r (°C) the reference temperature; ρ_s (kg m^{-3}) the density of solids in the soil; L_0 (J kg^{-1}) the latent heat of vaporization of water at temperature T_r; and W (J kg^{-1}) the differential heat of wetting (the amount of heat released when a small amount of free water is added to the soil matrix). The latent heat of vaporization varies with T according to $L(T) = L_0 - (c_L - c_v)(T - T_r) \approx 2.501 \times 10^6 - 2369.2\,T$ [70]. In accordance with Eq. (4.14), the conservation equation for energy transfer in the soil is given as

$$
\begin{aligned}
&\frac{\partial}{\partial t}\left[(\rho_s \theta_s c_s + \rho_L \theta_L c_L + \rho_{da} \theta_a c_a + \rho_V \theta_V c_V)(T - T_r) + \rho_V L_0 \theta_g\right] \\
&\quad - \rho_L W \frac{\partial \theta_L}{\partial t} = \frac{\partial}{\partial z}\left(\lambda_{eff} \frac{\partial T}{\partial z}\right) - \frac{\partial}{\partial z}[q_L c_L \cdot (T - T_r) \\
&\quad\quad + q_V(L_0 + c_V \cdot (T - T_r)) + q_a c_a \cdot (T - T_r)]
\end{aligned}
\tag{4.15}
$$

where λ_{eff} (W m^{-1} K^{-1}) is the effective thermal conductivity, combining the thermal conductivity of solid particles, liquid and dry air in the absence of flow. The parameters in the first term in the LHS of Eq. (4.15) and λ_{eff} can be

determined by de Vries' [11] scheme. Equations (4.10), (4.13) and (4.15) are solved jointly with the specified boundary and initial condition of the solution domain to obtain spatial and temporal variations of the three prime variables h, T and P_g. If the advective flux conveyed by the dry air flux ($q_a c_a \cdot (T - T_r)$) and the bulk volumetric heat content of dry air ($\rho_{da} \theta_a c_a$) were to be neglected, Eq. (4.15) would result in the heat balance equation of Milly [43].

4.2.2 Constitutive Equations

The constitutive equations link the independent variables (unknowns) and the dependent variables. Each governing equation is solved for a single unknown, for example, Eq. (4.10) for matric potential, Eq. (4.13) for atmospheric pressure and Eq. (4.15) for temperature. The closure of the model developed above requires all dependent variables to be computable from the set of unknowns. The governing equations are finally written in terms of the unknowns when the constitutive equations given below are substituted.

4.2.2.1 Unsaturated Hydraulic Conductivity

The pore-size distribution model of Mualem [50] was used to predict the unsaturated hydraulic conductivity from the saturated hydraulic conductivity [84]:

$$K = K_s K_r = K_s S_e^l [1 - (1 - S_e^{1/m})^m]^2 \tag{4.16}$$

where K_S (m s^{-1}) is the saturated hydraulic conductivity; K_r, the relative hydraulic conductivity; S_e the effective saturation ($S_e = (\theta - \theta_{res})/(\theta_{sat} - \theta_{res})$); θ_{res}, the residual water contents; and l and m empirical parameters ($l = 0.5$). The parameter m is a measure of the pore-size distribution and can be expressed as $m = 1 - 1/n$, which in turn can be determined by fitting van Genuchten's analytical model [84]

$$\theta(h) = \begin{cases} \theta_{res} + \frac{\theta_{sat} - \theta_{res}}{[1 + |\alpha h|^n]^m}, & h < 0 \\ \theta_{sat}, & h \geq 0 \end{cases} \tag{4.17}$$

where α (m^{-1}) is the parameter characteristic of the particular soil material. According to Eq. (4.16), the unsaturated hydraulic conductivity is a function of θ_{res}, which is subsequently a function of h [e.g. from Eq. (4.17)]. The h is actually temperature dependence, $h_{TemCorr} = h \cdot e^{-C_\psi(T - T_r)}$, where $C_\psi \equiv \frac{1}{h}\frac{\partial h}{\partial T}$ and C_ψ is assumed to be constant (=0.0068 °C^{-1}) [44, 45]. Such temperature dependence is implied by the temperature dependence of surface tension and viscous flow [42]. Therefore, the temperature apparently has an effect on the unsaturated hydraulic conductivity, due to the temperature dependence of h, which is given by Milly [43] as

$$K(\theta, T) = K_s K_r(\theta) K_T(T) \tag{4.18}$$

and K_T is given as

$$K_T = \frac{\mu_w(T_r)}{\mu_w(T)} \tag{4.19}$$

where μ_w is the dynamic viscosity of water and is given [18] as

$$\mu_w = \mu_{w0} \exp\left[\mu_1 / (R \cdot (T + 133.3))\right] \tag{4.20}$$

where $\mu_{w0} = 2.4152 \times 10^{-5}(\text{Pa s})$, $\mu_1 = 4.7428(\text{kJ mol}^{-1})$, $R = 8.314472$ (J mol^{-1} °C^{-1}), and T is in °C.

4.2.2.2 Gas Conductivity

In unsaturated soil, the pore space generally is occupied by gas and liquid. Under the ideal assumption that there is no interaction between the fluids (which is actually not the case in the reality), Darcy's law is applied to determine the gas conductivity. When the pore space is filled gradually by a single fluid, the permeability with respect to the other fluid will decrease accordingly, because of the cross-sectional area available for the flow of that fluid (other than the fluid occupying the pore space) is less. According to Darcy's law, the gas conductivity can be expressed as

$$K_g = \frac{K_{rg}(S_a) K_s \mu_w}{\rho_L g \mu_g} \tag{4.21}$$

where μ_g (=1.846 $\times$ 10^{-5} kg m^{-1} s^{-1}) the air viscosity; $K_{rg}(S_a)$ the relative gas conductivity, which is a function of effective gas saturation and is defined by Van Genuchten–Mualem model as

$$K_{rg}(S_a) = \left(1 - S_a^{0.5}\right)\left\{1 - \left[1 - (1 - S_a)^{1/m}\right]^m\right\}^2 \tag{4.22}$$

4.2.2.3 Gas-Phase Density

Gas phase density includes water vapor density and dry air density. The water vapor density, ρ_V, has been given [62, 70] as $\rho_V = \rho_{SV} H_r$; $H_r = \exp(hg/R_V T)$;

$$\rho_{SV} = \frac{10^{-3}}{T} \exp\left(31.3716 - \frac{6014.79}{T} - 7.92495 \times 10^{-3} T\right) \tag{4.23}$$

where ρ_{SV} is the density of saturated water vapor; H_r, the relative humidity; R_V, the specific gas constant for vapor (461.5 J kg^{-1} K^{-1}); g (m s^{-2}), the gravitational

acceleration; and T in K. The gradient of the water vapor density with respect to z can be expressed as

$$\frac{\partial \rho_V}{\partial z} = \rho_{SV} \frac{\partial H_r}{\partial T}|_h \frac{\partial T}{\partial z} + \rho_{SV} \frac{\partial H_r}{\partial h}|_T \frac{\partial h}{\partial z} + H_r \frac{\partial \rho_{SV}}{\partial T} \frac{\partial T}{\partial z} \qquad (4.24)$$

Assuming that pore-air and pore-vapor could be considered to be ideal gas, air and vapor density can be expressed as

$$\rho_{da} = \frac{P_{da}}{R_{da}T}, \text{ and } \rho_V = \frac{P_V}{R_V T} \qquad (4.25)$$

where R_{da} is the specific gas constant for dry air (=287.1 J kg^{-1} K^{-1}); P_{da} (Pa) and P_V (Pa) are the dry air pressure and vapor pressure; and T is in K. According to Dalton's law of partial pressure, the mixed soil air pressure (P_g) should be equal to the sum of the dry air pressure and the vapor pressure

$$P_g = P_{da} + P_v \qquad (4.26)$$

The dry air density could be rewritten as

$$\rho_{da} = \frac{P_g}{R_{da}T} - \frac{\rho_V R_V}{R_{da}} \qquad (4.27)$$

Differentiating Eq. (4.27) with respect to time (t) and space (z) yields

$$\frac{\partial \rho_{da}}{\partial t} = X_{aa} \frac{\partial P_g}{\partial t} + X_{aT} \frac{\partial T}{\partial t} + X_{ah} \frac{\partial h}{\partial t}$$

$$\frac{\partial \rho_{da}}{\partial z} = X_{aa} \frac{\partial P_g}{\partial z} + X_{aT} \frac{\partial T}{\partial z} + X_{ah} \frac{\partial h}{\partial z} \qquad (4.28)$$

where

$$X_{aa} = \frac{1}{R_{da}T}; \ X_{aT} = -\left[\frac{P_g}{R_{da}T^2} + \frac{R_V}{R_{da}}\left(H_r \frac{\partial \rho_{SV}}{\partial T} - \frac{\rho_{SV}hgH_r}{R_V T^2}\right)\right]; \ X_{ah} = -\frac{\rho_{SV}gH_r}{R_{da}T}$$

4.2.2.4 Vapor Diffusivity

The vapor diffusion described by Fick's law in the atmosphere has been modified so as to apply in porous media by Rollins [68] as

$$q_v = -D_{atm}\upsilon\tau\theta_a\nabla\rho_v \qquad (4.29)$$

where D_{atm} is the molecular diffusivity of water vapor in air (m^2 s^{-1}); τ a tortuosity factor allowing for the extra path length; and υ the 'mass flow factor' introduced to allow for the mass flow of vapor arising from the difference in boundary conditions governing the air and the vapor components of the diffusion

system. Be aware of that, with the vapor diffusivity here, the vapor diffusion can be referred to as an isothermal equation. Actually, the temperature effects are implicitly included in the sense that an accurate measurement of water vapor density would include the effect of a temperature gradient or any other soil property such as air, water content or solid particles [6].

With the thermodynamic relationship between the vapor density and the relative humidity in soil, which is a function of temperature and capillary pressure [14], Eq. (4.29) can be rewritten in a form that contains temperature gradient explicitly by transforming the vapor density gradient to an equivalent temperature gradient [6]. The vapor diffusion with respect to temperature can be expressed as

$$\frac{\partial q_V}{\partial T} = -D_{atm}\upsilon\tau\theta_a\frac{\partial \rho_V}{\partial T} = -D_{V\_Sim\_T}\nabla T, \; D_{V\_Sim\_T} = D_{atm}\upsilon\tau\theta_a H_r\beta \quad (4.30)$$

where β is for $\frac{\partial \rho_{SV}}{\partial T}$. Equation (4.30) is straightforward and logical adaptation of Eq. (4.29).

Equation (4.30) has been described as the 'simple theory' of thermal vapor transfer by Philip and De Vries [62] and has been proven not enough to explain the vapor transfer in soil. They proposed a semi-empirical theory to encounter the failure of 'simple theory'.

In a single air-filled pore, the product between tortuosity and the volumetric content of air can be considered as a unity, presuming similarity of temperature and vapor fields in the pore. Therefore, the vapor diffusion due to the air temperature gradient (∇T_a) in the pore should be considered and expressed as

$$\frac{\partial q_V}{\partial T} = -D_{atm}\upsilon H_r\beta\nabla T_a \quad (4.31)$$

In addition, Philip and De Vries [62] assumed that the vapor can transfer through 'liquid island' (i.e., the liquid capillary connecting soil particles) by condensing on the cold side of the 'liquid island' and evaporating on the warm side. With such assumption, the cross section available for vapor transfer is equal to that occupied by air and liquid (e.g. $= \theta_a + \theta_L$). Assuming that the mean flux density in the connecting liquid island is equal to that in the air-filled pores, we can get

$$\frac{\partial q_V}{\partial T} = -(\theta_a + \theta_L)D_{atm}\upsilon H_r\beta\nabla T_a = -D_{V\_Liquid\_Island}\nabla T_a \quad (4.32)$$

The ratio between the diffusivity proposed by Philip and De Vries $(D_{V\_Liquid\_Island})$ and the diffusivity for 'simple theory' $(D_{V\_Sim\_T})$ can be used to enhance the vapor diffusion predicted by 'simple theory'. This ratio is called as the enhancement factor for thermal vapor diffusion in soil and is given as

$$\eta = \frac{\theta_a + \theta_L}{\tau\theta_a}\frac{\nabla T_a}{\nabla T} \quad (4.33)$$

According to the equations and concepts described above, the thermal vapor diffusion can be rewritten as

$$\frac{\partial_{qv}}{\partial T} = -D_{atm}\tau\theta_a\eta\frac{\partial_{\rho v}}{\partial T}\nabla T \tag{4.34}$$

Note that, Eq. (4.34) doesn't include the 'mass flow factor' (v), which has been neglected considering its insignificant effects. With the inclusion of enhancement factor, η, the cross sectional area will vary with soil saturation degree. As soil is completely dry, there is no liquid water in the soil and the thermal vapor diffusion should follow 'simple theory' as Eq. (4.30) states. When soil is getting wetter, the liquid island starts to appear and the cross sectional area for vapor diffusion increases at the same time with the consideration of enhancement factor. With the consideration of varied cross sectional area for vapor diffusion, Eq. (4.34) is rewritten by [Philip and De Vries [62]] as

$$\frac{\partial_{qv}}{\partial T} = -D_{atm}\overbrace{(\theta_a + f(\theta_a)\theta_L)}^{\substack{\text{Cross section for}\\ \text{vapor diffusion}}}\frac{\nabla T_a}{\nabla T}\frac{\partial_{\rho v}}{\partial T}\nabla T \tag{4.35}$$

where $f(\theta_a)$ is a factor introduced to account for decreasing cross-section due to increasing moisture content and increasing degree of liquid continuity, after soil moisture content exceeds a certain key value. The $f(\theta_a)$ is given as

$$f(\theta_a) = \begin{cases} 1, & \theta_L \le \theta_k \\ \frac{\theta_a}{\epsilon - \theta_k}, & \theta_L > \theta_k \end{cases} \tag{4.36}$$

The θ_k is the moisture content at which liquid flow becomes negligible. If one substitutes $\theta_L = \epsilon - \theta_a$ into Eq. (4.35), the cross section for vapor diffusion will be equal to $\left[\theta_a + \frac{\theta_a}{\epsilon - \theta_k}(\epsilon - \theta_a)\right]$, when $\theta_L > \theta_k$. On the other hand, when the moisture content decreases till $\theta_k(\theta_L = \theta_k)$, the cross sectional area equals to $(\theta_a + \theta_L) = (\theta_a + \theta_k)$. At this every moment when θ_k merely equal to θ_L but less than θ_L, we can approximate that $\left[\theta_a + \frac{\theta_a}{\epsilon - \theta_k}(\epsilon - \theta_a)\right] \approx (\theta_a + \theta_k) \approx \epsilon$. It is easy to know that $\theta_a(\epsilon - \theta_a) \approx \theta_k(\epsilon - \theta_k)$, which means $\theta_a \approx \theta_k$. This indicates that the cross sectional area reach maximum when $\theta_a = \theta_L = \theta_k = 0.5\epsilon$. It means that at moderate moisture content, continuity of both liquid and vapor phases reaches maximum, together with islands of both phases.

In the enhancement factor, $\frac{\nabla T_a}{\nabla T}$ is regarded as the local temperature gradient effect due to a higher average pore-air temperature gradient compared to the average temperature gradient of the bulk medium, and is given by Philip and De Vries [62] as

$$\frac{\nabla T_a}{\nabla T} = \nabla T_a\left[\sum_{i=1}^{5}\nabla T_i\theta_i\right]^{-1} \tag{4.37}$$

where ∇T_i is the thermal gradient in the ith constituent, and θ_i the volumetric fraction of the ith constituent. Based on De Vries' approach [12], the ratio of the average temperature gradient in the constituent to the average temperature gradient of the bulk medium can be expressed by a conceptual model

$$k_i = \frac{2}{3}\left[1 + \left(\frac{\lambda_i}{\lambda_1} - 1\right)g_i\right]^{-1} + \frac{1}{3}\left[1 + \left(\frac{\lambda_i}{\lambda_1} - 1\right)(1 - 2g_i)\right]^{-1} \tag{4.38}$$

where k_i is the ratio; λ_i the thermal conductivity of the ith constituent (J cm^{-1} s^{-1} °C^{-1}); and g_i the 'shape factor' of the ith constituent (see Table 4.1). For the solid particles, constant values for g_i as given in Table 4.1 are assumed. For liquid water, no value is needed since its coefficient is zero. The value of g_2 is considered as a function of moisture content as follows [33]

$$g_2 = \begin{cases} 0.013 + \left(\frac{0.022}{\theta_{wilting}(pF=4.2)} + \frac{0.298}{\epsilon}\right)\theta_L, & \theta_L < \theta_{wilting} \\ 0.035 + \frac{0.298}{\epsilon}\theta_L, & \theta_L > \theta_{wilting} \end{cases} \tag{4.39}$$

By applying the definition of the k_i [12], Eq. (4.37) can be transformed as

$$\frac{\nabla T_a}{\nabla T} = k_2\left[\sum_{i=1}^{5} k_i\theta_i\right] \tag{4.40}$$

The value of $\frac{\nabla T_a}{\nabla T}$ is valid for θ_L down to θ_k. For $\theta_L = 0$, $\frac{\nabla T_a}{\nabla T}$ may be calculated using air as the continuous phase, and may be interpolated for θ_L between 0 and θ_k [44, 45].

4.2.2.5 Gas Dispersivity

The gas phase longitudinal dispersivity, D_{Vg}, was estimated [2] as

$$D_{Vg} = \alpha_{Li} \cdot q_{i(i=gas,\,liquid)} \tag{4.41}$$

where q_i is the pore fluid flux in phase i; and α_{Li} (m), the longitudinal dispersivity in phase i, which has been evaluated by various authors for different levels of soil saturation. Laboratory studies have shown that α_{Li} increases when the soil volumetric water content decreases. In this study, as done by Grifoll et al. [23], a

Table 4.1 Properties of Soil Constituents [12]

Constituent	i	C_i (J cm^{-3} °C^{-1})	λ_i (J cm^{-1} s^{-1} °C^{-1})	g_i
Liquid water	1	1.0	5.73×10^{-3}	$\cdots$
Air	2	1.25×10^{-3}	2.5×10^{-4} $+LD_a\left(\partial_{\rho v}/\partial T\right)\vert_h$	$\cdots$
Quartz	3	2.66	8.8×10^{-2}	0.125
Other materials	4	2.66	2.9×10^{-2}	0.125
Organic matter	5	1.3	2.5×10^{-3}	0.5

correlation made from simulation results [69] and experimental data obtained by Haga et al. [25] was used:

$$\alpha_{Li} = \alpha_{Li\_sat} \cdot \left[13.6 - 16 \cdot \left(\theta_g / \varepsilon\right) + 3.4 \cdot \left(\theta_g / \varepsilon\right)^5\right] \qquad (4.42)$$

As Grifoll et al. [23] pointed out, the lack of dispersivity values led to, the saturation dispersivity, α_{Li_sat}, used in the above correlation to be set at 0.078 m, the figure reported in the field experiments by Biggar and Nielsen [3] and shown to be a reasonable value in previous modeling studies [8].

4.2.2.6   Thermal Property

Heat Capacity
The volumetric heat capacity of a soil is a weighted average of the capacities of its constituents [12]

$$C = \sum_{i=1}^{5} C_i \theta_i \qquad (4.43)$$

where θ_i and C_i are the volumetric fraction and the volumetric heat capacity of the ith soil constituent (J cm^{-3} °C^{-1}). The five components are water, air, quartz particles, other minerals and organic matter (see Table 4.1).

Thermal Properties
The effective thermal conductivity of a moist soil is given by

$$\lambda_{eff} = \left(\sum_{i=1}^{5} k_i \theta_i \lambda_i\right)\left(\sum_{i=1}^{5} k_i \theta_i\right)^{-1} \qquad (4.44)$$

The unit of which is (J cm^{-1} s^{-1} °C^{-1}) (see Table 4.1).

Differential Heat of Wetting
The differential heat of wetting, W (J/Kg), is the amount of heat released when a small amount of free water is added to the soil matrix and is originally expressed by Edlefsen and Anderson [14]

$$W = -\rho_L\left(\psi - T\frac{\partial \psi}{\partial T}\right) = -0.01g\left(h + TC_\psi h\right) = -0.01gh\left(1 + TC_\psi\right)$$

where ψ (J kg^{-1}) = 0.01 gh (cm) at T = 293 K with the value of C_ψ = 0.0068 (K^{-1}) [47]. Thus, Prunty expressed the differential heat of wetting as [66]

$$W = -0.2932h \qquad (4.45)$$

unit of W is J kg^{-1} when h is in cm.

Transport Coefficient for Adsorbed Liquid Flow

The transport coefficient for adsorbed liquid flow due to temperature gradient could be expressed [24] as:

$$D_{TD} = \frac{H_w \varepsilon}{b\tau\mu_w(T + 273.15)}(1.5548 \cdot 10^{-15}) \qquad (4.46)$$

where H_w is the integral heat of wetting (J m^{-2}); b = 4×10^{-8} (m); T is in °C.

4.2.3 Numerical Approach

The governing differential equations are converted to non-linear ordinary differential equations whose unknowns are the values of the prime variables at a finite number of nodes by using Galerkin's method of weighted residuals. Then, a finite-difference time-stepping scheme is applied to evaluate the time derivatives, which is solved by a successive linearization iterative scheme. To describe the spatial discretization and time stepping of the governing equations, an example of the derivation is presented below, using the moisture equation. For the dry air equation and the energy equation, the procedure is similar.

The standard piecewise linear basis functions for approximation of the prime variables are expressed as

$$\hat{h}(z,t) = h_1\phi_1 + h_2\phi_2 = \sum_{j=1}^{2} h_j(t)\phi_j(z)$$

$$\hat{T}(z,t) = T_1\phi_1 + T_2\phi_2 = \sum_{j=1}^{2} T_j(t)\phi_j(z) \qquad (4.47)$$

$$\hat{P}_g(z,t) = P_{g1}\phi_1 + P_{g2}\phi_2 = \sum_{j=1}^{2} P_{gj}(t)\phi_j(z)$$

where j is the node index; and, $\phi_j(z)$ the usual shape function defined element by element. If the approximations given by Eq. (4.47) are substituted into the Eqs. (4.10), (4.13) and (4.15), residuals are obtained for each governing differential equation, which are then minimized using Galerkin's method. Introducing the new notation for the coefficients in the moisture mass conservation equation, Eq. (4.10) becomes,

$$
\begin{aligned}
M_{moisture}&(h,T) \\
&= c_1\frac{\partial h}{\partial t} + c_2\frac{\partial T}{\partial t} - \frac{\partial}{\partial z}\left(c_3\frac{\partial h}{\partial z} + c_4\frac{\partial T}{\partial z} + c_5\frac{\partial P_g}{\partial z} + c_6\right) - c_7\frac{\partial h}{\partial z} - c_8\frac{\partial T}{\partial z}
\end{aligned} \qquad (4.48)
$$

where c_1 to c_8 are defined implicitly by Eqs. (4.10) and (4.48). Following Galerkin's method of weighted residuals [63] for each element, the residuals obtained by substituting $\hat{h}$, $\hat{T}$, and $\hat{P}_g$ into Eq. (4.48) are required to be orthogonal to the set of trial functions.

$$\int_Z \left[c_1 \frac{\partial \hat{h}}{\partial t} + c_2 \frac{\partial \hat{T}}{\partial t} - \frac{\partial}{\partial z} \left(c_3 \frac{\partial \hat{h}}{\partial z} + c_4 \frac{\partial \hat{T}}{\partial z} + c_5 \frac{\partial \hat{P}_g}{\partial z} + c_6 \right) - c_7 \frac{\partial \hat{h}}{\partial z} - c_8 \frac{\partial \hat{T}}{\partial z} \right] \phi_i dz = 0, \quad i = 1, 2$$

(4.49)

where Z is the solution domain. We apply integration by part to the third, fourth and fifth term, which may be recognized as the flux divergence.

$$\int_Z \left(c_1 \frac{\partial \hat{h}}{\partial t} + c_2 \frac{\partial \hat{T}}{\partial t} \right) \phi_i dz + \int_Z \left(c_3 \frac{\partial \hat{h}}{\partial z} + c_4 \frac{\partial \hat{T}}{\partial z} + c_5 \frac{\partial \hat{P}_g}{\partial z} + c_6 \right) \phi'_i dz$$

$$+ \int_Z c_7 \hat{h} \phi'_i dz + \int_Z c_8 \hat{T} \phi'_i dz = \left[\left(\left(c_3 \frac{\partial \hat{h}}{\partial z} + c_4 \frac{\partial \hat{T}}{\partial z} + c_5 \frac{\partial \hat{P}_g}{\partial z} + c_6 \right) + c_7 \hat{h} + c_8 \hat{T} \right) \phi_i \right]_{z_1}^{z_2}$$

$$= [-Q_m \phi_i]_{z_1}^{z_2}, \, i = 1, 2$$

(4.50)

where z_1 and z_2 are two points in one element and subscripted according to a local numbering system. According to the definition of c_3, c_4, c_5, c_6, c_7 and c_8, Q_m is implicitly seen as the sum of liquid and vapor mass flux. Now, substituting from Eq. (4.47) into Eq. (4.50) yields

$$\sum_{j=1}^2 h'_j \int c_1 \phi_j \phi_i dz + \sum_{j=1}^2 T'_j \int c_2 \phi_j \phi_i dz + \sum_{j=1}^2 h_j \int c_3 \phi'_j \phi'_i dz + \sum_{j=1}^2 T_j \int c_4 \phi'_j \phi'_i dz$$

$$+ \sum_{j=1}^2 P_{gj} \int c_5 \phi'_j \phi'_i dz + \int c_6 \phi'_i dz + \sum_{j=1}^2 h_j \int c_7 \phi_j \phi'_i dz + \sum_{j=1}^2 T_j \int c_8 \phi_j \phi'_i dz$$

$$= [-Q_m \phi_i]_{z_1}^{z_2}, \, i = 1, 2$$

(4.51)

Considering the dependence of c_1 to c_8 on state variables, the linear assumption of the parameters inside an element is recognisable in the linear form of Eq. (4.47). In matrix form, Eq. (4.51) becomes

$$A \cdot \dot{h} + B \cdot \dot{T} + C \cdot h + D \cdot T + E \cdot P_g + F = Q_m|_\Gamma$$

(4.52)

where A, B, C, D, E, and F are defined implicitly by Eqs. (4.51) and (4.52); the subscript Γ denotes the boundary of the solution domain, by which the specific boundary conditions enter the equations associated with the two end nodes; while, $\dot{h}$ and $\dot{T}$ denote the time derivative of matric potential and the temperature, respectively. A fully implicit backward difference scheme is used to accomplish

the temporal solution of the governing differential equations, which means that all terms other than the time derivative are evaluated at the end of the time step. This scheme yields

$$
\left(\frac{1}{\Delta t}A^k + C^k\right) \cdot h^k + \left(\frac{1}{\Delta t}B^k + D^k\right) \cdot T^k
$$
$$
= \frac{1}{\Delta t}A^k \cdot h^{k-1} + \frac{1}{\Delta t}B^k \cdot T^{k-1} - E \cdot P_g^k - F + Q_m|_\Gamma \tag{4.53}
$$

where k is a time index and Δt is the length of the time step. The coefficient matrices in Eq. (4.53) are to be evaluated at the new time level with an iterative scheme, which updates the coefficient matrices at each iteration until desired convergence criteria are achieved. The prescribed upper limits are used to determine a new time step size automatically [46] in the form of

$$
\Delta t = \min\left[\frac{X_{\max}}{\max_i\left(\frac{d\theta_i}{dt}\right)}, \frac{T_{\max}}{\max_i\left(\frac{dT_i}{dt}\right)}, \frac{P_{g_{\max}}}{\max_i\left(\frac{dP_{g_i}}{dt}\right)}, \frac{h_{\max}}{\max_i\left(\frac{dh_i}{dt}\right)}\right] \tag{4.54}
$$

where max_i denotes maximization over all nodes i, and the changes of state variables are estimated from the most recent time step; $X_{\max}$ is the upper limit of change for volumetric water content; T_{Max} the upper change limit for temperature; $P_{g\max}$ for atmospheric pressure; and $h_{\max}$ for matric potential. If the change exceeds the desired upper limits, the calculation of that time step is erroneous, and the time step will be repeated with a decreased time length. This helps achieve a reasonable trade-off between the computational effort and the accuracy of the solution.

4.3 Numerical Model Discussion

As mentioned in the introduction, the mass and heat of the liquid and vapor transport part of the proposed model are based on Milly's work, while the air phase part is based on Thomas' work. This section discusses the connection between the proposed model and the model it is based on.

4.3.1 Air Phase Transport Part

The air transport in the soil is only valid under the continuum assumption, which is generally true when the degree of saturation is reduced to around 85 % or lower [10]. In Thomas' equation system, the air transport in unsaturated soil is considered to exist in two forms, bulk air and dissolved air [19]. The bulk air transport is driven by a gradient of air pressure, while the dissolved air transport is linked to the liquid flow. The air conservation equation is given as

$$\frac{\partial}{\partial t}\left[\varepsilon \cdot \rho_{da}(S_a + H_c S_r)\right] = \frac{\partial}{\partial z}\left[\rho_{da}K_g \frac{\partial P_g}{\partial z} - H_c \rho_{da} \frac{q_L}{\rho_L}\right] \tag{4.55}$$

The first term on the RHS represents the convective airflow due to the soil air pressure gradient. The second term denotes a different mechanism of convective movement of gases, the transfer of dissolved gases, which is the prevailing transfer mechanism when water is infiltrating into and percolating through soils, and is triggered by rain or irrigation. Apart from convection, the proposed model (Eq. 4.13) also takes diffusion and dispersion into account. In the case of convection, under a gradient of total gas pressure, the entire mass of air is transferred from a higher pressure zone to a lower one. While in the case of diffusion, the driving force is a gradient of partial pressure (concentration) of any constituent gas (vapor and dry air), which causes the molecules of air to distribute evenly from a higher concentration zone to a lower one while the gas as a whole may remain isobaric and stationary [31]. To certain extent, dispersion is similar to diffusion. However, dispersion only occurs when macroscopic motion (flow) exists and is always associated with flow. Accordingly, dispersion could be roughly defined as convection induced diffusion [36]. The dry air conservation equation of the proposed model is given as Eq. (4.13), which could be expanded as followed:

$$C_{aa}\frac{\partial P_g}{\partial t} + C_{aT}\frac{\partial T}{\partial t} + C_{ah}\frac{\partial h}{\partial t} = \frac{\partial}{\partial z}\left(K_{aa}\frac{\partial P_g}{\partial z} + K_{aT}\frac{\partial T}{\partial z} + K_{ah}\frac{\partial h}{\partial z}\right)$$
$$+ V_{aa}\frac{\partial P_g}{\partial z} + V_{aT}\frac{\partial T}{\partial z} + V_{ah}\frac{\partial h}{\partial z} + H_c \rho_{da}\frac{\partial K}{\partial z} \tag{4.56}$$

where

$$C_{aa} = X_{aa}[\varepsilon + (H_c - 1)\theta_L]$$
$$C_{aT} = X_{aT}[\varepsilon + (H_c - 1)\theta_L] + (H_c - 1)\rho_{da}\frac{\partial \theta_L}{\partial T}$$
$$C_{ah} = X_{ah}[\varepsilon + (H_c - 1)\theta_L] + (H_c - 1)\rho_{da}\frac{\partial \theta_L}{\partial h}$$

4.3.2 Simultaneous Mass and Heat Transport Part

4.3.2.1 Moisture Equation

In Milly's work [43], the moisture conservation equation is expressed [43] as

$$\left[\left(1 - \frac{\rho_V}{\rho_L}\right)\frac{\partial \theta_L}{\partial h} + \frac{\theta_V}{\rho_L}\frac{\partial \rho_V}{\partial h}\right]\frac{\partial h}{\partial t} + \left[\left(1 - \frac{\rho_V}{\rho_L}\right)\frac{\partial \theta_L}{\partial T} + \frac{\theta_V}{\rho_L}\frac{\partial \rho_V}{\partial T}\right]\frac{\partial T}{\partial t}$$
$$= \frac{\partial}{\partial z}\left[(K + D_{hv})\frac{\partial h}{\partial z} + (D_{Tv} + D_{Ta})\frac{\partial T}{\partial z} + K\right] \tag{4.57}$$

The LHS of Eq. (4.57) is the expansion of storage term, which includes liquid and vapor mass per unit volume of a porous medium and has exactly the same storage term as in Eq. (4.10). The RHS of Eq. (4.57) is the sum of liquid and vapor fluxes, where K is the unsaturated hydraulic conductivity, D_{Ta} is a transport coefficient for adsorbed liquid flow due to the thermal gradient [24], and D_{hv} and D_{Tv} are the vapor conductivity, due to the soil matric pressure gradient, and the thermal vapor diffusion coefficient, due to the soil temperature gradient, respectively. D_{Ta} is identical to D_{TD} in Eq. (4.3).

Equation (4.57) eliminates the extreme restrictions of Philip and de Vries' theory [62] (henceforth PdV) on the properties and the wetting history of the medium, and incorporates moisture retention hysteresis and soil inhomogeneities by using soil matric pressure head gradients instead of a soil moisture gradient. Due to the dependence of matric pressure on soil moisture and temperature, the liquid flux is separated into three components: a component due to the temperature gradient, one due to the moisture gradient, and one due to gravity. The vapor flux is separated into isothermal and thermal components. In Eq. (4.57), there is no explicit separation of liquid flux as PdV does. However, the temperature dependence of liquid flux is generalized implicitly by considering the temperature effect on K through the kinematic viscosity. The hydraulic conductivity, K, is expressed as

$$K = K_s K_r(\theta_L) \frac{\mu(T_0)}{\mu(T)} \tag{4.58}$$

where K_s is saturated hydraulic conductivity, $K_r(\theta_L)$ is relative hydraulic conductivity, and μ is viscosity, $\frac{\mu(T_0)}{\mu(T)}$ the term called a temperature correction factor by *Milly*. This approach is actually based on the well-known surface-tension viscous-flow (STVF) [42]. As far as the performance of the STVF approach is concerned, Constantz [9] and Nimmo and Miller [57] reported underestimation of the STVF in their experiments. They stated that temperature-induced changes in the liquid flux were under-predicted when only changes in surface-tension were taken into account. Their statements actually explain Milly's reporting of the insignificance of thermal liquid flux [44, 45], which is contrary to some investigators' experiment results [52, 67]. Accordingly, the liquid flux is separated into four components induced by the matric potential gradient, the temperature gradient, thermal absorption and gravity. D_{hv} and D_{Tv} in Eq. (4.48) actually demonstrate the ordinary diffusion (concentration) and thermal induced diffusion of water vapor. However, vapor transport in porous media does not only have to occur by diffusion, but can also occur by convection [61, 65] and dispersion [23, 59]. Hence, the major differences between the moisture equation of the proposed model (Eq. 4.10) and Eq. (4.57) are visible in the transport or kinetic coefficients, which become available after expansion of Eq. (4.10):

$$K_{hh} = \frac{D_{vh}}{\rho_L} + K$$

$$K_{hT} = \frac{D_{vT}}{\rho_L} + D_{TD}$$

$$K_{ha} = \frac{D_{va}}{\rho_L} + \frac{K}{\gamma_w} \qquad (4.59)$$

$$V_{Vh} = -V_a \frac{\rho_{sV}}{\rho_L} \frac{\partial H_r}{\partial h}$$

$$V_{VT} = -\frac{V_a}{\rho_L} \left(\rho_{sV} \frac{\partial H_r}{\partial T} + H_r \frac{\partial \rho_{sV}}{\partial T} \right)$$

where K_{hh}, K_{hT}, and K_{ha} are kinetic coefficients of moisture (liquid and vapor) flow due to matric potential gradient (ordinarily diffusive flow), temperature gradient (thermal induced diffusion) and air pressure gradient (air pressure flow), respectively, while V_{vh} and V_{vT} are the transport coefficients of vapor only due to the bulk flow of air (convective flow). The moisture equation of the proposed model, Eq. (4.10), could be rewritten as

$$C_{hh} \frac{\partial h}{\partial t} + C_{hT} \frac{\partial T}{\partial t}$$
$$= \frac{\partial}{\partial z} \left(K_{hh} \frac{\partial h}{\partial z} + K_{hT} \frac{\partial T}{\partial z} + K_{ha} \frac{\partial P_g}{\partial z} \right) + \rho_L \frac{\partial K_{Lh}}{\partial z} + V_{Vh} \frac{\partial h}{\partial z} + V_{VT} \frac{\partial T}{\partial z} \qquad (4.60)$$

where C_{hh} and C_{hT} are the storage coefficients defined implicitly in Eq. (4.60) and Eq. (4.10) or (4.57).

4.3.2.2 Heat Equation

The conservation of heat equation is stated by Milly [43] as:

$$\frac{\partial}{\partial z} [C(T - T_r)] + L_0 \frac{\partial}{\partial z} (\rho_V \theta_a) - \rho_L W \frac{\partial \theta_L}{\partial t}$$
$$= \frac{\partial}{\partial z} \left(\lambda\, frac \partial T \partial z + \rho_L (LD_{hV} + gTD_{Ta}) \frac{\partial h}{\partial z} - c_L (T - T_r) q_m \right) \qquad (4.61)$$

The LHS of Eq. (4.61) has the exact same form as that of Eq. (4.15), but they have been expanded in a different way. In Eq. (4.61), $C = C_d + c_L \rho_L \theta_L + c_V \rho_V \theta_a$ is the volumetric heat capacity of soil, C_d is the volumetric heat capacity of soil when dry [12], λ is the effective thermal conductivity, and q_m is the moisture flux, other notations are the same as those in Sect. 4.2. Considering the dependence of soil moisture and vapor density on matric potential and temperature, the LHS of Eq. (4.61) could be expanded as

$$\left(C + H_1 \frac{\partial \rho_V}{\partial T} + H_2 \frac{\partial \theta_L}{\partial T} \right) \frac{\partial T}{\partial t} + \left(H_1 \frac{\partial \rho_V}{\partial h} + H_2 \frac{\partial \theta_L}{\partial h} \right) \frac{\partial h}{\partial t} \qquad (4.62)$$

where $\quad H_1 = [L_0 + c_V(T - T_r)]\theta_a, \qquad H_2 = [(c_L \rho_L - c_V \rho_V)(T - T_r) - \rho_L W - \rho_V L_0]\theta_a$. According to de Vries [12], the volumetric heat capacity of soil, C, could be given as

$$C = \sum_{i=1}^{5} C_i \theta_i \qquad (4.63)$$

where θ_i and C_i are the volumetric fraction and the volumetric heat capacity of the ith soil constituent. The five components are water, air, quartz particles, other minerals and organic matter. In the above concept, the air phase is assumed to consist of vapor only, while the volume of dry air is considered implicitly to be unchanged (inert gas) under constant soil air pressure and atmospheric pressure [13]. In the proposed model, the dry air is considered to exist in two forms, bulk air and dissolved air, carrying various amounts of volume of heat due to the variable air volume. With this in mind, the LHS of Eq. (4.15) (same as the LHS of Eq. (4.61), $C_{unsat} = C$) is expanded to

$$\frac{\partial}{\partial z}[C(T - T_r)] + L_0 \frac{\partial}{\partial z}(\rho_V \theta_a) - \rho_L W \frac{\partial \theta_L}{\partial t}$$
$$= C_{Th} \frac{\partial h}{\partial t} + C_{TT} \frac{\partial T}{\partial t} + C_{Ta} \frac{\partial P_g}{\partial t} \qquad (4.64)$$

where

$$C_{Ta} = (T - T_r)(\epsilon - \theta_L)c_a X_{aa}$$

$$C_{Th} = [(T - T_r)(\rho_L c_L - \rho_{da} c_a - \rho_V c_V) - (L_0 \rho_V + \rho_L W)] \frac{\partial \theta_L}{\partial h} + (T - T_r)(\epsilon - \theta_L)c_a X_{ah}$$
$$+ [(T - T_r)(\epsilon - \theta_L)c_V + L_0(\epsilon - \theta_L)]\rho_{sV} \frac{\partial H_r}{\partial h}$$

$$C_{TT} = [(T - T_r)(\rho_L c_L - \rho_{da} c_a - \rho_V c_V) - (L_0 \rho_V + \rho_L W)] \frac{\partial \theta_L}{\partial T} + (T - T_r)(\epsilon - \theta_L)c_a X_{aT}$$
$$+ [(T - T_r)(\epsilon - \theta_L)c_V + L_0(\epsilon - \theta_L)](\rho_{sV} \frac{\partial H_r}{\partial T} + H_r \frac{\partial \rho_{sV}}{\partial T}) + C_{unsat}$$

According to de Vries [11], the first term in the RHS of Eq. (4.61) accounts for the combined effect of simple Fourier heat diffusion and latent heat transport by temperature-induced vapor diffusion. The second term represents the transfer of latent heat by vapor movement and the advection of the heat of wetting due to pressure head gradients, and the third term denotes the sensible heat transfer due to moisture flux. In the first term, the effective thermal conductivity is treated specially as the sum of the thermal conductivity of the ith constituent with special attention paid to the apparent thermal conductivity of the gas phase. This special

approach locates the contribution of latent heat transfer by vapor movement due to temperature gradient inside the gas filled pores, where it is dominant, instead of adding its volume-average value to the other forms of heat transfer [13]. In Eq. (4.61), λ is given as $\lambda^* + L\rho_L D_{TV}$, where λ^* is the pure conduction.

In the proposed model, the heat flux consists of: (i) conduction, via intermolecular flow of heat energy, (ii) convection, or flow of heat due to movement of the liquid phase, the vapor phase associated with a vapor pressure gradient (diffusive and dispersive flow), the vapor phase associated with the bulk flow of air (convective flow), and the air phase, (iii) latent heat flow associated with movement of vapor due to three mechanisms of vapor flow. Considering the heat transfer mechanism of the proposed model, de Vries' special consideration of the apparent thermal conductivity of the gas phase is compensated by including heat conveyed by air phase. After expanding the RHS of Eq. (4.15) and combining it with Eq. (4.64), the heat conservation equation can be rewritten as

$$
\begin{aligned}
&C_{Th}\frac{\partial h}{\partial t} + C_{TT}\frac{\partial T}{\partial t} + C_{Ta}\frac{\partial P_g}{\partial t} \\
&= \frac{\partial}{\partial z}\left(K_{TT}\frac{\partial T}{\partial z} + K_{Th}\frac{\partial h}{\partial z} + K_{Ta}\frac{\partial P_g}{\partial z} \right) + V_{TT}\frac{\partial T}{\partial z} + V_{Th}\frac{\partial h}{\partial z} + V_{Ta}\frac{\partial P_g}{\partial z} + C_{Tg}
\end{aligned}
\tag{4.65}
$$

where

$$
K_{TT} = \lambda_{eff} + c_L(T - T_r)K_{hT} + L(D_e + \theta_V D_{Vg})\frac{\partial \rho_V}{\partial T} + c_a(T - T_r)K_{aT}
$$

$$
K_{Th} = c_L(T - T_r)K_{hh} + L(D_e + \theta_V D_{Vg})\frac{\partial \rho_V}{\partial h} + c_a(T - T_r)K_{ah}
$$

$$
K_{Ta} = c_L(T - T_r)K_{ha} + L\rho_V K_g + c_a(T - T_r)K_{aa}
$$

$$
V_{TT} = -V_a[c_V \cdot (T - T_r) + L_0]\frac{\partial \rho_V}{\partial T} + c_a(T - T_r)\left(-V_a - H_c\frac{q_L}{\rho_L}\right)X_{aT}
$$

$$
V_{Th} = -V_a[c_V \cdot (T - T_r) + L_0]\frac{\partial \rho_V}{\partial h} + c_a(T - T_r)\left(-V_a - H_c\frac{q_L}{\rho_L}\right)X_{ah}
$$

$$
V_{Ta} = c_a(T - T_r)\left(-V_a - H_c\frac{q_L}{\rho_L}\right)X_{aa}; \quad C_{Tg} = [c_L\rho_L(T - T_r) + c_a H_c \rho_{da}(T - T_r)]\frac{\partial K_{Lh}}{\partial z}
$$

where K_{TT}, K_{Th}, K_{Ta}, V_{TT}, V_{Th}, and V_{Ta} are kinetic coefficients of heat flow, while C_{Tg} denotes the release of heat by gravity drainage of water and dissolved air.

4.4 Model Verification

Model performance was assessed against two benchmark studies. First, to verify the algorithm and to examine details of the isothermal two-phase flow, the experiments and associated numerical simulations of Touma and Vauclin [1986] (hereafter, TV86) were used. Secondly, to verify the simultaneous transport of moisture and heat under constant atmospheric pressure, a strong coupling problem solved analytically and numerically by Milly [43] was employed.

4.4.1 Case of TV86

The first verification of the model to be undertaken was to compare its outputs with published experiment data and numerical solutions for a two-phase air–water system. Several one-dimensional transient problems, including both flux and ponded experiments, are reported in TV86. The ponded experiment was performed by imposing a time constant positive water head (2.3 cm) at the surface using a Mariotte bottle device. The flux experiment was designed to apply time constant water fluxes (8.3 and 20 cm h^{-1}) at the surface, supplied by means of a volumetric pump through a series of 20 hypodermic needles. In this section, only the ponded experiment was used to verify the proposed model.

In accordance with TV86, the soil air and water hydrodynamic characteristics were determined by laboratory measurement. The water retention curve was fitted using the *Van Genuchten* model with the following parameters: $\theta_{res} = 0.0265$, $\theta_{sat} = 0.312$, $\alpha = 0.044 \, \text{cm}^{-1}$ and $n = 2.2$. TV86 stated that the natural water saturation (θ_{sat}) was significantly smaller than the porosity ($\epsilon = 0.37$) because of air entrapment and that the residual water content (θ_{res}) had to be viewed only as a fitting parameter and not necessarily as the actual residual water content. The air entry pressure was estimated at $h_{ae} = 14$ cm of water. The unsaturated hydraulic conductivity functions used were

$$K = A_w \theta^{B_w} \tag{4.66}$$

where, as in TV86, the two parameters are $A_w = 18130 \, \text{cm h}^{-1}$ and $B_w = 6.07$, implicitly entailing that $K = K_s = 15.4 \, \text{cm h}^{-1}$ when $\theta = \theta_{sat}$, and,

$$K_a = K_{as} \frac{A_a}{A_a + h^{B_a}} \tag{4.67}$$

where, as in TV86, the three parameters are $A_a = 3.86 \times 10^{-5}$, $B_a = -2.4$ and $K_{as} = 2800 \, \text{cm h}^{-1}$.

In order to check the influence of airflow on the infiltration, numerical experiments were conducted with bounded bottom and open bottom. In the open bottom case, the air was able to escape freely and infiltration was in accordance with the

Richards water flow approximation (single-phase flow). However, when the column was bounded, the infiltration process was significantly retarded. The soil column, with a length of 100 cm, was vertically discretized into 100 elements, which is equivalent to 101 nodes with $\Delta z = 1$ cm. Variable time stepping was applied with an initial time step of $\Delta t = 1$ s. The initial soil water content was obtained from TV86 (Fig. 4.1 in TV86), and is symbolized by a cross sign ($\times$) in Fig. 4.1b. The initial condition was obtained by draining the saturated soil column to the static equilibrium corresponding to a piezometric level at 120 cm below the surface. In accordance with the experimental setup by TV86, the boundary conditions were described as:

$$
\begin{aligned}
h(z, t) &= 2.3 \text{ cm} & t > 0 & & z = 0 \text{ cm} \\
q_a(z, t) &= 0 & 0 \leq t < t_{crit} & & z = 0 \text{ cm} \\
P_g(z, t) &= h_{ae} + 2.3 & t \geq t_{crit} & & z = 0 \text{ cm} \\
q_L(z, t) &= 0 & t \geq 0 & & z = L = -100 \text{ cm} \\
q_a(z, t) &= 0 & t \geq 0 & & z = L = -100 \text{ cm}
\end{aligned}
\tag{4.68}
$$

$$
\begin{aligned}
h(z, t) &= 2.3 \text{ cm} & t > 0 & & z = 0 \text{ cm} \\
h(z, t) &= -5.8 \text{ cm} & t \geq 0 & & z = -100 \text{ cm}
\end{aligned}
\tag{4.69}
$$

Equation (4.68) depicts the boundary conditions used in the modeling of the experiment run in the bounded column, and Eq. (4.69) depicts the open column
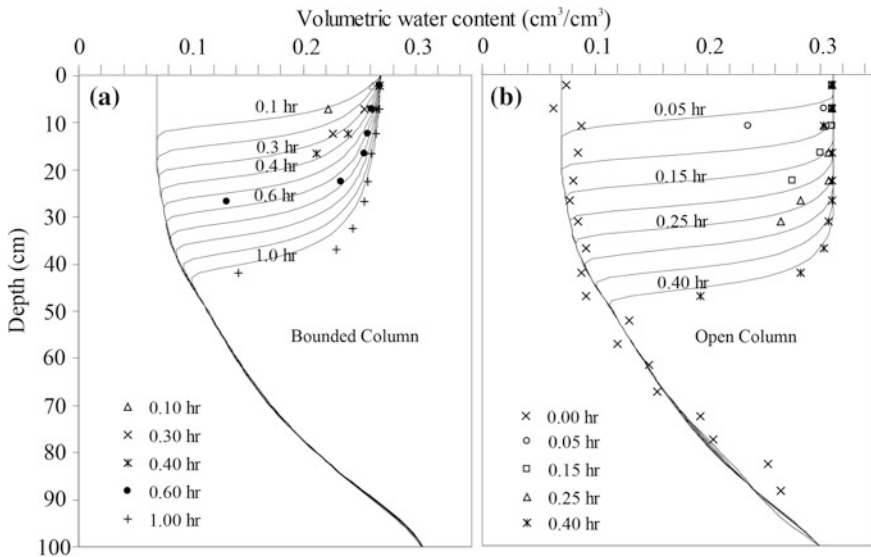

Fig. 4.1 Comparison of the simulated water profiles (*solid lines*) in the **a** bounded and **b** the open soil columns based on the data obtained in the TV86 experiment (data points), adapted from Fig. 4.5 in TV86

case. In the bounded column experiment, the time t_{crit} denoted the moment at which the pressure on the surface reached the value of h_{ae} +2.3 cm, above which the air freely escaped from the surface through the ponded water. In TV86's case, t_{crit} was determined to be at 12 s. Notice that the depth of ponding on the surface is 2.3 cm. In the open column experiment, the boundary conditions were simpler than in the bounded column experiment, because the air could freely escape from the bottom of the column. This free escape of the air prevented an increase of air pressure in the column, and as a result no air escaped from the surface through the ponded water.

Figure 4.1 shows satisfactory agreement between the data points and the simulation results. As can be seen in Fig. 4.1a, b, the infiltration obviously occurred faster in the open column than in the bounded column. After 0.4 h of infiltration, the wetting front reached a depth of about 50 cm in the open column, while reaching a depth of about 25 cm in the bounded column. The three major differences between the water content profiles in the open column and the bounded column are in excellent agreement with TV86's findings: first, the infiltration rate is drastically reduced when air cannot escape from the bounded bottom; second, the slopes are less abrupt when air phase transport is considered; third, because of the escape of air from the top of the column, the saturation water content is around 0.27, compared to 0.312 when only the liquid phase transport is considered. These results demonstrate the ability of the proposed model to analyze the two-phase flow.

4.4.2 Case of Milly (1982)

The second verification of the model to be undertaken was a comparison with Milly's solution for simultaneous mass and heat transport in a very dry soil. The basic idea is that water vapor diffusion in a vapor-dominated system (very dry soil) will cause water vapor condensation and consequently the release of latent heat, thus causing a temporary rise in the medium temperature. Subsequently, as the heat flux diffuses out of the system, the medium temperature will return to its original value. In order to check this, a sudden increase in water vapor supply was applied at one end of the soil column to examine the strong coupling process between moisture and heat fields.

Yolo light clay soil was used in this case, for which the water retention curve written by Haverkamp et al. [29] was

$$
\theta =
\begin{cases}
0.371 \cdot \left[1 + \left(\frac{\log(|h|)}{2.26}\right)^4\right]^{-1} + 0.124, & h < -1\,\text{cm} \\
0.495, & h \geq -1\,\text{cm}
\end{cases}
\tag{4.70}
$$

The hydraulic conductivity was given [29] as
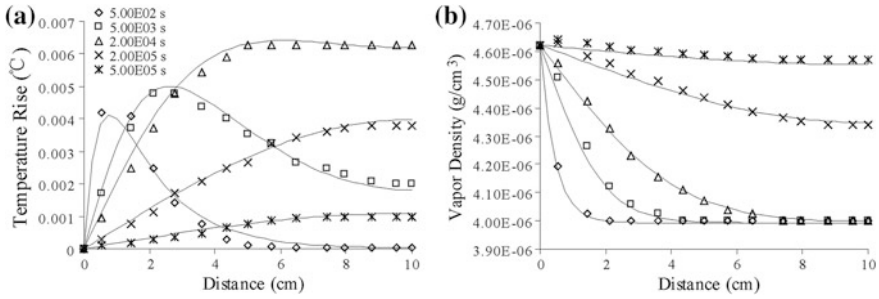
Fig. 4.2 Comparison between **a** the simulated (*solid lines*) soil temperature rise and **b** water vapor density based on the data obtained in the Milly's experiment (data points), adapted from Fig. 8 in Milly [43]

$$K = K_s \cdot \left[1 + \left(\frac{|h|}{15.3} \right)^{1.77} \right]^{-1} , \; K_s = 1.23 \times 10^{-5} \, \text{cm/s} \qquad (4.71)$$

The volumetric heat capacity was expressed as the first term in the square bracket of the left hand side (LHS) of Eq. (4.15) without considering dry air, in which $c_s = 0.47$, $c_L = 4.18$, and $c_v = 1(10^{-3} \, \text{J kg}^{-1} \, {}^\circ\text{C}^{-1})$. The soil specimen, with a length of 10 cm, was discretized vertically into 40 elements of 0.25 cm length. A convenient constant time stepping of 500 s was used for comparison with *Milly*'s results. The boundary and initial conditions selected were expressed as:

$$
\begin{array}{llc}
\rho_v(z,t) = \bar{\rho} & t = 0 & -10 \, \text{cm} \leq z \leq 0 \, \text{cm} \\
T(z,t) = \bar{T} & t = 0 & -10 \, \text{cm} \leq z \leq 0 \, \text{cm} \\
\rho_v(z,t) = \bar{\rho} + \Delta \rho & t > 0 & z = 0 \, \text{cm} \\
T(z,t) = \bar{T} & t > 0 & z = 0 \, \text{cm} \\
\partial \rho_v / \partial z = 0 & t > 0 & z = -10 \, \text{cm} \\
\partial T / \partial z = 0 & t > 0 & z = -10 \, \text{cm}
\end{array}
\qquad (4.72)
$$

The following numerical values were selected for the solution:

$$\bar{\rho} = 4.03 \times 10^{-6} \, \text{g cm}^{-3}, \; \Delta \rho = 0.63 \times 10^{-6} \, \text{g cm}^{-3}, \; \bar{T} = 20 \, {}^\circ\text{C} \qquad (4.73)$$

Figure 4.2 shows excellent agreement between the simulation results (solid lines) and Milly's results. Figure 4.2a shows that the sudden increase of water vapor supply on the surface raised the temperature near the surface steeply. As time elapsed, the temperature slowly reassumed its original value, as the soil specimen was equilibrated to the water vapor supply on the surface. In Fig. 4.2b, the propagation of water vapor density depicts the water vapor balancing process during water vapor diffusion into soil. As time elapsed, the difference in water vapor density between the top and the bottom of the specimen approached zero. After long enough diffusion, the whole soil specimen would have a constant

temperature and water vapor density. The success of this test case established the validity of the proposed model for modeling simultaneous heat and mass transfer in soil.

4.5 Numerical Analysis

4.5.1 Influence of Airflow in Milly's Case

In Milly's case, the gas phase flow in the unsaturated zone is considered in order to include only water vapor flux, while the dry air is assumed to be an inert gas. This assumption avoids the calculation of the air balance equation, though air may have a significant influence on the water vapor flux. As known from TV86's case, infiltration is retarded in the bounded column because of the effect of the air pressure in the soil. In this study, a 10 cm thick specimen was bounded to test the air effect on the coupled moisture and heat transport.

The simulation result shows that the transport of water vapor in soil displayed a similarly retarded phenomenon, caused by the outward air pressure gradient, which in turn was induced by the temperature rise because of the water vapor condensation. As can be seen in Fig. 4.3b, water vapor penetration was slowed down. Given the same time elapsed, the water vapor density profiles considering airflow (solid lines) is obviously farther away from reaching the equilibrium, than those (dashed lines) that did not consider the air balance equation. At the same time, Fig. 4.3a, the absolute temperature rise increased (the solid lines are above the dashed lines) because of retardation in the water vapor transport, causing more water vapor to be condensed and more heat to be released.

A note of caution about Figs. 4.2 and 4.3, however, is appropriate here. The scale of both temperature rise (10^{-3} °C) and vapor density (10^{-6} g cm^{-3}) was quite small and hardly detectable using instrumentation. However, the small scale
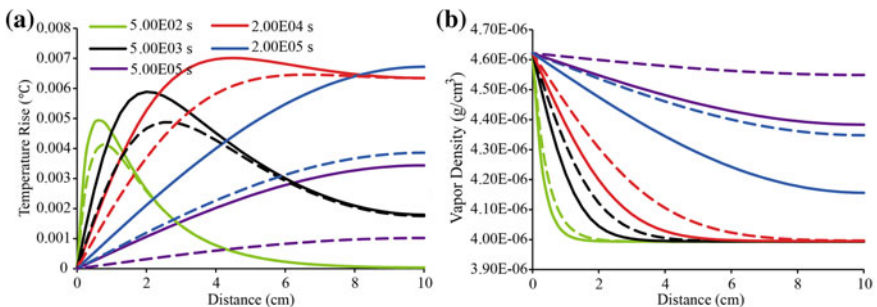

Fig. 4.3 Comparison of **a** temperature rise and **b** water vapor density profiles, with (*solid line*) and without (*dashed line*) considering the air balance equation
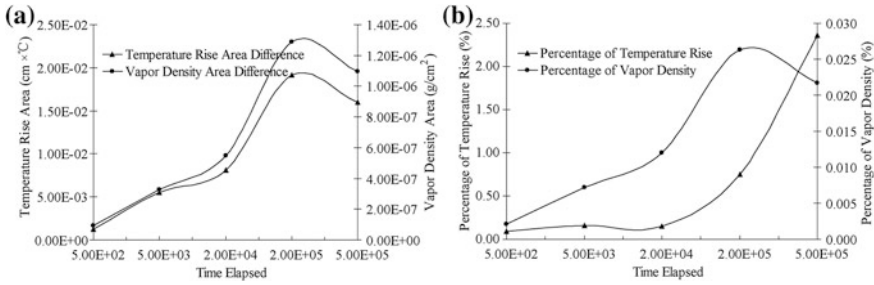
Fig. 4.4 **a** The absolute air effect expressed as the absolute difference between the integrated areas under the *solid lines* (with air) and *dashed lines* (without air) in Fig. 4.3a and b; **b** the relative air effect expressed as percentage of the absolute difference to the integrated areas under the *dashed lines*

is intended that the analytical solution for the Milly's case (e.g., strong coupling between moisture and heat fields), is feasible. The analytic solution for Milly's case required a small perturbation of the system and simplified assumptions [43] (i.e., the simultaneous transport of soil moisture and heat is carried only by vapor diffusion, and the sensible heat carried by water vapor is negligible). In order to match the requirements for the analytic solution, the numerical experiment was set up along Eqs. (4.72) and (4.73). According to Eq. (4.73), the percentage of perturbation of the water vapor supply was less than 16 %, causing the medium temperature to vary from 20 to 20.0065 °C (0.032 % variation) (Fig. 4.2). The capture of this undetectable variation (analytic solutions) by the model demonstrated its capability to simulate the dynamics of vapor-dominated systems with strong coupling between moisture and heat fields.

The aim of Sect. 4.5.1 was to check how airflow affected the coupled dynamics. Figure 4.3 shows that the inclusion of airflow, using the proposed model, decreased the vapor density and increased the temperature rise. The air effect should be quantified as absolute and as relative effect. The absolute air effect was calculated from absolute differences between the integrated areas under the solid (with air) and the dashed (without air) lines in Fig. 4.3a, b, i.e. the area between the green solid line and the green dashed line indicates the absolute difference caused by the air effect. The relative air effect was calculated by dividing the absolute differences into the integrated areas under the dashed lines (without air) and was expressed as a percentage, i.e., the absolute difference between the green solid line and the green dashed line is divided by the integrated area under the green dashed line. Figure 4.4a shows that the absolute air effect increased as time elapsed, till 2.00E05 *s*, and weakened afterwards for both temperature rise and vapor density. Compared to the undetectable absolute variation in Milly's case, the relative air effect demonstrated better how airflow affected the coupled dynamics. Figure 4.4b shows that the relative air effect of vapor density had the same variation as the absolute one, while the relative effect on the temperature rise showed a different pattern.

The relative air effect on the temperature rise increased further after 2×10^5 s, instead of being weakened (Fig. 4.4b). This increase actually explains the effect of the retardation in the water vapor transport, which caused more water vapor to be condensed and more heat to be released. The averaged percentages of the relative air effect on the temperature rise and the vapor density were 70.1 % and 1.39 %, respectively. Because of the extremely small temperature rise (<0.0011 °C) at the end (5×10^5 s) of the experiment run without airflow, the small air effect caused a huge perturbation (236 %) to the temperature rise at that time point, increasing the averaged percentage of the relative air effect on the temperature rise. Without considering this final perturbation, the averaged percentage of the relative air effect on temperature rise was 28.7 %.

4.5.2 Influence of Heat Flow in TV86's Case

For TV86's case, the ponding infiltration was examined in Sect. 4.4.1. Their work contains two more experiments: (1) a constant water flux of 8.3 cm h^{-1}, smaller than the saturated hydraulic conductivity applied at the surface, and (2) a constant water flux of 20 cm h^{-1}, greater than the saturated hydraulic conductivity applied at the surface. These two experiments were numerically replicated, both with and without considering the heat flow and transport. Not only were water fluxes different from the saturated hydraulic conductivity (15.4 cm h^{-1}) adopted as surface boundary condition, but the open and closed bottoms discussed in Sect. 4.4.1 were also included as boundary conditions. The lower boundary conditions for these two problems were the same as those described in Eqs. (4.68) and (4.69). In order to investigate how the heat flow influenced the two-phase flow process, two infiltration experiments were set up: one experiment was designed to have a uniform temperature profile of 20 °C during the whole simulation period (this experiment was named isothermal infiltration); the other one was set up providing a 10 °C increase in temperature at the surface (30 °C), while the bottom was kept at its original value (20 °C) during the whole simulation period (this experiment was named thermal infiltration).

Figure 4.5 does not show a large difference in the propagation of water content profiles in the isothermal and thermal infiltration. However, the wetting front did move slightly faster in the thermal infiltration than in the isothermal infiltration for both the open (Fig. 4.5b) and the bounded column (Fig. 4.5a). The movement of the wetting front was judged by the slope of the water content profiles. Figure 4.5a shows the slope of the water content profiles to be more abrupt in the thermal infiltration (slope = 3.38) than in the isothermal infiltration (slope = 1.7). In Fig. 4.5b, the slope of the moisture profile in the thermal infiltration (slope = 5.5) is also steeper than in the isothermal infiltration (slope = 3.3). This indicates that a certain amount of water, supposed to be stored at certain depth in the isothermal infiltration, was partially pushed down by the thermal liquid flux in the thermal infiltration. Therefore, at the same instant, the thermal infiltration caused the soil to

Fig. 4.5 Time evolution of the water content profile under an infiltration rate of 8.3 (cm h^{-1}), with and without considering the heat flow in **a** a bounded and **b** an open column

be less wet than the isothermal infiltrated soil at a certain depth. The volume of the water pushed down to the wetting front, was calculated by integrating the high-lighted grey areas between the water content profiles in the isothermal infiltration and the thermal infiltration.

Apart from the temperature effect, the two-phase isothermal infiltration with a prescribed flux rate of 8.3 (cm h^{-1}) at the top boundary, showed no large differ-ence between the open column and the bounded column in the propagation of soil moisture (Fig. 4.5a, b). Unlike in the first case in Sect. 4.4.1, there was no ponded water at the surface, because of the fact that the flux was lower than the saturated hydraulic conductivity, which meant that the infiltration rate was limited to 8.3 cm h^{-1}. Nevertheless, the surface soil wetness was slightly greater in the bounded column than in the open column, and thus the slope of the moisture profile in the bounded column (slope = 1.7) was less steep than in the open column (slope = 3.3). As Celia [7] pointed out, the air flux coming out of the top of the column would have to be essentially the same as the water going in, but flowing in the opposite direction. This opposite air flux did influence the water flux going in. As a result, a certain amount of water was held back, increasing the surface wetness. This phenomenon was in accordance with the transport of water vapor into soil discussed in Milly's case (Sect. 4.5.1), where air phase transport was considered.

Figure 4.6 shows the propagation of soil moisture with a prescribed flux at the surface higher than the saturated hydraulic conductivity (20 cm h^{-1}), causing ponded water to build up at the surface. With the buildup of ponded water at the

surface, the infiltration in the bounded column showed very clear retardation compared to the infiltration in the open column. This was in accordance with the first case discussed in Sect. 4.4.1. However, considering the temperature effect in the isothermal two-phase flow, the differences between the moisture profiles in the isothermal and the thermal infiltration were more obvious in the bounded column (Fig. 4.6a) than in the open column (Fig. 4.6b). This is also evident in Fig. 4.5, which shows the differences in moisture profiles were more obvious in the bounded column (Fig. 4.5a) than in the open column (Fig. 4.5b) (i.e., the high-lighted grey areas in Fig. 4.5a are larger than those in Fig. 4.5b).

The open column actually provided a path for the air to escape, creating a condition for the air in the soil column to equilibrate quickly with the atmospheric pressure, which meant that the air phase essentially had an infinitesimal effect on the solution of the equations for the water phase. However, when the column was sealed (no air escape from the bottom) and the top of the column saturated or close to saturation (no air escape from the top until the air entry value is reached), the air phase transport became a significant factor during the transient infiltration, as the results show in Figs. 4.1 and 4.6. In the case of surface boundary flux with a hydraulic conductivity lower than its saturated value, the top of the column was not saturated and air escaped freely from the top, but nevertheless the air phase slightly affected the water phase transport (Fig. 4.5). When the air phase effect plays a significant role in solving equations of the water phase, the inclusion of the heat flow becomes necessary. This necessity is clearly evident in Fig. 4.6.

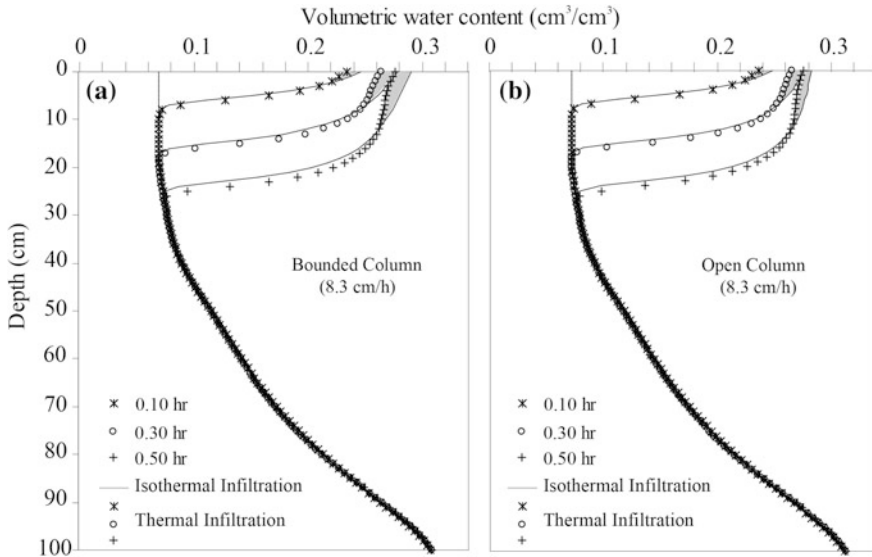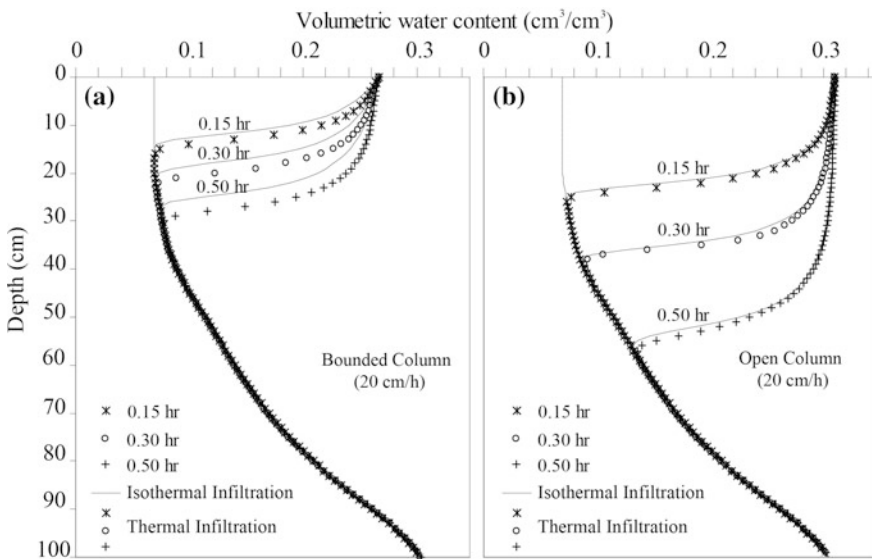**Fig. 4.6** Time evolution of the water content profile under an infiltration rate of 20 (cm h^{-1}), with and without considering the temperature effect in **a** a bounded and **b** an open column

4.6 Brief Summary

Based on the discussion about the importance of including mechanisms other than diffusion for vapor transport in the soil, this chapter developed a two-phase mass and heat flow model. The constitutive equations were introduced to link the independent variables (state variables) and the dependent variables. A brief introduction of the numerical approach was presented. How dry air acts as an independent variable in the equation system is discussed, based on the governing equations and the constitutive equations. How airflow enters the moisture balance and the heat balance equations is also shown in detail. The model was verified by testing its capacity to describe the physical processes involved in the isothermal two-phase flow [81] and the coupled moisture and heat transfer [43]. Excellent agreement was achieved between the proposed model and the published experimental and numerical studies.

On the basis of model verification, the fully coupled problem was investigated by introducing heat flow into the isothermal two-phase flow and dry airflow into the coupled moisture and heat flow. The results showed that in a very dry soil, airflow had a significant influence on the water vapor transfer. In a bounded soil column, 10 cm thick, the water vapor transfer was retarded because of the outward air pressure gradient. In the transient infiltration experiments, the simulation results showed that when the air effect was significant (i.e., in a bounded soil column), the inclusion of heat flow increased the infiltration process (Fig. 4.6a). However, the heat flow did not affect the two-phase flow (air–water flow) note worthily when the bottom of the column was opened. In that case, the soil air pressure equilibrated quickly with the atmospheric pressure. In the bounded column, where the air phase played a significant role in the water phase flow, the effect of the heat flow was outstanding. The thermal gradient driving forces partially pushed the water supposed to be stored at certain depth, down and made the water content profiles more abrupt.

References

1. Alonso EE, Gens A, Josa A (1990) A constitutive model for partially saturated soils. Geotechnique 40(3):405–430
2. Bear J (1972) Dynamics of fluid in porous media. Dover, New York
3. Biggar JW, Nielsen DR (1976) Spatial variability of the leaching characteristics of a field soil. Water Resour Res 1(1):78–84
4. Buckingham E (1904) Contributions to our knowledge of aeration of soils. Bull. 25, Bureau of Soils, United States Department of Agriculture, Washington
5. Cahill AT, Parlange MB (1998) On water vapor transport in field soils. Water Resour Res 34(4):731–739
6. Cass A, Campbell GS, Jones TL (1984) Enhancement of thermal water vapor diffusion in soil. Soil Sci Soc Am J 48:25–32

7. Celia MA, Binning P (1992) A mass conservative numerical-solution for 2-phase flow in porous-media with application to unsaturated flow. Water Resour Res 28(10):2819–2828

8. Cohen Y, Ryan PA (1989) Chemical transport in the topsoil zone. The role of moisture and temperature gradients. J Hazard Mater 22(3):283–304

9. Constantz J (1982) Temperature dependence of unsaturated hydraulic conductivity of two soils. Soil Sci Soc Am J 46:446–470

10. Corey AT (1957) Measurement of water and air permeability in unsaturated soil. Soil Sci Soc Am J 21(1):7–10

11. de Vries DA (1958) Simultaneous transfer of heat and moisture in porous media. Trans Am Geophys Union 39(5):909–916

12. de Vries DA. (1966) Thermal properties of soils. In: Van Wijk WR (ed) Physics of plant environment. North-Holland Publishing Company, Amsterdam, pp 210–234

13. de Vries DA (1987) The theory of heat and moisture transfer in porous media revisited. Int J Heat Mass Transf 30:1343–1350

14. Edlefsen NE, Anderson ABC (1943) Thermodynamics of soil moisture, HILGARDIA: A J Agr Sci 15:31–298

15. Falta RW, Pruess K, Javandel I, Witherspoon PA (1992) Numerical modeling of steam injection for the removal of nonaqueous phase liquids from the subsurface. 1. Numerical formulation. Water Resour Res 28(2):433–449

16. Fayer MJ (2000) UNSAT-H Version 3.0: unsaturated soil water and heat flow model-theory, user manual, and examples. Pacific Northwest National Laboratory, Washington, p 331

17. Flerchinger GN (2000) The simultaneous heat and water (SHAW) model: techincal documentation. NWRC, USDA ARS, Boise

18. Fogel'son RL, Likhachev ER (2000) Temperature dependence of diffusion coefficient. Phys Met Metalloved 90(1):58–61

19. Fredlund DG, Rahardjo H (1993) Soil mechanics for unsaturated soils. Wiley, New York

20. Gawin D, Baggio P, Schrefler BA (1995) Coupled heat, water and gas-flow in deformable porous-media. Int J Numer Meth Fluid 20(8–9):969–987

21. Gray WG, Hassanizadeh SM (1991) Unsaturated flow theory including interfacial phenomena. Water Resour Res 27(8):1855–1863

22. Gray WG, Miller CT (2005) Thermodynamically constrained averaging theory approach for modeling flow and transport phenomena in porous medium systems: 1. Motivation and overview. Adv Water Resour 28(2):161–180

23. Grifoll J, Gast JM, Cohen Y (2005) Non-isothermal soil water transport and evaporation. Adv Water Resour 28:1254–1266

24. Groenevelt PH, Kay BD (1974) On the interaction of water and heat transport in frozen and unfrozen soils: II. The liquid phase. Soil Sci Soc Am Proc 38:400–404

25. Haga D, Niibori Y, Chida T (1999) Hydrodynamic dispersion and mass transfer in unsaturated flow. Water Resour Res 35(4):1065–1077

26. Hassanizadeh M, Gray WG (1979) General conservation equations for multi-phase systems: 1. Averaging procedure. Adv Water Resour 2:131–144

27. Hassanizadeh M, Gray WG (1979) General conservation equations for multi-phase systems: 2. Mass, momenta, energy, and entropy equations. Adv Water Resour 2:191–203

28. Hassanizadeh M, Gray WG (1980) General conservation equations for multi-phase systems: 3. Constitutive theory for porous media flow. Adv Water Resour 3(1):25–40

29. Haverkamp R, Vauclin M, Touma J, Wierenga PJ, Vachaud G (1977) A comparison of numerical simulation models for one-dimensional infiltration. Soil Sci Soc Am J 41(2):285–294

30. Heitman JL, Horton R, Ren T, Nassar IN, Davis DD (2008) A test of coupled soil heat and water transfer prediction under transient boundary temperatures. Soil Sci Soc Am J 72(5):1197–1207

31. Hillel D (2004) Introduction to environmental soil physics. Elsevier Academic Press, Amsterdam

32. Jackson AS, Miller CT, Gray WG (2009) Thermodynamically constrained averaging theory approach for modeling flow and transport phenomena in porous medium systems: 6. Two-fluid-phase flow. Adv Water Resour 32(6):779–795

33. Kimball BA, Jackson RD, Reginato RJ, Nakayama FS, Idso SB (1976) Comparison of field-measured and calculated soil-heat fluxes. Soil Sci Soc Am Proc 40(1):18–25

34. Kowalski SJ (2008) R and D in thermo-hydro-mechanical aspect of drying. Drying Technol 26(3):258–259

35. Li Q, Wu Z, Bai Y, Yin X, Li X (2006) Thermo-hydro-mechanical modeling of CO2 sequestration system around fault environment. Pure Appl Geophys 163(11–12):2585–2593

36. Liu S, Masliyah JH (2005) Dispersion in porous media. Vafai K (ed) Handbook of porous media. Taylor and Francis Group, CRC Press, Boca Raton, pp 81–140

37. Massmann JW (1989) Applying groundwater-flow models in vapor extraction system-design. J Environ Eng ASCE 115(1):129–149

38. McWhorter DB (1990) Unsteady radial flow of gas in the vadose zone. J Contam Hydrol 5:297–314

39. Mendoza CA, Frind EO (1990) Advective-dispersive transport of dense organic vapors in the unsaturated zone.1. Model development. Water Resour Res 26(3):379–387

38. Miller CT, Christakos G, Imhoff PT, McBride JF, Pedit JA, Trangenstein JA (1998) Multiphase flow and transport modeling in heterogeneous porous media: challenges and approaches. Adv Water Resour 21(2):77–120

41. Miller CT, Gray WG (2005) Thermodynamically constrained averaging theory approach for modeling flow and transport phenomena in porous medium systems: 2. Foundation. Adv Water Resour 28(2):181–202

42. Miller EE, Miller RD (1956) Physical theory for capillary flow phenomena. J Appl Phys 27:324–332

43. Milly PCD (1982) Moisture and heat transport in hysteretic, inhomogeneous porous media: a matric head-based formulation and a numerical model. Water Resour Res 18(3):489–498

44. Milly PCD (1984) A linear analysis of thermal effects on evaporation from soil. Water Resour Res 20(8):1075–1085

45. Milly PCD (1984) A simulation analysis of thermal effects on evaporation from soil. Water Resour Res 20(8):1087–1098

46. Milly PCD, Eagleson PS (1980) The coupled transport of water and heat in a vertical soil column under atmospheric excitation. Massachusetts Institute of Technology, Department of Civil Engineering, Ralph M. Parsons Laboratory for Water Resources and Hydrodynamics

47. Milly PCD, Eagleson PS (1982) Parameterization of moisture and heat fluxes across the land surface for use in atmospheric general circulation models. Department of Civil Engineering, School of Engineering, Massachusetts Institute of Technology

48. Morel-Seytoux HJ, Billica JA (1985) A tow-phase numerical model for prediction of infiltration: application to a semi-infinte column. Water Resour Res 21(4):607–615

49. Moridis GJ, Reddell DL (1991) Secondary water recovery by air injection.1. The concept and the mathematical and numerical-model. Water Resour Res 27(9):2337–2352

50. Mualem Y (1976) A new model for predicting the hydraulic conductivity of unsaturated porous media. Water Resour Res 12(3):513–522

51. Nassar IN, Horton R (1997) Heat, water, and solution transfer in unsaturated porous media: 1–theory development and transport coefficient evaluation. Transp Porous Media 27(1): 17–38

52. Nassar IN, Horton R, Globus AM (1992) Simultaneous transfer of heat, water, and solute in porous media: II. Experiment and analysis. Soil Sci Soc Am J 56:1357–1365

53. Neaupane KM, Yamabe T, Yoshinaka R (1999) Simulation of a fully coupled thermo-hydro-mechanical system in freezing and thawing rock. Int J Rock Mech Min Sci 36(5):563–580

54. Niessner J, Hassanizadeh SM (2008) A model for two-phase flow in porous media including fluid–fluid interfacial area. Water Resour Res 44:W08439

55. Niessner J, Hassanizadeh SM (2009) Modeling kinetic interphase mass transfer for two-phase flow in porous media including fluid–fluid interfacial area. Transp Porous Media 80(2): 329–344
56. Niessner J, Hassanizadeh SM (2009) Non-equilibrium interphase heat and mass transfer during two-phase flow in porous media-theoretical considerations and modeling. Adv Water Resour 32(12):1756–1766
57. Nimmo JR, Miller EE (1986) The temperature dependence of isothermal moisture vs. potential characteristics of soils. Soil Sci Soc Am J 50:1105–1113
58. Oleson KW, Lawrence DM, Bonan GB, Flanner MG, Kluzek E, Lawrence PJ, Levis S, Swenson SC, Thornton PE, Dai A, Decker M, Dickinson R, Feddema J, Heald CL, Hoffman F, Lamarque J-F, Mahowald N, Niu G-Y, Qian T, Randerson J, Running S, Sakaguchi K, Slater A, Stockli R, Wang A, Yang Z-L, Zeng X (2010) Technical description of version 4.0 of the community land model (CLM). National Center for Atmospheric Research, Boulder
59. Olivella S, Gens A (2000) Vapor transport in low permeability unsaturated soils with capillary effects. Transp Porous Media 40(2):219–241
60. Parlange JY, Braddock RD, Simpson RW (1982) Optimization Principle for air and water movement. Soil Sci 133(1):4–9
61. Parlange MB, Cahill AT, Nielsen DR, Hopmans JW, Wendroth O (1998) Review of heat and water movement in field soils. Soil Tillage Res 47:5–10
62. Philip JR, de Vries DA (1957) Moisture movement in porous materials under temperature gradient. Trans Am Geophys Union 38(2):222–232
63. Pinder GF, Gray WG (1977) Finite element simulation in surface and subsurface hydrology. Academic, New York
64. Pruess K (2004) The TOUGH codes—a family of simulation tools for multiphase flow and transport processes in permeable media. VZJ 3(3):738–746
65. Pruess K, Calore C, Celati R, Wu YS (1987) An analytical solution for heat-transfer at a boiling front moving through a porous-medium. Int J Heat Mass Transf 30(12):2595–2602
66. Prunty L (2002) Spatial distribution of heat of wetting in porous media. ASAE Annual International Meeting/CIGR XVth World Congress, Chicago, Paper Number: 023119
67. Prunty L (2009) Thermomechanical theory of capillary soil water. Soil Sci Soc Am J 73(2):494–500
68. Rollins RL (1954) Movement of soil moisture under a thermal gradient. Highw Res Board Proc 33:492–508
69. Sahimi M, Heiba AA, Davis HT, Scriven LE (1986) Dispersion in flow through porous media. II. Two-phase flow. Chem Eng Sci 41(8):2123–2136
70. Saito H, Simunek J, Mohanty BP (2006) Numerical analysis of coupled water, vapor, and heat transport in the vadose zone. Vadose Zone J 5(2):784–800
71. Sakai M, Toride N, Simunek J (2009) Water and vapor movement with condensation and evaporation in a sandy column. Soil Sci Soc Am J 73(3):707–717
72. Scanlon BR (2000) Soil gas movement in unsaturated systems. Handbook of soil science. In: Sumner ME (ed) Handbook of soil science. CRC Press, Boca Raton, pp A277–A319
73. Schrefler BA (2004) Multiphase flow in deforming porous material. Int J Numer Meth Eng 60(1):27–50
74. Schrefler BA, Scotta R (2001) A fully coupled dynamic model for two-phase fluid flow in deformable porous media. Comput Methods Appl Mech Eng 190(24–25):3223–3246
75. Shan C (1995) Analytical solutions for determining vertical air permeability in unsaturated soils. Water Resour Res 31(9):2193–2200
76. Shan C (1999) An analytical solution for the capture zone of two arbitrarily located wells. J Hydrol 222(1–4): 123–128
77. Simunek J, van Genuchten MT (2008) Modeling nonequilibrium flow and transport processes using HYDRUS1D. Vadose Zone J 7(2):782–797
78. Thomas HR, Cleall PJ, Dixon D, Mitchell HP (2009) The coupled thermal-hydraulic-mechanical behaviour of a large-scale in situ heating experiment. Geotechnique 59(4):401–413

79. Thomas HR, He Y, Onofrei C (1998) Examination of the validation of a model of the hydro/thermo/mechanical behaviour of engineered clay barriers. Int J Numer Anal Meth Geomech 22(1):49–71

80. Thomas HR, Sansom MR (1995) Fully coupled analysis of heat, moisture, and air transfer in unsaturated soil. J Eng Mech 121(3):392–405

81. Touma J, Vauclin M (1986) Experimental and numerical analysis of two-phase infiltration in a partially saturated soil. Transp Porous Media 1(1):22–25

82. Twarakavi NKC, Simunek J, Seo S (2008) Evaluating interactions between groundwater and vadose zone using the HYDRUS1D-based flow package for MODFLOW. Vadose Zone J 7(2):757–768

83. van Dam JC, Groenendijk P, Hendriks RFA, Kroes JG (2008) Advances of modeling water flow in variably saturated soils with SWAP. Vadose Zone J 7(2):640–653

84. van Genuchten MT (1980) A closed-form equation for predicting the hydraulic conductivity of unsaturated soils. Soil Sci Soc Am J 44(5):892–898

85. Yang K, Chen YY, Qin J (2009) Some practical notes on the land surface modeling in the Tibetan Plateau. Hydrol Earth Syst Sci 13(5):687–701

Chapter 5
How Airflow Affects Soil Water Dynamics

5.1 Introduction

Evaporation from unsaturated soil involves physical processes, including phase change, vapor transport, liquid flow, and heat transfer. Assuming the evaporative demand is constant, the soil drying process in the absence of a water table has been conceptualized as three stages: a constant-rate stage, a falling-rate stage and a slow-rate stage [6]. In correspondence to the three different evaporation stages, the vertical distribution of soil moisture can be described to be a three-layer model. Each stage of evaporation connects to one of the three soil layers covering the surface [7]. In the first stage, an excess of liquid in soil pores (wet soil layer, WSL) covers the surface. In the second stage, liquid and vapor simultaneously transport and a phase transformation zone (PTZ) forms on the top of the WSL. In the final stage, the dry surface layer (DSL) forms over the PTZ where only vapor phase flow is allowed. Prat [16] labeled the same three soil layers as the dry zone, two-phase zone, and liquid zone, while Yiotis et al. [32, 33] call them the dry/gas region, film region, and liquid region. Among these papers, no large difference exists in distinguishing different soil layers associated with different evaporation stages, except for PTZ. The concurrent vapor and liquid flux in PTZ was originally described by Philip and de Vries [15] (hereafter PdV model) as the evaporation–condensation through a series of liquid islands. On the basis of this description, an enhancement factor for vapor transfer was put forward considering the micro-scopic-thermal-gradient in air-filled pores [15].

This chapter is based on: Zeng, Y., Z. Su, L. Wan, J. Wen (2011), Numerical analysis of air–water-heat flow in unsaturated soil: Is it necessary to consider airflow in land surface models? Journal of Geophysical Research, Vol. 116, D20107, doi: 10.1029/2011JD015835. Zeng, Y., Z. Su, L. Wan, J. Wen (2011), A Simulation Analysis of Advective Effect on Evaporation using a Two-Phase Heat and Mass Flow Model, Water Resources Research, Vol. 47, W10529, doi: 10.1029/2011WR010701

The enhanced vapor transfer has been questioned for more than a decade since Webb and Ho's [31] comprehensive review. The root of the doubt is on the lack of direct measurement evidence [25]. The enhancement factor in the PdV model is only valid when a temperature gradient exists. If there is no temperature gradient, there is no enhancement. However,Webb and Ho's [31] pointed out that vapor diffusion was enhanced even there was no temperature gradient, implying that an additional mechanism should be included in the PdV model. Before Webb and Ho's review, Rose [19, 20] claimed that the enhanced vapor transfer was perhaps partially caused by the advective mass flow of air through the soil. Following this idea, the advective flux induced by diurnal heating and cooling of the soil surface, was proposed to be the omitted mechanism in the PdV model by Cahill and Parlange [3] and Parlange et al. [14] (CP model). Notwithstanding a close match between the CP model and the field observation, the enhanced vapor flow due to other factors other than temperature effect was still not taken into account. Actually, the vapor can be transferred as part of the bulk flow of dry air that is purely driven by the air pressure gradient in the soil [13]. There is a need to study the air pressure gradient induced vapor transfer (advective vapor transfer) using a two-phase flow model that treats dry air as a gas phase and soil water as a liquid phase.

The thermal effect on evaporation from unsaturated soil has been studied by many researchers [2, 10, 11, 21, 22]. Most investigators employed the phenomenological scheme developed by Philip and de Vries [15]. Nevertheless, the neglect of airflow in the PdV model restrains the analysis of the advective effect on evaporation. A two-phase heat and mass flow model can be used to investigate the vapor transport induced by airflow, and has been applied in many engineering fields, such as geothermal engineering [26, 27], drying engineering [8] and environmental engineering [17, 24] and so on. However, no particular attention has been paid to examining the advective effect on evaporation. This chapter aims to investigate the advective effect on evaporation by using the newly developed model in Chap. 4. In the following sections, the field experiment in the Badain Jaran Desert is used to calibrate the model. In Sect. 5.3, the advective effect on the evaporation is examined by analyzing driving forces and conductivities. Discussion and conclusions are presented in Sect. 5.4.

5.2 Field Application

The field experiment was conducted at one flat dune foot in the Badain Jaran Desert (between $39°45'20''$ N to $39°47'27''$ N and $102°27'07''$ E to $102°28'58''$ E), in the northwest of the Alashan plateau in the western Inner Mongolia of China. The details on the field site and the observations made have been introduced by Zeng et al. [34]. To apply the proposed model in the field, boundary conditions and forcing field had to be defined.

5.2.1 Boundary Conditions

For this specific case, no ponding or surface runoff was considered. This means that the moisture flux out of the soil is always equal to evaporation minus precipitation.

$$q_m|_{z=0} = E - \rho_L P \tag{5.1}$$

where E (kg m^{-2} s^{-1}) is the evaporation rate; P (m s^{-1}) the precipitation rate. Considering the aerodynamic resistance and soil surface resistance to water vapor transfer from soil to atmosphere, the evaporation is expressed as [4]

$$E = \frac{\rho_{vs} - \rho_{va}}{r_a + r_s} \tag{5.2}$$

where ρ_{vs} (kg m^{-3}) is the water vapor density at the soil surface; ρ_{va} (kg m^{-3}) the atmospheric vapor density; r_s (s m^{-1}) the soil surface resistance to water vapor flow; and r_a(s m^{-1}) the aerodynamic resistance. Equation (5.1) forms the surface boundary condition for moisture transport. Without taking ponding and surface runoff into consideration, soil surface was open to the atmosphere and the measured atmospheric pressure was adopted as the surface boundary condition for dry air transport in the soil. The measured soil surface temperature was set as the boundary condition for heat transport.

   In the Badain Jaran Desert, according to Gates et al. [5], the thickness of unsaturated zone ranges from less than 1 m in interdune areas to approximately 400 m in large dunes. In this study, the length of the soil column was set to be 5 m. The bottom boundary condition for the moisture equation was free drainage (unit hydraulic head gradient). Considering the diurnal variation scale, the temperature gradient and the air pressure gradient at the bottom of the column were specified to be zero. A one-dimensional setting was adopted in this study, predominantly considering the vertical interactive process between the atmosphere and the soil [12]. The initial soil matric head and soil temperature were determined by interpolating the measured values at midnight on 12 June 2008 between measurement depths. The initial soil air pressure was set according to the daily average atmospheric pressure during the selected 6 days period.

5.2.2 Meteorological Forcing Data

In terms of finding a balance between computational efficiency and solution accuracy, the time step was required to be small enough for the moisture content and temperature not to exceed prescribed limits [12]. This meant that the time step was adjusted automatically during computing (1 to 1800 s). Accordingly, the time interval of the meteorological inputs was adjusted to match each new time step. In this study, the Fourier transform method was used to approximate the frequency
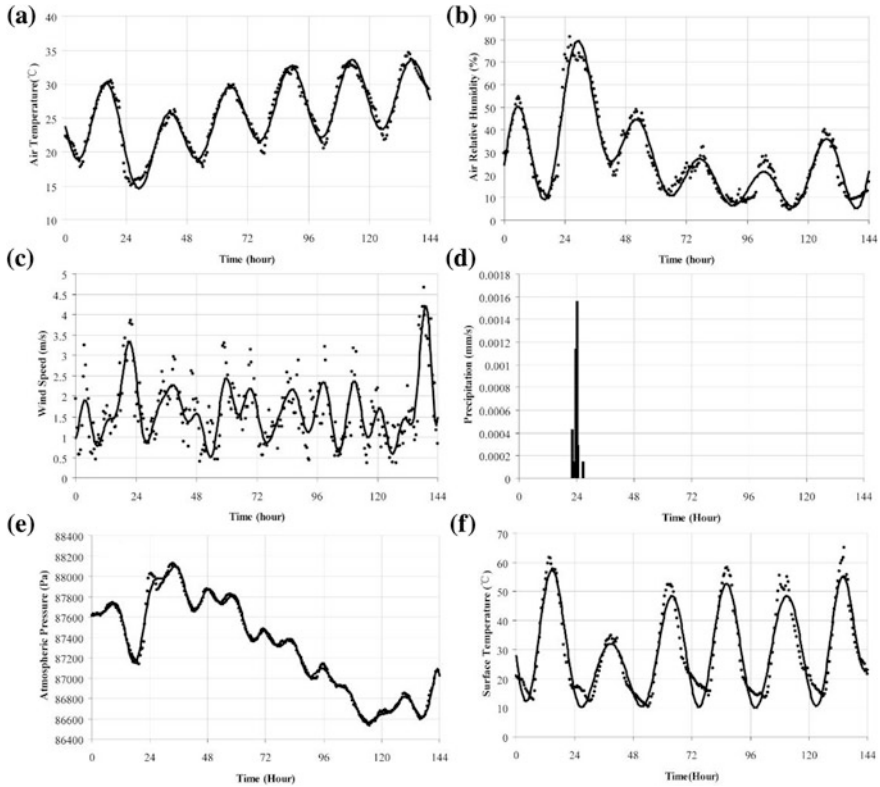
Fig. 5.1 Diurnal changes in meteorological variables: **a** air temperature, **b** relative humidity, **c** wind speed, **d** precipitation, **e** atmospheric pressure, and **f** surface temperature. They are recorded every 30 min from 13 to 19 June, 2008. The solid *line* is the approximation and the *dot* is the measurement

domain representation of the meteorological forcing data, and to reproduce the forcing data continuously.

Figure 5.1 shows the measurement and the approximation of meteorological variables, including air temperature, relative humidity, wind speed, precipitation, atmospheric pressure, and soil surface temperature (Fig. 5.1a–f), measured in the Badain Jaran Desert at a height of 2 m above the soil surface, and at 30 min intervals. The 6 days data were chosen to include a rainfall event at the end of the first day of the selected period. Except for wind speed data fluctuating irregularly because of inherent randomness, the records of other variables showed clearly typical diurnal behavior.

Figure 5.1a shows that the average air temperature was 24.3 °C 1 day before the rainfall and 20.4 °C 1 day after. From that day on, the average air temperature increased to 28.7 °C at the end of the selected period. As can be seen in Fig. 5.1b, the average daily relative humidity was 0.31 before and 0.51 after rainfalls,

followed by a 3 days gradual decrease to 0.14, with a slight increase on the final day to 0.21. As is seen in Fig. 5.1e, the atmospheric pressure followed the same variation pattern as the relative humidity did. The daily average atmospheric pressure was 87528.8 Pa before and 87907.2 Pa after the precipitation. From the second day onwards, the average atmospheric pressure first decreased to 86791.3 Pa on the fifth day, and then increased again to 86753.21 Pa on the last day.

Following van de Griend and Owe [29], the aerodynamic resistance (r_a) and soil surface resistance (r_s) was expressed as

$$r_a = \frac{1}{k^2 U} \left[\ln \left(\frac{z_m - d - z_{om}}{z_{om}} \right) - \psi_{sm} \right] \left[\ln \left(\frac{z_m - d - z_{oh}}{z_{oh}} \right) - \psi_{sh} \right],$$

$$r_s = r_{sl} e^{a(\theta_{\text{Min}} - \theta_{sur})}$$

(5.3)

where k is the von Karman constant (=0.41); U (m s^{-1}) the measured wind speed at certain height; Z_m (m) the height of wind-speed measurement; d (m) the zero plane displacement (=0 for bare soil); Z_{om} (=0.001 m) the surface roughness length for momentum flux; ψ_{sm} the atmospheric stability correction factor for momentum flux; Z_{oh} (=0.001 m) the surface roughness length for heat flux; ψ_{sh} the atmospheric stability correction factor for heat flux; r_{sl}(=10 s m^{-1}) the resistance to molecular diffusion across the water surface itself; a (=35.63) the fitted parameter; θ_{Min}(=0.15 m^{-3} m^3) the empirical minimum value above which the soil is able to deliver vapor at a potential rate; and θ_{sur} the soil water content in the topsoil layer.

5.2.3 Model Validation

The field measurements of soil moisture and temperature described by Zeng et al. [34], were used to validate the proposed model. The soil temperature was measured at depths of 2, 5, 10, 20 and 50 cm by soil temperature profile sensor (STP01, Hukseflux Thermal Sensors B.V., Delft, the Netherlands). According to Fig. 5.2, there was reasonably good agreement between simulated and measured soil temperatures at different depths. The simulation matched the diurnal variations on most days. The underestimation occurring at 2 cm depth during the whole simulation period should partially be attributed to the Fourier-transformed surface temperature in Fig. 5.1f. There were overestimations at other depths on some days. For example, overestimation occurred on day 1 at depths of 10, 20 and 50 cm, and on day 5 and 6 at depths of 10 and 20 cm. The simulations of temperature with and without considering airflow were compared in Fig. 5.2. At the selected depths, there is no large difference between the two models. The root mean square errors (RMSEs) between the simulation (considering airflow) and the measurement are 4.135, 3.047, 3.667, 3.559 and 1.532 °C at the depth of 2, 5, 10, 20 and 50 cm, respectively. For the simulation without considering airflow, the RMSEs are 4.131, 3.031, 3.572, 3.394 and 1.541 °C at the selected depths.
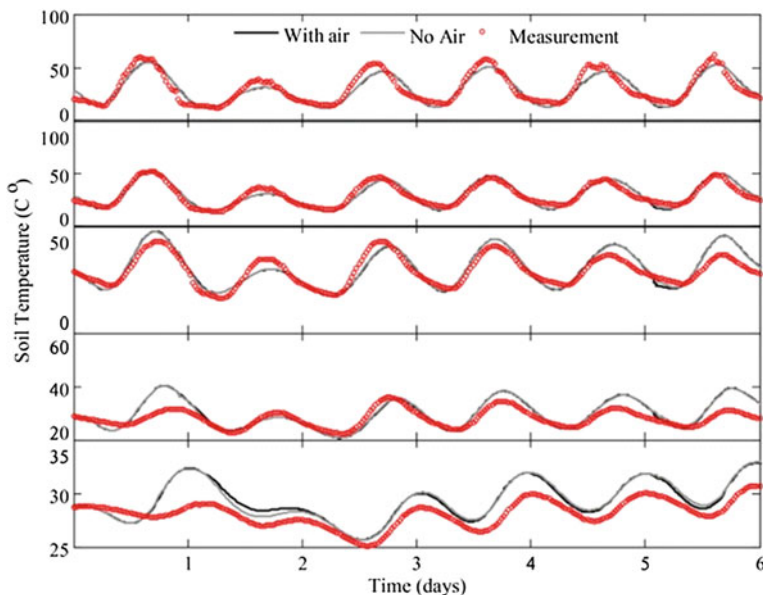
Fig. 5.2 Comparison between simulated (i.e., by model with and without considering airflow) and measured soil temperature during 13–19 June 2008, at selected depths: (*top* to *bottom*) 2, 5, 10, 20 and 50 cm. The solid *black line* is the simulation with airflow, the solid *grey line* is the simulation without airflow, and the *red open circle* is the measurement

The soil moisture was measured at a depth of 10, 20, 30, 40, and of 50 cm by soil water content profile sensor (EasyAG50, Sentek Pty. Ltd., Stepny, Australia). The quality of soil moisture measurement was quantitatively assessed and calibrated by Zeng et al. [34]. A major concern with measuring soil moisture in sand was the temperature effect. The temperature had an effect on readings of the moisture sensors of 14.4 % between 12 and 45 °C at 10 cm, of 13.9 % between 11 and 50 °C at 20 cm, of 14 % between 9 and 51 °C at 30 cm, of 13 % between 9 and 55 °C at 40 cm, and of 15 % between 8 and 55 °C at 50 cm. After calibration, the temperature effects at the depths of 10, 20, 30, 40, and 50 cm were reduced by 92, 93, 93.8, 88, and 82 %, respectively [34]. This ensured the quality of the measurements used to assess the model performance in simulating soil moisture variations.

While the temperature simulation was in close agreement with the measurements, the soil moisture simulation was not, except for the depths of 10 cm and 50 cm (Fig. 5.3). At a depth of 10 cm, the simulation captured the important trend, which was the response of soil moisture to the precipitation at the end of day 1. However, the measurements at depths 20, 30 and 40 cm did not follow the same trend as the simulation. HYDRUS1D [21] was also used to simulate soil moisture and temperature variations. Results of this showed that agreement between measured and modeled soil moisture content was not achieved throughout the profile [34]. It partially indicates that the parameters in soil hydraulic properties, assumed vertically homogeneous, are likely not correct. The low sensitivity of soil moisture sensor
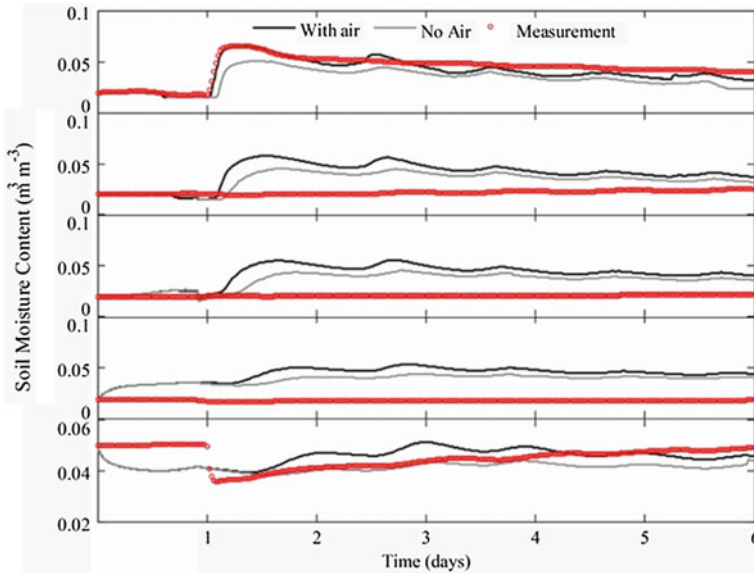
Fig. 5.3 Same as Fig. 5.2 but for soil moisture content at selected depths: (*top* to *bottom*) 10, 20, 30, 40 and 50 cm

in detecting moisture content in extremely dry environment [30] is another possible reason for the mismatch. Further investigation should be undertaken to quantify the heterogeneity of the sand at the field site.

Figure 5.3 shows also the simulation of soil water content without considering airflow. Compared to Fig. 5.2, the discrepancy between the two models in simulating soil water content is more obvious. The RMSEs between the simulated (considering airflow) and the measured volumetric soil water content are 0.0052, 0.0218, 0.0232, 0.0268 and 0.0051 $(m^{-3}\ m^3)$ at the depth of 10, 20, 30, 40 and 50 cm. For the simulation without considering airflow, the RMSEs are 0.0189, 0.0089, 0.0114, 0.018 and 0.0068 $(m^{-3}\ m^3)$ at the selected depths. Except for the depth of 20, 30 and 40 cm, the model considering airflow performs closer to the field measurement than without airflow. However, at these less-good-match depths, the model with airflow does have a much more sensitive response to the rainfall event than without considering airflow. Even at the depth of 50 cm, clear response to the rainfall event is shown by the model with airflow, while not by the model without considering airflow.

5.2.4 Comparisons with Evaporation Measurement

With boundary conditions and forcing data in place, the validated model was used to determine the surface evaporative flux, a crucial parameter subsequently affecting the atmospheric modeling. The observed evaporative flux was calculated
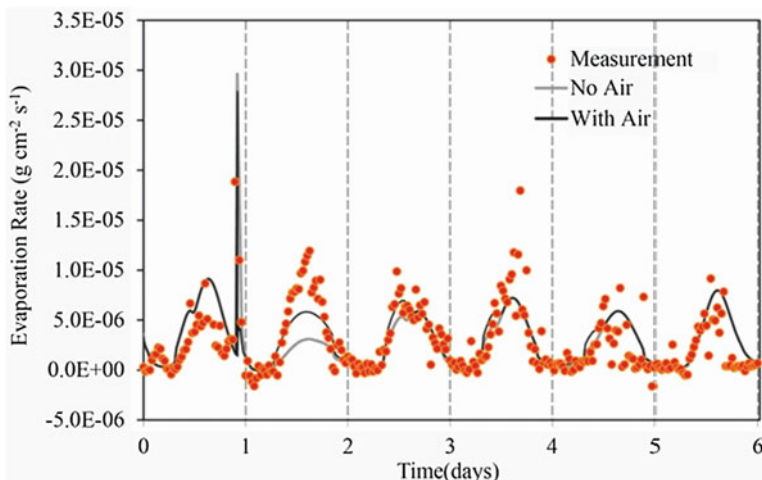
Fig. 5.4 Comparison between simulated evaporation rates and actual measurements from 13 to 19 June 2008

from the latent heat flux recorded by a three-dimensional eddy covariance system (Campbell Scientific, Inc., Logan, UT) installed 2 m above the surface. The system consisted of a CSAT3 three-dimensional sonic anemometer and a KH20 krypton hygrometer. The CSAT3 measured wind speed in three dimensions at a frequency of 10 Hz, and with the same frequency the KH20 measured vapor pressure. With the high frequency data from CSAT3 and KH20, the latent heat flux was obtained every 30 min. The sensible heat flux was also obtained by the eddy covariance system.

Figure 5.4 shows the comparison between evaporation rates, calculated by the proposed model and the model excluding airflow (e.g. PdV model), and the actual measurements. The normalized root mean squared deviation (NRMSD) was used to quantify the simulation's goodness of fit. NRMSD was expressed as percentage, where lower values indicated better agreement between simulation and measurement.

Except for the day immediately after rainfall (the second day), there was no large difference in the calculated evaporation rate, whether airflow was included or not. The NRMSDs for the selected simulation period were 13 and 14 % for the proposed model and the no-air model, respectively. However, if only the second day was taken into account, the NRMSD of the proposed model was 16 % and that of the no-air model 27 %. This meant that in this field case the proposed model did improve the simulation and made it come closer to reality than the no-air model did. The significant improvement seen on the second day was mainly attributed to the moist soil immediately after the rainfall event. During the rest of the simulation period, the topsoil layer dried up, diminishing the advantage of including the airflow mechanism.

5.3   Results and Analysis

The comparison between the proposed model and the PdV model in calculating surface evaporation indicates an advective effect. It implies that the neglect of soil airflow will cause an underestimation error in calculating evaporative flux (Fig. 5.4). To investigate the reason behind the advective effect, this section implemented a numerical experiment in both low- and high- permeability soils.

5.3.1   Advective Effect on Evaporation

With Eqs. (4.10), (4.13) and (4.15), the water flux in a two-phase heat and mass flow field can be identified as the isothermal flux, the thermal flux and the advective flux. With the exclusion or inclusion of thermal and advective fluxes, the thermal effect and advective effect on evaporation can be investigated. The thermal effect on evaporation has been studied in detail by Milly [10, 11] with linear and simulation analysis. However, in *Milly*'s analysis, the transport coefficient for adsorbed liquid flow due to the thermal gradient (D_{TD}) was not taken into account, although it was included in *Milly*'s formulation [9, 18]. We found that neglecting D_{TD} gives rise to errors in the calculated evaporation because of the intensive changes of the temperature gradient at the soil surface. The magnitude of order of the daily average evaporation was overestimated by about 2.3 % (results not shown here). The overestimation error deduced by neglecting D_{TD} occurs during the day because the soil was warming and hence the adsorbed liquid flow due to temperature gradient was directed downward. During the night, the evaporation is underestimated by neglecting D_{TD} but the error is negligibly small. For further understanding of the thermal effect on evaporation, readers are referred to *Milly*'s paper [10, 11].

According to the particle size distribution curve [34], the sand in the field was defined as fine sand, which means that K_s would be on the order of 10^{-6} to 10^{-3} cm s^{-1} [1]. In order to check the effect of K_s on the advective effect on evaporation, both high K_s (2×10^{-3} cm s^{-1}) and low K_s (7.87×10^{-4} cm s^{-1}) were used. The high K_s is determined by Soil Water Characteristics [23] with a bulk density of 1.67 g cm^{-3} and solid matter of 96 % sand and 2 % clay. The low K_s is calculated inversely by fitting the measurement of the soil water content at a depth of 20 cm. The r^2 for the regression of the prediction and observation of soil moisture is 0.66. For this purpose, the inverse solution of HYDRUS1D, version 4.09 (http://www.HYDRUS1D2d.com) was employed.

Figure 5.5 shows that neglecting the advective fluxes underestimate the diurnal evaporation. In the high-permeability soil, neglecting it leads to underestimation error in computed daily average evaporation (6-day period) on the order of 6.4 %. However, for the day right after the rainfall event (second day of the selected period), the underestimation error is high and reaches 33.3 %. As for the
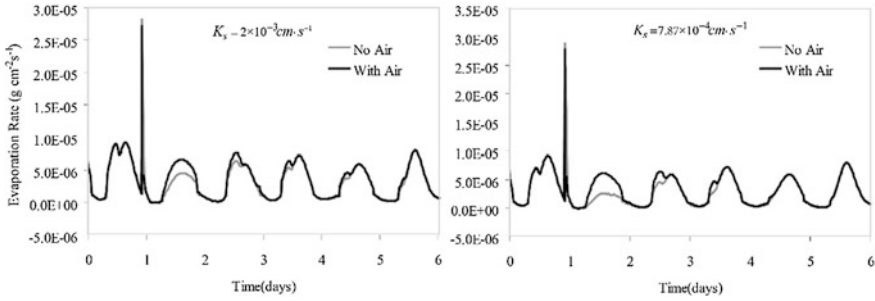
Fig. 5.5 Advective effects on the diurnal evaporation in both high- and low- permeability soil

low-permeability soil, the error induced by neglecting the advective flux in the daily average evaporation is 8.85 %, and the error in the diurnal evaporation on the second day reaches 53.3 %. The advective effect is much more evident in low permeability soil than in high permeability soil. High permeability leads to high soil air velocity. The diurnal average evaporation with airflow in high permeability soil at the second day is 3.35×10^{-6} g cm^{-2} s^{-1}, compared to 2.85×10^{-6} g cm^{-2} s^{-1} in low permeability soil. However, the high air velocity means the soil air pressure can equilibrate quickly with the atmospheric pressure, which will result in a small air pressure gradient in the soil. This is the reason that the advective effect is weaker in high permeability soil while strong in low permeability soil.

5.3.2 Driving Forces Considering Airflow

The strong or weak advective effect in different soils can be recognized by the soil air pressure head gradient field. Figure 5.6a, b show the scaled-color maps of the soil air pressure head gradient field (described positive upward) in both the high- and low-permeability soils. The diurnal variation patterns of soil air pressure head gradient in both soils are similar. In the shallow subsurface layer (from the surface to a depth of 20 cm), the gradient is downward during the day (roughly from 7:30 a.m. to 7:00 p.m.) and upward during the night (roughly from 7:00 p.m. to 7:30 a.m.). The fluctuation of pressure head gradient in the deeper soil (below a depth of 20 cm) follows the pattern in the shallow layer, albeit with a time delay and damped amplitude. At a depth of 50 cm, the fluctuation of the air pressure has a daily average time delay of 2 h. The maximum air pressure gradient damps from 2.5 cm (at the surface) to 0.71 cm in the high-permeability soil, and from 6.3 cm to 1.73 cm in the low-permeability soil. As seen in Fig. 5.6a, b, the amplitude of the air pressure head gradients in the high-permeability soil (-4.3 to 2.5 cm) is at least 2 times smaller than that in the low-permeability soil (-8 to 6.3 cm). This can be identified easily from the weak color contrast in Fig. 5.6a and the strong
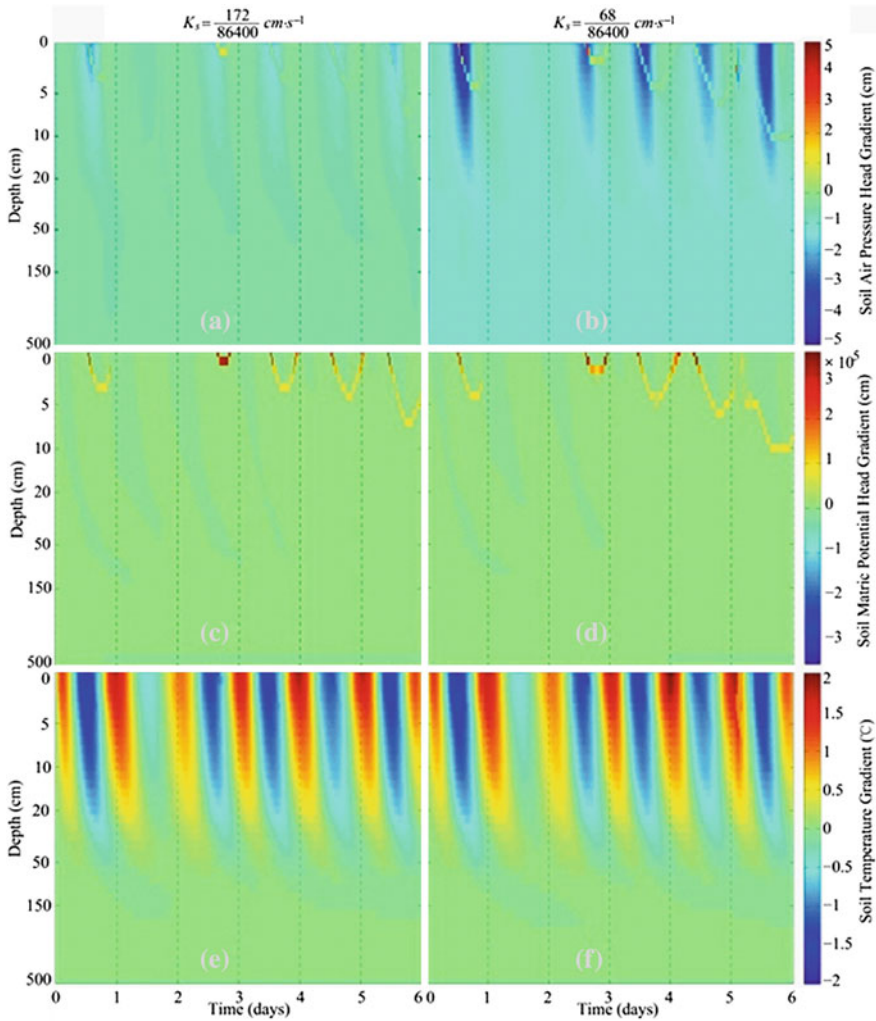
Fig. 5.6 Spatial and temporal distributions of **a**, **b** soil air pressure head gradient, **c**, **d** soil matric potential head gradient and **e**, **f** soil temperature gradient in both the high- and low- permeability soils when the airflow is considered

color contrast in Fig. 5.6b. This indicates that in the high-permeability soil the air pressure can equilibrate quickly with the atmospheric pressure, which minifies the air pressure head gradients and leads to a small advective effect. It follows the description that the higher the permeability, the lower the air pressure gradient is ([28], Fig. 4).

In Fig. 5.6a, b, there are embedded upward gradients presented at the surface around the middle of the selected days, except for the second day, which is right after the rainfall event. The embedded upward gradients propagate into the shallow

soil layer and vanish back to the surface near midnight. They actually correspond to the sharp upward matric potential head gradient induced by the drying of the shallow soil layer (7 cm thick in the high-permeability soil and 10 cm thick in the low permeability soil). Figure 5.6c, d show the same pattern of an embedded sharp upward gradient in the soil matric potential head gradient field as the air pressure head gradient field does.

The soil matric potential head gradient (described positive upward) in the soil layer above a depth of 50 cm varies diurnally, upward during the day and downward during the night. Below this layer, the gradient remains upward during the selected period. The fluctuation of the gradient has a time delay and damped amplitude. The strongest fluctuations in the shallow surface layer (7 cm thick in the high-permeability soil and 10 cm thick in the low-permeability soil) are 2–5 orders of magnitude larger than those in the layer below. The huge differences in gradient fluctuation between the shallow surface layer and the layer underneath it make the scaled color maps only visible for the sharp upward gradients induced by the drying of the shallow surface layer. The match in the embedded upward gradients between Fig. 5.6a–d implies a relationship between the matric potential and the soil air pressure expressed by Eq. (4.4). During the drying of the shallow surface layer, the matric potential drops dramatically (absolute value increases steeply) and minifies the soil air pressure (absolute value decreases).

Figure 5.6e, f show the scaled color maps of the soil temperature gradient field (described positive upward). There is no big difference in temperature gradient between the two soils. The fluctuation of the temperature gradient follows the general principle of downward during the day and upward during the night, with a time delay and damped amplitude. Below a depth of 50 cm, the soil temperature remains almost stable, and the soil temperature gradient is less than 0.1 $°C \ cm^{-1}$.

5.3.3 Comparison of Driving Forces and Conductivities

According to Fig. 5.5, it seems that the underestimation error of daily evaporation is due to the lack of upward advective fluxes during the day when the airflow is neglected. However, with the description of the diurnal variation of the soil air pressure gradient, which is downward during the day and upward during the night in the shallow soil layer (above a depth of 50 cm), it is evident that the underestimation error is not directly induced by the advective fluxes.

Considering the soil temperature gradient has a diurnal variation similar to the soil air pressure gradient, downward during the day and upward during the night, the soil matric potential gradient is the only driving force that can cause the underestimation error directly, which is upward during the day and downward during the night in the shallow soil layer (above the depth of 50 cm). Then, it seems as if the relatively lower evaporative flux is initiated by the lower upward

matric potential gradient, while the relatively higher evaporative flux is triggered by the higher upward matric potential gradient. Presumably, the upward matric potential gradient generated by including airflow should be greater than that generated by neglecting airflow because of the higher evaporative flux presented in the simulation including airflow.

This is not the case, however (as we can see in Figs. 5.7b, 5.9b). The upward potential gradient generated by neglecting airflow is larger than that generated by including airflow, which is the opposite of the presumption made above. There should be other factors contributing to the underestimation error, which may be the isothermal hydraulic conductivity and the isothermal vapor transport coefficient. Compensating the lower upward potential gradient, the isothermal hydraulic conductivity in the simulation considering airflow should be larger than that neglecting airflow, to have a relatively higher evaporative flux on the surface. Thus, the underestimation error induced by neglecting airflow can be demonstrated mechanically.

On the other hand, it is possible to have an indirect reason for the underestimation error. For instance, when neglecting airflow, the downward thermal liquid and vapor fluxes are much higher than those when including airflow, and thus suppress the evaporative flux on the surface, which causes the underestimation error. In the Sects. 5.3.3.1–5.3.3.3, the direct and indirect reasons will be analyzed through comparisons of the driving forces and the conductivities in different model runs.

5.3.3.1 Normalized Scale Index

In order to investigate and verify the above discussion, there is a need to compare the gradients (soil matric potential gradient and soil temperature gradient) and the conductivities (thermal and isothermal hydraulic conductivities and vapor transport coefficients) with and without considering soil airflow. The comparison is implemented with a normalized scale index, (NSI), which is calculated differently with respect to gradients and conductivity.

For the soil temperature gradient, the *NSI* is calculated as

$$NSI = Average(sum(GradDiff))$$

$$GradDiff = \pm \frac{Grad_{no\_air}}{Grad_{air}} \quad \begin{cases} +, \ Grad_{no\_air} \ \& \ Grad_{air} > 0 \\ -, \ Grad_{no\_air} \ \& \ Grad_{air} < 0 \end{cases} \quad (5.4)$$

where *GradDiff* is used to express the ratio of the gradient changed by neglecting airflow to that considering airflow. The *NSI* is the mean value of *GradDiff* at different depths during the selected period. $Grad_{air}$ and $Grad_{no\_air}$ are the gradients generated with and without considering airflow, respectively. *GradDiff* is only calculated when both $Grad_{air}$ and $Grad_{no\_air}$ are either positive or negative.
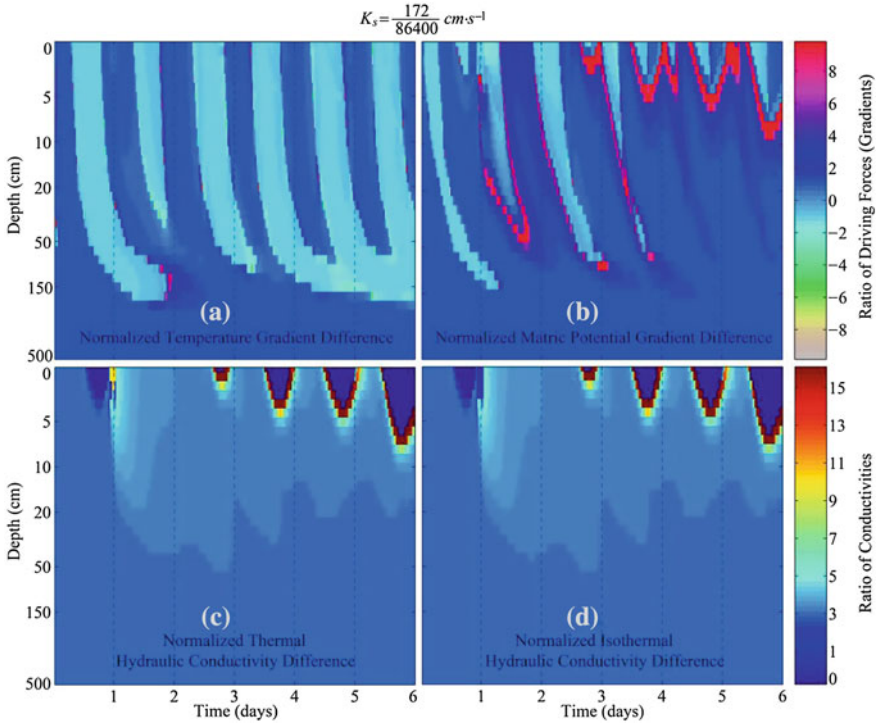
Fig. 5.7 Spatial and temporal distributions of ratios of **a** soil temperature gradient, **b** soil matric potential gradient, **c** thermal hydraulic conductivity and **d** isothermal hydraulic conductivity induced by neglecting soil airflow in the high-permeability soil

Thus, the summation of *GradDiff* can show if the upward gradient or the downward gradient is dominant. The sign before the ratio of $Grad_{no\_air}$ to $Grad_{air}$ indicates the direction of the gradient (positive upward). If the absolute value of *GradDiff* is less than 1, it means that the gradient induced by neglecting airflow is lower than that induced by including airflow, and vice versa.

For the conductivities, the *NSI* is calculated as

$$NSI = Average\,(sum(CondDiff)), \; CondDiff = \frac{Cond_{air}}{Cond_{no\_air}} \qquad (5.5)$$

where *CondDiff* is used to express the ratio of the conductivity changed by considering airflow to that neglecting airflow. $Cond_{air}$ and $Cond_{no\_air}$ are the conductivities with and without airflow, respectively. There is no positive or negative sign before the ratio of $Cond_{no\_air}$ to $Cond_{air}$, because the conductivity is always positive.

5.3.3.2 Comparison in the High-Permeability Soil

In the high-permeability soil, results are shown only for the comparison of the thermal and the isothermal hydraulic conductivity. The reason for not showing the comparison results for the vapor transport coefficients is that they only differed significantly during the rainfall event. In the rest of the simulation period, the average *NSI* (i.e. over the whole simulation period) for the isothermal vapor transport coefficient is only 0.97, which means the isothermal vapor transport coefficient with airflow is close to that without airflow. Note that the *NSI* is averaged over the whole simulation period. In the following discussion, without special notification, the averaged *NSI* means the *NSI* is averaged over time domain. Another reason for not comparing the isothermal vapor transport coefficient is its small order of magnitude (1×10^{-12}), which is at least 6 orders of magnitude smaller than the hydraulic conductivities and the thermal vapor transport coefficient. The thermal vapor transport coefficient is not shown due to its small deviation induced by neglecting airflow (average *NSI* = 1.002).

Figure 5.7a shows the diurnal variation of the soil temperature gradient difference induced by neglecting airflow in the high-permeability soil. The average *NSI* of the soil temperature gradient difference throughout the soil profile is 0.21. This indicates that the amplitude of the temperature gradient variation without airflow is lower than that with airflow (*NSI* is less than 1). When only the top surface layer is considered (0.25 cm thick), the larger temperature gradient in the simulation with airflow is much more evident, with an average *NSI* of 0.07. The top surface layer is set as 0.25 cm thick, which is accordant with the thickness of the top element in the discretization of the soil column. According to Eq. (5.4), the smaller the value of *NSI* (in the range of 0 to 1), the larger the temperature gradient with airflow is, compared to that without airflow. If only the day right after the rainfall event is selected, the difference between the temperature gradient is reduced with a larger average *NSI* of 0.29, because of the moist top surface layer. If only the period with a downward temperature gradient is selected, the average *NSI* is −0.21, which means that the downward temperature gradient with airflow is higher than that without airflow.

The comparison of the temperature gradient demonstrates that the possible indirect reason for the underestimation error (higher downward thermal fluxes in the simulation without airflow) can only be attributed to the thermal conductivity for liquid and vapor. However, the thermal vapor transport coefficient remains almost unchanged during the whole simulation period. The thermal hydraulic conductivity should be the key factor for the indirect reason. The thermal hydraulic conductivity with airflow should be smaller than that without airflow, and the magnitude of the difference between them should be larger than the difference between soil temperature gradients in order to have a higher downward thermal flux to suppress the evaporation. This is not the case, however, (as can be seen in Figs. 5.8d and 5.10d). A detailed demonstration is as follows.
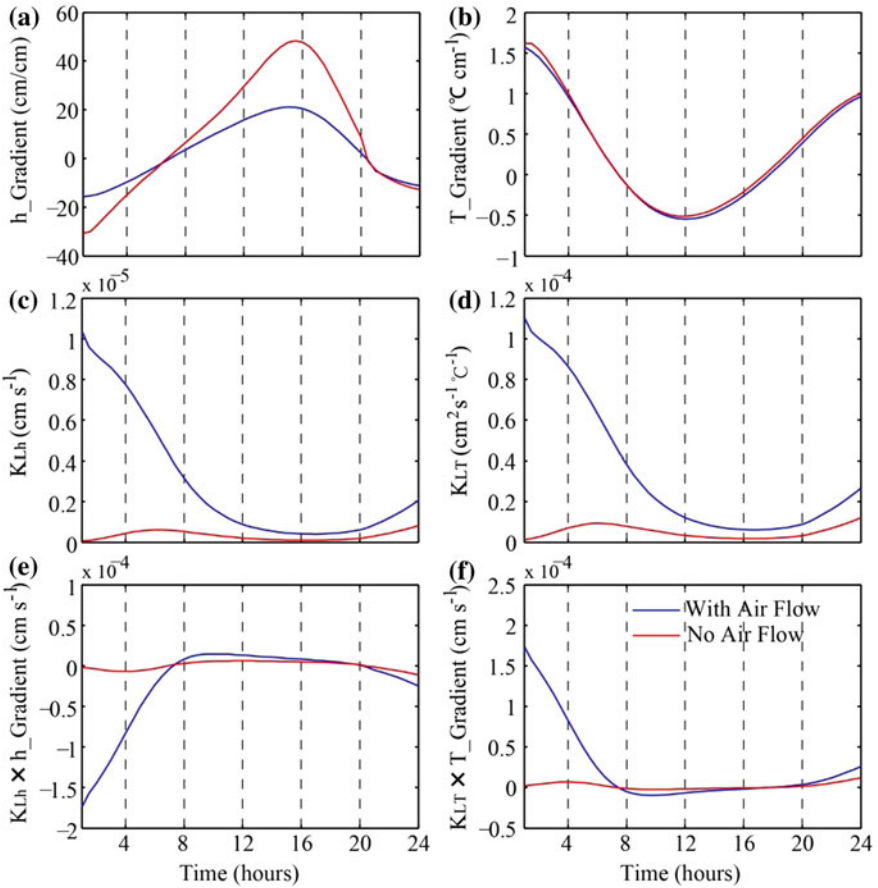
Fig. 5.8 The comparison of gradients and conductivities in the *top* surface layer on the day right after rainfall for the high-permeability soil

Figure 5.7c shows the diurnal variation of the thermal hydraulic conductivity difference induced by neglecting airflow. It is easy to identify that the variation pattern is in agreement with the sharp variation of the soil matric potential (Fig. 5.6c). Because of the extreme low soil matric potential (absolute value is extremely large) in the shallow surface layer during drying, the conductivity in the top layer is equal to zero (dark blue zones in Fig. 5.7c), which means no thermal liquid flow in the top layer during the corresponding period occupied by dark blue zones. There is no dark blue zone in the day right after rainfall. This is also true for the isothermal hydraulic conductivity (Fig. 5.7d). This partially explains the most significant advective effect (or underestimation error) occurring on the second day.

During the second day, in the top surface layer, the average *NSI* of the thermal hydraulic conductivity is 3.6, and the average *NSI* of the isothermal hydraulic conductivity is 4.3. According to Eq. (5.5), this means that K_{LT} and K_{Lh} with airflow

are 3.6 and 4.3 times larger than those without airflow, respectively. This validates the direct reason assumed for the underestimation error, and invalidates the indirect reason. The isothermal hydraulic conductivity in the simulation including airflow does be over that neglecting airflow, as the beginning of Sect. 5.3.3 assumed. However, with the downward temperature gradient (day) in mind (no large difference in temperature gradient as Figs. 5.7a, 5.8b show), the higher thermal hydraulic conductivity in the simulation including airflow can induce higher downward thermal fluxes than that neglecting airflow, which is the opposite of the assumed indirect reason for the underestimation error. This invalidates the indirect reason for the underestimation error. The underestimation error should be mainly attributed to the combined effect between the isothermal hydraulic conductivity and the soil matric potential gradient, as discussed at the beginning of Sect. 5.3.3.

Figure 5.7b shows the diurnal variation of the soil matric potential gradient difference induced by neglecting airflow. With the above analysis in mind, only the second day is selected. In the top surface layer, the average *NSI* is 2.13, the maximum *NSI* is 7.8 and the minimum *NSI* is -1.4. This denotes that the average soil matric potential gradient in the surface layer without airflow is 2.13 times larger, on average, than that with airflow, which means that the isothermal hydraulic conductivity with airflow should be larger than that without airflow, in order to have a higher evaporative flux on the surface, which is exactly the case, as Fig. 5.8c and the *NSI* index of conductivity show.

Figure 5.8 shows a comparison of gradients, conductivities, and the products of the two in the top surface layer on the second day of the selected period for the high-permeability soil. It is clear that the upward matric potential gradient without airflow is higher than that with airflow (Fig. 5.8a); the downward temperature gradient is slightly higher when the airflow is considered (Fig. 5.8b), and the isothermal and thermal hydraulic conductivities with airflow are much higher than those without airflow (Fig. 5.8c, d). Then the products of the gradients and conductivities produce the isothermal liquid flux and the thermal liquid flux (Fig. 5.8e, f). After comparing Fig. 5.8e to Fig. 5.5a, it is evident that only the isothermal liquid flux can contribute directly to the advective effect on evaporation.

5.3.3.3 Comparison in the Low-Permeability Soil

Figure 5.9 shows that the variation pattern of the differences in driving forces and conductivities induced by neglecting airflow in the low-permeability soil is similar to that in the high-permeability soil. The average *NSI* of the soil temperature gradient difference is 0.18 throughout the profile for the selected period. For the day right after the rainfall event, the average *NSI* becomes 0.32 for the profile. When only the downward temperature gradient is considered, the average *NSI* for the profile is -0.11 in the day. If only the top surface layer (0.25 cm thick) is selected, the average *NSI* is -0.848 in the day. Compared to the high-permeability soil, the temperature gradient difference is much smaller in the low-permeability

$$K_s = \frac{172}{86400}\, cm\cdot s^{-1}$$
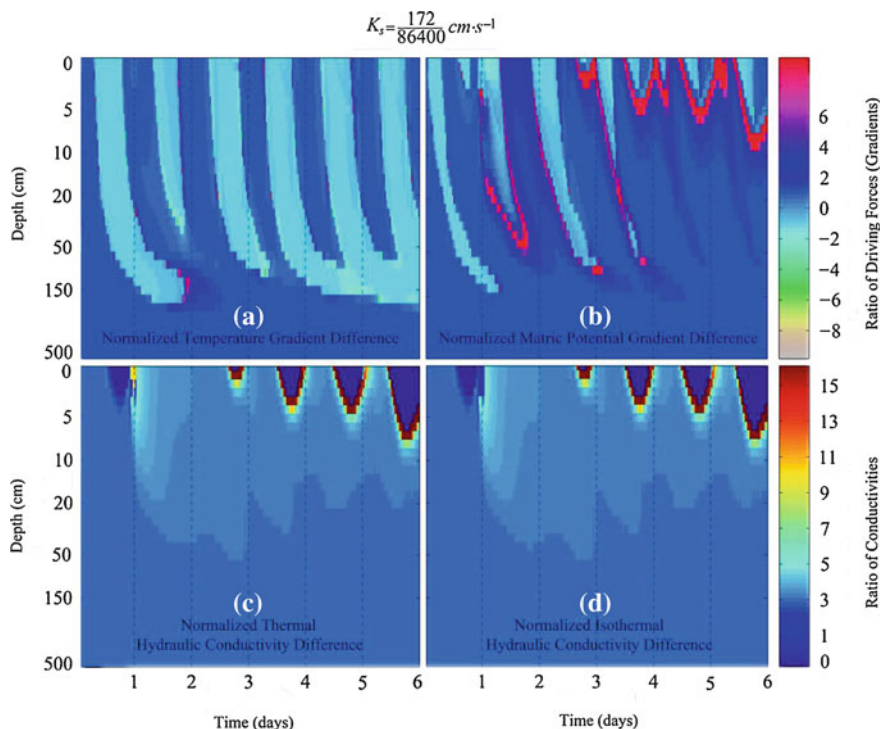
Fig. 5.9 The same as Fig. 5.7, but for the low-permeability soil

soil, especially for the top surface layer (Fig. 5.9a). The downward temperature gradient with airflow remains higher than that without airflow (Fig. 5.10b), which produces no change in the pattern of the thermal liquid fluxes (Fig. 5.10f), compared to that in the high-permeability soil (Fig. 5.8f).

In the top surface layer, the thermal hydraulic conductivity without airflow (Fig. 5.10d) remains almost unchanged compared to that with airflow. This is also true for the isothermal hydraulic conductivity (Fig. 5.10c). The difference (between with and without airflow) in the thermal hydraulic conductivity in the low permeability soil (Fig. 5.9c, *NSI* = 38.8) is about 10 times higher than that in the high permeability soil (Fig. 5.7c, *NSI* = 3.6). Likewise, the isothermal hydraulic conductivity difference in the low permeability (Fig. 5.9d, *NSI* = 57.2) is also much higher than that in the high permeability soil (Fig. 5.7d, *NSI* = 4.3).

Compared to the pattern in Fig. 5.8e (the high-permeability soil), the pattern of the isothermal liquid flux in the low-permeability soil (Fig. 5.10e) doesn't change, despite of that the soil matric potential gradient without airflow is much higher than that with airflow (Figs. 5.9b and 5.10a, *NSI* = 24.1). This also indicates the dominant role the isothermal liquid flux plays in the advective effect on evaporation.
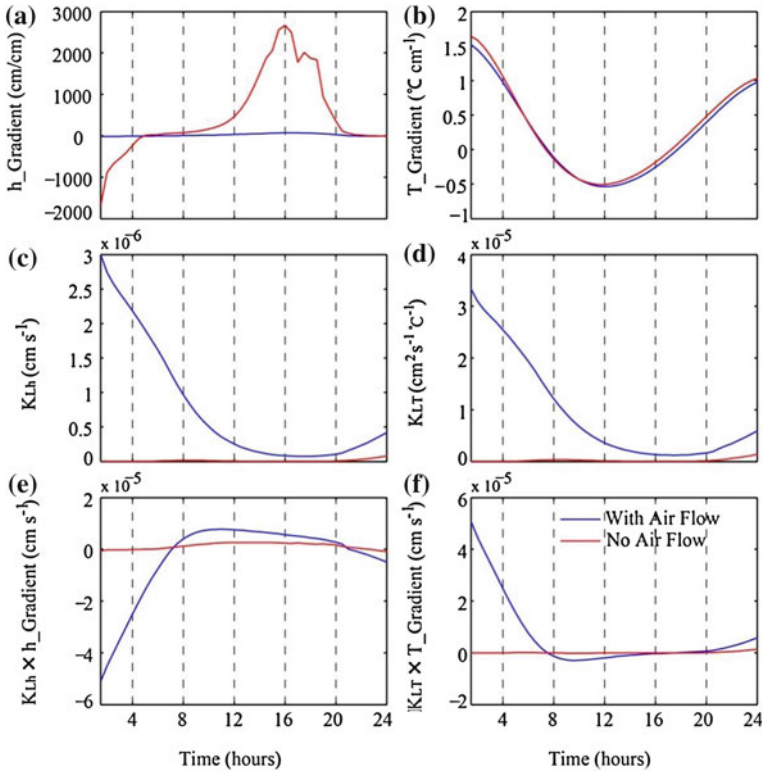
Fig. 5.10 The same as Fig. 5.8, but for the low permeability soil

5.4 Brief Summary

The proposed model was applied to investigate a field experiment, in which soil
moisture, temperature and evaporation rate were measured. With the boundary
conditions and the atmospheric forcing, the model generated good agreement
between simulated and measured soil temperature. However, the comparison with
measured soil moisture indicated that the parameters in soil hydraulic properties,
assumed vertically homogeneous, were likely not correct. Further investigation is
needed to quantify the heterogeneity of the sand in the field site. The comparison
between the measured and the simulated evaporation rates, by both the proposed
model and the no-air model, demonstrated that the proposed model did improve
the simulation of evaporation and made it come closer to reality. The comparison
between the PdV model and the proposed model indicates an underestimation error
in calculating surface evaporative flux when neglecting airflow, which can be
described as the advective effect on evaporation.

   To explore the mechanism behind the advective effect on evaporation, the
chapter implemented a numerical experiment in both the high- and low-

permeability soils. Neglecting the soil airflow can cause an underestimation of evaporation by 8.85 % in the low-permeability soil, and 6.4 % in the high-permeability soil. The most noticeable underestimation error occurred in the day right after the rainfall event. In the day, the underestimation error is 33.3 % in the high-permeability soil, and 53.3 % in the low-permeability soil. In the rest of the selected period, because of the drying of the shallow surface layer, the soil matric potential is extremely low and makes the hydraulic conductivity equal to zero, which subsequently leads to an insignificant advective effect on evaporation. The advective effect is much more evident in the low-permeability soil than in the high-permeability soil. The high permeability leads to high soil air velocity. However, the high air velocity means that the soil air pressure can equilibrate quickly with the atmospheric pressure, which will result in small air pressure head gradient in the soil.

The analysis of the gradient fields (Fig. 5.6) in the simulation with airflow showed that the soil matric potential gradient should be the direct driving force for the underestimation error induced by neglecting airflow. Considering the soil temperature gradient is downward during the day, it was thought to be the possible indirect driving force for the error. The downward thermal flux is possibly higher in the simulation neglecting airflow than that considering airflow, which suppresses the evaporative flux on the surface. After comparing the gradient fields and the conductivity fields (Figs. 5.7 and 5.9), the indirect reason for the underestimation error was excluded. The underestimation error induced by neglecting airflow is mainly attributed to the isothermal liquid flux, because of the upward soil matric potential gradient during the day.

However, the soil matric potential gradient is still not the direct driving force for the underestimation error. The difference of the hydraulic conductivity induced by neglecting airflow is the key to explaining the error. When the airflow is neglected, the isothermal hydraulic conductivity is reduced tremendously. In the top surface layer, it is reduced 4.3 and 57.2 times in the high- and low-permeability soils, respectively. This is further supported by the fact that even when the soil matric potential gradient in the top surface layer increases by a large amount after neglecting airflow (it was increased 2.13 and 24.1 times in the high- and low-permeability soils, respectively), the upward isothermal liquid flux is still lower than that when considering airflow (Figs. 5.8 and 5.10e). This discussion also explains why the advective effect is more evident in the low-permeability soil.

The sharp decrease of the isothermal hydraulic conductivity due to the lack of airflow can be explained by the absence of downward advective fluxes. During the day, the soil air pressure gradient is downward, which directs the advective liquid and vapor flux downward, as Fig. 5.11 shows. Although the magnitude of the advective flux is at least 3 orders less than those of the thermal and isothermal liquid fluxes, the downward advective fluxes still can moisten the top surface layer and thus increase the hydraulic conductivity. When the airflow is neglected, the lack of downward advective fluxes in the top surface layer makes the hydraulic conductivity almost stable during the day, especially in the low-permeability soil (Figs. 5.8c and 5.10c). The small spike in the fluctuation of the advective flux in
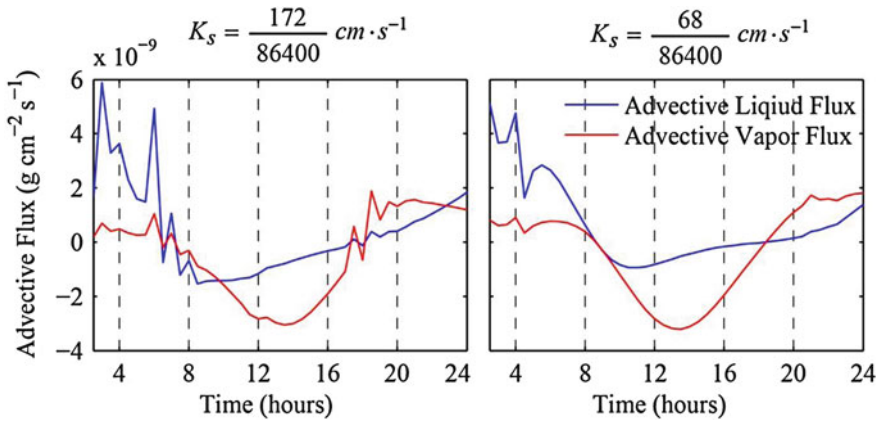
Fig. 5.11 The advective liquid and vapor fluxes in the *top* surface layer on the day right after rainfall for the high- and low-permeability soil

the top surface layer is partially due to the strong variation of the soil matric potential gradient, which subsequently affects the soil air pressure gradient at the surface and is partially due to the atmospheric pressure variation and the unstable wind speed at the surface.

From this discussion, the advective effect on evaporation is dominant in the low-permeability soil, while it is relatively insignificant in the high permeability soil. The advective effect on evaporation is reflected by the underestimation error induced by neglecting airflow. It indicates that when the soil was very dry (e.g. desert sand) the enhanced vapor transfer induced by the air pressure gradient can increase the hydraulic conductivity tremendously, and thus indirectly causes the high upward isothermal liquid flux. This fact denotes that the vapor transfer can be enhanced not only by the temperature gradient but also by the air pressure gradient. The simulation analysis was based on the field measurement in a desert, and more analysis should be conducted with a wider range of soil wetness, soil materials, and weather conditions and so on. Last but not least, the vapor transfer can be enhanced further when a solute in the soil water is considered [31]. Future studies should be conducted that include the solute effect on evaporation using a two-phase flow approach.

References

1. Bear J (1972) Dynamics of fluid in porous media. Dover, New York
2. Bittelli M, Ventura F, Campbell GS, Snyder RL, Gallegati F, Pisa PR (2008) Coupling of heat, water vapor, and liquid water fluxes to compute evaporation in bare soils. J Hydrol 362(3–4):191–205
3. Cahill AT, Parlange MB (1998) On water vapor transport in field soils. Water Resour Res 34(4):731–739

4. Camillo PJ, Gurney RJ (1986) A resistance parameter for bare-soil evaporation models. Soil Sci 141(2):95–105

5. Gates JB, Edmunds W, Ma J, Scanlon BR (2008) Estimating groundwater recharge in a cold desert environment in northern China using chloride. Hydrogeol J 16(5):893–910

6. Hillel D (2004) Introduction to environmental soil physics. Elsevier Academic Press, Amsterdam

7. Kobayashi T, He WJ, Nagai H (1998) Mechanisms of evaporation from soil with a dry surface. Hydrol Process 12(13–14):2185–2191

8. Kowalski SJ (2008) RandD in thermo-hydro-mechanical aspect of drying. Drying Technol 26(3):258–259

9. Milly PCD (1982) Moisture and heat transport in hysteretic, inhomogeneous porous media: A matric head-based formulation and a numerical model. Water Resour Res 18(3):489–498

10. Milly PCD (1984) A linear analysis of thermal effects on evaporation from soil. Water Resour Res 20(8):1075–1085

11. Milly PCD (1984) A simulation analysis of thermal effects on evaporation from soil. Water Resour Res 20(8):1087–1098

12. Milly PCD, Eagleson PS (1980) The coupled transport of water and heat in a vertical soil column under atmospheric excitation. Massachusetts Institute of Technology, Department of Civil Engineering, Ralph M. Parsons Laboratory for Water Resources and Hydrodynamics

13. Olivella S, Gens A (2000) Vapor transport in low permeability unsaturated soils with capillary effects. Transp Porous Media 40(2):219–241

14. Parlange MB, Cahill AT, Nielsen DR, Hopmans JW, Wendroth O (1998) Review of heat and water movement in field soils. Soil and Tillage Res 47:5–10

15. Philip JR, de Vries DA (1957) Moisture movement in porous materials under temperature gradient. Trans Am Geophys Union 38(2):222–232

16. Prat M (2002) Recent advances in pore-scale models for drying of porous media. Chem Eng J 86(1–2):153–164

17. Pruess K (2004) The TOUGH codes: a family of simulation tools for multiphase flow and transport processes in permeable media. VZJ 3(3):738–746

18. Prunty L (2009) Thermo mechanical theory of capillary soil water. Soil Sci Soc Am J 73(2):494–500

19. Rose CW (1968) Water transport in soil with a daily temperature wave I. Theory and experiment. Aust J Soil Res 6:31–44

20. Rose CW (1968) Water transport in soil with a daily temperature wave II. Analysis. Aust J Soil Res 6:45–57

21. Saito H, Simunek J, Mohanty BP (2006) Numerical analysis of coupled water, vapor, and heat transport in the vadose zone. Vadose Zone J 5(2):784–800

22. Sakai M, Toride N, Simunek J (2009) Water and vapor movement with condensation and evaporation in a sandy column. Soil Sci Soc Am J 73(3):707–717

23. Saxton KE, Rawls WJ (2006) Soil water characteristic estimates by texture and organic matter for hydrologic solutions. Soil Sci Soc Am J 70(5):1569–1578

24. Schrefler BA (2004) Multiphase flow in deforming porous material. Int J Numer Meth Eng 60(1):27–50

25. Shokri N, Lehmann P, Or D (2009) Critical evaluation of enhancement factors for vapor transport through unsaturated porous media. Water Resour Res 45:W10433

26. Thomas HR, Sansom MR (1995) Fully coupled analysis of heat, moisture, and air transfer in unsaturated soil. J Eng Mech 121(3):392–405

27. Thomas HR, He Y, Onofrei C (1998) Examination of the validation of a model of the hydro/thermo/mechanical behaviour of engineered clay barriers. Int J Numer Anal Meth Geomech 22(1):49–71

28. Tillman FD, Smith JA (2005) Site characteristics controlling airflow in the shallow unsaturated zone in response to atmospheric pressure changes. Environ Eng Sci 22(1):25–37

29. van de Griend AA, Owe M (1994) Bare soil surface resistance to evaporation by vapor diffusion under semiarid conditions. Water Resour Res 30(2):181–188

30. Vereecken H, Huisman J, Bogena H, Vanderborght J, Vrugt J, Hopmans J (2008) On the value of soil moisture measurements in vadose zone hydrology: A review. Water Resour Res 44:W00D06
31. Webb SW, CK Ho (1998) Review of enhanced vapor diffusion in porous media. Sandia National Laboratories SAND-98-1819C, Albuquerque, USA
32. Yiotis AG, Boudouvis AG, Stubos AK, Tsimpanogiannis IN, Yortsos YC (2004) Effect of liquid films on the drying of porous media. AIChE J 50(11):2721–2737
33. Yiotis AG, Stubos AK, Boudouvis AG, Tsimpanogiannis IN, Yortsos YC (2005) Pore-network modeling of isothermal drying in porous media. Transp Porous Media 58(1–2):63–86
34. Zeng Y, Wan L, Su Z, Saito H, Huang K, Wang X (2009) Dirnal soil water dynamics in the shallow vadose zone. Environ Geol 58:11–23

Chapter 6
Impact of Model Physics on Retrieving Soil Moisture and Soil Temperature

6.1 Introduction

6.1.1 Reviews of Previous Work

Recent efforts to determine an optimal soil moisture (or wetness) product for the initialization of the land surface component of global weather and climate forecast models have found that the transferability of soil moisture from one land surface model to another is not straightforward [1–3]. This nontransferability is exemplified in that even when land surface models (LSMs) are driven by identical atmospheric forcing data, large differences exist between the soil moisture products generated by the different LSMs [4]. This large diversity in LSMs has been an acknowledged problem since 1992, when the World Climate Research Programme (WCRP) launched the Project for the Intercomparison of Land-surface Parameterization Schemes [5, 6].

To understand the large diversity, PILPS Phase 1 and 2 investigated the physical self-consistency of LSMs. The results showed that model-generated soil moisture is sensitive to the choice of soil hydraulic properties [7], the initialization and the model scheme [8], and the arbitrary specification of soil depth [9]. In the following PILPS Phases, a multimode land surface model (CHAmeleon Surface Model (CHASM) [10]) was developed to investigate the impact of land-surface parameterization complexity on the simulation of land-surface climates by atmospheric models. Investigation of the impact of parameter calibration on model simulations revealed that a complex representation of land surface processes in atmospheric models is preferred to a simple one with tunable parameters, despite

better performance of the latter [11]. The major reason the complex model is preferred, is attributed to its more physics-based parameterizations. Desborough [10] shows that the models with more complex physics contain substantial geographic and daily functionality not present in the simpler model.

Research by Kato et al. [12] on the relationship between complexity and model performance highlights the importance of calibrating LSMs and improving their physics in order to increase the accuracy of simulated soil state variables. Their results are identical to those stated by Desborough [10]. However, it is appropriate to note that the relationship between complexity and model performance is not straightforward [13]. Although more complex LSMs do improve simulations of soil state variables [14–22], higher complexity does not always lead to increased accuracy in simulations [23, 24]. Increased complexity may cause decreased model-performance on an annual time scale, while being recognized as essential for realistic land surface behavior on shorter time scales [25]. Most LSMs used in atmospheric circulation and numerical weather prediction are simplifications of the coupled heat and mass transfer models in the soil, essential to reflect the impacts of the actual amount of soil moisture and energy on agriculture system, hydrology system, regional and global climate system etc. [26].

6.1.2 Motivation

The inherent vertical coupling strength (e.g. the relationship between the upper layer soil moisture and the deeper profile soil moisture) in LSMs determines how accurately the observed surface information (ground-based or satellite data) can be propagated into deeper soil layers in the land data assimilation system [32]. When facing operational efforts to assimilate remotely sensed observation, the LDAS typically simplifies or avoids a number of key complexities in land-surface processes [33]. In terms of the assimilation of soil moisture and soil temperature, the most common simplification is the decoupling of concurrent flow of water and heat in soil. The simplification constrains the coupling between the heat and moisture solely through the heat capacity of the soil and through the influence of moisture on thermal conductivity [34].

Since Milly [35] used a simple linear reservoir model and the thermal inertia, to correlate soil heat and moisture diffusion in the soil, one-dimensional soil heat and moisture diffusion model has been widely used in data assimilation system (hereafter DAS) [34, 36–38]. On the other hand, the development of land surface models (LSMs), addressing the coupled heat and mass transfer process in the soil, has been ongoing for decades [27, 28, 29–31], and shows promising improvement in providing good estimates of soil state variable profiles and surface energy balance components from bare soils.

The LSMs considering the coupled process [31] perform better over the simplified models [34, 35] on the consideration of water vapor flux, which is crucial in

calculating evaporation that subsequently affects the atmospheric modeling. As can be seen in Chap. 5, neglecting airflow can lead to the underestimation error of 33–53 % on the day immediately after a rainfall event. This highlights the necessity of checking how soil airflow can affect LSMs' performance in a DAS. Nevertheless, there is little literature discussing the inclusion of airflow mechanisms in LSMs to retrieve soil moisture and temperature profiles simultaneously in a DAS.

6.1.3 Focus of Chapter

With the above-mentioned concerns, the focus of this chapter is to check the feasibility of retrieving soil state variable profiles in an ensemble-based DAS, considering soil airflow, and to evaluate how different model complexities can affect the model performance in a DAS. This chapter employs three models with gradually-increased complexities: one-dimensional soil moisture and heat diffusion model (hereafter DM), DM including vapor transport (hereafter DMV), and DMV considering airflow mechanism (hereafter DMVA). The data assimilation method considered here is the ensemble Kalman Filter (EnKF), which has been applied successfully in hydrological data assimilation [39, 40].

   This chapter is organized as follows: Sect. 6.2 presents how models with different complexities are related and the EnKF formulations; Sect. 6.3 introduces the field data, model calibration and the data assimilation setup. In addition, it introduces the determinations of the model error, observation error and the filter parameters; Sect. 6.4 analyzes and compares the data assimilation results from the three models; discussion and conclusions are drawn in Sect. 6.5.

6.2 Methodologies

6.2.1 Model Formulations

In this section, the continuity equations for liquid water, vapor, dry air and heat will be formulated individually; thus, combinations of different components can lead to DM, DMV, and DMVA. In this way, the gradually-increasing model complexities can be demonstrated clearly. The related parameterizations for the closure of the continuity equations were referred to Chap. 4. For the sake of the consistence in this chapter, part of the governing equation in Chap. 4 is reintroduced in this section.

6.2.1.1 Liquid Transfer

Soil water is present in a liquid and a gaseous phase, and following Milly [41], the total moisture balance is expressed as

$$\frac{\partial}{\partial t}(\rho_L \theta_L + \rho_V \theta_V) = -\frac{\partial}{\partial z}(q_L + q_V) \tag{6.1}$$

where ρ_L (kg m^{-3}) represents the density of liquid water; ρ_V (kg m^{-3}) the density of water vapor; θ_L (m^3 m^{-3}) the volumetric water content; z (m) the vertical space coordinate, positive upwards; θ_V (m^3 m^{-3}) the volumetric vapor content; q_L (kg m^{-2} s^{-1}) the liquid flux; and q_V (kg m^{-2} s^{-1}) the vapor flux. The liquid flux is expressed by a generalized form of Darcy's law

$$q_L = -\rho_L K \frac{\partial\left(\frac{h_w}{\gamma_w} + z\right)}{\partial z} \tag{6.2}$$

where h_w (Pa) is the pore-water pressure; γ_w (kg m^{-2} s^{-2}) the specific weight of water; and K (m s^{-1}) the unsaturated hydraulic conductivity. According to Groenevelt and Kay [42], the effect of the heat of wetting on the pressure field and the resulting flow is taken into account by Milly [41], which leads to an additional liquid flow term in Eq. (6.2) resulting in

$$q_L = -\rho_L K \frac{\partial\left(\frac{h_w}{\gamma_w} + z\right)}{\partial z} - \rho_L D_{TD} \frac{\partial T}{\partial z} \tag{6.3}$$

where D_{TD} (m^2 s^{-1} °C^{-1}) is the transport coefficient for adsorbed liquid flow due to temperature gradient; and T(°C) the temperature. According to the definition of capillary potential, h could be expressed as the difference between the pore-air pressure and the pore-water pressure [43–45]

$$h = \frac{h_w - P_g}{\gamma_w} \tag{6.4}$$

where h(m) is the capillary pressure head; and P_g (Pa) the pore-air pressure. Substituting Eqs. (6.4) into (6.3) yields

$$q_L = -\rho_L K \frac{\partial}{\partial z}\left(h + \frac{P_g}{\gamma_w} + z\right) - \rho_L D_{TD} \frac{\partial T}{\partial z} \tag{6.5}$$

Equation (6.5) can be rewritten [41] as

$$q_L = -\rho_L \left[\underbrace{K \frac{\partial}{\partial z}\left(h + \frac{P_g}{\gamma_w}\right)}_{q_{Lh}+q_{La}} + \underbrace{D_{TD}\frac{\partial T}{\partial z} + K}_{q_{LT}} \right] \tag{6.6}$$

in which q_{Lh} (kg m^{-2} s^{-1}) is the isothermal liquid flux; q_{LT} (kg m^{-2} s^{-1}) the thermal liquid flux; q_{La} (kg m^{-2} s^{-1}) ($= \rho_L \frac{K}{\gamma_w}\frac{\partial P_g}{\partial z} = K_{La}\frac{\partial P_g}{\partial z}$) the advective liquid flux due to air pressure gradient; K_{La}(s) the advective liquid transport coefficient.

6.2.1.2 Vapor Transfer

The vapor flux is expressed by a generalized form of Fick's law

$$q_V = -D_e \frac{\partial \rho_V}{\partial z} \tag{6.7}$$

where D_e (m^2 s^{-1}) is the molecular diffusivity of water vapor in soil. When dry air is considered, the vapor flow is assumed to be induced in three ways: firstly diffusive transfer, driven by a vapor pressure gradient (Eq. 6.7); secondly advective transfer, as part of the bulk flows of air ($\rho_V \frac{q_{aa}}{\rho_{da}}$); and thirdly dispersive transfer, due to longitudinal dispersivity ($-D_{vg}\frac{\partial \rho_V}{\partial z}$). Accordingly, Eq. (6.7) can be rewritten as

$$q_V = -\left[\underbrace{D_e \frac{\partial \rho_V}{\partial z}}_{Diffusion} - \underbrace{\rho_V \frac{q_{aa}}{\rho_{da}}}_{Advection} + \underbrace{\theta_V D_{vg}\frac{\partial \rho_V}{\partial z}}_{Dispersion} \right] \tag{6.8}$$

where q_{aa} (kg m^{-2} s^{-1}) is the advective dry air flux $\left(q_{aa} = -\rho_{da}K_g\frac{\partial P_g}{\partial z}\right)$; ρ_{da} (kg m^{-3}) the dry air density; D_{vg} (m^2 s^{-1}) the gas-phase longitudinal dispersion coefficient; and K_g the gas conductivity (m s^{-1}).

Considering vapor density to be a function of matric potential and temperature, the vapor flux can be divided into isothermal and thermal components. According to the chain rule for partial derivatives, the vapor flux in Eq. (6.8) could be rewritten using the three state variables as

$$\begin{aligned} q_V &= q_{Vh} + q_{VT} + q_{Va} \\ &= -\left[\left(D_e + \theta_V D_{vg}\right)\frac{\partial \rho_V}{\partial h}\frac{\partial h}{\partial z} + \left(D_e + \theta_V D_{vg}\right)\frac{\partial \rho_V}{\partial T}\frac{\partial T}{\partial z} + \rho_V K_g \frac{\partial P_g}{\partial z} \right] \end{aligned} \tag{6.9}$$

where q_{Vh} (kg m^{-2} s^{-1}) is the isothermal vapor flux; q_{VT} (kg m^{-2} s^{-1}) the thermal vapor flux; and q_{Va} (kg m^{-2} s^{-1}) the advective vapor flux.

Combining the governing equations for liquid water (Eq. 6.6) and vapor flow (Eq. 6.9) leads to the governing differential equation for moisture transfer:

$$
\begin{aligned}
\frac{\partial}{\partial t}(\rho_L \theta_L + \rho_V \theta_V) &= -\frac{\partial}{\partial z}(q_L + q_V) \\
&= -\frac{\partial}{\partial z}(q_{Lh} + q_{LT} + q_{La}) - \frac{\partial}{\partial z}(q_{Vh} + q_{VT} + q_{Va}) \\
&= \rho_L \frac{\partial}{\partial z}\left[K\left(\frac{\partial h}{\partial z} + 1\right) + D_{TD}\frac{\partial T}{\partial z} + \frac{K}{\gamma_w}\frac{\partial P_g}{\partial z}\right] \\
&\quad + \frac{\partial}{\partial z}\left[D_{vh}\frac{\partial h}{\partial z} + D_{vT}\frac{\partial T}{\partial z} + D_{va}\frac{\partial P_g}{\partial z}\right]
\end{aligned}
\tag{6.10}
$$

where

$$
D_{vh} = (D_e + \theta_V D_{Vg})\frac{\partial \rho_V}{\partial h}; \quad D_{va} = \rho_V K_g; \quad D_{vT} = (D_e + \theta_V D_{vg})\frac{\partial \rho_V}{\partial T}
$$

D_{vh} (kg m^{-2} s^{-1}) is the isothermal vapor conductivity; D_{vT} (kg m^{-1} s^{-1} $^\circ$C^{-1}) the thermal vapor diffusion coefficient; and D_{va} (s) the advective vapor transfer coefficient.

6.2.1.3 Dry Air Transport

Dry air transport in unsaturated soil is driven by two main gradients, the dry air concentration or density gradient and the air pressure gradient. The first one diffuses dry air in soil pores, while the second one causes advective flux of dry air. At the same time, the dispersive transfer of dry air should also be considered. In addition, to maintain mechanical and chemical equilibrium, a certain amount of dry air will dissolve into liquid according to Henry's law. Considering the above four effects, the balance equation for dry air may be presented [45] as

$$
\frac{\partial}{\partial t}[\epsilon \cdot \rho_{da}(S_a + H_c S_r)] = -\frac{\partial q_a}{\partial z}
\tag{6.11}
$$

and

$$
q_a = \underbrace{-D_e \frac{\partial \rho_{da}}{\partial z}}_{Diffusion} - \underbrace{\rho_{da} K_g \frac{\partial P_g}{\partial z}}_{Convection} - \underbrace{\theta_a D_{vg} \frac{\partial \rho_{da}}{\partial z}}_{Dispersion} + \underbrace{H_c \rho_{da} \frac{q_L}{\rho_L}}_{Dissolving}
\tag{6.12}
$$

where q_a (kg m^{-2} s^{-1}) is the dry air flux; and H_c (= 0.02 for air at 1 atm and 25 °C) Henry's constant; S_a (= $1 - S_r$) the degree of air saturation of soil; S_r (= θ_L/ϵ) the degree of saturation of soil; ϵ the porosity. In the RHS of Eq. (6.12), the first term depicts diffusive flux (Fick's law), the second term

advective flux (Darcy's law), the third dispersive flux (Fick's law), and the fourth advective flux due to dissolved air (Henry's law). Considering dry air density is a function of matric potential, temperature and air pressure, Eq. (6.12) could be rewritten with three state variables. Combining Eq. (6.12) with Eq. (6.11), the governing equation for dry air can be expressed as

$$
\begin{aligned}
\frac{\partial}{\partial t}[\epsilon \cdot \rho_{da}(S_a + H_c S_r)] &= -\frac{\partial}{\partial z}(q_{ah} + q_{aT} + q_{aa}) \\
&= \frac{\partial}{\partial z}\left[K_{ah}\frac{\partial h}{\partial z} + K_{aT}\frac{\partial T}{\partial z} + K_{aa}\frac{\partial P_g}{\partial z}\right] \\
&\quad + V_{ah}\frac{\partial h}{\partial z} + V_{aT}\frac{\partial T}{\partial z} + V_{aa}\frac{\partial P_g}{\partial z} + H_c\rho_{da}\frac{\partial K}{\partial z}
\end{aligned}
\tag{6.13}
$$

where q_{ah} (kg m^{-2} s^{-1}) is the isothermal air flux; q_{aT} (kg m^{-2} s^{-1}) the thermal air flux; q_{aa} (kg m^{-2} s^{-1}) the advective flux; and

$$
K_{ah} = (D_e + \theta_a D_{vg})\frac{\partial \rho_{da}}{\partial h} + H_c\rho_{da}K
$$

$$
K_{aT} = (D_e + \theta_a D_{vg})\frac{\partial \rho_{da}}{\partial T} + H_c\rho_{da}D_{TD}
$$

$$
K_{aa} = (D_e + \theta_a D_{vg})\frac{\partial \rho_{da}}{\partial P_g} + \rho_{da}\left(K_g + H_c\frac{K}{\gamma_w}\right)
$$

$$
V_{ah} = \left[K_g\frac{\partial P_g}{\partial z} - H_c\frac{q_L}{\rho_L}\right]X_{ah}
$$

$$
V_{aT} = \left[K_g\frac{\partial P_g}{\partial z} - H_c\frac{q_L}{\rho_L}\right]X_{aT}
$$

$$
V_{aa} = \left[K_g\frac{\partial P_g}{\partial z} - H_c\frac{q_L}{\rho_L}\right]X_{aa}
$$

where X_{ah}, X_{aT} and X_{aa} are introduced in Sect. 4.2.2.3.

6.2.1.4 Heat Transport

In the vadose zone, the mechanisms for energy transport include conduction and convection. The conductive heat transfer contains contributions from liquids, solids and gas. Conduction is the main mechanism for heat transfer in soil and contributes to the energy conservation by solids, liquids and air. Advective heat in soil is conveyed by liquid flux, vapor flux, and dry air flux. On the other hand, heat storage in soil includes the bulk volumetric heat content, the latent heat of vaporization and a source term associated with the exothermic process of wetting of a porous medium (integral heat of wetting) [46]. Accordingly, following the general approach by de Vries [46], the energy balance equation in unsaturated soil may be written as four parts

Solid: $\frac{\partial [\rho_s \theta_s c_s (T - T_r)]}{\partial t} = \frac{\partial}{\partial z}\left(\lambda_s \theta_s \frac{\partial T}{\partial z}\right)$

Liquid: $\frac{\partial [\rho_L \theta_L c_L (T - T_r)]}{\partial t} = \frac{\partial}{\partial z}\left(\lambda_L \theta_L \frac{\partial T}{\partial z}\right) - \frac{\partial}{\partial z}[q_L c_L \cdot (T - T_r)]$

Air and vapor:

$$\frac{\partial}{\partial t}\left[(\rho_{da} c_a + \rho_V c_V)\theta_g (T - T_r) + \rho_V L_0 \theta_g\right]$$
$$= \frac{\partial}{\partial z}\left(\lambda_g \theta_g \frac{\partial T}{\partial z}\right) - \frac{\partial}{\partial z}\{q_V (c_V \cdot (T - T_r) + L_0) + q_a c_a \cdot (T - T_r)\} \tag{6.14}$$

Heat of wetting: $H_w = -\rho_L W \frac{\partial \theta_L}{\partial t}$

where λ_s, λ_L and λ_g (w m^{-1} °C^{-1}) represent the thermal conductivities of solids, liquids and pore gas (= $\lambda_a + \lambda_V$) respectively; θ_s the volumetric content of solids in the soil; θ_g the volumetric content of gas (= $\theta_V = \theta_a$) in the soil; c_s, c_L, c_a and c_v (J kg^{-1} °C^{-1}) specific heat of solids, liquids, air and vapor, respectively; T_r (°C) the reference temperature; ρ_s (kg m^{-3}) the density of solids in the soil; L_0 (J kg^{-1}) the latent heat of vaporization of water at temperature T_r; and W (J kg^{-1}) the differential heat of wetting (the amount of heat released when a small amount of free water is added to the soil matrix). The latent heat of vaporization varies with T according to $L(T) = L_0 - (c_L - c_v)(T - T_r) \approx 2.501 \times 10^6 - 2369.2T$ [47]. In accordance with Eq. (6.14), the conservation equation for energy transfer in the soil is given as

$$\frac{\partial}{\partial t}\left[(\rho_s \theta_s c_s + \rho_L \theta_L c_L + \rho_{da} \theta_a c_a + \rho_V \theta_V c_V)(T - T_r) + \rho_V L_0 \theta_g\right]$$
$$- \rho_L W \frac{\partial \theta_L}{\partial t} = \frac{\partial}{\partial z}\left(\lambda_{eff} \frac{\partial T}{\partial z}\right) - \frac{\partial}{\partial z}[q_L c_L \cdot (T - T_r) \tag{6.15}$$
$$+ q_V (L_0 + c_V \cdot (T - T_r)) + q_a c_a \cdot (T - T_r)]$$

where λ_{eff} (W m^{-1} K^{-1}) is the effective thermal conductivity, combining the thermal conductivity of solid particles, liquid and dry air in the absence of flow.

6.2.2 DM and DMV

With the above continuity equations for liquid, vapor, dry air and heat, Eqs. (6.6, 6.9, 6.13) and (6.15) represent the most complex model physics included in DMVA. Subsequently, DM and DMV simplified from DMVA are described as follows.

6.2.2.1 DM

The one-dimensional soil moisture and heat diffusion equation [34] can be expressed by Eq. (6.6) neglecting q_{LT} and q_{La}, and by Eq. (6.15) neglecting the heat of wetting as well as air and vapor terms. The coupling strength between the soil moisture and heat in DM is the weakest, because they are only coupled through the heat capacity of the soil and the influence of moisture on thermal conductivity.

Neglecting q_{LT} and q_{La} from Eq. (6.6), the governing equation for liquid transport of DM can be expressed as

$$\frac{\partial(\rho_L\theta_L)}{\partial t} = -\frac{\partial q_{Lh}}{\partial z} = \rho_L\frac{\partial}{\partial z}\left[K\left(\frac{\partial h}{\partial z} + 1\right)\right] \tag{6.16}$$

and neglecting the differential heat of wetting as well as air and vapor terms, the governing equation for heat transport of DM becomes

$$\frac{\partial}{\partial t}[(\rho_s\theta_s c_s + \rho_L\theta c_L)(T - T_r)] = \frac{\partial}{\partial z}\left(\lambda_{eff}\frac{\partial T}{\partial z}\right) - \frac{\partial}{\partial z}[q_L c_L \cdot (T - T_r)] \tag{6.17}$$

6.2.2.2 DMV

In the DMV, the coupling strength between the soil moisture and heat is increased by considering vapor transport (Eq. 6.9), the heat of wetting and the vapor term in Eq. (6.15), as well as q_{LT} in Eq. (6.15). However, the part of vapor transport due to bulk flow of dry air (q_{Va}) is neglected. The governing equation for moisture of DMV can be given as

$$\begin{aligned}
\frac{\partial}{\partial t}(\rho_L\theta_L + \rho_V\theta_V) &= -\frac{\partial}{\partial z}(q_{Lh} + q_{LT}) - \frac{\partial}{\partial z}(q_{Vh} + q_{VT}) \\
&= \rho_L\frac{\partial}{\partial z}\left[K\left(\frac{\partial h}{\partial z} + 1\right) + D_{TD}\frac{\partial T}{\partial z}\right] + \frac{\partial}{\partial z}[D_{vh}\frac{\partial h}{\partial z} + D_{vT}\frac{\partial T}{\partial z}]
\end{aligned} \tag{6.18}$$

where the D_{vg} will be neglected in D_{vh} due to the absence of advective transfer (q_{Va}), which is the basis for the dispersive vapor transfer. Correspondingly, the governing equation for heat transport of DMV can be expressed as

$$\begin{aligned}
&\frac{\partial}{\partial t}[(\rho_s\theta_s c_s + \rho_L\theta_L c_L + \rho_V\theta_V c_V)(T - T_r) + \rho_V L_0\theta_g] - \rho_L W\frac{\partial\theta_L}{\partial t} \\
&= \frac{\partial}{\partial z}\left(\lambda_{eff}\frac{\partial T}{\partial z}\right) - \frac{\partial}{\partial z}[q_L c_L \cdot (T - T_r) + q_V(L_0 + c_V \cdot (T - T_r))]
\end{aligned} \tag{6.19}$$

6.2.3 Ensemble Transformation Kalman Filter (ETKF)

The ensemble Kalman filter (EnKF) is a sequential Monte Carlo method [48] that provides an alternative to the traditional Kalman Filter (KF) [49]. The EnKF is typically developed to overcome the infeasible manipulation of KF with relatively high-dimensional discrete systems (highly nonlinear system, e.g. two phase heat and mass transport in soil), in which it is not practical or possible to maintain the state error covariance matrix ($\mathbf{P}$) explicitly. The KF equations can be given as [50]:

$$\text{State variable update (analysis) : } \mathbf{x}^{\mathrm{a}} = \mathbf{x}^{\mathrm{f}} + \mathbf{K}(\mathbf{d} - \mathbf{H}\mathbf{x}^{\mathrm{f}}) \tag{6.20}$$

$$\text{State error covariance matrix : } \mathbf{P}^{\mathrm{a}} = (\mathbf{I} - \mathbf{K}\mathbf{H})\mathbf{P}^{\mathrm{f}} \tag{6.21}$$

(analysis error covariance matrix)

$$\text{Kalman gain factor : } \mathbf{K} = \mathbf{P}^{\mathrm{f}}\mathbf{H}^{\mathrm{T}}(\mathbf{H}\mathbf{P}^{\mathrm{f}}\mathbf{H}^{\mathrm{T}} + \mathbf{R})^{-1} \tag{6.22}$$

$\mathbf{x}^{\mathrm{a}}$ is the updated state vector (or the analysis), which is calculated by using the measurement (observation) vector ($\mathbf{d}$) and the estimated state vector (or the forecast, $\mathbf{x}^{\mathrm{f}}$). $\mathbf{H}$ is the operator that is used to relate the estimated state vector to the measurement vector (or mapping state vector space to observation space). $\mathbf{P}^{\mathrm{a}}$ is the updated (or the analysis) error covariance matrix, which is calculated by using the Kalman gain factor ($\mathbf{K}$) and the estimated (or the forecast) error covariance matrix ($\mathbf{x}^{\mathrm{f}}$). $\mathbf{R}$ is the observation error covariance matrix. The superscripts f and a denote forecast and analysis, respectively. Due to the explicit maintaining of $\mathbf{P}$ [Eqs. (6.20–6.22)], the KF is not feasible computationally for high-dimensional system [51]. Furthermore, the use of KF requires linearization of nonlinear system, which is not practical for our case (i.e. two phase heat and mass transport in soil). On the other hand, EnKF avoids evolving the state error covariance matrix, and the error covariance in EnKF is manipulated implicitly via an ensemble $\mathbf{X}$ of model states, $\mathbf{X} = [\mathbf{X}_1, \ldots, \mathbf{X}_{\mathrm{m}}]$, where m is the ensemble size. The error covariance matrix $\mathbf{X}$ is typically assumed to be carried by the ensemble and is given by Evensen [52] as

$$\mathbf{P} = \frac{1}{m-1}\sum_{i=1}^{m}(\mathbf{X}_i - \mathbf{x})(\mathbf{X}_i - \mathbf{x})^{\mathrm{T}} = \frac{1}{m-1}\mathbf{A}\mathbf{A}^{\mathrm{T}} \tag{6.23}$$

where $\mathbf{x}$ is the ensemble mean,

$$\mathbf{x} = \frac{1}{m}\sum_{i=1}^{m}\mathbf{X}_i \tag{6.24}$$

and $\mathbf{A} = [\mathbf{A}_1, \ldots, \mathbf{A}_{\mathrm{m}}]$ is the ensemble of anomalies, or perturbations, $\mathbf{A}_i = \mathbf{X}_i - \mathbf{x}$; and the model state is considered to be represented by the ensemble mean. Thus, the update of the state vector ($\mathbf{x}^a$) and the state error covariance ($\mathbf{P}^{\mathrm{a}}$) in KF [Eqs. (6.20) and (6.21)] is replaced by the update of the ensemble mean and the

ensemble of anomalies in EnKF. Accordingly, Sakov et al. [53] used a generic form to express the ensemble updates:

$$\text{Ensemble mean update}: \ \mathbf{x}^a - \mathbf{x}^f = \mathbf{A}^f \mathbf{G} \mathbf{s} \qquad (6.25)$$

where $\mathbf{s}$ is the scaled innovation vector, $\mathbf{s} = \mathbf{R}^{-1/2}(\mathbf{d} - \mathbf{H}\mathbf{x}^f)/\sqrt{m-1}$; $\mathbf{G}$ is an introduced matrix for simplicity, $\mathbf{G} = (\mathbf{I} + \mathbf{S}^T\mathbf{S})^{-1}\mathbf{S}^T$, where $\mathbf{S}$ is the scaled ensemble observation anomalies, $\mathbf{S} = \mathbf{R}^{-1/2}\mathbf{H}\mathbf{A}^f/\sqrt{m-1}$.

$$\text{Ensemble anomalies update}: \ \mathbf{A}^a - \mathbf{A}^f = \mathbf{A}^f \mathbf{T} \qquad (6.26)$$

Use of the traditional update of ensemble anomalies, $\mathbf{A}^a = \mathbf{A}^f + \mathbf{K}(\mathbf{D} - \mathbf{H}\mathbf{A}^f)$, with Eq. (6.23), results in an analysis error covariance $\mathbf{P}^a$ smaller than the KF analysis error covariance defined in Eq. (6.21). This will lead to an ensemble collapse with a too rapid reduction in ensemble spread [54, 55]. In order to make the resulting analysis error covariance matching the theoretical KF covariance in Eq. (6.21), $\mathbf{T}$ in Eq. (6.26) is developed as the transform matrix by Bishop et al. [56], $\mathbf{T} = (\mathbf{I} + \mathbf{S}^T\mathbf{S})^{-1/2} - \mathbf{I}$. This approach is called as ensemble transform Kalman filter and associated with the acronym ETKF, which actually has the flavor of the ensemble square root filter (ESRF) that allows a deterministic update of the ensemble anomalies [57]. Although a number of deterministic methods have been proposed for the same purpose of $\mathbf{T}$ in Eq. (6.26), the ETKF is chosen for its natural characteristics and its equivalency to other flavors of ESRF [55]. In order to implement the ETKF, the platform named as EnKF-Matlab (version 0.28) developed by Sakov (http://enkf.nersc.no/Code/EnKF-Matlab/) is applied because of its equivalency to the aforementioned development of EnKF.

6.3 Data Assimilation Setup

Considering this study is focused toward evaluating the impact of model physics on the retrieval of soil state variable profiles, only the vertical interactive process (point-scale) between the atmosphere and the soil is considered. The regional-scale and lateral processes in the atmosphere and the soil are beyond the scope of this study. The field data acquired from the Badain Jaran Desert is chosen for this study, because it implies strong soil/atmosphere coupling at the surface [58].

Firstly, with the field-observed meteorological forcing data and initial soil state variables, DM, DMV and DMVA are integrated without assimilating the observed truth (i.e. observed soil moisture and soil temperature). The model integration without assimilation is called the "open loop" integration, representing the best model estimation of the truth. Then, with a known set of perturbations on the forcing data, an ensemble integration of the model is conducted for DM, DMV and DMVA, respectively. Next, the ensemble mean and anomalies from the three

different ensemble integrations are updated by EnKF-Matlab. At last, the resulting assimilated estimates will be compared against the open loop estimates and the observed truth data.

6.3.1 Field Data

The details on the field site and the observations made have been introduced in Sect. 3.2. The Table 6.1 shows that the average air temperature was 24.29 °C 1 day before the rainfall and 20.49 °C 1 day after. From that day on, the average air temperature increased to 28.57 °C at the end of the selected period. The average daily relative humidity was 0.31 before and 0.51 after rainfalls, followed by a 3-days gradual decrease to 0.14, with a slight increase on the final day to 0.21. The daily average atmospheric pressure was 87530.3 Pa before and 87903.83 Pa after the precipitation. From the second day onwards, the average atmospheric pressure decreased to 86757.59 Pa on the last day. The 6 days-average maximum and minimum values of the variables were used to constrain the variation range of model state variables (i.e. soil moisture and soil temperature) and keep the solution of the governing equations stable. The 6-days averaged standard deviations were used to generate the perturbation on the meteorological forcing data.

6.3.2 Model Calibration

6.3.2.1 Numerical Setup

In the Badain Jaran Desert, according to Gates et al. [60], the thickness of unsaturated zone ranges from less than 1 m in inter-dune areas to approximately 400 m in high dunes. In this study, the length of the soil column was set to be 1 m. The bottom boundary condition for the moisture equation was free drainage (unit hydraulic head gradient). Considering the diurnal variation, the temperature gradient and the air pressure gradient at the bottom of the column were specified to be zero. A one-dimensional setting was adopted in this study, predominantly considering the vertical interactive process between the atmosphere and the soil [61]. The initial soil matric head and soil temperature were determined by interpolating the measured values at midnight on 12 June 2008 between measurement depths. The initial soil air pressure was set according to the daily averaged atmospheric pressure during the selected 6 days period.

For the 1 m soil column, the nodal spacing was determined automatically with a spacing factor, which led to 27 discretization nodes across the problem domain. The smallest nodal space of 0.25 cm lies in the top surface layer while the bottom layer has the biggest nodal space of 50 cm. A finite-difference time-stepping scheme was applied to evaluate the time derivatives, and solved by a successive

Table 6.1 The statistics of the meteorological variables

		Air pressure (Pa)	Surface temperature (°C)	Air temperature (°C)	Air relative humidity (%)	Wind speed (m s^{-1})
Standard deviation	1st day	199.15	15.76	3.92	14.46	0.77
	2nd day	143.10	7.64	4.03	20.15	0.44
	3rd day	182.27	13.81	3.98	12.95	0.57
	4th day	149.55	15.13	4.00	7.78	0.41
	5th day	178.12	13.67	4.14	5.33	0.56
	6th day	127.88	15.32	3.64	10.66	1.05
Mean	1st day	87530.30	33.67	24.29	31.21	1.76
	2nd day	87903.83	22.07	20.49	51.15	1.66
	3rd day	87642.27	28.59	24.45	27.01	1.61
	4th day	87240.30	30.65	27.11	16.73	1.49
	5th day	86789.74	30.37	27.88	14.15	1.58
	6th day	86757.59	31.67	28.57	21.39	1.84
Maximum	1st day	87789.84	57.30	30.16	53.43	3.33
	2nd day	88102.92	32.01	25.75	79.37	2.45
	3rd day	87874.99	48.43	29.64	44.60	2.43
	4th day	87457.50	52.56	32.58	27.17	2.16
	5th day	87087.41	48.41	33.60	21.45	2.36
	6th day	87086.93	55.21	33.57	35.96	4.21
Minimum	1st day	87147.63	12.24	18.93	9.28	0.79
	2nd day	87653.32	10.27	14.64	26.11	0.87
	3rd day	87361.15	10.44	18.97	11.07	0.50
	4th day	87016.03	10.27	21.67	6.55	0.87
	5th day	86558.23	9.98	22.13	6.08	0.64
	6th day	86616.95	10.58	23.34	5.30	0.59

iterative linearization scheme (See Chap. 4). The governing equations subject to the boundary and initial conditions were solved numerically by an in-house script with MATLAB (The Math-Works Inc., Natick, MA, Version 7.4).

6.3.2.2 Calibration Results

Considering this study is focused towards identifying the performance of model physics in retrieving soil state variables using data assimilation technique, one common set of calibrated model parameters is needed for all the three models (i.e. DM, DMV and DMVA). Although both soil moisture and soil temperature were measured from surface to a depth of 50 cm, only the soil moisture at the depth of 10 cm and the soil temperature at 2, 5, 10 and 20 cm were chosen for the calibration. The main reason of this was that the soil moisture and the soil temperature at other depths kept almost the same value during the selected period [59]. The average standard deviation of soil moisture content was 0.00163 m^3 m^{-3} for

Table 6.2 The common set of model parameters based on the calibration of DMVA

Soil hydraulic properties		Heat transport properties		Initial condition		
Parameter	Value	Parameter	Value	Depth (cm)	Soil temperature (°C)	Soil moisture $(m^3\ m^{-3})$
$K_s\ (m\ s^{-1})$	1.99E-05	c_s (J kg^{-1} $^{\circ}$C^{-1})	837	0	20.84	0.02
$\theta_{sat}\ (m^3\ m^{-3})$	0.382	c_L (J kg^{-1} $^{\circ}$C^{-1})	4186	2	20.92	0.02
$\theta_{res}\ (m^3\ m^{-3})$	0.015	c_V (J kg^{-1} $^{\circ}$C^{-1})	1870	5	24.49	0.021
$\alpha\ (m^{-1})$	3.610	c_a (J kg^{-1} $^{\circ}$C^{-1})	1005	10	28.17	0.023
n	0.00236	b_1 (W m^{-1} $^{\circ}$C^{-1})	0.228	20	28.83	0.025
ε	0.41	b_2 (W m^{-1} $^{\circ}$C^{-1})	2.406	50	28.73	0.052
$\rho_s\ (kg\ m^{-3})$	1670	b_3 (W m^{-1} $^{\circ}$C^{-1})	4.909	100	29	0.1
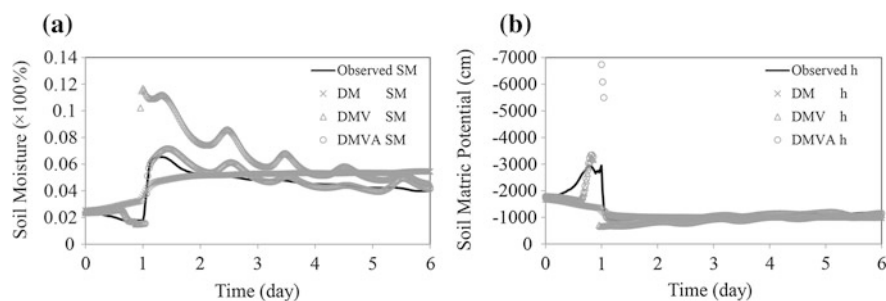
Fig. 6.1 Comparison between the observation and the simulation of soil moisture and matric potential head at the depth of 10 cm

the depths of 20, 30, 40 and 50 cm, and soil temperature 1.2 °C for the depth of 50 cm.

Chosen as the baseline model, DMVA is calibrated for determining the common set of model parameters (see Table 6.2), with which the simulated soil state variables of all three models were compared to the observation at the selected depths. Figure 6.1 shows the comparisons of soil moisture content (SM) and associated soil matric potential (h) at the depth of 10 cm. The DMVA has soil moisture RMSE of 0.0044 m^3 m^{-3}, DMV 0.0242 m^3 m^{-3}, and DM 0.0094 m^3 m^{-3}, respectively. The DMVA simulation is the best estimate of the observed soil moisture among the three models. The DM is the second best one to the observation. However, DM cannot capture the typical trend of soil moisture content variation after rainfalls as the DMVA and DMV do (Fig. 6.1).

The DMVA is the closest to the "natural" system among the three models, and the second close one is DMV, considering it captures the trends of soil moisture variation after rainfalls, which DM cannot. One note of caution, however, is appropriate here. Figure 6.1 does not imply that the more complex model physics
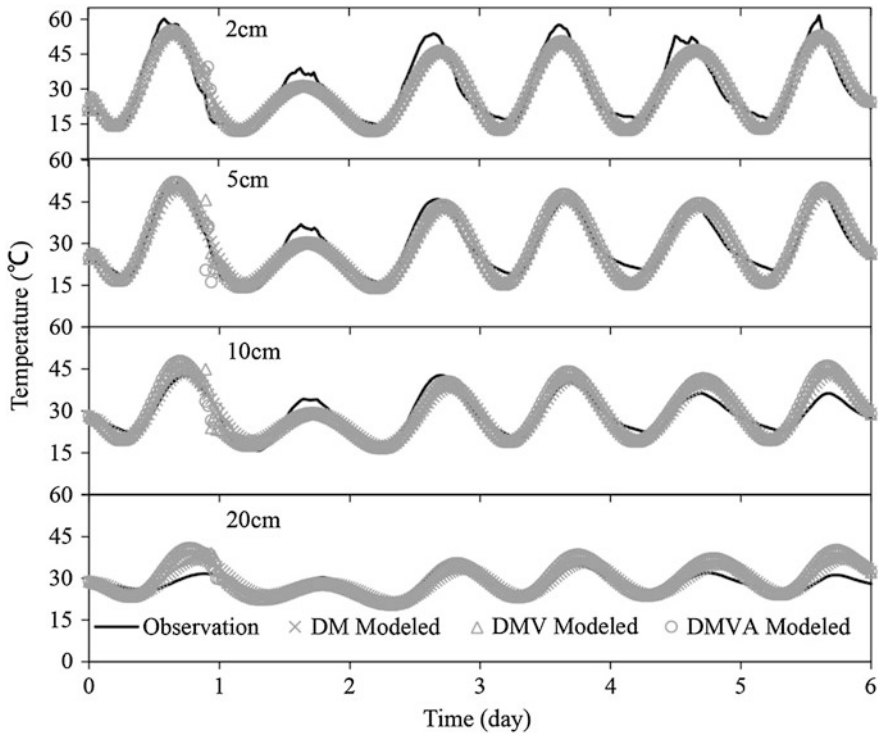
Fig. 6.2 Comparison for soil temperature

(e.g. DMVA) can perform better than the simple model physics (DMV and DM). The DMV and DM can also be calibrated with the observations to get two different sets of "behavioural" model parameters, the resulting model output of which can match observed data well. We did not calibrate DMV and DM tentatively. Thus, with the baseline model calibration, the DMVA can be considered as the most "correct" model, and then the DMV, and the DM the "poorest" physics model. The gradually-increased/decreased complexities models can be subsequently used to check the impact of complexity in model physics on retrieving soil state variables in the DAS.

Figure 6.2 shows the comparisons of modelled temperatures with the observation at the depth of 2, 5, 10 and 20 cm. Unlike the comparisons of soil moisture simulation, all three models performed similarly in reproducing soil temperature variations, except that the DMVA and the DMV were much more sensitive to the perturbation of rainfalls than the DM at the end of the first day. The averaged soil temperature RMSE at the depths of 2, 5, 10 and 20 cm were 4.79, 3.34, 3.85 and 4 °C for DMVA, 4.69, 3.29, 3.91 and 3.81 °C for DMV, and 4.89, 3.2, 3.16 and 2.5 °C for DM, respectively.

The accuracy of soil temperature simulation depends on the heat transport scheme and the coupling (with soil moisture) scheme used. There are three heat

transport scheme used widely in modern operational land surface models [62]: zero-storage, force-restore and heat conduction. The three models used the heat conduction scheme. According to Luo et al. [63], using the same heat transport scheme without considering the coupling scheme, the soil temperature simulation of different LSMs can achieve similar agreement with observation. In this case, although with different coupling scheme, the soil temperature simulation still performed similarly throughout the soil column. This was mainly attributed to the same heat transport scheme used and the extremely dry environment of the field site. In addition to the soil temperature RMSEs mentioned-above, the standard deviations of soil temperature in Table 6.4 (see Sect. 6.3.3.1) also indicated similar soil temperature simulations among the three models, except for the first day.

6.3.3 Filter Calibration

6.3.3.1 Model Error Estimation

The model error usually includes two parts [64]: parameter values that do not best represent the "natural" system, and model structure (or, model physics) that the chosen representation and coupling of physical processes is not capable of producing the natural system's behavior. Abramowitz [64] stated that the systematic error resulting from model physics limitations played a greater role in the inability to match observational data than the "bad" chosen behavioural parameter values. Considering the focus of this study is to check the performance of different model physics complexities in DAS, only the model error related to the model structure will be discussed here. According to *Reichle*'s studies, the model errors were accounted for the uncertainties in the forcing data [39, 65]. Therefore, the 6 days averaged standard deviations of the meteorological variables (Table 6.2) were used to detect the model error and listed in Table 6.3. They were used to perturb the meteorological forcing data for generating ensemble integrations of the three models. The 6-days averaged values were adopted with the consideration of that the daily variation of the forcing data affected the soil/atmosphere interaction.

6.3.3.2 Observation Error Estimation

The observation error includes measurement errors that can be specified according to the knowledge of instrumental characteristics and representation errors that cannot be well represented in model space [66]. The quality of soil moisture and soil temperature measurements was quantitatively assessed and calibrated by Zeng et al. [59], the observation bias of which were removed from the observed values before entering the EnKF-Matlab. Thus, the determination of observation error is concerned with the estimation of representation errors, which are often called representativeness errors (RE) [67]. RE represents any physical processes

Table 6.3 Averaged 6-days standard deviations of the meteorological forcing data (model error)

	Air pressure (Pa)	Surface temperature (°C)	Air temperature (°C)	Air relative humidity (%)	Wind speed (m s^{-1})	Precipitation (m s^{-1})
Standard deviation	163.34	13.55	3.95	11.89	0.63	6.77E-08

appearing in the observations but not in the model [68]. Accordingly, the observation error can be described as the differences between the model simulations (open loop) and observations, and be expressed as the standard deviations of the differences:

$$Diff_i = V_{sim\_i} - V_{obs\_i}, i = 1, \ldots, nstep, SD(Diff_{1,\ldots,nstep}) = \sqrt{\frac{\sum_{i=1}^{nstep} (Diff_i - \overline{Diff})^2}{nstep - 1}}$$

(6.27)

where $Diff_i$ is the model deviation at time step i; V_{sim_i} and V_{obs_i} the simulated and observed soil state variables (i.e. soil temperature and soil moisture); $n\ step$ the total time step for the model integration; and SD the standard deviation.

Table 6.4 lists the daily standard deviation of soil moisture and soil temperature at the selected depths during the simulation period. Considering that the soil matric potential is the independent state variable, the soil moisture was expressed as the soil matric potential head at the depth of 10 cm. The standard deviations of soil temperatures were averaged across the depths and over the simulation period for different models. The standard deviations of soil matric potential heads were only averaged daily for different models with one selected observation depth. The last row and column indicate the daily averages over all the three models and each model's 6-days averages, respectively. Although the DMVA simulation is the best estimate of the observed soil moisture among the three models while DM is the worst estimate (Fig. 6.1), DM has the smallest 6-days averaged standard deviation of soil matric potential heads among the three simulations.

In the second part of Table 6.4, the standard deviation of 6-days soil temperature averaged over all the three models at the depth of 2, 5, 10 and 20 cm, were 4.52, 3.14, 3.1 and 2.32 °C, respectively. The standard deviations of 6-days soil temperature averaged across all the selected depths for each model were 3.05 °C for DM, 3.36 °C for DMV and 3.4 °C for DMVA. The standard deviations averaged over all the three models were considered having fair error parameters for all the applied models in DAS. For those averaged over the simulation period and across the selected depths, the spatial and temporal characteristics of the standard deviations were considered. However, the spatial and temporal correlation of error parameters was not implemented in this study.

Table 6.4 Standard deviations of soil moisture (expressed as matric potential head) and soil temperature at the selected depths during the simulation period

|		Soil matric potential head (m^3 m^{-3}) at the depth of 10 cm						
		1st day	2nd day	3rd day	4th day	5th day	6th day	Average
DM		417.90	286.33	22.37	17.80	18.12	23.90	131.07
DMV		12552.00	341.28	35.33	31.01	27.53	25.63	2168.79
DMVA		6152.15	991.99	31.71	21.44	15.77	57.26	1211.72
Average		6374.02	539.87	29.80	23.42	20.47	35.60	1170.53
Soil temperature (°C)								
DM	2 cm	5.20	3.42	5.38	3.59	5.50	4.57	4.61
	5 cm	2.15	3.44	3.30	2.28	3.86	3.41	3.07
	10 cm	1.47	3.32	3.16	1.35	3.07	3.93	2.72
	20 cm	2.74	1.31	1.69	0.88	1.76	2.37	1.79
	Average	2.89	2.87	3.38	2.02	3.55	3.57	3.05
DMV	2 cm	4.99	3.24	5.14	3.36	5.32	4.39	4.41
	5 cm	2.45	2.95	2.88	2.86	3.91	3.67	3.12
	10 cm	3.99	2.78	2.38	2.25	3.61	4.95	3.33
	20 cm	5.58	1.04	1.05	1.79	2.48	3.50	2.57
	Average	4.25	2.50	2.86	2.56	3.83	4.13	3.36
DMVA	2 cm	5.65	3.27	5.13	3.40	5.32	4.40	4.53
	5 cm	3.01	3.07	2.84	2.85	3.86	3.69	3.22
	10 cm	3.75	2.68	2.30	2.29	3.53	4.98	3.26
	20 cm	5.81	0.84	1.08	1.86	2.46	3.54	2.60
	Average	4.56	2.47	2.84	2.60	3.79	4.15	3.40

6.3.3.3 Filter Parameters

The filter performance depends on the choice of model error, observation error and ensemble size. Ideally, the error parameters should be determined adaptively within the cycling assimilation system based on information from internal diagnostics such as the innovations [69], because the estimation of the error parameters outside of DAS (off-line) may well be different from the true error parameters that may be changing with time. However, we only aim to investigate the performance of different model physics complexities in the EnKF-Matlab for retrieving soil state variables. This does not critically depend on how complete the size of the forcing perturbations and the observation error are optimized.

Ensemble Size

In this study, we choose the averages of standard deviations of the meteorological variables as the perturbations on the forcing data. Thus, the calibration of error parameters was mainly implemented for the observation error. Before calibrating model and observation error parameters, initial error values should be assigned to

Fig. 6.3 Soil moisture and temperature RMSEs varied with different ensemble sizes. The RMSEs are calculated as the averaged RMSEs with respect to all three models
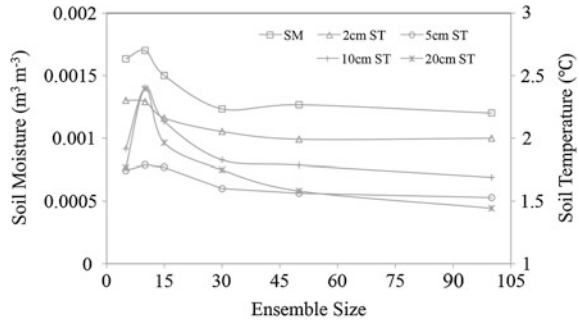
determine the ensemble size. With the model error listed in Table 6.3, the observation errors were initialized as 400 cm for soil matric potential head and 4 °C for soil temperature. The observed soil moisture and soil temperature were assimilated into DM, DMV and DMVA with ensemble sizes of 5, 10, 15, 30, 50 and 100. With respect to the three models, the averaged soil moisture and soil temperature RMSEs (i.e. the difference between the observation and its EnKF estimate) were compared with ensemble sizes in Fig. 6.3.

Figure 6.3 shows that the averaged RMSEs decreased and converged with increasing ensemble size. Although the soil temperatures at different depths converged toward different values, all the RMSEs (including soil moisture RMSE) did not decrease significantly further with the ensemble size bigger than 15. The standard deviations of RMSEs, with ensemble size of bigger than 15, were 3.3E-05 $m^3 \ m^{-3}$ for soil moisture, while 0.033, 0.036, 0.07 and 0.15 °C for soil temperature at the depth of 2, 5, 10 and 20 cm, respectively. Considering the trade-off between the computation cost and the RMSEs, the ensemble size was fixed as 15. The absolute difference between the soil moisture RMSEs produced by using 15 ensemble members and by using 30 ensemble members was 1.67E-04 $m^3 \ m^{-3}$; while it was 0.11, 0.17, 0.31 and 0.21 °C for soil temperature at the four selected depths, respectively.

Observation Error-Pairs

With different soil moisture and soil temperature observation error-pairs, the assimilation estimates can vary around the measurement truth. With each error-pair, the soil moisture and soil temperature RMSEs (i.e. difference between the assimilation estimates and the observation truth) was averaged over all the three models. To detect how the assimilation estimates vary with different error-pairs, the observation errors of the soil moisture (expressed as the soil matric potential head) were set as 400, 900, 1600 and 2500 cm, while the soil temperature 4, 9, 16 and 25 °C. The error-pairs and associated RMSEs were listed in Table 6.5. The smallest soil moisture RMSE of 0.0014 ($m^3 \ m^{-3}$) was associated with the smallest soil moisture observation error (expressed as the soil matric potential head of

Table 6.5 Averaged (over the three models) soil moisture and soil temperature RMSEs obtained with different combinations of observation errors

| Soil matric potential head observation error (cm)		Soil temperature observation error (°C)			
		4	9	16	25
400	SM ($m^3\ m^{-3}$)	0.0015	0.0014	0.0016	0.0016
	ST (°C)	1.7659	2.0911	2.0924	2.5227
900	SM ($m^3\ m^{-3}$)	0.0018	0.0019	0.0022	0.0018
	ST (°C)	2.0742	2.4659	2.7441	3.1940
1600	SM ($m^3\ m^{-3}$)	0.0023	0.0027	0.0022	0.0021
	ST (°C)	2.1869	2.5000	2.6659	2.9869
2500	SM ($m^3\ m^{-3}$)	0.0027	0.0026	0.0026	0.0026
	ST (°C)	1.7516	2.5484	2.6659	3.0477
1440000	SM ($m^3\ m^{-3}$)	0.01250	0.01303	0.01198	0.01167
	ST (°C)	1.72526	2.22777	2.80572	2.95674
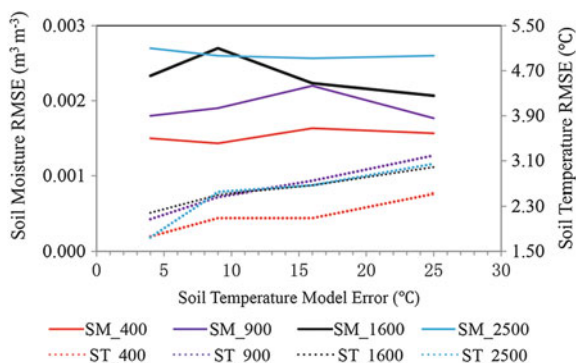
Fig. 6.4 The averaged (over the three models) soil moisture and temperature RMSE patterns under different error-pairs. SM represents soil moisture RMSE and ST soil temperature RMSE. SM_400 means the soil moisture observation error is 400 cm, and so on for SM_900, SM_1600 and SM_2500. The x-axis represents the soil temperature observation error

400 cm), while the smallest soil temperature RMSE of 1.725 °C was associated with the smallest soil temperature observation error. The RMSEs increased with increasing soil moisture and soil temperature observation errors.

As Fig. 6.4 shows, the bigger the soil moisture observation errors, the bigger the soil moisture RMSEs was produced, so did the soil temperature RMSEs. However, the impact of changing soil moisture observation error on the soil moisture RMSE was bigger than that of changing soil temperature observation error. The soil moisture RMSE for each observation error level was calculated as the averaged RMSE over all soil temperature observation error levels; while the soil temperature RMSE for each observation error level was calculated as the averaged RMSE over all soil moisture observation error levels.

The range of the soil moisture RMSE was 0.0011 $m^3 m^{-3}$, which was 73.3 % of the smallest soil moisture RMSE. For soil temperature, the RMSE range was 51.1 % of the smallest soil temperature RMSE. When the biggest soil moisture observation error was included, the percentage for soil moisture reached 702 %, while that for soil temperature kept almost the same (from 51.1 to 54.8 %). In this research, no fixed observation error was chosen. Instead, different observation error-pairs were used to examine the performance of all three models in assimilating soil moisture and soil temperature.

6.4 Results and Analysis

We first adopted all the observation information to check the performance of the three models in the EnKF-Matlab for the retrieval of soil moisture and soil temperature. Various temporal observation intervals were employed to check the impact of sparse observation on the performance. With the increasing temporal observation interval, how the assimilation estimates from different model physics mime the diurnal variation of the measurement can be checked. We also examined the assimilation estimates with reduced observation points (e.g. instead of using all soil temperature measurement at four selected depths, only the soil temperature observation at the depth of 2 cm was used). Furthermore, considering soil moisture is much more sensitive and problematic than soil temperature due to the highly nonlinear representativeness of its governing equations, we tested the performance of different model physics in the EnKF-Matlab only with soil moisture observation information. Thus, we will infer how the retrieval of soil temperature can benefit from three model physics, when the soil temperature observation is sparse.

6.4.1 Effect of Temporal Observation Interval

6.4.1.1 Dense Temporal Observations

With all the soil moisture and soil temperature observation information, different model physics did not affect the assimilation estimates of soil state variables. Figure 6.5 shows that even the DM, which was the worst model in simulating soil moisture, could get quite reasonable assimilation estimates of soil temperature, with the observation error-pairs of 400 cm and 4 °C. The soil moisture RMSE (i.e. difference between the assimilation estimates and observations) of DM was 0.0012 $m^3 m^{-3}$, while 0.0016 and 0.0017 $m^3 m^{-3}$ for DMV and DMVA, respectively.

From the comparison at the depth of 2, 5 and 10 cm, Fig. 6.6 does not show large difference among different model physics in assimilating soil temperature. However, at the depth of 20 cm, it was clearly shown that DM performs better than
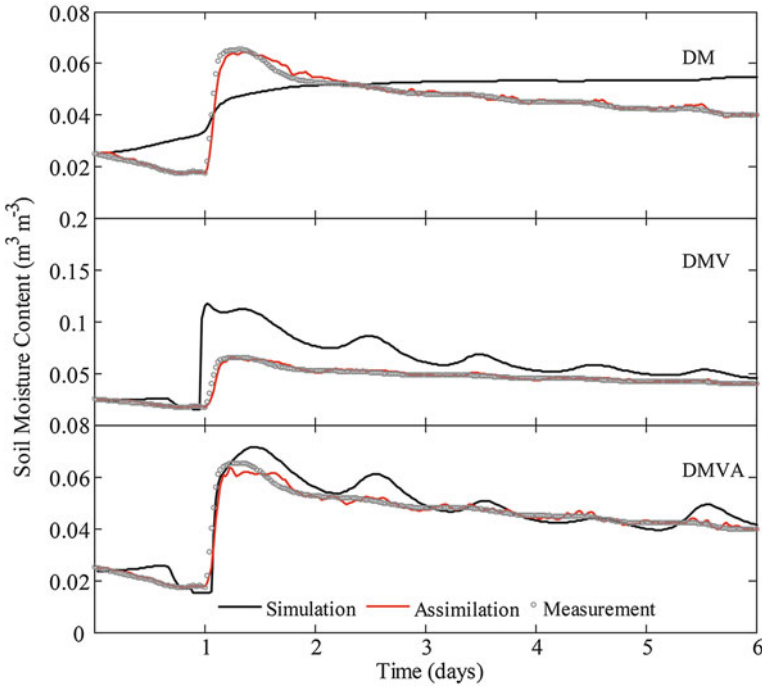
Fig. 6.5 The assimilated and simulated soil moisture content from different model physics compared with the observation, with the observation error-pairs of 400 cm and 4 °C

DMV and DMVA, while DMVA's estimation was the farthest from the observation (Fig. 6.6). As discussed in Sect. 6.3.2.2, because of the same heat transport scheme used, the simulation of soil temperature would not differ from each other significantly. The soil temperature RMSE of DM was 1.4 °C, while 2.5 and 2.1 °C for DMV and DMVA, respectively. The soil temperature RMSEs between the assimilation and observation were calculated individually for each depth. Then, they were averaged over all depths to account for the soil temperature RMSEs of different models.

From the above description, it seemed that the performance of different model physics did not vary significantly, although slight difference existed. For soil moisture assimilation, the difference between the best and worst estimates was 0.0005 $m^3\ m^{-3}$, while for soil temperature, it was 1.1 °C. With full observation information, the soil moisture assimilation results were closer to the observations than to the model simulations (Fig. 6.5), regardless of the difference in model physics. However, for soil temperature assimilation, it was not so obvious (Fig. 6.6). Considering only the smallest observation error-pair (i.e. 400 cm and 4 °C) was used for Figs. 6.5 and 6.6, checks on other error-pairs are needed to tell how different model physics perform in assimilating soil moisture and soil temperature.
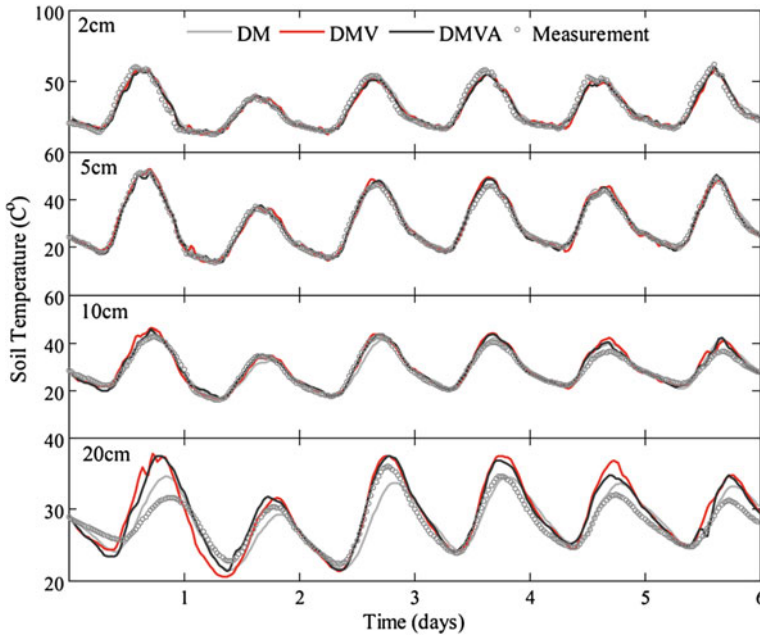
Fig. 6.6 The assimilation estimates of soil temperature from different model physics compared with the observation at the selected depths, with the observation error-pairs of 400 cm and 4 °C

According to the above calculated soil moisture and soil temperature RMSEs for one observation error-pair, all 16 observation error-pairs can produce 16 RMSE values. Then, three models can have three sets of RMSE values, each of which has 16 RMSE values. The RMSE sets can be used to assess the performance of different model physics accordingly. Figure 6.7a shows that at the soil temperature observation error of 4 °C the soil moisture RMSE of all three models increased with increasing soil moisture observation error. With other soil temperature observation errors, the soil moisture RMSE of DMV and DMVA followed the same pattern (i.e. increasing soil moisture observation error increases soil moisture RMSE). However, DM's soil moisture RMSE did not follow this pattern and had the biggest RMSE with the observation error-pair of 1600 cm and 9 °C. The effect of soil moisture observation errors dominated over that of soil temperature observation errors on the model performance in soil moisture assimilation. Figure 6.7b shows the performance pattern for soil temperature assimilation. All the three models followed the principle shown in Fig. 6.4 that was the RMSE increased with increasing soil temperature observation error. The effect of soil temperature observation error dominated over that of soil moisture observation error on the model performance in soil temperature assimilation.

Following the above-description, when the observation information is dense (e.g. half-hour interval), the difference in model physics does not significantly affect the assimilation estimates of soil moisture and soil temperature. The
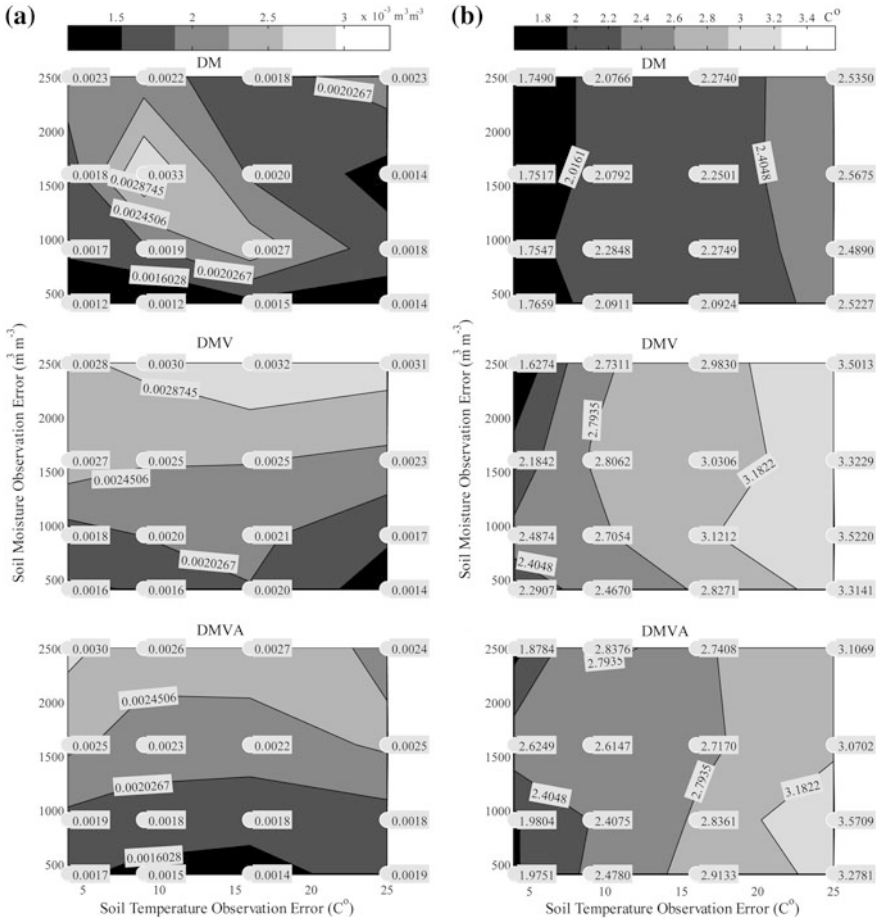
Fig. 6.7 RMSE for EnKF estimates for soil moisture (**a**) and soil temperature (**b**) as a function of observation error-pairs

observation error is the dominant factor determining the accuracy of assimilation estimates. For soil moisture assimilation, the model performance mainly depends on the soil moisture observation error, while for the soil temperature assimilation the model performance is principally decided by the soil temperature observation error. In Figure 6.4, the model-averaged performance (i.e. over all three models) against each observation error-pair were shown. Here, the mean RMSE averaged over all observation error-pairs (hereafter RMSE$_{err}$) for each model was employed to assess the overall performance of model physics associated with various observation error-pairs. With the observation error-pairs in Fig. 6.7, the soil moisture RMSE$_{err}$ was 0.0021, 0.0022, and 0.0019 m^3 m^{-3} for DMVA, DMV and DM, respectively; while the mean soil temperature RMSE$_{err}$ was 2.7, 2.8 and 2.2 °C, accordingly. According to the mean soil moisture and soil temperature

$RMSE_{err}$, the three model physics did not differ significantly from each other, with respect to the performance in assimilating soil moisture and temperature with dense temporal observations.

6.4.1.2 Sparse Temporal Observations

When the available observation was less, with the same filter parameters, RMSE between the assimilation estimates and the observation would vary depending on different model physics. Seven observation intervals (0.5, 6, 12, 24, 30, 36 and 48 h) were employed to check that. In the previous subsection (Sect. 6.4.1.1), the $RMSE_{err}$ with observation interval of 0.5 h was used to assess the performance of different model physics. In this section, the averaged assimilation estimate of soil moisture and temperature over all 16 observation error-pairs was employed. Thus, each observation interval would produce an averaged assimilation estimate of soil moisture and temperature (e.g. over 16 error-pairs) for each model physics. Then, the RMSE between the averaged assimilation estimate and the observation (hereafter $RMSE_{obs}$) was used to assess the overall performance of different models.

Figure 6.8a shows that the soil temperature $RMSE_{obs}$ was increased steeply from the observation interval of 0.5–6 h. With further increasing observation interval, the $RMSE_{obs}$ was much more stable except for that of DMVA. There was a more than 3 °C variation at observation interval of 48 and 96 h. It seemed that the assimilation estimates at observation interval of 48 and 96 h (i.e. only observation at midnight) were inferior to other observation intervals. This was mainly due to the lack of observation information during day when the strong coupling between soil moisture and soil heat transport occurred [59, 70], which weakened the performance in assimilating soil moisture and temperature. Not only the soil temperature but also the soil moisture assimilation estimates of DMVA were disturbed by the lack of day information. This indicated the strong coupling model physics of DMVA.

Figure 6.8a explicitly shows that the overall performance of DMVA and DMV in assimilating soil temperature was better than DM, while DMV was slightly superior to DMVA. The averaged $RMSE_{obs}$ were 5.2, 4.1 and 4.7 °C for DM, DMV and DMVA, respectively. Figure 6.8b shows the variation of soil moisture $RMSE_{obs}$ with different observation intervals. Except for the $RMSE_{obs}$ of DM, which kept relatively stable after the observation interval of 12 h, the $RMSE_{obs}$ of both DMVA and DMV increased with increasing observation intervals. The averaged soil moisture $RMSE_{obs}$ over all observation intervals were 0.0159, 0.0141 and 0.0099 $m^3\ m^{-3}$, for DMVA, DMV and DM, respectively. The performances of DMVA and DMV in assimilating soil moisture were similar. However, DMV was superior to DMVA at small observation intervals (i.e. <30 h) while it was reverse at intervals bigger than 30 h. Although DM had the lowest averaged soil moisture $RMSE_{obs}$, it did not mean the assimilation estimates from
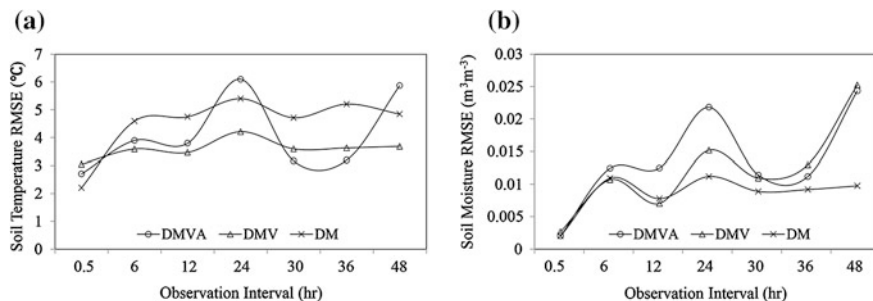
Fig. 6.8 Soil temperature and soil moisture RMSE$_{obs}$ vary with observation intervals

DM was the best. The lowest RMSE$_{obs}$ was due to DM's weakest coupling strength among the three models, which would be shown in Fig. 6.9.

The averaged assimilation estimates for calculating RMSE$_{obs}$ were further averaged over 7 observation intervals for the direct comparison to the observation in Fig. 6.9. The averaged assimilation estimates for calculating RMSE$_{obs}$ can be regarded as the observation-error ensemble mean, while the averaged assimilation estimates in Fig. 6.9 can be described as the observation-interval ensemble mean of the observation-error ensemble means. Figure 6.9b shows that although DM's assimilation estimate was the closet to the observed soil moisture, there was no daily variation of assimilated soil moisture. It was due to the weak coupling between soil moisture and heat transport in DM. When the coupling strength was increased, the assimilated soil moisture of DMV and DMVA did show typical daily behavior (Fig. 6.9b). One note here is that the observation of soil moisture itself (at the depth of 10 cm) did not show very clear daily variation as DMV and DMVA did. The main reason was the low sensitivity of soil moisture sensor in detecting moisture content in extremely dry environment [71]. The soil moisture RMSEs between the averaged assimilation estimates and observation in Fig. 6.9b were 0.0116, 0.0094 and 0.0076 m^3 m^{-3} for DMVA, DMV and DM, respectively. This was accordant with Fig. 6.8b that DMV was superior to DMVA and DM in soil moisture assimilation. Figure 6.9a shows the overall averaged performance of different model physics in assimilating soil temperature, from where the DM was inferior to DMV and DMVA in soil temperature assimilation. The soil temperature RMSEs in Fig. 6.9a were 3.85, 3.47 and 4.93 °C for DMVA, DMV and DM, respectively.

When the dense temporal observation information was fully used, DAS could provide close-to-observation estimates of soil moisture and temperature without regarding the complexity of the model physics as Sect. 6.4.1.1 showed. However, when observation was sparse, the assimilation estimates depended mainly on the model physics. In Fig. 6.9a, DM had the biggest RMSE value. However, as mentioned above, the lowest/biggest RMSE does not have to represent the best/worst assimilation. The goodness of fit expressed by the R-squared value was used
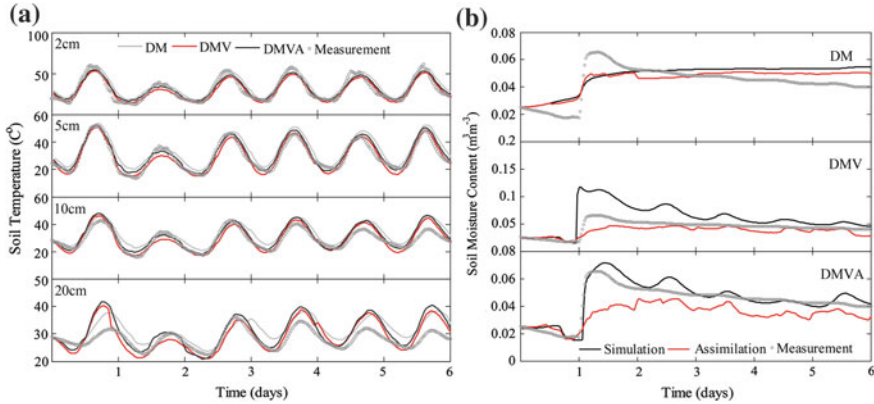
Fig. 6.9 The averaged assimilation estimates of soil temperature and soil moisture over all observation intervals

to illustrate this quantitatively. It is to estimate how good the assimilation estimates mimic the observation.

For soil temperature, the R-squared value was calculated for each depth and then averaged to account for the overall performance of different models. The averaged R-squared values are 0.854, 0.843 and 0.839 for DMVA, DMV and DM, respectively. The R-squared values indicate that DMVA and DMV are superior to DM in soil temperature assimilation as the RMSE values indicate. Although DMV has lower RMSE (3.47 °C) than DMVA (3.85 °C) in Fig. 6.9a, it does not mean that DMV's assimilation estimates of soil temperature can mimic the observation better than DMVA. This is indicated by the biggest R-squared value of DMVA. For soil moisture, the R-squared values are 0.678, 0.723 and 0.655 for DMVA, DMV and DM, respectively. Different from soil temperature assimilation comparison, both the soil moisture RMSE and R-squared values indicate that DMV was better than DMVA in soil moisture assimilation. While for DM, the lowest R-squared value fortifies the fact that although DM has the lowest soil moisture RMSE it does not mean DM has the best fit to the observation.

6.4.2 Effect of Surface Temperature Observation

In the previous section, with all the soil temperature observation at the selected depths, the effect of temporal observation interval on the performance of different models was evaluated. In this section, the EnKF-Matlab used only the soil temperature observation (e.g. with the soil moisture observation at the depth of 10 cm) at the depth of 2 cm, which was closely representative of the surface soil temperature. The R-squared value between the surface temperature and the observation at 2 cm was 0.92, with a RMSE of 4.1 °C between them.
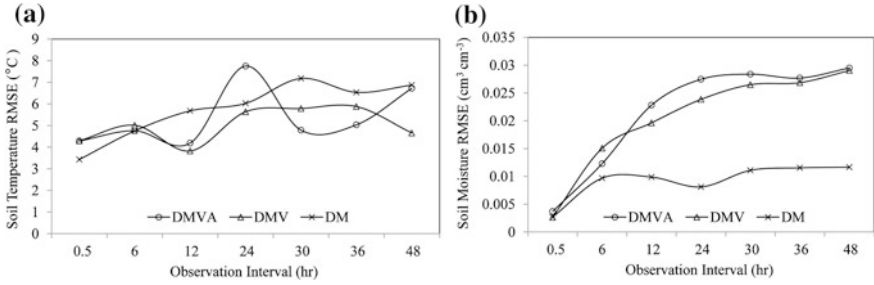
Fig. 6.10 The same as Fig. 6.8, but for assimilation result with only surface observation
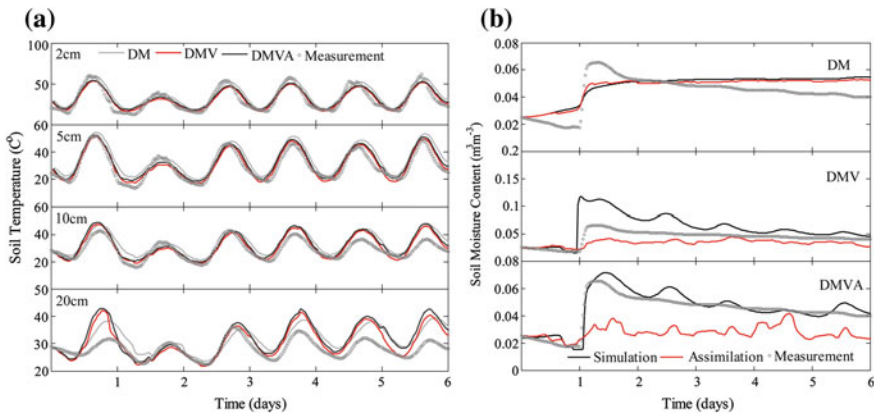

Fig. 6.11 The same as Fig. 6.9, but for assimilation result with only surface observation

Figure 6.10 shows the similar pattern of RMSE$_{obs}$ in Fig. 6.8. The mean soil temperature RMSE$_{obs}$ of DMV (5.01 °C) was lower than DMVA (5.36 °C), while both of them were lower than that of DM (5.78 °C). The mean soil moisture RMSE$_{obs}$ of DM was the lowest (0.0092 m^3 m^{-3}), while that of DMV (0.0205 m^3 m^{-3}) was lower than DMVA (0.0217 m^3 m^{-3}). However, Fig. 6.10 does not clearly show the coupling strength of different model physics as Fig. 6.8 does. The lack of observation information during the day only weakened the performance in assimilating soil temperature, but not soil moisture. The result with only surface temperature was generally inferior, compared to the assimilation result with all soil temperature observation information. The mean soil moisture and temperature RMSE$_{obs}$ in Fig. 6.10 was generally higher than that in Fig. 6.8, except for DM's soil moisture RMSE$_{obs}$.

Figure 6.11 indicates that DMV performed better than DMVA in assimilating both soil moisture and soil temperature. The soil temperature RMSEs in Fig. 6.11a were 4.74, 3.88 and 5.51 °C for DMVA, DMV and DM, respectively. The associated R-squared values were 0.821, 0.839 and 0.827. Although the RMSE value

of DMVA in Fig. 6.11a was lower than DM, the bigger R-squared value of DM indicated its better fit to the observation than DMVA. The DMV performed the best among the three models in assimilating soil temperature. For soil moisture, the RMSEs in Fig. 6.11b were 0.019, 0.013 and 0.008 m^3 m^{-3} for DMVA, DMV and DM, respectively. The associated R-squared values were 0.322, 0.604 and 0.665. In Fig. 6.11b, DMVA did not clearly show the typical daily variation of soil moisture. This indicated that the coupling strength did not affect the assimilation result when only the surface moisture and temperature observation were used. However, the DMV showed the daily behaviours lightly.

6.4.3 Effect of Assimilation with Soil Moisture Only

In this section, only soil moisture observation information was employed to assess the performance of different models. Figure 6.12a shows that the mean soil temperature $RMSE_{obs}$ were 4.44, 4.39 and 5.58 °C, for DMVA, DMV and DM, respectively. Accordingly, for soil moisture (Fig. 6.12b), the mean $RMSE_{obs}$ were 0.017, 0.021, and 0.01 m^3 m^{-3}. In previous sections, the $RMSE_{obs}$ pattern among the three models was: both soil moisture and soil temperature $RMSE_{obs}$ of DMVA were higher than those of DMV, while both DMVA and DMV had lower $RMSE_{obs}$ than DM in regard to soil temperature, and higher $RMSE_{obs}$ with regard to soil moisture. When only the soil moisture observation was used, with respect to soil temperature, DMVA's $RMSE_{obs}$ was higher than that of DMV. However, DMVA's soil moisture $RMSE_{obs}$ was lower than that of DMV. It suggests that the performance of DMVA in assimilating soil moisture is superior to DMV, which can be verified by Fig. 6.13.

As can be seen in Fig. 6.13b, the DMVA showed the typical daily variation of soil moisture while the DMV did not show clearly. The soil moisture RMSEs in Fig. 6.13b were 0.012, 0.018 and 0.009 m^3 m^{-3} for DMVA, DMV and DM, respectively; while the associated R-squared values were 0.513, 0.399 and 0.588. The DMVA was superior to DMV in assimilating soil moisture when only soil moisture observation was used. Although both the RMSE and R-squared value
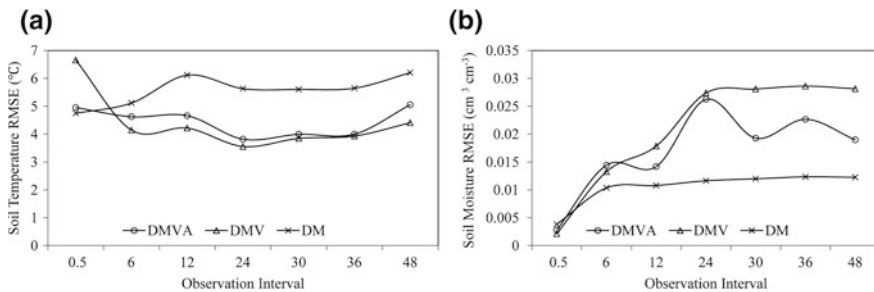

Fig. 6.12 The same as Fig. 6.10, but for assimilation result with only soil moisture observation
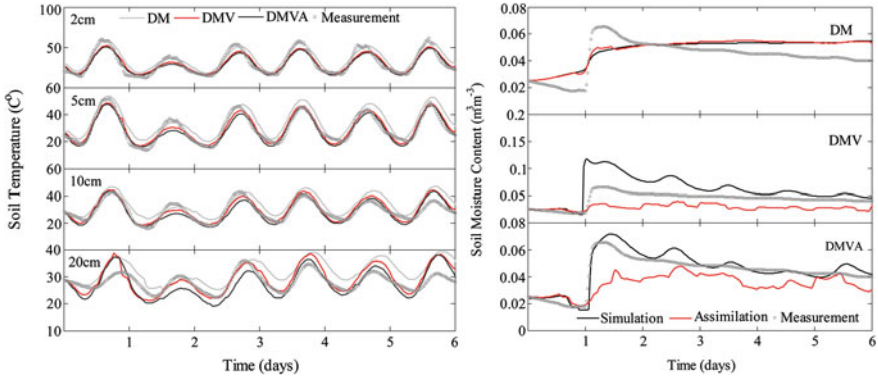
Fig. 6.13 The same as Fig. 6.11, but for assimilation result with only soil moisture observation

indicated that DM was the closet to the observation, Fig. 6.13b shows that its assimilation estimates of soil moisture mainly followed the model simulation without listening to the observation. The soil temperature RMSEs in Fig. 6.13a were 3.78, 3.46 and 5.39 °C for DMVA, DMV and DM, respectively; while the associated R-squared values were 0.82, 0.84 and 0.819. Again, DMV's assimilation result was better than DMVA in assimilating soil moisture, and both of them were superior to DM.

6.5 Brief Summary

To evaluate how different complexities in model physics could affect the model performance in the DAS, three models (DM, DMV and DMVA) with gradually-increased complexities were introduced. The field experiment in the Badain Jaran Desert [59] was tentatively used to calibrate DMVA, which could be regarded as the most "correct" model. The calibrated parameters from DMVA were then applied in the less complex model DMV, and the "poorest" physics model DM. The three different complexity models were subsequently evaluated in a DAS.

With dense temporal observations of soil moisture and soil temperature, the model performances of three model physics differed slightly from each other (Sect. 6.4.1). The assimilation estimate was critically dependent on the observation information, while the model physics didn't play a crucial role in it. If the available observation were less, different model physics should perform divergently. Seven observation intervals (0.5, 6, 12, 24, 30, 36 and 48 h) were used to check the hypothesis. The assimilation results showed that DMV was superior to DMVA in retrieving soil temperature and both of them produced better fit than DM to the observation. For soil moisture, although the DM produced the closet assimilation estimate to the observation, it did not show clear daily variation as the DMV and DMVA did.

   The assimilation result with seven observation intervals could be regarded as the effect of sparse temporal observation on the model performance. The observation information was further diluted by considering only the surface observation. With only the surface moisture and temperature observation information, the DMVA and DMV did not display their coupling strength in assimilating soil moisture, although the DMV slightly showed the typical daily variation of soil moisture. Under such condition, the DM outperformed the complex model physics in assimilating soil moisture. For soil temperature, the DMV performed the best among the three models.

   To further assess how different model physics performed with less observation information, only the surface moisture observation was used. With less observation (without soil temperature observation information), DMVA showed the advantage of the most complex model physics in assimilating soil moisture and outperformed the DMV. Compared to the assimilation result with surface temperature observation information, the DMVA and DMV showed the daily variation of soil moisture, although DMV only show it slightly with an R-Squared value of 0.399. For retrieving soil temperature, the DMV still performed the best among the three models, while the DM was the most inferior in assimilating soil temperature.

References

1. Dirmeyer PA, Guo ZC, Gao X (2004) Comparison, validation, and transferability of eight multiyear global soil wetness products. J Hydrometeorol 5(6):1011–1033
2. Koster RD, Guo ZC, Yang RQ, Dirmeyer PA, Mitchell K, Puma MJ (2009) On the nature of soil moisture in land surface models. J Clim 22(16):4322–4335
3. Rosero E, Yang ZL, Wagener T, Gulden LE, Yatheendradas S, Niu GY (2010) Quantifying parameter sensitivity, interaction, and transferability in hydrologically enhanced versions of the Noah land surface model over transition zones during the warm season. J Geophys Res-Atmos 115:D03106
4. Dirmeyer PA, Koster RD, Guo ZC (2006) Do global models properly represent the feedback between land and atmosphere? J Hydrometeorol 7(6):1177–1198
5. Schlosser CA, Slater AG, Robock A, Pitman AJ, Vinnikov KY, Henderson-Sellers A, Speranskaya NA, Mitchell K, Contributors PD (2000) Simulations of a boreal grassland hydrology at Valdai, Russia: PILPS phase 2(D). Mon Weather Rev 128(2):301–321
6. Henderson-Sellers A, Yang ZL, Dickinson RE (1993) The project for Intercomparison of land-surface parameterization schemes. Bull Am Meteorol Soc 74(7):1335–1349
7. Shao YP, Henderson-Sellers A (1996) Modeling soil moisture: a project for intercomparison of land surface parameterization schemes phase 2(b). J Geophys Res-Atmos 101(D3):7227–7250
8. Pitman AJ, Henderson-Sellers A, Desborough CE, Yang ZL, Abramopoulos F, Boone A, Dickinson RE, Gedney N, Koster R, Kowalczyk E, Lettenmaier D, Liang X, Mahfouf JF, Noilhan J, Polcher J, Qu W, Robock A, Rosenzweig C, Schlosser CA, Shmakin AB, Smith J, Suarez M, Verseghy D, Wetzel P, Wood E, Xue Y (1999) Key results and implications from phase 1(c) of the project for intercomparison of land-surface parametrization schemes. Clim Dyn 15(9):673–684
9. Slater AG, Schlosser CA, Desborough CE, Pitman AJ, Henderson-Sellers A, Robock A, Vinnikov KY, Mitchell K, Boone A, Braden H, Chen F, Cox PM, de Rosnay P, Dickinson

RE, Dai YJ, Duan Q, Entin J, Etchevers P, Gedney N, Gusev YM, Habets F, Kim J, Koren V, Kowalczyk EA, Nasonova ON, Noilhan J, Schaake S, Shmakin AB, Smirnova TG, Verseghy D, Wetzel P, Yue X, Yang ZL, Zeng Q (2001) The representation of snow in land surface schemes: results from PILPS 2(d). J Hydrometeorol 2(1):7–25

10. Desborough CE (1999) Surface energy balance complexity in GCM land surface models. Clim Dyn 15(5):389–403

11. Gupta HV, Bastidas LA, Sorooshian S, Shuttleworth WJ, Yang ZL (1999) Parameter estimation of a land surface scheme using multicriteria methods. J Geophys Res-Atmos 104(D16):19491–19503

12. Kato H, Rodell M, Beyrich F, Cleugh H, van Gorsel E, Liu HZ, Meyers TP (2007) Sensitivity of land surface simulations to model physics, land characteristics, and forcings, at four CEOP sites. J Meteorol Soc Jpn 85A:187–204

13. Bastidas LA, Hogue TS, Sorooshian S, Gupta HV, Shuttleworth WJ (2006) Parameter sensitivity analysis for different complexity land surface models using multicriteria methods. J Geophys Res-Atmos 111:D20101

14. van den Hurk BJJM, Beljaars ACM, Betts AK (2000) Offline validation of the ERA-40 surface scheme. ECMWF Tech Memo 295:1–43

15. Dong JR, Salvucci GD, Myneni RB (2001) Improving the precision of simulated hydrologic fluxes in land surface models. J Geophys Res-Atmos 106(D13):14357–14368

16. Ek MB, Mitchell KE, Lin Y, Rogers E, Grunmann P, Koren V, Gayno G, Tarpley JD (2003) Implementation of Noah land surface model advances in the National Centers for Environmental Prediction operational mesoscale Eta model. J Geophys Res-Atmos 108:D22,8851

17. Miguez-Macho G, Fan Y, Weaver CP, Walko R, Robock A (2007) Incorporating water table dynamics in climate modeling: 2. Formulation, validation, and soil moisture simulation. J Geophys Res-Atmos 112:D13108

18. Niu GY, Yang ZL, Dickinson RE, Gulden LE, Su H (2007) Development of a simple groundwater model for use in climate models and evaluation with Gravity Recovery and Climate Experiment data. J Geophys Res-Atmos 112:D07103

19. Oleson KW, Niu GY, Yang ZL, Lawrence DM, Thornton PE, Lawrence PJ, Stockli R, Dickinson RE, Bonan GB, Levis S, Dai A, Qian T (2008) Improvements to the Community Land Model and their impact on the hydrological cycle. J Geophys Res-Biogeosci 113:G01021

20. Balsamo G, Beljaars A, Scipal K, Viterbo P, van den Hurk B, Hirschi M, Betts AK (2009) A revised hydrology for the ECMWF model: verification from field site to terrestrial water storage and impact in the Integrated Forecast System. J Hydrometeorol 10(3):623–643

21. de Rooij GH (2010) Comments on "improving the numerical simulation of soil moisture-based Richards equation for land models with a deep or shallow water table. J Hydrometeorol 11(4):1044–1050

22. Zeng XB, Decker M (2010) Comments on "improving the numerical simulation of soil moisture-based Richards equation for land models with a deep or shallow water table''-reply. J Hydrometeorol 11(4):1051–1054

23. Hogue TS, Bastidas LA, Gupta HV, Sorooshian S (2006) Evaluating model performance and parameter behavior for varying levels of land surface model complexity. Water Resour Res 42:W08430

24. Rosero E, Yang ZL, Gulden LE, Niu GY, Gochis DJ (2009) Evaluating enhanced hydrological representations in Noah LSM over transition zones: implications for model development. J Hydrometeorol 10(3):600–622

25. Koster RD, Oki T, Suarez MJ (1999) The offline validation of land surface models: assessing success at the annual timescale. J Meteorol Soc Jpn 77(1B):257–263

26. Robock A, Schlosser CA, Vinnikov KY, Speranskaya NA, Entin JK, Qiu S (1998) Evaluation of the AMIP soil moisture simulations. Glob Planet Change 19(1–4):181–208

27. Avissar R, Pielke RA (1989) A parameterization of heterogeneous land surfaces for atmospheric numerical-models and its impact on regional meteorology. Mon Weather Rev 117(10):2113–2136
28. Flerchinger GN, Saxton KE (1989) Simultaneous heat and water model of a freezing snow-residue-soil system 1: theory and development. Trans ASAE 32(2):565–571
29. Avissar R (1992) Conceptual aspects of a statistical-dynamic approach to represent landscape subgrid-scale heterogeneities in atmospheric models. J Geophys Res-Atmos 97(D3):2729–2742
30. Braud I, Dantasantonino AC, Vauclin M, Thony JL, Ruelle P (1995) A simple soil-plant-atmosphere transfer model (SiSPAT) development and field verification. J Hydrol 166(3–4):213–250
31. Jassal RS, Novak MD, Black TA (2003) Effect of surface layer thickness on simultaneous transport of heat and water in a bare soil and its implications for land surface schemes. Atmos Ocean 41(4):259–272
32. Hazeleger W, Severijns C, Semmler T, Stefanescu S, Yang ST, Wang XL, Wyser K, Dutra E, Baldasano JM, Bintanja R, Bougeault P, Caballero R, Ekman AML, Christensen JH, van den Hurk B, Jimenez P, Jones C, Kallberg P, Koenigk T, McGrath R, Miranda P, Van Noije T, Palmer T, Parodi JA, Schmith T, Selten F, Storelvmo T, Sterl A, Tapamo H, Vancoppenolle M, Viterbo P, Willen U (2010) EC-Earth: a seamless earth-system prediction approach in action. Bull Am Meteorol Soc 91(10):1357–1363
33. Stieglitz M, Rind D, Famiglietti J, Rosenzweig C (1997) An efficient approach to modeling the topographic control of surface hydrology for regional and global climate modeling. J Clim 10(1):118–137
34. Entekhabi D, Nakamura H, Njoku EG (1994) Solving the inverse problems for soil-moisture and temperature profiles by sequential assimilation of multifrequency remotely-sensed observations. IEEE Trans Geosci Remote Sens 32(2):438–448
35. Milly PCD (1986) Integrated remote sensing modelling of soil moisture: sampling frequency, response time, and accuracy of estimates. Integrated design of hydrological networks-proceedings of the budapest symposium, Budapest, IAHS. Publication No 158, pp 201–211
36. Galantowicz JF, Entekhabi D, Njoku EG (1999) Tests of sequential data assimilation for retrieving profile soil moisture and temperature from observed L-band radiobrightness. IEEE Trans Geosci Remote Sens 37(4):1860–1870
37. Walker JP, Willgoose GR, Kalma JD (2001) One-dimensional soil moisture profile retrieval by assimilation of near-surface measurements: a simplified soil moisture model and field application. J Hydrometeorol 2(4):356–373
38. Walker JP, Willgoose GR, Kalma JD (2001) One-dimensional soil moisture profile retrieval by assimilation of near-surface observations: a comparison of retrieval algorithms. Adv Water Resour 24(6):631–650
39. Reichle RH, McLaughlin DB, Entekhabi D (2002) Hydrologic data assimilation with the ensemble Kalman filter. Mon Weather Rev 130(1):103–114
40. Dong JR, Salvucci GD et al. (2011) Improving the precision of simulated hydrologic fluxes in land surface models. J Geophys Res-Atmospheres 106(D13):14357–14368
41. Milly PCD (1982) Moisture and heat transport in hysteretic, inhomogeneous porous media: a matric head-based formulation and a numerical model. Water Resour Res 18(3):489–498
42. Groenevelt PH, Kay BD (1974) On the interaction of water and heat transport in frozen and unfrozen soils: II. The Liquid Phase. Soil Sci Soc Am Proc 38:400–404
43. Gray WG, Hassanizadeh SM (1991) Unsaturated flow theory including interfacial phenomena. Water Resour Res 27(8):1855–1863
44. Fredlund DG, Rahardjo H (1993) Soil mechanics for unsaturated soils. Wiley, New York
45. Thomas HR, Sansom MR (1995) Fully coupled analysis of heat, moisture, and air transfer in unsaturated soil. J Eng Mech 121(3):392–405
46. de Vries DA (1958) Simultaneous transfer of heat and moisture in porous media. Trans Am Geophys Union 39(5):909–916

47. Saito H, Simunek J, Mohanty BP (2006) Numerical analysis of coupled water, vapor, and heat transport in the vadose zone. Vadose Zone J 5(2):784–800
48. Evensen G (2009) The Ensemble Kalman filter for combined state and parameter estimation. IEEE Control Syst Mag 29(3):83–104
49. Kalman RE (1960) A new approach to linear filtering and prediction problems. J Basic Eng 82(1):35–45
50. Ide K (1997) United notation for data assimilation: operational, sequential and variational. Practice 75(1B):181–189
51. Evensen G (1994) Inverse methods and data assimilation in nonlinear ocean models. Physica D 77:108–129
52. Evensen G (2003) The ensemble Kalman filter: theoretical formulation and practical implementation. Ocean Dyn 53(4):343–367
53. Sakov P, Evensen G, Bertino L (2010) Asynchronous data assimilation with the EnKF. Tellus A 62(1):24–29
54. Burgers G, van Leeuwen PJ, Evensen G, Instituut KNM (1998) Analysis scheme in the ensemble Kalman filter. Mon Weather Rev 126(6):1719–1724
55. Sakov P, Oke PR (2008) A deterministic formulation of the ensemble Kalman filter: an alternative to ensemble square root filters. Tellus A 60(2):361–371
56. Bishop CH, Etherton BJ, Majumdar SJ (2001) Adaptive sampling with the ensemble transform Kalman filter. Part I: Theoretical aspects. Mon Weather Rev 129(3):420–436
57. Tippett MK, Anderson JL, Bishop CH, Hamill TM, Whitaker JS (2003) Ensemble square root filters. Mon Weather Rev 131:1485–1490
58. Zeng Y, Su Z, Wan L, Wen J (2011) Numerical analysis of air-water-heat flow in the unsaturated soil is it necessary to consider airflow in land surface models. J Geophys Res-Atmos 116(20):D20107. doi:10.1029/2011JD015835
59. Zeng Y, Wan L, Su Z, Saito H, Huang K, Wang X (2009) Dirnal soil water dynamics in the shallow vadose zone. Environ Geol 58:11–23
60. Gates JB, Edmunds WM, Ma JZ (2008) Estimating groundwater recharge in a cold desert environment in northern China using chloride. Hydrogeol J 16:893–910
61. Milly PCD, Eagleson PS (1980) The coupled transport of water and heat in a vertical soil column under atmospheric excitation. Department of Civil Engineering, Ralph M. Parsons Laboratory for Water Resources and Hydrodynamics, Massachusetts Institute of Technology
62. Luo LF, Robock A, Vinnikov KY, Schlosser CA, Slater AG, Boone A, Braden H, Cox P, de Rosnay P, Dickinson RE, Dai YJ, Duan QY, Etchevers P, Henderson-Sellers A, Gedney N, Gusev YM, Habets F, Kim JW, Kowalczyk E, Mitchell K, Nasonova ON, Noilhan J, Pitman AJ, Schaake J, Shmakin AB, Smirnova TG, Wetzel P, Xue YK, Yang ZL, Zeng QC (2003) Effects of frozen soil on soil temperature, spring infiltration, and runoff: results from the PILPS 2(d) experiment at Valdai, Russia. J Hydrometeorol 4(2):334–351
63. Luo LF, Robock A, Mitchell KE, Houser PR, Wood EF, Schaake JC, Lohmann D, Cosgrove B, Wen FH, Sheffield J, Duan QY, Higgins RW, Pinker RT, Tarpley JD (2003a) Validation of the North American Land Data Assimilation System (NLDAS) retrospective forcing over the southern Great Plains. J Geophys Res-Atmos 108:8843 (10 pp)
64. Abramowitz G, Gupta HV, Pitman A, Wang Y, Leuning R, Cleugh H, Hsu K (2006) Neural error regression diagnosis (NERD): a tool for model bias identification and prognostic data assimilation. J Hydrometeorol 7(1):160–177
65. Reichle RH, Walker JP, Koster RD, Houser PR (2002) Extended versus ensemble Kalman filtering for land data assimilation. J Hydrometeorol 3(6):728–740
66. Bouttier F, Courtier P (1999) Data assimilation concepts and methods. Meteorological training course lecture series. ECMWF, Reading
67. Janic T, Cohn SE (2006) Treatment of observation error due to unresolved scales in atmospheric data assimilation. Mon Weather Rev 134:2900–2915
68. Oke PR, Sakov P (2008) Representation error of oceanic observations for data assimilation. J Atmos Ocean Technol 25(6):1004–1017

69. Reichle RH, Crow WT, Keppenne CL (2008) An adaptive ensemble Kalman filter for soil moisture data assimilation. Water Resour Res 44(3):W03423
70. Zeng Y, Su Z, Wan L, Yang Z, Zhang T, Tian H, Shi X, Wang X, Cao W (2009) Diurnal pattern of the drying front in desert and its application for determining the effective infiltration. Hydrol Earth Syst Sci 13(6):703–714
71. Vereecken H, Huisman J, Bogena H, Vanderborght J, Vrugt J, Hopmans J (2008) On the value of soil moisture measurements in vadose zone hydrology: a review. Water Resour Res 44:W00D06

Chapter 7
Concluding Remarks

7.1 Results

It is well known that soil water transport is driven by the soil matric potential gradient and the soil temperature gradient. However, very little literature discussed the continuous changes in soil water dynamics, regarding profile information. With an in-situ experiment, Chap. 2 employs the classical coupled moisture and heat transport scheme to show the pattern of driving forces (i.e. soil matric potential gradient and soil temperature gradient), hydraulic conductivities, soil water fluxes and water vapor fluxes. The fluxes are described as isothermal and thermal (or non-isothermal) depending on the driving force. The results show that there are three stages in the diurnal soil water dynamics. The thermal vapor and the thermal liquid flux were identified as the dominant fluxes in the uppermost soil layer at night, while the isothermal liquid flux dominated during the day and in deeper soil layers. It is suggested that the isothermal liquid flux, the thermal liquid flux and the thermal vapor flux should be considered for analysing soil water dynamics in arid and semi-arid area. Based on these results, a schematic map of the diurnal soil water dynamics is presented.

In the desert, it is important to understand how much of the precipitation can be absorbed by the unsaturated zone. This portion of the precipitation can be defined as the effective infiltration. Chapter 3 applies the pattern described above to understand the soil water dynamics of the Badain Jaran Desert field site, and to determine the effective infiltration. Based on the soil water dynamics pattern understood from Chap. 2 (e.g. driving forces pattern, soil moisture fluxes pattern etc.), a schematic figure is presented to calculate the effective infiltration. The results show that considering the maximum annual precipitation of 120 mm, the effective infiltration is estimated to be 0.336 mm/yr, which is lower than the historic records based on hydro-chemical and isotopic methods. Considering the short term and point-scale observations made of the soil water dynamics at the field site in the Badain Jaran Desert, the estimated value cannot be representative for the whole region.

More long-term and regional scale observation information is necessary to estimate the effective infiltration.

Chapter 4 tackles the inclusion of airflow in the classical coupled moisture and heat transport scheme (i.e. PdV model). The reason to do this is discussed in detail in the introduction. The difference between the proposed two-phase mass and heat flow model and the PdV model is explained for the governing equations and the constitutive equations. With the published experimental and analytical results, the two-phase mass and heat flow model was verified. Based on the verification results, how airflow affects the coupled moisture and heat flow, and how temperature influences the isothermal water-air two-phase flow are both examined. The investigation shows that when the air phase plays a significant role in the water-airflow domain, the temperature exerts noticeable effect on the soil moisture fluxes. As for the coupled moisture and heat flow, the airflow plays a great role in affecting soil moisture fluxes.

The field experiment in the Badain Jaran Desert is employed to examine the performance of the proposed model. The results show that the proposed model can better calculate the surface evaporative fluxes, especially when the soil is moist, than the PdV model can. When neglecting airflow (e.g. using the PdV model), the calculation of the surface evaporative flux will result in an underestimation error. In order to understand why neglecting airflow can lead to the error, Chap. 5 investigates the driving forces and the conductivities. The direct cause is assumed to be the inclusion of airflow increase in the evaporation flux due to outgoing airflow from the soil; while the indirect cause is postulated to be the temperature gradient generated being larger in the PdV model than in the proposed model. This would mean that the downward thermal liquid and vapor flux depresses the evaporation flux. After comparison of the driving forces and conductivities, none of the causes are found to be true. The underestimation error is induced by the upward isothermal liquid flux being larger in the proposed model than in the PdV model. The greater upward isothermal liquid flux of the proposed model is induced by the downward airflow-induced soil moisture flux, which moistens the top shallow soil layer and tremendously increases the associated unsaturated hydraulic conductivity. While the PdV model shows no airflow-induced flux.

In the hydrological data assimilation research context, most of land surface models employ the diffusive soil moisture and heat transport model to represent the soil water dynamics in land surface processes. It is operational for regional, continental or global applications, because the simplification of the soil water dynamics enormously reduces the computation cost and the model complexity. However, such simplification may cause underestimation errors as stated in Chap. 5. Chapter 6 combines the proposed model and a data assimilation platform to check the feasibility of retrieving soil state variable profiles considering the airflow mechanism. Furthermore, to illustrate how model physics affects model performance in data assimilation systems, the diffusive soil moisture and heat transport model, the PdV model and the proposed model are implemented with a common set of filter parameters and model parameters. The results show that the most complex model

does not always perform the best in retrieving soil state variable profiles. The medium complex model (the PdV model) performs better than the proposed model (i.e. the most complex model), when the sparse temporal observations or the surface only observations of moisture and temperature were assimilated. When only the surface moisture is assimilated, the proposed model outperforms the other two. Nevertheless, when the observation frequency is dense (e.g. every half hour), the model complexity will not affect the assimilation estimate of soil state variables.

7.2 Limitations

The major contribution to PdV theory of this thesis is the development of the two-phase mass and heat flow model and the discussion on the difference between the proposed model and the PdV model regarding the numerical aspect (e.g. Chap. 4) and the application aspect (e.g. Chaps. 5–7). From a soil physics point of view, there is very little literature discussing how temperature may affect the isothermal water-air two-phase flow and how airflow may influence the coupled moisture and heat transport. The application of a two-phase mass and heat flow model to calculate surface evaporation is seldom reported. In this sense, this thesis presents some new findings on how a two-phase model can affect soil water transport. In the land-atmosphere interaction research (or hydrological data assimilation) context, this thesis attempts to combine the two-phase model and data assimilation system to retrieve soil moisture and soil temperature profiles. Usual methods (e.g. statistical approach: correlation matrix, artificial neural network) testing the model performance for retrieving soil state variables are not adopted in this thesis. Instead, the model performance is evaluated solely on the grounds of model physics. However, there are at least two major limitations:

Firstly, the proposed two-phase model is one dimensional, which is sufficient for local land-atmosphere interaction research. However, for larger scales (e.g. continental or global scales), the assumption of one-dimensional interaction between the atmosphere and the land will cause unpredictable errors. Furthermore, a one-dimensional model setup does not allow detailed inspection of the vapor-liquid circulation in the soil, which is implicitly included in the PdV model. With the two-phase model, the vapor convection is not visible under a one-dimensional setup either.

Secondly, to be able to consider more complex and realistic processes in the soil, the proposed model needs further development. It is clear that the proposed model lacks the inclusion of freezing and thawing processes, where frozen soil can impede water infiltration and influence the hydrological cycle [2], and soil thaw can enhance soil-atmosphere gas exchanges [8, 13]. Although there is a risk of over-parameterization of land-surface processes [5] by including the freezing/ thawing process in the two-phase model, from a subsurface physical point of view,

soil moisture and soil temperature are still under-parameterized, even though they are the most studied estimation variables in land surface models (LSMs) [4]. The recently launched soil moisture and ocean salinity satellite (SMOS) by the European Space Agency (ESA) is expected to provide insights into how a changing climate may be affecting patterns of evaporation over land and over the ocean by monitoring global surface-soil moisture every three days [10]. However, such insight may only be achieved using the appropriate combination of land model physics and data assimilation techniques [1]. In the near future, NASA's Soil Moisture Active and Passive (SMAP) mission will be launched for mapping soil moisture and freeze/thaw states. To not only include the airflow mechanism discussed above, but to also assimilate the extra satellite data, a land model considering the freezing/thawing process should be developed.

7.3 Discussion and Future Work

Considering the proposed two-phase mass and heat flow model can act as a land surface model, it is worth discussing if it is necessary to include airflow mechanisms in the land surface model, or not.

As mentioned previously, most of the LSMs do not consider two-phase flows. Soil water dynamics remain highly simplified in the LSMs, even though they have evolved from first-generation to third-generation models [14]. This simplification has resulted in the transforming of soil moisture into an index used for calculating evapotranspiration and runoff, rather than representing the actual mass of moisture in the soil [12]. This has led to poor simulation of soil moisture dynamics in extremely dry environments [17], such as deserts. The invalidity of this simplification has contributed to the lack of realistic physical coupling between soil moisture and temperature. Only diffusive forms of the conservation equations for soil moisture and temperature are used in the LSMs [15]. The coupled moisture and heat transfer model has hardly been used to retrieve soil moisture profiles with a data assimilation technique, even though it has been proven to be successful [18]. Furthermore, there are very few studies tackling the inclusion of atmospheric pressure in the LSMs based on a two-phase flow approach.

In fact, atmospheric pressure variation (e.g. from 86535 to 88123 Pa in the field study) can dynamically move water vapor and dry air in and out of soil [16]. The discussion in Sects. 4.4 and 4.5 shows that airflow is actually strongly coupled to simultaneous moisture and heat transport in the soil. When compared to measured evaporation, the model including airflow mechanisms did improve the simulation of evaporation and brought it closer to reality. On the day immediately after a rainfall event, the effect of including airflow was significant and showed an underestimation error of 33 % if airflow was neglected. It is clear that the coupled liquid, water vapor, dry air and heat transport mechanism (i.e. simultaneous moisture and heat transport including airflow) should be considered in LSMs.

Although the necessity to include airflow mechanisms is discussed, the integration of the proposed model into the land surface model has not been done; this should be done in the near future. With the incorporation of the two-phase model in the land surface model and the data assimilation system, land-atmosphere interaction can consider soil airflow mechanisms as well. For the application of the two-phase model in the data assimilation system, attention needs to be paid to certain matters.

First, the model error, the observation error and the common set of model parameters were fixed. This may produce errors through the non-optimization of the error and filter parameters [11], which may change over time. Secondly, only the measurement of surface soil moisture content was used in the DAS, due to the lack of understanding the heterogeneity of soil hydraulic properties and the difficulties measuring soil moisture content in the extremely dry environment [19, 20]. The third limitation is that the current study is only based on point scale. At regional scale, investigation is needed to evaluate how different model physics perform retrieving soil state variables.

The model performance evaluations focus on model development by identifying dominant parameters that dictate the physical realism of LSMs. These are responsible for correct physical interactions between land-surface and atmosphere. On the other hand, some of the key complexities have to be simplified in the operational off-line mode of LDAS, due to the far from comprehensive model-physics representation of the complicated feedbacks between the surface and the atmosphere. In order to understand the local state and processes in environmental or agricultural management studies, LSMs should be developed with a higher degree of complexity [7, 9]. Nonetheless, Beven [3] and Duan et al. [6] have stated that more complex LSMs will result in more parameters to be estimated, and will probably be over-parameterized given the data typically available for calibration. The results in Chap. 6 verify the latter statement. The comparison result in Chap. 6 shows that the most complex model without soil temperature observations performs better in the DAS than the model with surface observations. It is worthwhile to investigate which combination of the observation and the model physics can optimally retrieve soil state variables.

References

1. Balsamo G, Beljaars A, Scipal K, Viterbo P, van den Hurk B, Hirschi M, Betts AK (2009) A revised hydrology for the ECMWF model: verification from field site to terrestrial water storage and impact in the integrated forecast system. J Hydrometeorol 10(3):623–643
2. Bayard D, Stahli M, Parriaux A, Fluhler H (2005) The influence of seasonally frozen soil on the snowmelt runoff at two Alpine sites in southern Switzerland. J Hydrol 309:66–84
3. Beven K (1989) Changing ideas in hydrology—the case of physically-based models. J Hydrol 105(1–2):157–172
4. Cornwell AR, Harvey LDD (2007) Soil moisture: a residual problem underlying AGCMs. Clim Change 84(3–4):313–336

5. Demaria EM, Nijssen B, Wagener T (2007) Monte Carlo sensitivity analysis of land surface parameters using the Variable Infiltration Capacity model. J Geophys Res Atmos 112(D11):D11113

6. Duan QY, Sorooshian S, Gupta V (1992) Effective and efficient global optimization for conceptual rainfall-runoff models. Water Resour Res 28(4):1015–1031

7. Ek MB, Mitchell KE, Lin Y, Rogers E, Grunmann P, Koren V, Gayno G, Tarpley JD (2003) Implementation of Noah land surface model advances in the national centers for environmental prediction operational mesoscale Eta model. J Geophys Res Atmos 108(D22):8851

8. Goulden ML, Wofsy SC, Harden JW, Trumbore SE, Crill PM, Gower ST, Fries T, Daube BC, Fan S-M, Sutton DJ, Bazzaz A, Munger JW (1998) Sensitivity of boreal forest carbon balance to soil thaw. Science 279(5348):214–217

9. Houser PR, De Lannoy GJM, Walker JP (2010) Land surface data assimilation. In: Lahoz W, Khattatov B, Menard R (eds) Data assimilation: making sense of observation. Springer, Berlin, pp 549–597

10. Kerr YH, Waldteufel P, Wigneron J-P, Delwart S, Cabot F, Boutin J, Escorihuela M-J, Font J, Reul N, Gruhier C, Juglea SE, Drinkwater MR, Hahne A, Martín-Neira M, Mecklenburg S (2010) The SMOS mission: new tool for monitoring key elements of the global water cycle. Proc IEEE 98(5):666–687

11. Reichle RH, Crow WT, Keppenne CL (2008) An adaptive ensemble Kalman filter for soil moisture data assimilation. Water Resour Res 44(3):W03423

12. Robock A, Schlosser CA, Vinnikov KY, Speranskaya NA, Entin JK, Qiu S (1998) Evaluation of the AMIP soil moisture simulations. Glob Planet Change 19(1–4):181–208

13. Schuur EAG, Vogel JG, Crummer KG, Lee H, Sickman JO, Osterkamp TE (2009) The effect of permafrost thaw on old carbon release and net carbon exchange from tundra. Nature 459(7246):556–559

14. Sellers PJ, Dickinson RE, Randall DA, Betts AK, Hall FG, Berry JA, Collatz GJ, Denning AS, Mooney HA, Nobre CA, Sato N, Field CB, HendersonSellers A (1997) Modeling the exchanges of energy, water, and carbon between continents and the atmosphere. Science 275(5299):502–509

15. Shao YP, Henderson-Sellers A (1996) Modeling soil moisture: a project for intercomparison of land surface parameterization schemes phase 2(b). J Geophys Res Atmos 101(D3):7227–7250

16. Tillman FD, Smith JA (2005) Site characteristics controlling airflow in the shallow unsaturated zone in response to atmospheric pressure changes. Environ Eng Sci 22(1):25–37

17. Walker JP, Willgoose GR, Kalma JD (2001) One-dimensional soil moisture profile retrieval by assimilation of near-surface measurements: a simplified soil moisture model and field application. J Hydrometeorol 2(4):356–373

18. Walker JP, Willgoose GR, Kalma JD (2001) One-dimensional soil moisture profile retrieval by assimilation of near-surface observations: a comparison of retrieval algorithms. Adv Water Resour 24(6):631–650

19. Zeng Y, Wan L, Su Z, Saito H, Huang K, Wang X (2009) Dirnal soil water dynamics in the shallow vadose zone. Environ Geol 58:11–23

20. Zeng Y, Su Z, Wan L, Wen J (2011) Numerical analysis of air-water-heat flow in the unsaturated soil Is it necessary to consider airflow in land surface models. J Geophys Res Atmos 116(20):D20107. doi:10.1029/2011JD015835